Damage Prevention After Cable Failure in Redundant Parallel Cable Robots

–

Schadensvermeidung nach Seilversagen bei redundanten parallelen Seilrobotern

Von der Fakultät für Ingenieurwissenschaften,
Abteilung Maschinenbau und Verfahrenstechnik
der Universität Duisburg-Essen
zur Erlangung des akademischen Grades
eines

Doktors der Ingenieurwissenschaften
Dr.-Ing.

genehmigte Dissertation

von
Roland Boumann
aus
Moers

Gutachter:
Prof. Dr.-Ing. Dr. h.c. Dieter Schramm
Univ.-Prof. Dr.-Ing. Dr. h.c. Burkhard Corves
Tag der mündlichen Prüfung: 20. März 2024

"It is incredibly empowering to know that your future is in your hands."
Keanu Reeves

Foreword of the Author

This doctoral thesis was created during my time at the Chair of Mechatronics at the University of Duisburg-Essen. It evolved from my master thesis and was expanded during several research projects on cable robots in which I participated from 2017 until today. Since all of them involved practical applications, considering the safety was always crucial. This holds especially true for the EXIST science transfer program to industrialize cable robots within our spin-off company red cable robots GmbH. Furthermore, we acquired the upcoming DFG funded project STRADAC to expand our research on cable failure.

First and foremost, I would like to thank Prof. Dr.-Ing. Dr. hc. Dieter Schramm for his excellent supervision as a doctoral advisor, his great leadership of the department and for the freedom I enjoyed as a doctoral student under his care. Furthermore, my gratitude belongs to Univ.-Prof. Dr.-Ing. Dr. hc. Burkhard Corves for taking the co-supervision of my thesis, for asking the first question at my first scientific conference and for accompanying me on my path to my doctorate up to the last question in my defense. My very special thanks also belongs to Prof. Dr.-Ing. Tobias Bruckmann for his genuine trust in me, for countless hours of joint research and programming, for many instructive moments, both professionally and personally, and for his support and encouragement of my first scientific endeavours.

A further very special thanks goes to Patrik Lemmen and Robin Heidel, who provided me with the best team I could have imagined during all the projects. There was no one I would rather have worked night shifts with to meet deadlines and get projects off the ground! I would also like to thank them and Tobias Burger in the context of RCR for their support and the freedom to complete this work. I look forward with excitement to our further journey together.

I also want to express my deep thanks to Manfred Schedl who inspired me to become a better engineer, for his advice and his open door; to Edoardo Idà for being an engineering role model, for many discussions on cable robots, for enjoying several CableCons and maintaining our friendship despite the distance; to Clément Gosselin who greatly motivated me with his enthusiastic compliments for my presented research in Taipeh; to Lars Mikelsons for very enjoyable conference attendances and exciting discussions; to Andreas Pott for his exemplary function as an excellent scientist; to Philipp Sieberg who was a few steps ahead and always

encouraged me; to Christian Sturm for his open ear and sharing his experiences; to Christoph Jeziorek, Patrick Gust and Ferdinand Elhardt for their ongoing support with my research work, experiments and proof-reading; to Lukas Herrmann for his support with drone models; to Anton Uselmann for a ride in the erl king; to my office neighbor Markus Nieradzik who has been with me since our first bachelor semester; and to Niko Maas for bringing me to the chair as a student assistant back in 2015 and for seeing potential in me way before I was able to. Joining the department ignited a spark in me! My special thanks moreover belongs to Patrik Lemmen and Michael Meik for bringing up the idea of my research on cable failure back in 2017.

My fellow students who accompanied me both during my studies and my doctorate, all colleagues from the department, as well as external and former doctoral students also deserve my gratitude. I want to thank them for long and productive evenings, celebrations, legendary doctoral seminars, valuable exchange and friendships! It is impossible to list all of them here. Still, in the context of my doctoral phase, I would particularly like to thank Dominic Neumann, Kai Horwat, Laurin Vasile, Maximilian Hohn, Janosch Luttmer and Judith Laichter.

My gratitude further goes to the great and educational people I got to know during project partnerships. In particular, I would like to mention Aileen Pfeil, Wolfgang Eden, Arnim Spengler, Jens Diepenbruck, David Hahlbrock, Martin Heumos and Marco de Stefano. I am also very glad for the community within the IFToMM organization and the countless inspiring and wonderful people I met which I cannot name here, the discussions I had and the conferences I enjoyed all over the world. This exchange has enriched me greatly. My thanks further goes to all the motivated and determined students that I was able to supervise as part of courses, theses and student jobs. I hope I was able to give a lot to them for their engineering careers. They have always encouraged me to become a better teacher.

I am sincerely thankful for the ongoing support of my family and friends, to whom I was not able to give as much time as I would have liked during my studies and the doctoral phase. Further, I want to express my deepest gratitude to my partner for her unwavering support and understanding in chasing my dreams. Finally, I would like to thank my parents, who have encouraged me from an early age that I can achieve anything I dream of. They have been there for me in every easy and difficult time and have given me the necessary backing and unlimited support on every path I have ever taken in life!

Mülheim an der Ruhr, April 2024 Roland Boumann

Abstract

The goal of this thesis is to increase safety and reliability of redundant cable-driven parallel robots (CDPRs). A CDPR uses a set of computerized winches to move a common platform carrying a robotic tool. Towards industrial application of such robots, e.g. in automated masonry work, potential cases of failure need to be considered. A rare but hazardous fault is the failure of a cable, which is focused in this dissertation.

Initially, it is elaborated how this failure affects a redundant CDPR. Besides a drastic reduction of the workspace, the failure can lead to an uncontrolled platform movement. This may result in a loss of payload or a crash of the platform, potentially causing system or environmental damage and harm to people nearby. To prevent subsequent damage, two new emergency strategies are developed, utilizing the remaining cables of a redundant CDPR to bring the post-failure system into a safe state.

Various emergency strategies for cable failure in CDPRs exist. However, to the authors best knowledge, none of them has been validated on a real spatial redundant CDPR with six degrees of freedom. In addition, most of the known strategies use trajectory planning along pre-defined paths, which might be time critical in case of failure. The two strategies developed, on the opposite, recreate a reflexive behavior that does not require pre-defined trajectories.

The first strategy presented in this work aims at minimizing the systems kinetic energy, which leads the robot into a static force equilibrium pose. It is based on a nonlinear model predictive control forecasting the platform's movement that follows from set-point cable forces. The second strategy presented uses potential fields in the workspace that introduce virtual forces and torques to the platform. While an attractive field guides the platform into a static force equilibrium pose, repulsive fields avoid collisions with obstacles in the workspace. As the required platform wrench might be unfeasible, the so-called Nearest Corner Method is developed to obtain approximated cable force distributions in real-time outside the wrench-feasible workspace. Furthermore, a conventional CDPR controller ignoring the failed cable as well as the usage of motor brakes are considered.

For low-risk testing of the developed strategies, a multibody simulation representing the SEGESTA prototype owned by the Chair of Mechatronics at the University of Duisburg-

Essen is set up and a variety of simulations is conducted. Simulation results show that the conventional controller with fault tolerance and the use of motor brakes mainly stabilize the platform only in the post-failure workspace. Conversely, the two proposed emergency strategies can rescue the platform from outside of it in various scenarios while preventing it from crashing. As both methods have many parameter setting options, their influences are carefully elaborated.

Based on the successful simulative assessment of the strategies, a practical examination is conducted with experiments on the SEGESTA prototype. To mimic a cable failure, a mechatronic cable decoupling device is developed and tested based on a requirement analysis. Furthermore, a simple yet effective and reliable failure detection algorithm to determine a cable failure is introduced and tested. Both emergency strategies are subsequently validated in successful rescue scenarios on the SEGESTA prototype. Additionally, the robot operation with a reduced set of cables in the post-failure workspace after successful stabilization is demonstrated.

Finally, practical examples of CDPRs in the construction industry are considered, including large scale 3D-printing of concrete as well as automated masonry work. For both applications, full scale prototypes are realized within the research group during the path of this work. An approach for generating optimal trajectories based on cost functions and penalty terms is further introduced and demonstrated. In a simulated cable failure scenario of a CDPR performing automated masonry work, the emergency strategies are also applied. It is demonstrated that both approaches can prevent the platform from crashing into the already erected building structures. Moreover, a vertical pulley reconfiguration feature is used to extend the capability of the Kinetic Energy Minimization Method. This feature can also recover lost workspace after a cable failure, increasing the operational range of the robot. This allows for more effective operation until the robot is repaired and maintained.

In summary, it can be stated that the developed emergency strategies for damage prevention after cable failure in redundant CDPRs are successfully validated in simulation as well as on a real prototype. Both approaches are not limited to an emergency situation and may also serve for regular CDPR control. Especially their practical validation emphasizes their benefit for upcoming industrial usage of cable-driven parallel robots and empowers the transfer of knowledge from research into practice.

Kurzfassung

Das Ziel dieser Arbeit ist die Erhöhung der Sicherheit und Zuverlässigkeit von redundanten parallelen Seilrobotern. Ein Seilroboter nutzt mehrere computergesteuerte Winden, um eine gemeinsame Plattform zu bewegen, die ein Roboterwerkzeug trägt. Im Hinblick auf den industriellen Einsatz solcher Roboter, z. B. beim automatisierten Mauerwerksbau, müssen potenzielle Versagensfälle berücksichtigt werden. Ein seltener aber gefährlicher Fehler ist das Versagen eines Seils. Dieser steht hier im Fokus.

Es wird zunächst herausgearbeitet, wie sich dieser Ausfall auf einen redundanten Seilroboter auswirkt. Neben einer drastischen Reduzierung des Arbeitsraumes kann der Ausfall zu einer unkontrollierten Plattformbewegung führen. Dies kann in einem Verlust der Nutzlast oder einem Absturz der Plattform resultieren und zu Schäden am System, der Umwelt oder Personen in der Nähe führen. Zur Vermeidung von Folgeschäden werden zwei Notfallstrategien entwickelt, welche die verbleibenden Seile eines Seilroboters nutzen, um das System nach einem Seilversagen in einen sicheren Zustand zu bringen.

Es existieren diverse Strategien bei Seilversagen eines Seilroboters. Jedoch wurde nach bestem Wissen des Autors bisher keine davon auf einem realen redundanten Seilroboter mit sechs Freiheitsgraden validiert. Darüber hinaus nutzen die meisten der bekannten Strategien eine Trajektorienplanung entlang vordefinierter Pfade, was im Falle eines Fehlers zeitkritisch sein kann. Die beiden entwickelten Strategien bilden dagegen ein reflexartiges Verhalten nach, welches ohne vordefinierte Trajektorien auskommt.

Die erste in dieser Arbeit präsentierte Strategie zielt darauf ab, die kinetische Energie des Systems zu minimieren, was den Roboter in eine Pose mit statischem Kräftegleichgewicht leitet. Sie basiert auf einer nichtlinearen modellprädiktiven Regelung, welche die Plattformbewegung anhand von gestellten Seilkräften vorhersagt. Die zweite präsentierte Strategie nutzt Potentialfelder im Arbeitsraum, die virtuelle Kräfte und Momente auf die Plattform einprägen. Während ein anziehendes Feld die Plattform in eine Pose mit statischem Kräftegleichgewicht bringt, vermeiden abstoßende Felder Kollisionen mit Hindernissen im Arbeitsraum. Da der benötigte Kraftwinder an der Plattform möglicherweise nicht realisierbar ist, wird die so genannte Nearest-Corner Methode entwickelt, um in Echtzeit approximierte Seilkraftverteilungen außerhalb des *Wrench-Feasible Workspace* zu erhalten. Weiterhin wer-

den ein konventioneller Seilroboter-Regler, welcher das gerissene Seil ignoriert, sowie die Verwendung von Motorbremsen betrachtet.

Für risikoarme Tests der entwickelten Strategien wird eine Mehrkörpersimulation aufgebaut, welche den SEGESTA-Prototyp des Lehrstuhls für Mechatronik der Universität Duisburg-Essen repräsentiert, und eine Vielzahl von Simulationen wird durchgeführt. Simulationsergebnisse zeigen, dass der konventionelle Regler mit Fehlertoleranz sowie der Einsatz von Motorbremsen die Plattform hauptsächlich nur im *Post-Failure Workspace* stabilisieren. Die beiden Notfallstrategien allerdings können die Plattform auch von einer Vielzahl außerhalb liegender Posen aus bergen und verhindern einen Absturz. Da beide Methoden viele Parametereinstellmöglichkeiten besitzen, wird deren Einfluss sorgfältig herausgearbeitet.

Basierend auf der erfolgreichen simulativen Bewertung der Strategien wird eine praktische Untersuchung mit Experimenten am SEGESTA-Prototyp durchgeführt. Um ein Seilversagen nachzustellen, wird eine mechatronische Seilentkopplungsvorrichtung auf der Grundlage einer Anforderungsanalyse entwickelt und getestet. Weiterhin wird ein einfacher aber zuverlässiger Fehlerdetektionsalgorithmus zur Ermittlung eines Seilversagens vorgestellt und erprobt. Beide Notfallstrategien werden anschließend in erfolgreichen Rettungsszenarien am SEGESTA-Prototyp validiert. Auch der Betrieb des Seilroboters mit einer reduzierten Seilzahl im *Post-Failure Workspace* wird nach erfolgreicher Stabilisierung demonstriert.

Abschließend werden praktische Beispiele für Seilroboter im Bauwesen betrachtet, einschließlich des großflächigen 3D-Betondrucks und der automatisierten Errichtung von Mauerwerk. Für beide Anwendungen werden innerhalb der Forschungsgruppe im Verlauf dieser Arbeit Prototypen in Originalgröße realisiert. Ein Ansatz für die Generierung optimaler Trajektorien auf der Grundlage von Kostenfunktionen und Straftermen wird vorgestellt und demonstriert. In einem simulierten Seilrissszenario eines mauernden Seilroboters werden die Notfallstrategien ebenfalls angewendet. Es wird gezeigt, dass beide Ansätze einen Absturz der Plattform in die bereits errichteten Gebäudestrukturen verhindern können. Darüber hinaus wird die Notfallstrategie basierend auf kinetischer Energieminimierung durch eine dynamische vertikale Rekonfiguration der Umlenkrollen erweitert. Diese Funktion kann ebenfalls verlorenen Arbeitsbereich nach einem Seilversagen wiederherstellen, was eine effektivere Weiternutzung ermöglicht, bis der Roboter repariert und gewartet wird.

Zusammenfassend ist festzustellen, dass die entwickelten Notfallstrategien zur Schadensvermeidung nach Seilversagen in redundanten parallelen Seilrobotern sowohl in der Simulation als auch an einem realen Prototyp erfolgreich validiert werden. Beide Ansätze sind nicht auf die Notfallsituation limitiert, sondern können auch zur herkömmlichen Roboterregelung dienen. Insbesondere ihre praktische Validierung unterstreicht ihren Nutzen für den kommenden industriellen Einsatz von parallelen Seilrobotern und stärkt den Wissenstransfer von der Forschung in die Praxis.

Contents

List of Figures

List of Tables

List of Commonly Used Symbols and Abbreviations

Symbol	Description
General Definitions	
${}^{A}_{B}\boldsymbol{d}_{C}$	General vector $\boldsymbol{d}$ from point B to point C referenced within the system $\uparrow_{\rightarrow}^{A}$
d_x	x component of the vector $\boldsymbol{d}$
d_1	First entry of the vector $\boldsymbol{d}$
$\dot{\boldsymbol{d}}$	First time derivative of the vector $\boldsymbol{d}$
$\ddot{\boldsymbol{d}}$	Second time derivative of the vector $\boldsymbol{d}$
$\dddot{\boldsymbol{d}}$	Third time derivative of the vector $\boldsymbol{d}$
$\boldsymbol{d}^*$	Vector $\boldsymbol{d}$ excluding the entry for the failed cable
$\boldsymbol{D}^*$	Matrix $\boldsymbol{D}$ excluding the entry for the failed cable
${}^{A}\boldsymbol{R}_{B}$	Rotational matrix from system $\uparrow_{\rightarrow}^{B}$ to system $\uparrow_{\rightarrow}^{A}$
$\boldsymbol{R}_x$	Elemental rotation about x-axis
$[\boldsymbol{a}_{\min}, \boldsymbol{a}_{\max}]$	Interval describing the lowest and highest values allowed for $\boldsymbol{a}$ if not defined otherwise
Abbreviations	
AABB	Axis aligned bounding boxes
APD	Augmented PD
BIM	Building information modeling
CARLO	Cable robot for large scale operations
CDPR	Cable-driven parallel robot
CRPM	Completely restrained positioning mechanism
DFG	Deutsche Forschungsgemeinschaft (German research foundation)
DOF	Degrees of freedom (of the mobile platform)
FMEA	Failure mode and effects analysis
IFC	Industry foundation classes

IRPM	Incompletely restrained positioning mechanism
NMPC	Nonlinear model predictive control
MPC	Model predictive control
OBB	Object oriented bounding boxes
PLC	Programmable logic controller
R	Rotational DOF
RRPM	Redundantly restrained positioning mechanism
SEGESTA	Seilgesteuerte Stewart-Plattformen in Theorie und Anwendung (Cable-driven stewart platforms in theory and application)
SQP	Sequential quadratic programming
T	Translational DOF
TRL	Technology readiness level

Calligraphic Abbreviations

$\mathcal{C}$	Hypercube containing feasible cable force distributions
$\mathcal{D}$	Demand
$\mathcal{DEW}$	Dynamic equilibrium workspace
$\mathcal{F}$	Manifold containing all feasible cable force distributions
$\mathcal{G}$	Discrete grid for workspace definition
$\mathcal{G}_{\mathcal{SECOW}}$	Feasible Poses in $\mathcal{G}$ belonging to the $\mathcal{SECOW}$
$\mathcal{G}_{\mathcal{SEOW}}$	Feasible Poses in $\mathcal{G}$ belonging to the $\mathcal{SEOW}$
$\mathcal{H}$	Support matrix for kinematic KARDAN equations
$\mathcal{P}$	Penalty term
$\mathcal{R}$	Requirement
$\mathcal{REW}$	Reachable workspace
$\mathcal{S}$	Solution space of cable forces
$\mathcal{SECOW}$	Static equilibrium constant orientation workspace
$\mathcal{SEOW}$	Static equilibrium orientation workspace
$\mathcal{SEW}$	Static equilibrium workspace
$\mathcal{SSW}$	Statically stable workspace
$\mathcal{V}$	Cost value
$\mathcal{V}_{\text{total}}$	Total costs
$\mathcal{W}$	Cost weighting
$\mathcal{WCW}$	Wrench-closure workspace
$\mathcal{WEC}$	Wrench-exertion capability
$\mathcal{WFW}$	Wrench-feasible workspace

Coordinate Systems

$\underline{B}$	Inertial frame
$\underline{D_i}$	Frame fixed at i-th pulley
$\underline{P}$	Platform fixed frame

Latin Symbols

a	Polynomial coefficient
$\boldsymbol{A}^{\mathrm{T}}$	Structure matrix of the CDPR
$\boldsymbol{A}^{+\mathrm{T}}$	Moore-Penrose-Pseudo-Inverse of $\boldsymbol{A}^{\mathrm{T}}$
A_c	Cable cross section
$\boldsymbol{A}_e^{\mathrm{T}}$	Estimated structure matrix of the CDPR
$\boldsymbol{A}_h^{\mathrm{T}}$	Homogenized structure matrix of the CDPR
$\boldsymbol{b}_{d,i}$	Vector from inertial frame to cable exit point of the i-th pulley
$\boldsymbol{b}_i$	Vector to pulley of i-th cable
$\boldsymbol{B}$	Matrix containing all $\boldsymbol{b}_i$
$\boldsymbol{c}$	Weighting factors
$\boldsymbol{C}$	Output matrix
$\boldsymbol{C}_s$	Compliance matrix
d_b	Border distance between quadratic and conic potential
$d_{c,i}$	Damping of i-th cable
$\boldsymbol{d}_i$	Vector from pulley frame to cable exit point of the i-th pulley
d_{mea}	Measured distance
d_{min}	Influence distance of an object
$d_{o,ij}$	Distance to each object for the mobile platform
$d_{S,j}$	Distance of j-th corner to the solution space $\mathcal{S}$
$\boldsymbol{D}_1$,$\boldsymbol{D}_2$	Diagonal gain matrices for virtual damping
e	Optimization function to solve cable force distribution
e_c	Elongation of cable at working point
E_c	Cable Young modulus
E_{Kin}	Kinetic system energy
E_{total}	Total Energy
$\boldsymbol{f}$	Vector containing all cable tensions
$\tilde{\boldsymbol{f}}$	Desired tension level in cable force distribution
f_b	Breaking load of a cable
$\boldsymbol{f}_D$	Set point cable forces
$\boldsymbol{f}_e$	Vector of external forces acting at gravitational center of the mobile platform

$\boldsymbol{f}_{FK}$	Forward kinematics mapping
f_i	Cable tension of i-th cable in cable direction
$\boldsymbol{f}_i$	Vector of force applied to the platform by the i-th cable
$\boldsymbol{f}_{IK}$	Inverse kinematics mapping
$\boldsymbol{f}_{\text{is}}$	Vector containing current cable tensions
$f_{\max}$	Upper cable force limit
$\boldsymbol{f}_{\text{mea}}$	Vector containing measured cable tensions
$f_{\min}$	Lower cable force limit
$\boldsymbol{f}_0$	Projection of desired wrench onto solution space
$\boldsymbol{F}$	Virtual Force resulting from potential fields
$\boldsymbol{F}_{\text{att}}$	Attractive virtual force
F_c	Stribeck sliding friction
$\boldsymbol{F}_{E,j}$	j-th corner of the hypercube $\mathcal{C}$
F_f	Stribeck frictional Torque
$\boldsymbol{F}_{P,j}$	j-th corner projected onto the solution space $\mathcal{S}$
$\boldsymbol{F}_{\text{rep}}$	Repulsive virtual force
F_s	Stribeck static friction
F_v, $F_{v,s}$	Stribeck viscous friction for drives and pulley slides
g	Gravitational acceleration
g_j	Weight of each corner
G	Sum of weights
h_i	Length between the center of the i-th pulley and $\boldsymbol{p}_i$
$\boldsymbol{H}$	Kernel of the structure matrix
i	Count variable
$\boldsymbol{I}_m$	$m \times m$ identity Matrix
j	Count variable
J	Cost function value
$\boldsymbol{J}$	Jacobian matrix of the CDPR
$J_{c,i}$	Rotational inertia of i-th coupling
$J_{d,i}$	Rotational inertia of i-th drive unit
J_{Ekin}	Cost function for kinetic energy minimization
$J_{g,i}$	Rotational inertia of i-th gear
$J_{m,i}$	Rotational inertia of i-th motor
$\boldsymbol{J}_v$	Diagonal homogenization matrix
$J_{w,i}$	Rotational inertia of i-th cable drum
j_x, j_y, j_z	Medium platform radii
k	Count variable

$\boldsymbol{K}$	Vector of Coriolis and centrifugal forces and torques at the mobile platform
$k_{c,i}$	Stiffness of i-th cable
$\boldsymbol{K}_c$	Passive stiffness matrix
$\boldsymbol{K}_D$	Derivative gain matrix
$\boldsymbol{K}_g$	Active stiffness matrix
$\boldsymbol{K}_P$	Proportional gain matrix
$\boldsymbol{K}_s$	Stiffness matrix
$\boldsymbol{l}$	Vector containing all cable lengths
L	Summarized distance
$l_{d,i}$	Cable length between drum and pulley
$\boldsymbol{l}_D$	Vector of desired cable lengths
l_i	Length of i-th cable
$\boldsymbol{l}_i$	Vector of i-th cable
Δl_i	Cable length difference
$l_{i,0}$	Length of i-th cable at starting pose $\boldsymbol{x}_{P,0}$
$l_{i,tot}$	Total length of i-th cable
$\boldsymbol{l}_\theta$	Vector of all cable lengths derived from encoder measurements
m	Number of cables
m_P	Mass of mobile platform
m_s	Mass of pulley sliding mechanism
$\boldsymbol{M}$	Mass matrix of the mobile platform
n	Number of DOF of the mobile platform
$\boldsymbol{N}$	Matrix describing cable force boundaries
n_c	Control horizon
n_d	Number of discretization steps
$\boldsymbol{n}_g$	Diagonal matrix containing all m gear ratios
$n_{\max}$	Maximum optimization iterations
n_o	Number of objects
n_p	Prediction horizon
n_{post}	Number of feasible workspace points post reconfiguration
n_{pre}	Number of feasible workspace points pre reconfiguration
n_r	Number of rotational DOF
n_s	Number of splines
n_t	Number of translational DOF
n_ζ	Gear transmission at pulley slide drive
o	Number of repulsive fields

$\boldsymbol{o}_b$	Nearest point to the mobile platform on obstacle border
p	Exponential weight
$\boldsymbol{P}$	Matrix containing all vectors $\boldsymbol{p}_i$
$\boldsymbol{p}_i$	Vector to cable attachment of the i-th cable at the platform
P_E	Power
p_r	Maximum platform radius
$\boldsymbol{q}$	Vector of joint coordinates
$\boldsymbol{Q}$	Vector of external forces and torques at the mobile platform
q_i	i-th joint coordinate
r	Degree of kinematic redundancy
$\boldsymbol{R}$	Weighting matrix
$\boldsymbol{r}_D$	Desired position of the mobile platform
${}_s\boldsymbol{r}_i$	Vector from center of gravity to i-th cable attachment point at the mobile platform
$\boldsymbol{r}_P$	Position vector of the mobile platform
$\boldsymbol{r}_{P,e}$	Estimated position vector of the mobile platform
$\boldsymbol{r}_{P,\text{err}}$	Position error
$\boldsymbol{r}_{P,\text{final}}$	Potential Field: Desired final position
$\boldsymbol{r}_S$	Position vector to the center of gravity of the mobile platform
${}_P\boldsymbol{r}_S$	Vector from platform frame to it's center of gravity
$\boldsymbol{s}$	Vector containing magnitudes of upwards pulley movements
S	Center of gravity
Δt_c	Prediction time step
t_f	Final time
t_k	k-th discrete time step
$\boldsymbol{t}_s$	Vector containing all spline times
T_t	Dead time
t_{total}	Total time
t_0	Starting time
T_1	Time constant
$\boldsymbol{u}$	Control variables
$\boldsymbol{U}_{\text{pot}}$	Artificial potential field
$\boldsymbol{U}_{\text{att}}$	Artificial attractive potential field
$\boldsymbol{U}_{\text{rep}}$	Artificial repulsive potential field
v	Forward kinematic optimization problem
v_s	Stribeck velocity pulley sliding mechanism
$\boldsymbol{v}$	Vector describing cable force boundaries

$\boldsymbol{w}_E$	External wrench at the mobile platform
$w_{\min}$	Influence distance of an object
$w_{o,ij}$	Distance to each object for each cable
$\boldsymbol{w}_{\mathrm{PD}}$	Wrench obtained by model based controller
$\boldsymbol{W}_1$,$\boldsymbol{W}_2$	Weighting matrices
$\boldsymbol{x}$	System state
$\tilde{\boldsymbol{x}}$	Observed system state
$\boldsymbol{x}_D$	Desired platform pose
$\boldsymbol{x}_e$	Platform pose estimation
$\boldsymbol{x}_{\mathrm{err}}$	Pose error
$\boldsymbol{x}_P$	Platform pose
$\boldsymbol{x}_{P,0}$	Starting pose
$\boldsymbol{x}_{P,\mathrm{final}}$	Origin of attractive potential field
$\Delta\boldsymbol{x}_P$	Discretization step of platform pose within workspace definition
$\delta\boldsymbol{x}_{P,h}$	Homogenized displacement of the pose
$\boldsymbol{y}$	System output
$\boldsymbol{y}_r$	System reference output
z_b	Building height
$\boldsymbol{z}$	Vector describing cable force equation
$\boldsymbol{Z}$	Matrix describing cable force equation

Greek Symbols

α_i	Rotation angle of i-th pulley
β_i	Wrapping angle of i-th cable around it's pulley
γ	Count variable
δ	Deviation
ϵ, ϵ_s	Stribeck form factors
ζ	Gain factor of attractive potential
$\boldsymbol{\zeta}_r$	Diagonal gain matrix for attractive potential on position level
$\boldsymbol{\zeta}_\Phi$	Diagonal gain matrix for attractive potential on orientation level
η	Gain factor of repulsive potential
η_s	Torque transmission efficiency of pulley sliding mechanism gear
η_g	Torque transmission efficiency of drive unit gear
η_n	Inverter efficiency
η_r	Recuperation efficiency
ϑ	Rotation angle about the y-axis of the inertial frame
$\boldsymbol{\Theta}_S$	Inertial tensor of the mobile platform in the center of gravity

$\boldsymbol{\Theta}_P$	Inertial tensor of the mobile platform with reference to the platform frame
$\boldsymbol{\theta}$	Vector of cable drum angles
θ_s	Stribeck rotational velocity
κ	Stiffness criterion
$\boldsymbol{\lambda}$	Vector of multipliers in the nullspace of the structure matrix
Λ	Polytope containing wrench-feasible solutions
μ_c	Static friction coefficient
μ_s	Sliding friction coefficient
$\boldsymbol{\nu}_i$	Unit vector of the i-th cable
$\rho_{d,i}$	Radius of i-th cable drum
ρ_f	Euclidean distance between pose and attractive field
ρ_i	Radius of the i-th pulley
ρ_{rep}	Shortest distance between mobile platform and an obstacle
ρ_s	Sprocket radius
ρ_0	Influence distance of an obstacle
$\boldsymbol{\varsigma}$	Vector of slack variables
τ	Torque
$\boldsymbol{\tau}_{\text{att}}$	Vector of attractive virtual torque
$\boldsymbol{\tau}_c$	Vector of produced motor torques
$\boldsymbol{\tau}_D$	Vector of set-point motor torques
$\boldsymbol{\tau}_e$	Vector of external torques acting at gravitational center of the mobile platform
$\boldsymbol{\tau}_f$	Vector of torques at the mobile platform resulting from cable forces
$\boldsymbol{\tau}_s$	Vector of motor torques to move sliding pulleys
$\boldsymbol{\Upsilon}$	Forward kinematics support function
φ	Rotation angle about the x-axis of the inertial frame
$\boldsymbol{\Phi}$	Orientation of the platform with respect to the inertial frame
$\boldsymbol{\Phi}_D$	Desired orientation of the mobile platform
$\boldsymbol{\Phi}_e$	Estimated orientation of the platform
$\boldsymbol{\Phi}_{P,\text{err}}$	Orientation error
$\boldsymbol{\Phi}_{\text{final}}$	Potential Field: Desired final orientation
χ	Cost function criteria
ψ	Rotation angle about the z-axis of the inertial frame
$\boldsymbol{\omega}_P$	Angular platform velocity

Chapter 1

Introduction

This chapter provides an introduction to the robot technology addressed in this work, which is based on cable-driven parallel robots. It includes a categorization of these robots based on their kinematic structure, an explanation of their main parts and working principles, and a discussion of their advantages and disadvantages compared to conventional robot systems. Additionally, it presents an overview of prototypes and applications worldwide, featuring some of the most popular cable robots. Furthermore, this chapter briefly describes the history of cable robots at the Chair of Mechatronics at the University of Duisburg-Essen, leading to an overview of the current prototype situation. Thereupon, the motivation to consider cable failure in particular is explained, followed by a presentation of this problem. The work of various researchers in this field is presented and discussed, forming the current state of the art. Based on this, the research gap and questions are identified, leading to the work program of this thesis. Finally, an overview of the content is provided.

1.1 Preamble on Cable-Driven Parallel Robots

Although research has been conducted on cable-driven parallel robots (CDPRs) since the 1980's [Pott, 2018], the term may require a brief explanation. The principle of CDPRs is straightforward and can be explained concisely: Cables are connected to a mobile platform (also called end effector) and move it in space, typically by winding or unwinding the cables

on winches.[1] The platform usually carries a tool to perform a specific task or the cables may be directly connected to an object being transported. In general, the winches consist of a cable drum that coils a cable and a controlled drive that powers the rotating motion. This lightweight robot design offers several advantages, which are explained at the end of the upcoming section. Furthermore, the categorization of CDPRs within robotics is presented and a more detailed explanation of their working principle is provided.

1.1.1 Serial, Parallel and Cable Robots

A robot can be defined as "a machine controlled by a computer that is used to perform jobs automatically" [Cambridge University Press, 2023]. They can be categorized by their kinematic[2] structure [Siciliano and Khatib, 2008].

The most common structure is the serial kinematic structure, which resembles a human arm and consists of a series of joints. Figure 1.1a displays a conventional serial industrial robot from the popular company KUKA. The kinematic of such a mechanism is serial, as only

(a) Serial industrial robot from the company KUKA.

(b) Hexapod robot from the company FANUC.

(c) Delta robot (Flexpicker) from the company ABB.

Figure 1.1: Comparison of robots with different kinematics. Image source: [DGUV, 2015].

one chain of links and joints exists, leading to the end effector.

This is in contrast to parallel kinematic structures, where multiple kinematic chains connect the end effector and the robot's base [Pott, 2018]. As a result, closed-loop kinematic chains (also known as kinematic loops) emerge. This alternates the analysis of such structures

[1] Alternative solutions, such as rail-based systems with constant cable lengths, exist. In these systems, the platform's motion is generated by the translational movement of the cable anchor points on the rails [Sturm et al., 2011].

[2] Kinematics is the study of motion in bodies, such as those found in robotic mechanisms, without taking into account the forces and torques that cause the motion. [Siciliano and Khatib, 2008]

in comparison to their serial counterparts [Siciliano and Khatib, 2008]. It is important to note that in this case, parallelism refers to the topological structure of the robot and not to its geometry.[3]

The STEWART-GOUGH-Platform, shown in fig. 1.1b, is a special type of parallel kinematic machine. It consists of six translational joints based on linear actuators that move a platform in space [Wenz, 2008].[4] The STEWART-GOUGH-Platform dates back to the universal tire test machine originally developed by Dr. E. Gough in 1962 [Gough and Whitehall, 1962] and a flight simulator concept by D. Stewart in 1965 [Stewart, 1965, Stewart, 1966]. Both applications, including further additional ones, continue to be commercially successful today [Bruckmann, 2010]. Another well-known example of parallel robots is the delta robot, as pictured in fig. 1.1c.

As stated by [Bruckmann, 2010, Merlet, 2010, Pott, 2018], parallel robots have a better payload-to-weight ratio compared to serial robots. They also exhibit higher stiffness at the same weight and higher dynamics due to reduced moving masses, resulting in improved energy efficiency. Specific designs can also increase the precision of the platform since a single actuator position error does not have a full impact on the platform position due to the remaining kinematic loops. Using identical joints can reduce manufacturing costs through the principle of equal parts. However, conventional parallel machines typically have a smaller workspace[5] than serial robots, which also accounts for the ratio between the volumes of the workspace and the construction space. This restriction is primarily due to the limited range of the linear actuators used.

If the linear actuators are replaced by cables and winches, as proposed by Landsberger [Landsberger and Sheridan, 1985] in 1985, a cable robot is created. Other common names for the term cable-driven parallel robot (CDPR) are: “wire robot“ [Merlet, 2004a], “cable-based parallel manipulator“ [Ceccarelli et al., 2007], “tendon-based parallel manipulator“ [Fang, 2005] or “tendon-based Stewart platform“ [Verhoeven, 2006]. These names all involve different terminologies for the cable, such as tendon, wire or just cable. The latter is used throughout this work as it has become the most widely accepted term in the literature [Bruckmann and Pott, 2012, Caro et al., 2023, Gosselin et al., 2017, Gouttefarde et al., 2021, Pott and Bruckmann, 2014, Pott and Bruckmann, 2019, Pott, 2018]. Other common names refer to a hanging platform on cables such as “cable-suspended parallel robot“ [Fattah and Agrawal, 2005] or “cable suspension manipulator“

[3] An illustrative example to explain this remark is comparing a parallel kinematic topology to an electrical circuit with parallel resistance elements [Pott, 2018]. Just as the current is divided between the resistors, the force is divided between the joints.

[4] Another common name for the STEWART-GOUGH-Platform is Hexapod, coming from the Greek words hexa (meaning six) and pod (meaning foot) [Bruckmann, 2010].

[5] Workspace is a term commonly used in robotics to describe the area in which the end effector can operate. A more precise definition can be found in Section 2.4.

[Heyden et al., 2002]. Another common abbreviation is simply “cable robot“.

The use of cables involves several aspects that should be considered, as elaborated in [Bruckmann, 2010, Pott, 2018]. First, CDPRs have a series of advantages which are listed below:

- Cables can be coiled on drums, allowing for kinematic chains of almost any length and therefore expanding workspaces. This eliminates the general disadvantage of small workspace volumes in parallel robots.
- Typically, steel cables or highly durable synthetic fiber cables are used. Both of which have excellent load-bearing capacity, which enables heavy payload handling. Only synthetic fiber cables are considered in this work.
- CDPRs have a very lightweight design. Cable mass is negligible compared to rigid robot arm elements. This promotes energy efficiency, especially using synthetic fiber cables.
- Cables can be wound and unwound very quickly. Combined with a low own mass, this allows for very high platform speed and acceleration.
- Typically, identical components can be used for each winch (e.g. electronic drives, cable drum, cable, bearings). This promotes the cost-effectiveness of cable robots.
- The drives can be placed decentralized and outside of the workspace. This can be highly advantageous in various applications, e.g. where dirt and dust are present.
- The robot and the resulting workspace can be optimized to perform a given task. This procedure is called design-to-task [Bruckmann et al., 2011]. Adding cables, e.g., can improve the load capacity but it also increases cost and complexity and further complicates collision avoidance. However, a higher number of redundant cables may also increase the system's resistance against cable failures, since more operational cables remain after one cable fails. This is further elaborated in Section 1.2 and Section 3.1.

In addition to the benefits listed above, some further aspects need to be considered when using cables to actuate a platform [Bruckmann, 2010, Pott, 2018]:

- In general, cables can only transmit tensile forces and are assumed to be massless[6]. Therefore, tensioning of the system must be provided either by the action of external loads such as gravity or by tensioning multiple cables against each other. In a system with antagonizing cables and electronic drives, recuperation is possible, which also promotes energy efficiency.

[6]While this is a very common assumption for most CDPRs, the cable mass and the resulting impact on the platform might be non neglectable for very large robots [Riehl et al., 2009].

- Cables generally have a stretch behavior making them more flexible than rigid links or conventional linear actuators. In comparison to a conventional parallel robot, a CDPR platform is expected to be less stiff[7]. However, for a CDPR with antagonizing cables, the platform stiffness can be increased by enhancing the inner tension of the system. Still, it is useful to consider the eigendynamics and the change in length of the flexible joints within the kinematic models and the control.

- Above a certain ratio of mass-to-cable-length, the cables may also sag, which affects the kinematic models and the point of force application on the platform [Merlet, 2015].

- The arrangement of cable attachment points at the robot platform, the number of cables, and the positions of their entry into the workspace lead to fundamentally different workspace shapes and sizes. This arrangement is further called robot configuration.

The most common setup of a cable robot is built up as follows: Typically, a mobile platform (end effector) is used with m cables attached in a parallel configuration. The cables are guided to the platform by pivoting or fixed pulleys attached to a stationary base, such as a steel or aluminum frame. The platform is moved by winding or unwinding the cables on computerized drums powered by electric drives. There are divergent setups, e.g. using linear actuators to move cables of constant lengths [Sturm et al., 2011, Sturm, 2020] or incorporating a rod and passive springs [Zhang et al., 2020a, Zhang et al., 2020b]. Such approaches will not be discussed further here, as they are beyond the scope of this thesis. Further details on the theoretical foundations of CDPRs are given in Chapter 2.

1.1.2 Overview on Prototypes and Applications

Using cables to manipulate objects has a tradition going back thousands of years. The hoist was one of the early advanced technologies that allowed people to lift heavy objects, dating back to the pyramid buildings of ancient Egypt [Bruckmann, 2010]. In addition, cables and winches have been utilized in construction work for centuries, making them well-known components. Based on this, tremendously impressive cable-based robot prototypes have been developed by various research groups that have emerged to study CDPRs. At this point, it is not feasible to list all groups that have contributed to progress in this area. Credit is due to all concerned. Nevertheless, a few prominent examples shall be mentioned here without valuation by naming. Note that the focus here is on projects outside of the work group to which the author belongs. The latter will be taken up in the following section.

[7]The stiffness of the platform describes it's resistance against displacement caused by external forces and torques, see Section 2.2.8.

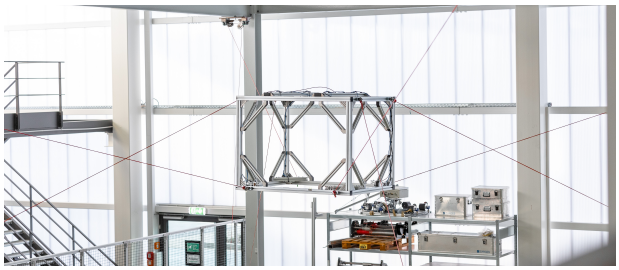

(a) IPAnema 3 prototype. Image courtesy of Marc Fabritius, Fraunhofer IPA.

(b) LIRMM/TECNALIA CoGiRo prototype. Image courtesy of Marc Gouttefarde, LIRMM.

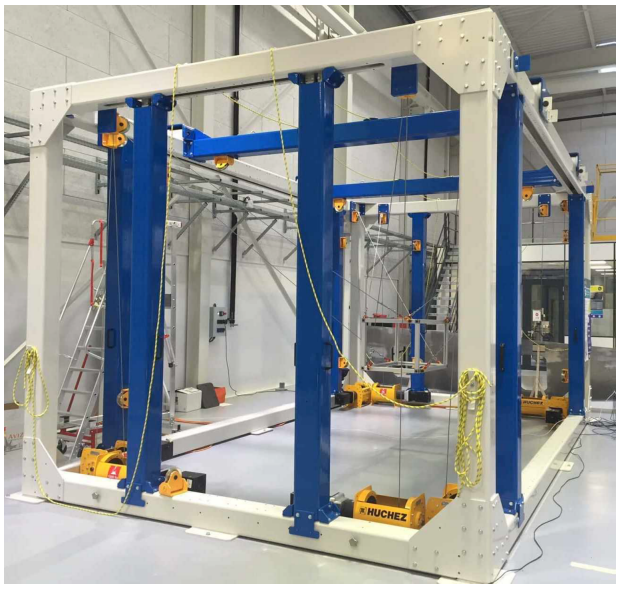

(c) CAROCA prototype. Image courtesy of Nicolò Pedemonte, IRT Jules Verne.

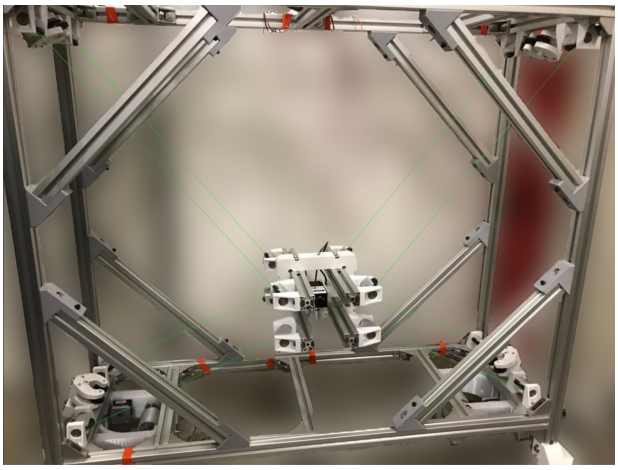

(d) Research prototype of the IRMA Lab. Image courtesy of Edoardo Idà, UNIBO.

Figure 1.2: Various cable robot prototypes.

Figure 1.2 depicts some of the following examples. In Stuttgart, Germany, the IPAnema robot family was developed featuring various prototypes of different sizes [Pott, 2018, Pott et al., 2013], mainly with more cables than degrees of freedom at the platform, see fig. 1.2a. The most recently developed robot is the IPAnema Silent for spatial hearing experiments [Martin et al., 2023]. The Copacabana prototype, also developed in Stuttgart, allows the operation of two cooperating cable robots in one frame [Trautwein et al., 2021]. The CableRobot-Simulator at the Max-Planck Institute for Biological Cybernetics in Tübingen, Germany, is a large scale motion simulator cable robot [Miermeister et al., 2016]. The CoGiRo, see fig. 1.2b was developed by the Laboratoire d'Informatique, de Robotique et de Microélectronique de Montpellier (LIRMM) and Tecnalia, Montpellier, France, as a large suspended cable robot for heavy load handling [Tempel et al., 2017]. At the IRT Jules

Verne, France, the CAROCA prototype, see fig. 1.2c, was built to carry out various industrial applications [Picard et al., 2018]. A research platform prototype, see fig. 1.2d, was built at the IRMA Lab in Bologna, Italy, focusing in particular on underactuated CDPRs [Idà et al., 2019].

Companies such as `Spydercam` [Spydercam, 2023] or `XD motion` [XD motion SAS, 2023] offer cable suspended camera systems for sports, television, and movies. This application seems to be the most commercialized at the time of this work.

The William-E.-Gordon radio telescope within the Arecibo observatory in Puerto Rico [Goldsmith, 2007] and the FAST telescope in China [Li et al., 2018] were built using very long steel cables. Here, the cables are used to position a feed antenna above a dish constructed in natural basins. The FAST telescope has a diameter of 500 m, making it the world's largest filled-aperture radio telescope [Brinks, 2016]. Another branch of research that diverges from the above can be found in cable-driven exoskeletons [Dežman et al., 2022, Hidayah et al., 2020, Mao and Agrawal, 2012, Sanjuan et al., 2020].

1.1.3 Research on CDPRs at the Chair of Mechatronics

The worldwide research field of cable-driven parallel robots has a long tradition at the Chair of Mechatronics, University of Duisburg-Essen. The basis for the research on CDPRs at the chair was created by the SEGESTA project (1999), which was funded by the German Research Foundation (DFG). SEGESTA is an acronym for "Seilgesteuerte Stewart-Plattformen in Theorie und Anwendung". In addition to valuable fundamentals of workspace analysis [Verhoeven and Hiller, 2002, Verhoeven et al., 1998], a first early version of the SEGESTA prototype was developed [Fang et al., 2004, Hiller et al., 2005], which has been continuously refined and is utilized in this thesis, see fig. 1.4. This was the basis for the DFG project ARTIST (2004). The project resulted in methods for calculating and visualizing the workspace, for calculating optimal cable force distributions (especially for redundant parallel manipulators), and for workspace and trajectory optimization [Bruckmann, 2010].

In cooperation with the Technical University of Hamburg-Harburg, Germany, a cable-based wind tunnel robot was developed in the mid-2000s for the motion simulation of flowed-on test bodies, see fig. 1.3a. The cable system allows for a particularly undisturbed inflow of the test bodies. [Sturm et al., 2011, Sturm, 2020]

In the joint project "Regalbediengerät auf Basis der Stewart-Gough-Plattform" of the research initiative EffizienzCluster LogistikRuhr, a cable-based storage and retrieval system for high-rack warehouses was developed from 2010 to 2015 [Bruckmann et al., 2012]. For this project, it was highly beneficial that the moved masses were quite low in comparison to conventional systems, which allowed for high platform dynamics [Lalo et al., 2013] and more energy saving potential [Bruckmann et al., 2013, Zitzewitz et al., 2013]. This project

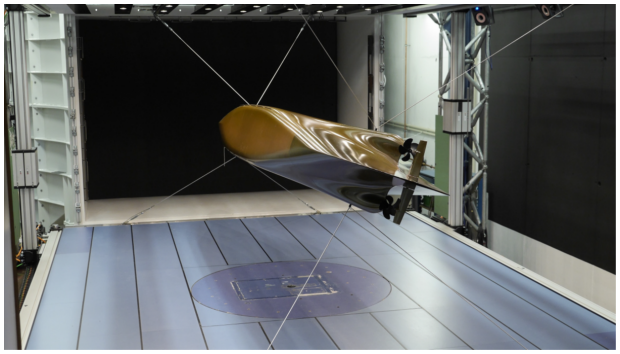

(a) Cable robot for motion simulation of flowed-on test bodies.

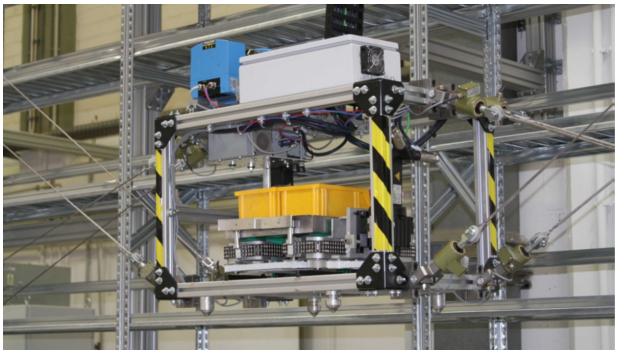

(b) CABLAR prototype for storage and retrieval in high-rack warehouses.

Figure 1.3: CDPR prototypes developed by the Chair of Mechatronics, University of Duisburg-Essen. Image courtesy of Christian Sturm.

resulted in the prototype CABLAR, see fig. 1.3b. It has a flat workspace of about 10×5 m in width and height and can reach speeds of 6 m/s with a weight of up to 100 kg (including platform and payload).

From 2011 to 2014, the chair participated in the European Project CableBOT, where CDPR systems for the transport of large components were tested. Within the project, a new algorithm for calculating cable force distributions was developed and tested on the SEGESTA prototype [Gouttefarde et al., 2015]. Furthermore, the control of contact forces was investigated [Reichert and Bruckmann, 2015]. The SEGESTA prototype was upgraded to ten cables and equipped with movable pulley mechanisms on linear slides. Algorithms were developed to enable the design and operation of highly redundant and reconfigurable CDPRs. The additional cables can be used, for example, to install passive elements, to optimize the energy consumption or to transport higher loads [Reichert et al., 2015b]. Furthermore, the reconfiguration of the CDPR along a trajectory to increase the stiffness of the platform was demonstrated [Reichert et al., 2015a].

Based on previous investigations on the cable-based storage and retrieval system CABLAR, the chair participated in the project “Entwicklung von Leichtbau-Regalbediengeräten auf Basis von Seilroboter-Technik aus NRW“ from 2016 to 2019. Within the project, many questions regarding certification, work safety and continuous operation for industrial usage arose. This initiated the author’s research on cable failure [Boumann and Bruckmann, 2019a, Boumann and Bruckmann, 2019b]. In addition, a trajectory planner for Cartesian movement with constant velocity under consideration of the workspace boundaries was developed within the project [Lemmen et al., 2019].

In 2016, a feasibility study on automated masonry construction with a CDPR was conducted, funded by the Mercator Research Center Ruhr [Bruckmann et al., 2016, Bruckmann et al., 2018]. For this purpose, the CABLAR prototype was modified and ex-

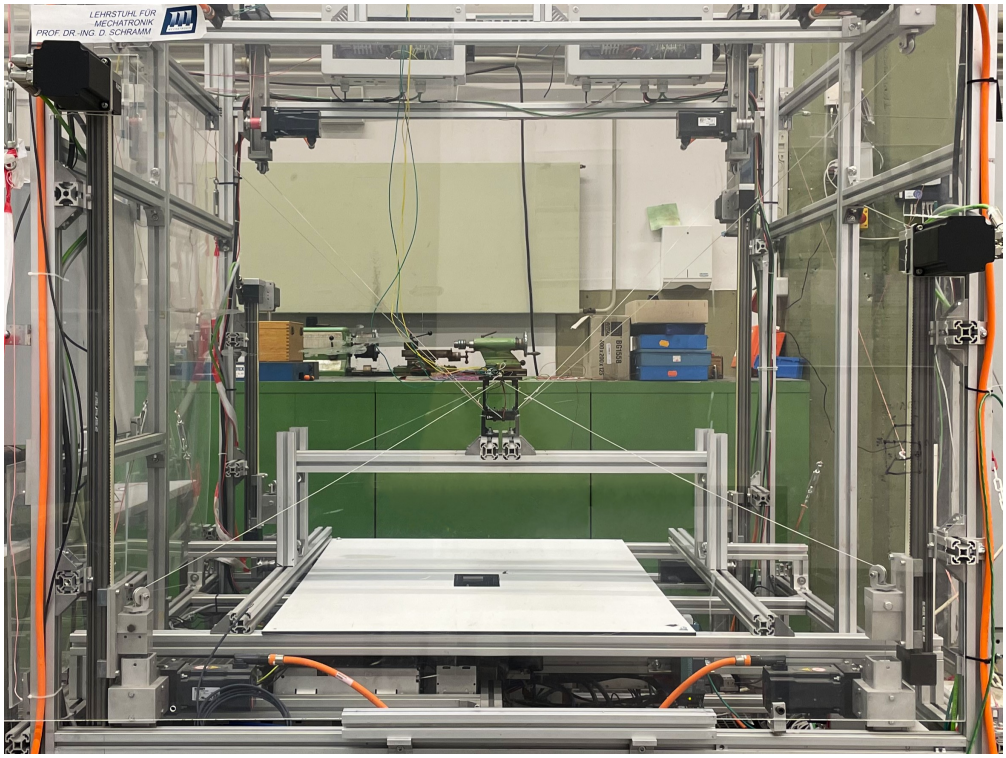

Figure 1.4: Segesta prototype at the Chair of Mechatronics, University of Duisburg-Essen. Cables coming from above are attached at the platform bottom and vice versa.

tended by an in-house developed gripper for calcium silicate units. The advantages of easy scalability and the coverage of very large workspaces with high load capacities predestine a cable system for use on the construction site.

For the 100$^{\text{th}}$ anniversary celebration of the Bauhaus University Weimar in 2019, a CDPR for large-scale 3D-printing of concrete facade elements was developed and presented to the public in July 2019 [Hahlbrock et al., 2022]. Further details about the prototype and the project team can be found in Section 6.1.3.

Based on the feasibility study for masonry construction using a CDPR, the chair participated in the AIF-IGF funded project "Entwicklung von Seilrobotern für die Erstellung von Kalksandstein-Mauerwerk auf der Baustelle" from 2019 to 2021 [Roske et al., 2021a]. Together with the project partners, the prototype as shown in fig. 1.5a was presented to the public for the first time on October 27th, 2021 [Wittek, 2021]. It allows the automated construction of a ground floor in the shell using calcium silicate units and thin-bed mortar. It is also equipped with vertically movable pivoting pulleys. For further details about the prototype and the project, it is referred to Section 6.1.4.

To support the activities in automated masonry construction and 3D-printing using CDPRs, the chair also received funding from the Ministry of Regional Identity, Communities and Local Government, Building and Digitalization of the Land of North Rhine-Westphalia

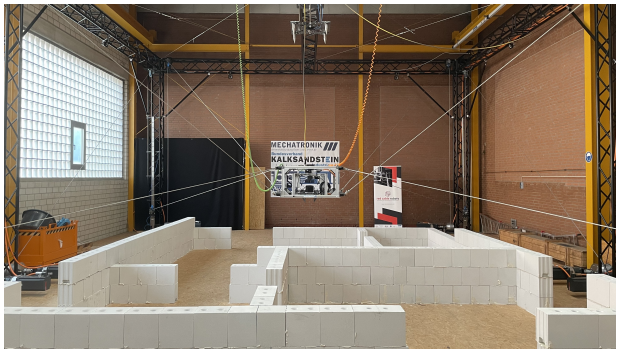

(a) CARLO prototype in Duisburg for automated masonry construction using calcium silicate units and mortar.

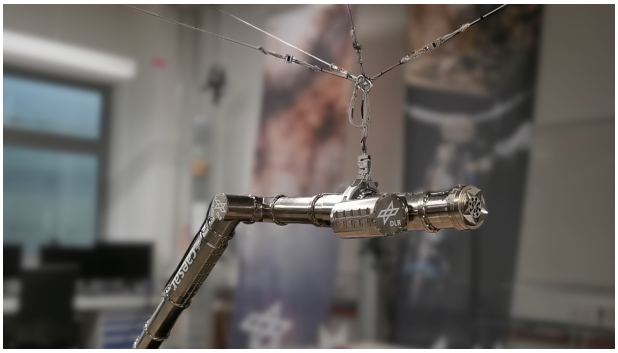

(b) MSS prototype in Oberpfaffenhofen connected to space-robot CAESAR. Image courtesy of Ferdinand Elhardt (DLR RMC).

Figure 1.5: Most recent CDPR prototypes developed by the Chair of Mechatronics, University of Duisburg-Essen.

within the projects “Langfristige experimentelle Untersuchung und Demonstration von automatisiertem Mauern und 3D-Druck mit Seilrobotern“ and “Auf dem Weg zur digitalen Bauausführung: Automatisierung des Rohbaus mit Seilroboter-Technik“.

In cooperation with the Robotics and Mechatronics Center (RMC) of the German Aerospace Center (Deutsches Zentrum für Luft- und Raumfahrt, DLR), the Motion Suspension System (MSS) is being developed since 2020. This is a four-cable robot that uses admittance-based control algorithms to provide three-dimensional force compensation (up to 60 kg) for other robotic systems. Within the project, it was used to compensate gravitational forces for the space robot CAESAR. Both systems are depicted in fig. 1.5b. The system allows for realistic on-ground testing of CAESAR in order to qualify the robot for use in space. Note that CAESAR cannot operate on-ground without support, as it is too long and too heavy. For more details, see [De Stefano et al., 2023, Elhardt et al., 2023a, Elhardt et al., 2023b].

Finally, since 2023, the project red cable robots [red cable robots GmbH, 2023] funded within the EXIST science transfer program supported by the European Union and the Federal Ministry for Economics and Climate Action has started. The aim of the project is to leverage the technology within the research group up to a product status in order to bring cable robots for industrial applications to the market. For this purpose, the spin-off company red cable robots GmbH is founded during the project.

In conclusion, it can be said that, based on the methodological basic research on CDPRs, especially in the most recent projects, a comprehensive body of knowledge has been generated in order to plan, realize and operate CDPRs for industrial application scenarios. The prototypes described above can also be classified according to their Technology Readiness

Level (TRL)[8]. For example, the MSS prototype is already being used in its final operational environment (TRL7: System prototype demonstration in operational environment). In contrast, the CARLO prototype has only been demonstrated in a factory hall and not yet on a construction site (TRL4: Technology validated in lab). The prototype for 3D-printing of concrete has been demonstrated in its final operational environment (outdoors and mounted within an arbitrary steel structure), which yields TRL6: Technology demonstrated in relevant environment. Consequently, experience with a prototype in permanent use must be gained and questions of wear, temperature dependency, maintenance intervals, accuracy, repeatability and safety need to be addressed, which is also part of the ongoing project work. In order to qualify and certify a CDPR for industrial use (considering e.g. the Machinery Directive 2006/42/EC [European Parliament, 2006]), it is clear that especially safety issues need to be addressed, which leads to the upcoming section.

1.2 Motivation and Problem Statement

As mentioned earlier, the application range of CDPRs has expanded significantly over the past few decades. As a result, the advancing industrial application is putting more and more emphasis on the safety[9] of these systems to prevent damage and to increase work safety. Especially in applications with high robot dynamics or large payloads, the risk of severe damage due to an accident is large because the energy in the system is higher and thus, the outcome can be hazardous. The same applies to CDPRs in the presence of people, such as cable cameras at a sport event, since human injury is considered a worst-case scenario and is potentially irreversible.

In Germany alone, 22 000 new industrial robot units have been installed in the year 2020 [International Federation of Robotics, 2022]. In the meantime, only 100 reportable work accidents involving industrial robots have been registered in Germany [Umbreit, 2022]. Thus, despite a yearly increasing number of robots, the number of accidents seems to remain steady, which is certainly due to successful standardization work and a high safety level of industrial robot systems [Umbreit, 2022].

Taking this as an example, the necessity to implement such standards and guidelines for

[8]The Technology Readiness Level (TRL) is a method for estimating the maturity of a technology. The TRL was established by the NASA in the 1970s. It has been adopted by the European Union and used in the EU's Horizon 2020 program [Héder, 2017]. Moreover, it was standardized within DIN EN 16603-11:2020-02 [DIN EN, 2020]. The TRL is based on a numerical score. Using the definition of the European Union, the lowest score (1) means that the basic principals have been observed, while the highest score (9) means that the actual system has been proven to be operational in its designated environment.

[9]Safety can be generally understood as the absence of any danger [Frevel, 2016]. In a technical context, it is defined, e.g., within DIN EN ISO 12100: "The concept of machine safety considers the ability of a machine to perform its intended function(s) during its service life, whereby the risk has been sufficiently reduced" [DIN EN ISO, 2011].

CDPRs also arises. Proven tools for this are, for example, Hazard Assessment or Failure Mode and Effects Analysis (FMEA) [Werdich, 2012]. Consequently, possible failures in CDPRs must be considered and classified according to severity and probability of occurrence. While a lot of faults may occur in general [Bruckmann, 2010, Salah et al., 2015], this work focuses solely on a single specific case:

A rare but particularly serious fault that can be determined is the failure of a CDPR's joint, especially of the cable. Even though norms and guidelines for cables and pulleys exist [DIN, 1974, DIN EN, 2009, ISO, 2013, Vogel and Wehking, 2004], a cable failure can still occur [Boumann and Bruckmann, 2019a, Boumann and Bruckmann, 2019b]. [Pott, 2018] shows, e.g., that a synthetic fiber cable with a breaking load of 5 kN might already fail under a load of 3.3 kN. In case of a cable failure, the consequences can be dramatic. Without a specific emergency strategy, mis- or uncontrolled movement of the robot platform can be expected, which may lead to a crash, collisions or loss of the payload. Recent examples show the potentially dramatic consequences of a cable failure:

- In December of 2011, a `Skycam` crashes during a football game, almost hitting a player due to a cable failure [Tribune News Services, 2011].
- In December of 2020, the radio telescope in the Arecibo observatory collapses after a cable failure, leaving devastation and dust [Witze, 2020].
- In October of 2022, a `Spidercam` interrupts a soccer game due to a slack cable that falls on the ground [Eurosport, 2022].
- In November of 2022, another `Skycam` crashes during a football game after a cable breaks, at least without hitting the ground [Costello and Dunleavy, 2022].

Fortunately, to the best of the author's knowledge, no one was seriously injured in any of the above mentioned accidents.

When considering cable failure, the following is defined for this work: The denomination joint failure is a superordinate term, since the joint includes a cable element as well as the components of a drive unit system in general. It should be noted that this work focuses solely on cable failure. In addition, the denotations cable break and cable failure are used interchangeably. The term cable failure includes any fault that results in loss of controllability of the platform through that joint because it is decoupled. Concretely, it is assumed that this cable no longer imposes a relevant force onto the platform. Corresponding faults which cause this effect are indicated in fig. 1.6. They might include but are not limited to:

- breaking of a cable within the workspace (e.g. due to material failure or wear), see (1),
- a rupture of the cable attachment point at the mobile platform (e.g. due to material failure), see (2),

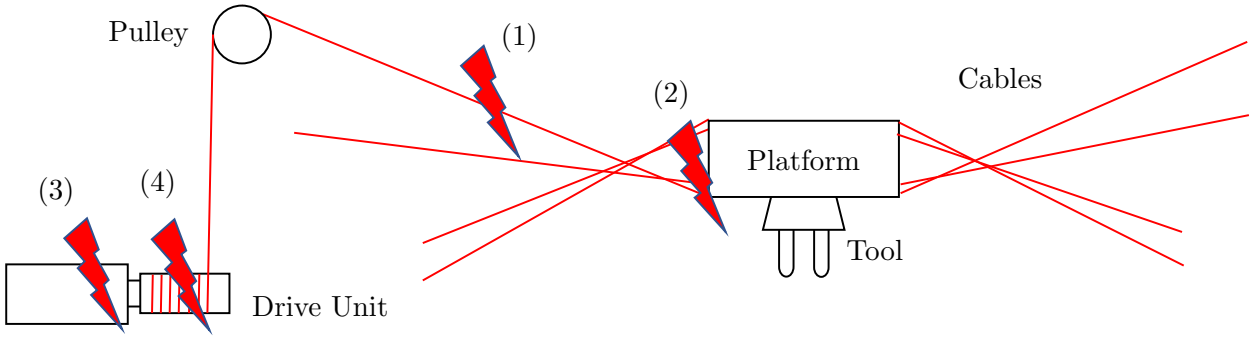

Figure 1.6: Schematic drawing of a cable-robot depicting possible points of cable failure.

- a free and unbraked movement of the corresponding winch that unwinds the cable (e.g. due to software error or gear breakage), see (3),

- a rupture of the cable attachment at the cable drum (e.g. due to material failure or wear), see (4).

Contrary, the blocking of a motor or a gear within the drive unit does not correspond, as the cable still imposes forces onto the platform in this case. Further conceivable failures in CDPRs are described in [Caro and Merlet, 2020]: A motor encoder or controller can fail. A loop in the cable can occur when it is unwound and rewound while being slack. After an emergency braking, the stored energy can cause the platform to sway. Finally, a cable can become entangled in a winch or pulley during operation.

In this work, the focus after a cable break is on the mobile platform and the remaining cables. Neither a lashing of the broken cable, nor the platform getting stuck due to the remaining piece of cable at the platform after failure is considered. From an application point of view, the cable failure itself is usually not as threatening as the potential damage resulting from possible collisions of the platform with objects in the workspace, e.g. products, machines or even people. This applies in particular when using synthetic fiber cables. Furthermore, from an economic point of view, rapid recovery and repair of the robot is essential. For this purpose, the end effector should be brought to a statically stable resting position after failure, hereafter referred to as a safe state. The potential loss of payload, which might occur when the platform tips over, must also be avoided. In addition, a cable robot can basically be operated with a reduced set of cables, e.g. until a repair can be carried out.

In the following, a CDPR operated with multiple cables is assumed. As shown in [Boumann and Bruckmann, 2019a, Boumann and Bruckmann, 2019b, Caro and Merlet, 2020], the workspace of a CDPR after a cable failure can be drastically reduced due to the missing cable. This workspace is referred to as post-failure

workspace within this work.[10] This increases the likelihood that the robot's platform will be outside the post-failure workspace after a cable failure. If now the cable failure is detected, the expected reaction would be to engage all motor brakes, attempting to shut down and brake the system. However, since the robot is no longer inside its workspace, it cannot be braked at its current pose and is expected to move uncontrollably, even with the winches stopped. In addition, un- or miscontrolled motion may also occur if the control system fails after the cable break and the motors no longer receive correct command values [Boumann and Bruckmann, 2022]. However, if one or multiple cables fail in a CDPR with many cables, a robot remains that can still be controlled. Thus, strategies are required to act in this situation, using the remaining cables to guide the platform to a save pose where it can be stopped and stabilized without collisions along the path. All of the above, however, requires the failure to be detected at first. On the other hand, if the robot is within the post-failure workspace after cable break, it might be controlled properly using the remaining cables or stopped using motor brakes. The latter, still, requires the CDPR to have brakes at each winch. Still, even in this situation, a cable break may remain undetected or there may be no action defined in the control system to act accordingly. In this case, the control system might set control values as if the failed cable was still in operation, which is also likely to result in miscontrolled movement or even a platform crash. Consequently, the failure must be detected and specific strategies must be implemented to control or brake the motors after the failure, depending on the situation. In this work, the strategies for avoiding damage after cable failure are also referred to as emergency strategies or emergency methods.

1.3 State of the Art and Research Gap

As elaborated within the problem statement, it is necessary to consider the possible situation of cable failure and to take decisive action if it occurs. Within the literature, the problem has been studied and some approaches and ideas exist on how to act in case of cable failure. Starting from the upcoming state of the art, the research gap is set forth subsequently to introduce the author's own work.

1.3.1 Existing Approaches to Cable Failure in Cable Robots

Fault detection and fault tolerance is a well-known problem in robotics [Visinsky et al., 1994]. Early work considers, for example, the fault-tolerance properties of kinematically redundant manipulators [Maciejewski, 1990, Notash, 2000, Notash and Huang, 2003, Ting et al., 1995].

[10] For further details on CDPR workspace and workspace reduction after cable failure it is referred to Section 2.4 and Section 3.2.

Various approaches can be identified in the literature that address possible faults, failures and fault tolerance in cable-driven parallel robots, which are highly relevant to this work:

First scientific approaches covering possible faults and fault tolerance in cable robots are proposed by [Roberts et al., 1998]. Herein, the effects of a missing cable on the null space of the robot's Jacobian matrix are considered. The null space can be used to determine whether a static equilibrium of forces can be achieved in a given situation, which allows statements about the fault tolerance of the system. However, corresponding strategies for dealing with failures are not yet formulated.

[Notash, 2012, Notash, 2013] also considers fault cases in cable-driven parallel manipulators. Specifically, the effects of loose cables or incorrect or limited cable force on the force and moment capacity at the end effector are investigated. The proposed method is based on a projection of the lost cable force onto the orthogonal complement of the null space of the manipulator's Jacobian matrix. Based on this, corrective forces in the remaining cables are calculated in an attempt to reconstruct the lost wrench. Criteria are further established to assess the recoverability of the wrench. Still, it is assumed that the platform remains in the workspace at the time of failure and is also kinematically overdetermined.

A method for calculating cable forces when the end effector is located outside the wrench-feasible workspace $\mathcal{WFW}$ [Gouttefarde et al., 2007], see Section 2.4, is proposed by [Côté et al., 2016]. Based on a quadratic programming algorithm, cable forces are generated that approximate the desired end effector wrench. The computing time is demonstrated to be effective. Nevertheless, problems may arise in a real-time implementation due to the iterative approach. For the solution of the cable force equation, the problem is extended by a slack variable, which is minimized together with the cable forces in the optimization process under consideration of the given boundaries, see Section 3.5.1. The approach is applied to a haptic device, but not in the context of a cable failure.

[Berti et al., 2018] propose an emergency strategy based on the planning of a dynamic trajectory in case of a cable failure. Parts of the trajectory may be outside the static equilibrium workspace, see Section 2.4. Two sinusoids are combined to form an elliptical trajectory, but its parameters must be determined manually in advance. This strategy is suitable for certain applications. Nonetheless, it cannot be applied to cable robots with any number of cables and degrees of freedom (DOF), see Section 2.1.1, at the platform.

[Ghaffar and Hassan, 2015] simulatively investigate the effect of cable failure on a deep-sea manipulator that is attached to and controlled by ship-guided cables. Uncontrolled trajectories and cable force progressions after failure are studied. Based on the results, an optimization algorithm is used to find ship positions where the effects of uncontrolled cable failure are minimized. This approach is conducive to a system design that is as fault-tolerant as possible, but it is not a strategy for acute damage prevention in the event of a failure.

In [Boschetti et al., 2017], an algorithm is presented that takes into account the reduced workspace after a cable break, identifies a suitable target position, and plans a trajectory along a straight-line path. In this process, the cable forces can be kept within valid limits in the simulation. [Boschetti et al., 2020] build upon [Boschetti et al., 2017] and address the inclusion of actuator models with inertia and friction to improve the proposed strategy. In [Boschetti et al., 2021], a validation of the algorithm is performed on a simple laboratory system with four cables and three DOF. The cable failure is mimicked by unwinding a cable.

A strategy that detects a cable failure and tries to suppress a subsequent movement is proposed in [Boschetti et al., 2019a, Boschetti et al., 2019b]. Here, an attempt is made to generate a wrench that counteracts the current motion of the platform to bring it to a safe position. For this purpose, the Wrench Exertion Capability ($\mathcal{WEC}$) – a measure of the wrench that can be generated at the end effector – is considered [Boschetti et al., 2018, Boschetti and Trevisani, 2018]. However, the proposed strategy is only suitable for the case where the end effector is within in the remaining workspace after cable failure. A successful failure detection is assumed to be given, but is not elaborated further.

In [Passarini et al., 2019], algorithms are proposed to plan dynamic trajectories for a cable-guided camera system after a cable failure, leading to a standstill of the system in the reduced workspace. An oscillating trajectory is used that guarantees compliance with the cable force limits and returns the platform to the reduced workspace. Still, the target position is numerically optimized to minimize the trajectory time while avoiding collisions with the robot's installation space constraints.

In [Winter and Ament, 2021], safety concepts for CDPRs are outlined. The focus here is on emergency braking and workspace monitoring during regular operation, rather than considering cable failure.

Conceivable failures of CDPRs are also analyzed in [Caro and Merlet, 2020], focusing on the collaborative use of CDPRs with human workers. A concept to use auxiliary cables is proposed to increase safety in case of a cable failure, and strategies are formulated depending on the occurring failure. Yet, only a CDPR with four cables and three DOF is considered.

[Raman et al., 2022] propose strategies to identify and recover from failure in planar CDPRs using reconfiguration. To detect the failure, an interactive multiple model filter [Blom and Bar-Shalom, 1988] is proposed that identifies model changes that occur suddenly or gradually over time. Subsequently, the robot is reconfigured for automated task recovery. This work is extended by studies on failure tolerant control and trajectory tracking [Raman et al., 2023]. Here, it is attempted to return the platform to its previous position after a cable failure in order to continue its task and trajectory tracking. Multiple cable failures are also considered. However, only simulative experiments are conducted and the CDPR considered is only planar.

1.3.2 Research Gap and Research Questions

As the state of research shows, there are currently only a few methods for guiding a cable robot back into its workspace after a cable break. Most of them only aim at calculating a cable force distribution that guides the robot back into the remaining workspace with the reduced set of cable forces, or mostly use very simple trajectories with little room for adaptation to different situations, such as potential collisions with obstacles. These are not further considered on the way back to the workspace, except for the work of Passarini et al. [Passarini et al., 2019]. Furthermore, finding feasible dynamic trajectories outside of the workspace seems to be computationally expensive [Barrette and Gosselin, 2005, Jiang and Gosselin, 2016], which might be time critical in case of emergency. Also, the demonstration of the procedures in the literature is mostly limited to planar examples with a reduced number of DOF and no payload. Only one of these strategies for cable failure has been experimentally tested using a very simple prototype with four cables and three DOF by Boschetti et al. [Boschetti et al., 2021], which yields to a kinematic redundancy of one.

In summary, no strategy for the case of cable breaks is known in the state of the art that has been experimentally validated, allowing for higher redundancies and spatial systems with all six DOF in a real-time capable implementation that works outside of the $\mathcal{WFW}$. Additionally, neither a cable decoupling (to mimic the failure) nor a cable failure detection before using an emergency strategy on a prototype has been demonstrated in any work.

Since most of the proposed strategies rely on a trajectory planning, the author proposes two new strategies for platform recovery, in which the trajectory does not need to be predefined, see Section 3.3 and Section 3.4. These strategies can handle higher redundancies and spatial systems with all six DOF. In order to perform experimental validations of these strategies, according preparatory work needs to be conducted. Since testing on robot hardware involves more risk, preliminary simulative experiments are highly useful. With a simulation it is conceivable to find suitable parameter sets to carry out promising tests on the prototype. If this simulation then proves to be an adequate representation of reality, it can also be used to develop and test further methods. In order to test the author's methods on a prototype, they must be integrated into a cable robot control loop. Furthermore, they must be integrated on the hardware and function in real-time. Finally, the cable break must be provoked or mimicked and also detected. Moreover the questions arise, what happens to the CDPR if the failure remains undetected, and whether a conventional controller stabilizes the platform, provided that the failure is successfully detected. After a successful stabilization of the platform after a failure, it is expected that a cable robot can continue to operate

within the post-failure workspace. However, this has not yet been demonstrated in practice. As CDPRs are increasingly used in applications, it would be very beneficial, if the authors' methods could be applied in an application scenario and if collisions with objects in the workspace could be avoided. Finally, some CDPRs have reconfigurable pulleys which might be utilized in case of cable failure.[11] Based on the above discussion, the following research questions for this work are stated:

- How can a computationally efficient simulation be set up to adequately represent a redundant CDPR?
- How can the author's proposed emergency strategies be implemented within a closed loop control for a redundant CDPR?
- Is it possible to rescue the platform of a redundant CDPR after a cable failure using the author's strategies in simulation?
- Can the author's strategies be applied to a real redundant CDPR prototype and is it possible to rescue the platform after a cable failure using them?
- Does the simulation provide suitable parameter sets for testing on a real redundant CDPR prototype?
- How can a cable failure be mimicked or provoked in a CDPR to enable testing of emergency strategies?
- How can a cable failure in a CDPR be detected fast and reliably?
- If a cable failure remains undetected, what will happen to a redundant CDPR?
- Is a conventional controller able to stabilize the platform of a redundant CDPR after a cable failure if the failure is detected and the controller is adjusted?
- When does the use of motor brakes bring a redundant CDPR platform to a safe state?
- After a cable failure, can a redundant CDPR continue to operate in the reduced workspace?
- Do the emergency strategies generally work for a large, redundant CDPR in application, and can they prevent collisions after failure?
- How can a reconfiguration feature of a redundant CDPR be utilized to support emergency strategies and to recover the system?

[11] Reconfiguration of (linear) systems after faults is well-known [Lunze and Steffen, 2003].

The problem statement, discussion, and research questions are now summarized in the following proposed flowchart fig. 1.7, which forms the basis of this work.

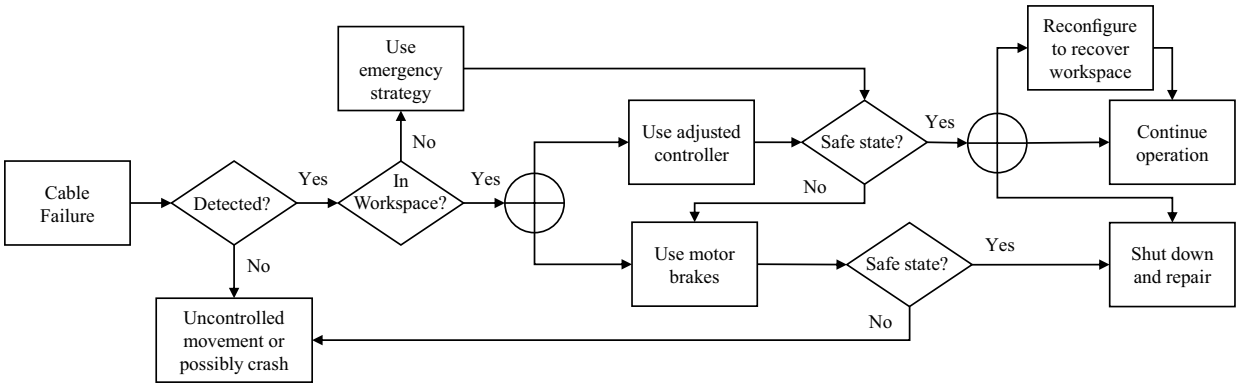

Figure 1.7: Proposed flowchart after cable failure.

1.4 Content Overview

In the first chapter of this doctoral thesis, an introduction to the topic is given. A brief history of cable robots and an overview of applications and research groups are presented, followed by a motivation to consider cable failure, which describes the central problem of this thesis. Existing considerations, strategies and approaches are presented. Therefrom, the research gap and the research questions are concluded, which are to be addressed and answered within this thesis.

The second chapter describes the fundamentals of cable-driven parallel robots. This includes classification of these systems, modeling fundamentals, cable force and workspace calculations, as well as motion planning and control approaches used within this thesis.

An algorithm to determine the workspace before and after cable failure is set forth and strategies for damage avoidance after cable failure developed by the author are outlined in the third chapter. These are strictly model based. The first approach is based on nonlinear model prediction to control the system and minimize its kinetic energy. The second approach utilizes potential fields. Both approaches aim to guide the robot's platform to a stable static position after a cable failure. Since the robot may be outside its workspace after cable failure, non-standard methods to determine cable forces are required to obtain cable force distributions, which are also presented.

In the fourth chapter, a simulation environment based on the SEGESTA prototype is set up, since this prototype is used for experimental validation within this thesis. The simulation is parametrized based on prototype measurements and the system's workspace before and after cable failure is analyzed, additionally considering rotation of the platform. An example trajectory is performed to assess ordinary simulation behavior. The outcome of

a cable failure with and without failure detection is examined in different scenarios using a conventional controller. In addition, the methods presented in the third chapter are studied and verified within the simulation. Aside from that, it is examined how the robot would behave if motor brakes were used after failure. Finally, a conclusion is drawn that critically reflects on the results and hurdles towards hardware implementation.

After the successful verification of the proposed emergency strategies in simulation, experiments on the SEGESTA prototype are carried out within the fifth chapter. A mechatronic device is developed to decouple the cable from the robot's platform. Using this device, cable failures are mimicked and a suitable detection method is developed. The damage avoidance strategies are implemented and validated through experiments on the prototype hardware, considering forward kinematic pose estimation and real-time requirements in particular. Moreover, the robot behavior after a cable failure without damage avoidance strategies is recorded and analyzed, and a conventional controller with failure detection is tested. Finally, the CDPR operation after successful rescue is demonstrated and discussed. In the end, the results are concluded and compared with the simulation.

The sixth chapter shows practical applications of CDPRs on automated construction sites that are developed during the time period of this thesis, and two prototypes are presented. Additionally, an automated toolchain for integrating BIM-Data into the automated construction process using CDPRs is introduced. Using the CDPR for automated masonry construction CARLO, a framework for trajectory planning and optimization is set up. The trajectories are based on splines and the framework uses global optimization algorithms, cost functions with weights and penalties.

Moreover, the CARLO application example is used to extend the results of this work: The simulation framework introduced in the fourth chapter is parametrized with parameters of CARLO to verify the practical suitability of the proposed emergency strategies. They are applied in simulation to study the outcome of cable failure within automated masonry construction, with particular attention to collision avoidance with already built structures. Lastly, the reconfiguration feature is studied in the simulation to recover workspace after failure and to dynamically support an emergency strategy.

The thesis is closed by a final conclusion and discussion of the results, highlighting the scientific contribution. Finally, an outlook on future work is given, highlighting in particular the upcoming project STRADAC, which is based on this work and funded by the German Research Foundation (DFG).

Chapter 2

Fundamentals of Cable-Driven Parallel Robots

In this chapter the underlying cable robot modeling is described, which is well-known from literature and forms the basis of this work. This includes the classification of cable robots, as well as for the modeling of robot kinematics, dynamics, cables, drive units and stiffness. Further, the calculation of feasible cable forces is addressed and several methods to obtain valid forces are briefly described. Workspace definitions for cable robots and methods for determination of the latter are presented. Some of them are based upon geometrical considerations, while others employ the calculation of cable forces. In the end, motion planning and a model-based cable robot control strategy are outlined.

2.1 Classification

As presented by Pott [Pott, 2018], several criteria for the classification of cable-driven parallel robots exist – such as degree-of-parallelism, actuation system or function of the robot – which will not be further elaborated here. Within this work, two main criteria for classification are employed, which are kinematic classification and classification by the motion patterns of the mobile platform.

2.1.1 Kinematic Classification

The kinematic classification is manly based on the kinematic redundancy of the robot as proposed by Ming and Higuchi [Ming and Higuchi, 1994a, Ming and Higuchi, 1994b]. Similar proposals for classification have been made by Verhoeven [Verhoeven, 2006] and Fang [Fang, 2005]. Verhoeven proposes a separation of the categories introduced by Ming and Higuchi, based on the tensionablity of the system. Whereas Fang subdivides cable robots in three classes based on the kinematics of the system.

Summing up the previous authors, the following distinction as presented by Pott [Pott, 2018] can be made: Let m be the number of cables of the robot and n the number of controllable degrees of freedom (DOF) of the robot platform. Then the kinematic redundancy is $r = m - n$. The following classes can be distinguished:

- *Incompletely restrained positioning mechanism* (IRPM) with $m < n \leq 6$: The robot is under-constrained and an external force (e.g. gravitational force) is necessary to tense all cables, defining the platform pose. In general, some DOF cannot be controlled by the cables and the robot cannot withstand arbitrary forces and torques. The number of controllable DOF may vary throughout the workspace.

- *Incompletely restrained positioning mechanism* (IRPM) with $m = n$: As cables are unilateral constraints, the robot is kinematically fully-constrained but the force equilibrium and the forces and torques that can be generated at the mobile platform still depend on external forces like gravitational force.

- *Completely restrained positioning mechanism* (CRPM) with $m = n+1$: A redundancy of $r = 1$ is required to fully constrain the platform's pose (position and orientation) through the tensed cables. In this case, the robot can withstand forces and torques at the mobile platform, dependent on the minimum and maximum forces that can be generated in the cables.

- *Redundantly restrained positioning mechanism* (RRPM) with $m > n + 1$, The situation is similar to CRPM, except that additional cables are employed and the robot is redundantly constrained by the degree of redundancy r. Moreover, the forces have to be redistributed in between the cables and the system tension can be adjusted. The higher number of cables might also have impact on the workspace of the system.

It is to note, that a robot of the type RRPM or CRPM can leave its restrained configuration and operate in a suspended configuration with the aid of gravity. Within this work, mainly robots within the classes CRPM and RRPM are considered. A comprehensive treatment of the type IRPM can be found in e.g. in [Heyden et al., 2002].

2.1.2 Classification by Motion Patterns

Besides their kinematic redundancy, cable robots can also be classified related to their motion pattern. This classification is based on the number of controllable DOF of the robot platform as proposed by Verhoeven [Verhoeven et al., 1998]. The motion pattern of a cable robot include a subset of generalized virtual displacements which can be executed by the mobile platform in consideration of the kinematic constraints [Pott, 2018]. In spatial Euclidean motion, six independent virtual displacements exist. In this work, the motion patterns are restricted to three purely rotational displacements around and three purely translational displacements along the axis of an Euclidian coordinate system. In the following, the number of the translational degrees of freedom T is n_T and the number of the rotational degrees of freedom R is n_R, following the notation n_RRn_TT for class description. Table 2.1 shows the complete classification. Note, that Verhoeven [Verhoeven et al., 1998] proved, that this list

Class	n	Possible end effector movement
1T	1	linear movement of a point-mass
2T	2	planar movement of a point-mass
1R2T	3	planar movement of a body
3T	3	spatial movement of a point-mass
2R3T	5	spatial movement of a beam
3R3T	6	spatial movement of a body

Table 2.1: Classification of cable robots according to [Verhoeven, 2006].

is complete. Examples for the given classes are illustrated within fig. 2.1. Within this work, the classes of 3R3T are of particular importance.

2.2 Modeling

This section introduces kinematic and dynamic models for cable-driven parallel robots, including inverse and forward kinematics, as well as inverse dynamics. Moreover, the dynamic models for the mechanical drive unit components and cables are described. The modeling is fundamental for all subsequent steps in this work, particularly for robot simulation and control. Note, that the system needs to be calibrated in practice, in order to determine all model parameters with appropriate quality. Existing models may differ in complexity, assumptions, and cable guidance design, which will be briefly discussed in this section. The modeling foundations used are based upon former work of [Bruckmann et al., 2008a, Bruckmann et al., 2008b, Lalo, 2014, Pott, 2018] and [Verhoeven, 2006].

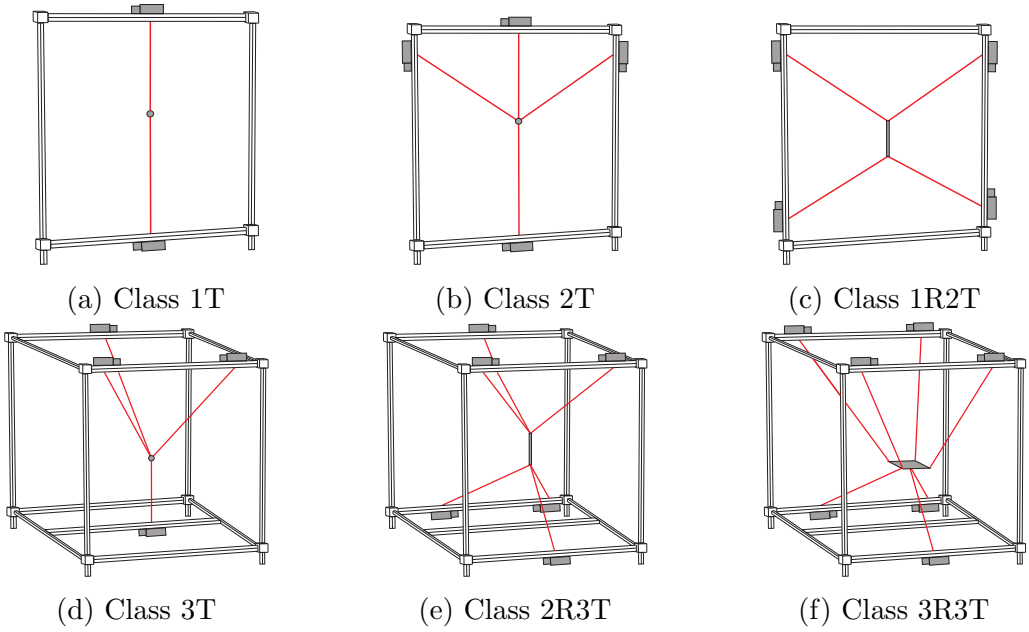

(a) Class 1T (b) Class 2T (c) Class 1R2T

(d) Class 3T (e) Class 2R3T (f) Class 3R3T

Figure 2.1: CDPR classification based on DOF, adapted from [Bruckmann et al., 2008a].

2.2.1 Kinematics of the End Effector Movement

In general, kinematics is the description of motion without consideration of the causing forces [Wittenburg, 2016]. The end effector with the platform fixed coordinate system $\underline{P}$ can be arbitrarily positioned and orientated within space, referred to the inertial frame $\underline{B}$, as shown in fig. 2.2. Let ${}^{B}\boldsymbol{r}_{P} = [r_x, r_y, r_z]^{\mathrm{T}}$ be the position vector of the robot platform in the inertial frame $\underline{B}$ and $\boldsymbol{\Phi} = [\varphi, \vartheta, \psi]^{\mathrm{T}}$ the orientation of the platform with respect to the inertial frame. Note that φ is the rotation angle about the x-axis, ϑ about the y-axis and ψ about the z-axis, respectively. Then the robot pose, composed of position and orientation of the robot is

$$ {}^{B}\boldsymbol{x}_{P} = \begin{bmatrix} {}^{B}\boldsymbol{r}_{P} \\ \boldsymbol{\Phi} \end{bmatrix}, \tag{2.1} $$

which corresponds to the vector of generalized coordinates. The orientation of the platform with respect to the inertial frame $\underline{B}$ is described by the rotation matrix ${}^{B}\boldsymbol{R}_{P}$, employing yaw-pitch-roll angles[1] with z-y-x-convention as described in [Schramm et al., 2018]:

$$ {}^{B}\boldsymbol{R}_{P} = \boldsymbol{R}_z(\psi)\, \boldsymbol{R}_y(\vartheta)\, \boldsymbol{R}_x(\varphi). \tag{2.2} $$

Herein, the three elemental rotations $\boldsymbol{R}_x$, $\boldsymbol{R}_y$, and $\boldsymbol{R}_z$, are defined as pure rotations about the axes of the inertial frame.

[1] Yaw-pitch-roll angles correspond to KARDAN angles.

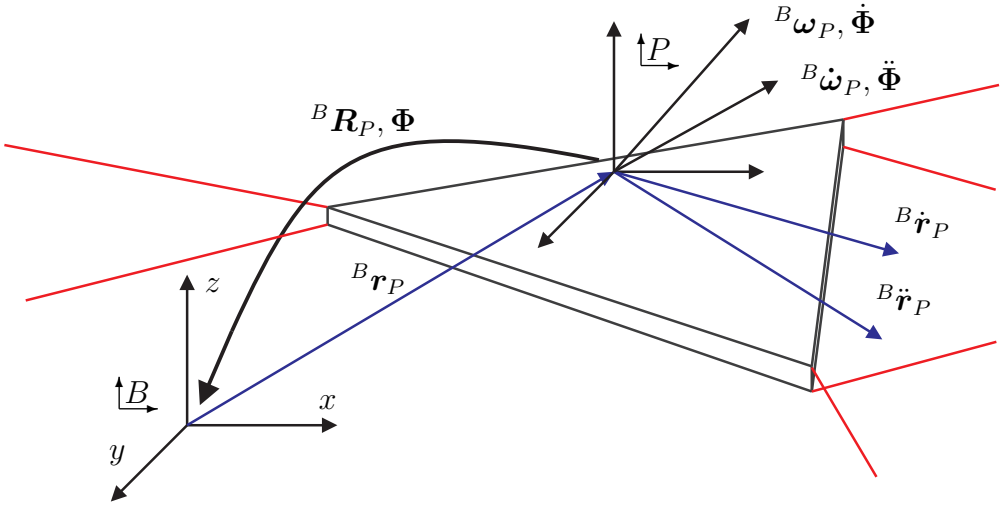

Figure 2.2: Kinematics of the end effector movement.

To obtain velocity and acceleration of the platform in generalized coordinates, the first and second time derivative respectively, lead to

$$ {}^B\dot{\boldsymbol{x}}_P = [\dot{r}_x,\, \dot{r}_y,\, \dot{r}_z,\, \dot{\varphi},\, \dot{\vartheta},\, \dot{\psi}]^{\mathrm{T}} \tag{2.3} $$

$$ {}^B\ddot{\boldsymbol{x}}_P = [\ddot{r}_x,\, \ddot{r}_y,\, \ddot{r}_z,\, \ddot{\varphi},\, \ddot{\vartheta},\, \ddot{\psi}]^{\mathrm{T}}. \tag{2.4} $$

From kinematic KARDAN equations [Schramm et al., 2018], the angular velocity of the platform ${}^B\boldsymbol{\omega}_P$ with respect to the inertial frame can be obtained using the angular velocities $\dot{\varphi}$, $\dot{\vartheta}$ and $\dot{\psi}$ as derived by [Lalo, 2014]:

$$ {}^B\boldsymbol{\omega}_P = \begin{bmatrix} \cos\psi\cos\vartheta & -\sin\psi & 0 \\ \sin\psi\cos\vartheta & \cos\psi & 0 \\ -\sin\vartheta & 0 & 1 \end{bmatrix} \begin{bmatrix} \dot{\varphi} \\ \dot{\vartheta} \\ \dot{\psi} \end{bmatrix} = \boldsymbol{\mathcal{H}}\dot{\boldsymbol{\Phi}}. \tag{2.5} $$

Consequently, the angular acceleration of the platform with respect to the inertial frame results as time derivative of the above:

$$ {}^B\dot{\boldsymbol{\omega}}_P = \boldsymbol{\mathcal{H}}\ddot{\boldsymbol{\Phi}} + \dot{\boldsymbol{\mathcal{H}}}\dot{\boldsymbol{\Phi}}, \tag{2.6} $$

employing $\dot{\boldsymbol{\mathcal{H}}}$ as the time derivative of $\boldsymbol{\mathcal{H}}$, which is

$$ \dot{\boldsymbol{\mathcal{H}}} = \begin{bmatrix} -\dot{\psi}\sin\psi\cos\vartheta - \dot{\vartheta}\cos\psi\sin\vartheta & -\dot{\psi}\cos\psi & 0 \\ \dot{\psi}\cos\psi\cos\vartheta - \dot{\vartheta}\sin\psi\sin\vartheta & -\dot{\psi}\sin\psi & 0 \\ -\dot{\vartheta}\cos\vartheta & 0 & 0 \end{bmatrix}. \tag{2.7} $$

2.2.2 Inverse Kinematics

The inverse kinematics denotes the problem to determine the joint variables of a robot from a given pose of the end effector [Spong et al., 2005]. For a serial robot, the inverse kinematics problem is often nonlinear and the solution is nontrivial and needs to be carried out iterative in most cases. However, for a parallel mechanism like a cable robot in general, the inverse kinematic can be determined straightforward and solved explicitly [Bruckmann, 2010]. To control the joint coordinates of the robot, the inverse kinematics is favorable to generate set point values out of a given desired pose or trajectory, respectively. Therefore, the theoretical foundations will be given in the following.

As mentioned previously, a CDPR consists of a platform with n DOF, which is connected to a base with m parallel cables, resulting in m parallel kinematic chains. Since a cable robot does not have conventional joints (e.g. linear actuators), the joint variables are defined as cable lengths. For simplicity, it is assumed in this work that the cables are line-shaped and massless. Therefore, they appear to be unilateral constraints and moreover do not sag. Details on the employed cable modeling will be given in Section 2.2.6.

As described by [Lalo, 2014], a closed nonlinear mapping $\boldsymbol{f}_{IK} : \mathbb{R}^n \rightarrow \mathbb{R}^m$ exists to transform the space of end effector coordinates $\boldsymbol{x}_P$ into the space of joint coordinates $\boldsymbol{q}$. Those are further referred to as operational space and joint space [Pott, 2018]. Following, the vector of generalized coordinates in joint space is

$$\boldsymbol{q} = \boldsymbol{f}_{IK}(\boldsymbol{x}_P), \quad \boldsymbol{q} \in \mathbb{R}^{m \times 1}. \tag{2.8}$$

Let ${}^P\boldsymbol{p}_i$ be the position vector to the point, where the i^{th} cable is connected to the end effector – also called platform vector – referenced within the platform fixed frame $\underrightarrow{P}$. Moreover, let ${}^B\boldsymbol{b}_i$ be the position vector to the point, where this cable enters the robots workspace – also called base vector – referenced within the inertial frame $\underrightarrow{B}$. In the following, these vectors will be denoted within the matrices $\boldsymbol{P} = [{}^P\boldsymbol{p}_1 \dots {}^P\boldsymbol{p}_m]$ and $\boldsymbol{B} = \left[{}^B\boldsymbol{b}_1 \dots {}^B\boldsymbol{b}_m\right]$, with $1 \leq i \leq m$. Furthermore, it is assumed that $\boldsymbol{P}$, $\boldsymbol{B}$ and ${}^B\boldsymbol{R}_P$ as well as the platform pose ${}^B\boldsymbol{x}_P$ are known. In practice, this might require measurement [Martin et al., 2021] or calibration [Miermeister et al., 2012] of the system.

Point-shaped Cable Guidance

For a cable robot, the cable guidances are usually either point-shaped or pulley based. Firstly, it is assumed that the cables can be led from the cable drum into the robots workspace towards the platform through nearly point shaped guidances. For that purpose, some researchers use e.g. ceramic eyes [Hiller et al., 2005]. In this case, the vectors ${}^B\boldsymbol{b}_i$ are non

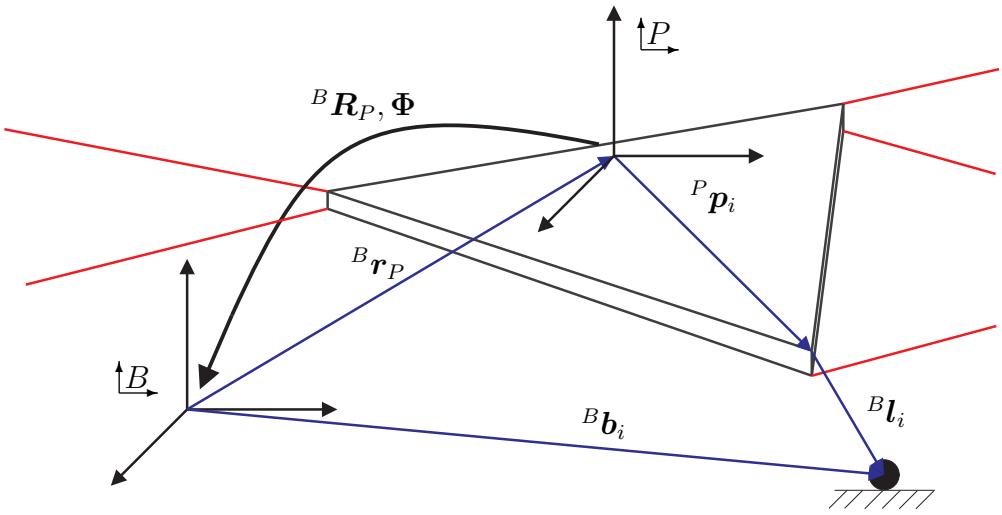

Figure 2.3: Inverse kinematics of a CDPR with point-shaped cable guidance.

variant. Following fig. 2.3 the vector loop for each cable can be determined as

$$ {}^B\boldsymbol{l}_i = {}^B\boldsymbol{b}_i - \underbrace{({}^B\boldsymbol{r}_P + {}^B\boldsymbol{R}_P {}^P\boldsymbol{p}_i)}_{{}^B\boldsymbol{p}_i}, \quad 1 \leq i \leq m. \tag{2.9} $$

Therefore the length of the i^{th} cable, which corresponds to the generalized coordinate within joint space is

$$ q_i = \|{}^B\boldsymbol{l}_i\|_2, \quad 1 \leq i \leq m. \tag{2.10} $$

In practice, this approach causes a short service life of the cables due to high wear between the motionless ceramic eyes and the moving cables [Bruckmann, 2010] and is therefore rarely used. Nevertheless, the implementation e.g. for simulation purposes is simple and straightforward [Boumann and Bruckmann, 2019a].

Pulley based Cable Guidance

Using a pulley based cable guidance, the issue of high cable wear can be mitigated. However, the kinematic modeling is becoming more complex. Moreover, the additional inertia within the pulleys is influencing the dynamics of the system [Lalo, 2014].

As described in [Bruckmann, 2010], pivoting pulleys – also called swiveling pulleys by some authors [Kraus, 2016] – are commonly used for most cable robot applications. They are mounted rotatable, swiveling and follow the direction of the cable when the end effector is moving. Consequently, the position vector to the point where the cable enters the workspace becomes a function of the end effector pose. The following brief presentation of the geometric dependencies of pulley based cable guidance is adapted from [Kraus, 2016, Schmidt and Pott, 2013] and [Sturm, 2020]. Further elaboration can be found

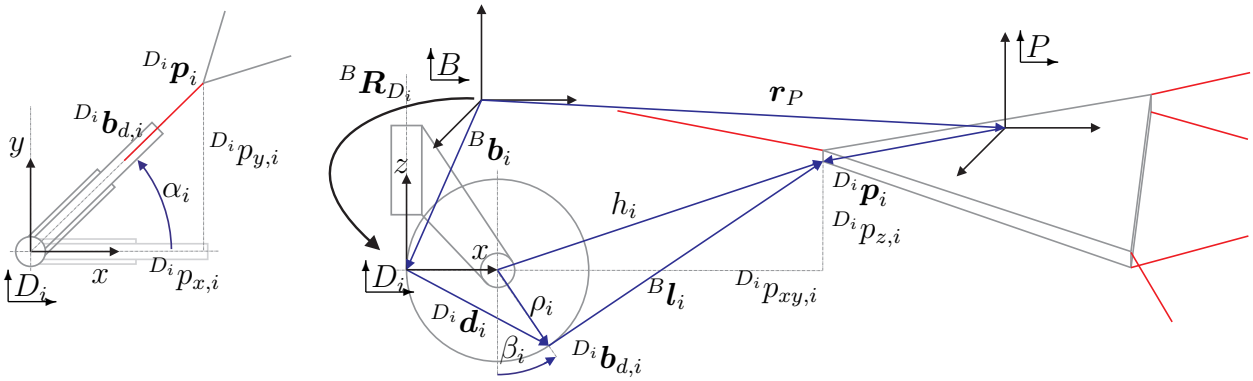

(a) Pulley pivoted within xy-plane

(b) Kinematic relations and cable exit point in pulley plane

Figure 2.4: Inverse kinematics of a CDPR with pulley based cable guidance.

in [Bruckmann, 2010, Lalo, 2014, Pott, 2018]. Each i^{th} pivoting pulley is referenced within a frame $\underline{D_i}$, see fig. 2.4. The origin of each frame is described by the vectors ${}^{B}\boldsymbol{b}_i$. Let ${}^{B}\boldsymbol{R}_{D_i}$ be the rotation matrix between each pulley frame and $\underline{B}$.[2] Each frame is set such that the pivoting axis of each pulley coincides with the z-axis. Now, the vector to the cable attachment point at the end effector ${}^{B}\boldsymbol{p}_i$, see eq. (2.9), can be transformed into the pulley frame:

$$ {}^{D_i}\boldsymbol{p}_i = {}^{B}\boldsymbol{R}_{D_i}^{\mathrm{T}} \left({}^{B}\boldsymbol{p}_i - {}^{B}\boldsymbol{b}_i\right) = [{}^{D_i}p_{x,i},\ {}^{D_i}p_{y,i},\ {}^{D_i}p_{z,i}]^{\mathrm{T}}. \tag{2.11} $$

Consequently, the rotation angle of each pulley $\alpha_i = \arctan2({}^{D_i}p_{y,i},\ {}^{D_i}p_{x,i})$ can be determined, see fig. 2.4a. It is zero in initial position of a pulley. Figure 2.4b displays the point where the cable leaves the pulley in plane of the pulley. The length ${}^{D_i}p_{xy,i}$ can be determined by

$$ {}^{D_i}p_{xy,i} = \sqrt{{}^{D_i}p_{x,i}^2 + {}^{D_i}p_{y,i}^2}. \tag{2.12} $$

With the radius of a pulley ρ_i and the Pythagorean theorem, the length h_i between $\boldsymbol{p}_i$ and the center point of the pulley is

$$ h_i = \sqrt{({}^{D_i}p_{xy,i} - \rho_i)^2 + ({}^{D_i}p_{z,i})^2}. \tag{2.13} $$

Hence, the length of the i^{th} free cable can be calculated as

$$ l_i = \sqrt{h_i^2 - \rho_i^2}. \tag{2.14} $$

[2]The rotation matrix ${}^{B}\boldsymbol{R}_{D_i}$ for each pulley frame can be determined using KARDAN angles. The angles result from constructive design of the robot and may vary. For further details it is referred to [Pott, 2018, Schmidt and Pott, 2013, Sturm, 2020].

Using trigonometric relations, the wrapping angle β_i of the cable around the pulley is determined by

$$\beta_i = \frac{\pi}{2} - \text{atan2}\left(({}^{D_i}p_{xy,i} - \rho_i), {}^{D_i}p_{z,i} \right) + \text{atan2}(\rho_i, l_i). \tag{2.15}$$

Now to fully describe the inverse kinematics, the point where the cable leaves the pulley needs to be identified with respect to the inertial frame. Using α_i and β_i, the vector from the origin of the pulley frame to the cable exit point can be determined as

$${}^{D_i}\boldsymbol{d}_i = \begin{bmatrix} \rho_i \cos\alpha_i \, (1 + \sin\beta_i) \\ \rho_i \sin\alpha_i \, (1 + \sin\beta_i) \\ -\rho_i \cos\beta_i \end{bmatrix}, \tag{2.16}$$

and finally the cable vector is

$${}^{B}\boldsymbol{l}_i = {}^{B}\boldsymbol{R}_{D_i}({}^{D_i}\boldsymbol{d}_i - {}^{D_i}\,\boldsymbol{p}_i). \tag{2.17}$$

Moreover, it can be useful to explicitly describe the point $\boldsymbol{b}_{d,i}$, where the cable leaves the pulley, in coordinates of the inertial frame:

$${}^{B}\boldsymbol{b}_{d,i} = {}^{B}\boldsymbol{b}_i + {}^{B}\boldsymbol{R}_{D_i}\,{}^{D_i}\boldsymbol{d}_i. \tag{2.18}$$

2.2.3 Velocity Kinematics

Note that within this thesis, cables are assumed to be non-sagging and straight lines. Therefore, from the cable vectors ${}^{B}\boldsymbol{l}_i$ derived by inverse kinematics (see eq. (2.9) or eq. (2.17), respectively) the unit vectors ${}^{B}\boldsymbol{\nu}_i$ in cable direction can be determined:

$${}^{B}\boldsymbol{\nu}_i = \frac{{}^{B}\boldsymbol{l}_i}{\|{}^{B}\boldsymbol{l}_i\|_2}, \quad 1 \leq i \leq m. \tag{2.19}$$

Using the unit vectors, the so-called structure matrix ${}^{B}\boldsymbol{A}^{\mathrm{T}} \in \mathbb{R}^{n \times m}$ can be derived:

$${}^{B}\boldsymbol{A}^{\mathrm{T}} = \begin{bmatrix} {}^{B}\boldsymbol{\nu}_1 & \dots & {}^{B}\boldsymbol{\nu}_m \\ \left({}^{B}\boldsymbol{R}_P\,{}^{P}\boldsymbol{p}_1\right) \times {}^{B}\boldsymbol{\nu}_1 & \dots & \left({}^{B}\boldsymbol{R}_P\,{}^{P}\boldsymbol{p}_m\right) \times {}^{B}\boldsymbol{\nu}_m \end{bmatrix}. \tag{2.20}$$

Matrix $\boldsymbol{A}^{\mathrm{T}}$ corresponds to the transpose of the robot's Jacobian matrix $\boldsymbol{J}$[3]. It can be used to transform cable forces from joint space of the actuators into a wrench at the end effector in operational space [Pott, 2018]. The Jacobian can be derived via different approaches, e.g. using Lagrange's equation of the first kind [Reichert et al., 2014]. Nevertheless, the approach

[3] As described by [Pott, 2018], the structure matrix $\boldsymbol{A}^{\mathrm{T}}$ which relates cable forces to platform wrench, is identical to the transposed kinematic Jacobian matrix. This leads to $\boldsymbol{J} = -\boldsymbol{A}$.

shown here appears to be more straightforward, since it is based on geometric relations [Verhoeven, 2006]. With the structure matrix, the cable velocities can be determined for a given velocity in operational space ${}^{B}\dot{\boldsymbol{x}}_P$ as [Kraus, 2016]

$$\dot{\boldsymbol{q}} = -{}^{B}\boldsymbol{A}\,{}^{B}\dot{\boldsymbol{x}}_P. \tag{2.21}$$

Correspondingly with the given acceleration in operational space ${}^{B}\ddot{\boldsymbol{x}}_P$, the cable acceleration results to [Kraus, 2016]:

$$\ddot{\boldsymbol{q}} = -{}^{B}\boldsymbol{A}\,{}^{B}\ddot{\boldsymbol{x}}_P - {}^{B}\dot{\boldsymbol{A}}\,{}^{B}\dot{\boldsymbol{x}}_P. \tag{2.22}$$

The time derivative of $\boldsymbol{A}$ can be determined analytically by separately deriving the row elements of $\boldsymbol{A}$ [Pott, 2018].

2.2.4 Forward Kinematics

In contrast to the inverse kinematics, the forward kinematics (or direct kinematics) denotes the problem to determine the pose of the robot's end effector from given joint variables [Spong et al., 2005]. For a serial robot without a loop structure, the forward kinematics problem can be determined straightforward and solved explicitly. Conversely, for a parallel mechanism like a CDPR, the forward kinematics can only be solved explicitly in special cases. In general, the solution is nontrivial [Husty et al., 2001, Husty et al., 2002, Taghirad and Nahon, 2008] and might need iterative solution schemes. Generally, a solution needs to be found for the problem

$$\boldsymbol{x}_P = \boldsymbol{f}_{IK}^{-1}(\boldsymbol{q}) = \boldsymbol{f}_{FK}(\boldsymbol{q}), \tag{2.23}$$

which is the inverted problem of eq. (2.8) [Lalo, 2014]. In special cases or under simplifying assumptions, the problem can be solved explicitly, see e.g. [Pott, 2008, Williams II et al., 2004]. Such assumptions are not applied within this work and thus are not further considered here. To solve eq. (2.23) for CDPRs, several approaches exist, differing e.g. in complexity, computational costs – and thus real-time capability – or the underlying modeling assumptions [Pott, 2018]. Some examples are given in the following.

Under the assumption of point-shaped cable guidance, Fang [Fang, 2005] proposes to solve the forward kinematic problem using a Newton Raphson scheme. An iterative algorithm considering pulley based cable guidance is shown by Williams [Williams II et al., 2004]. However, the pivoting angles of the pulleys are neglected. On the other hand, Merlet [Merlet, 2004b] presents methods based on Interval arithmetic, which guarantee to find solutions if they exist.

Within this work, the approach presented by Pott [Pott, 2010] is used as a basis since

it is well-known. Let $\boldsymbol{q}({}^{B}\boldsymbol{x}_e) = [q_i, ...q_m]^{\mathrm{T}}$ be the vector of cable lengths derived by the inverse kinematics dependent on a pose estimation ${}^{B}\boldsymbol{x}_e$, see Section 2.2.2. Furthermore, $\boldsymbol{l}_\theta$ shall be the vector of cable lengths derived by angular motor encoder measurements, see Section 2.2.6. Considering a redundant manipulator, this results in an overdetermined problem, since the number of equations m exceeds the number of unknown elements n. Now, the m-dimensional function $\boldsymbol{\Upsilon}({}^{B}\boldsymbol{x}_e, \boldsymbol{l}_\theta)$ is set up as

$$\boldsymbol{\Upsilon}({}^{B}\boldsymbol{x}_e, \boldsymbol{l}_\theta) = \boldsymbol{q}({}^{B}\boldsymbol{x}_e) - \boldsymbol{l}_\theta, \quad \boldsymbol{l}_\theta \in \mathbb{R}^{m\times 1}. \tag{2.24}$$

To find the corresponding pose to the given angular measurements, the optimization problem can be formulated as

$$\upsilon(\boldsymbol{l}_\theta) = \min_{\boldsymbol{x}_e} \sum_{i=1}^{m} \Upsilon_i^2({}^{B}\boldsymbol{x}_e, \boldsymbol{l}_\theta). \tag{2.25}$$

Note that in this case, the error for each cable is equally weighted. Equation (2.25) can be solved employing a numerical optimization algorithm. In this work, a Levenberg Marquard Fletcher Algorithm [Balda, 2007] is used. This approach in general can cause trouble with real-time feasibility on a prototype because of its iterative structure. Therefore, in practice, the optimization algorithm is constrained with a number of maximum permitted iterations. Moreover, proper calibration and referencing of the robot is essential. For further information, it is referred to [Pott, 2010, Pott, 2018].

2.2.5 Equations of Motion of the End Effector

For simplicity, the top left symbol is omitted from now on for all elements referenced in the inertial frame $\underline{B}$. To describe the dynamic movement of the end effector, the equations

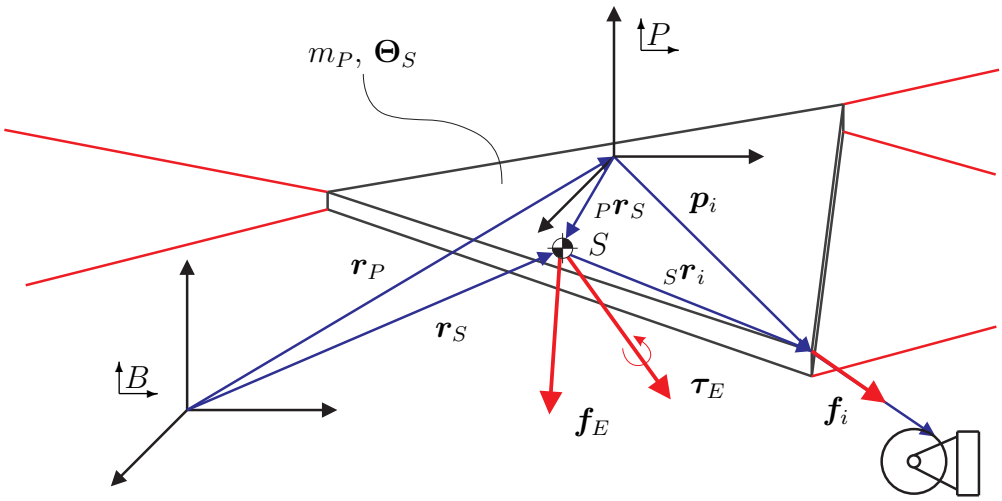

Figure 2.5: Forces, torques and center of gravity at the platform.

of motion are now derived based on [Hahn, 2002, Lalo, 2014]. For this purpose, Newton-Euler equations are formulated in relation to the gravitational center S of the platform, see fig. 2.5. Let m_P be the mass of the platform and $\boldsymbol{\Theta}_S$ the inertial tensor referred to the center of gravity. Each cable applies the force vector $\boldsymbol{f}_i$ to the platform. The scalar force in each cable f_i acts along the cable direction described by the unit vector $\boldsymbol{\nu}_i$. This yields

$$\boldsymbol{f}_i = f_i \cdot \frac{\boldsymbol{l}_i}{\|\boldsymbol{l}_i\|_2} = f_i \cdot \boldsymbol{\nu}_i, \quad 1 \leq i \leq m. \tag{2.26}$$

All forces f_i are merged within the vector $\boldsymbol{f} \in \mathbb{R}^{m\times 1}$, further referred to as cable force distribution. The forces and torques acting on the platform's gravitational center are described by $\boldsymbol{f}_E$ and $\boldsymbol{\tau}_E$. Now setting up the balances of linear and angular momentum [Nolting, W., 1997] under consideration of the m cables leads to

$$m_P\, \ddot{\boldsymbol{r}}_S = \boldsymbol{f}_E + \sum_{i=1}^{m} \boldsymbol{f}_i, \tag{2.27}$$

$$\boldsymbol{\Theta}_S\, \dot{\boldsymbol{\omega}}_P + \boldsymbol{\omega}_P \times (\boldsymbol{\Theta}_S\, \boldsymbol{\omega}_P) = \boldsymbol{\tau}_E + \sum_{i=1}^{m} {}_S\boldsymbol{r}_i \times \boldsymbol{f}_i. \tag{2.28}$$

Note, that the angular velocity and acceleration of the platform can be obtained by eqs. (2.5) and (2.6). ${}_S\boldsymbol{r}_i$ is the vector from the center of gravity to the i^{th} cable attachment point at the platform. Typically, the cable attachment points are referenced in frame $\underset{\rightarrow}{\uparrow P}$. Additionally, it can be useful to reference trajectories of the end effector with respect to the platform frame. Consequently, the equations of motion are now transformed with respect to $\underset{\rightarrow}{\uparrow P}$. The position vector to the center of gravity (see fig. 2.5) can be derived as

$$\boldsymbol{r}_S = \boldsymbol{r}_P + {}_P\boldsymbol{r}_S, \tag{2.29}$$

where ${}_P\boldsymbol{r}_S$ is the vector from $\underset{\rightarrow}{\uparrow P}$ to the gravitational center of the platform. Now velocity and acceleration of $\boldsymbol{r}_S$ can be determined as [Schramm et al., 2018]

$$\dot{\boldsymbol{r}}_S = \dot{\boldsymbol{r}}_P + \boldsymbol{\omega}_P \times {}_P\boldsymbol{r}_S \tag{2.30}$$

$$\ddot{\boldsymbol{r}}_S = \ddot{\boldsymbol{r}}_P + \dot{\boldsymbol{\omega}}_P \times {}_P\boldsymbol{r}_S + \boldsymbol{\omega}_P \times (\boldsymbol{\omega}_P \times {}_P\boldsymbol{r}_S). \tag{2.31}$$

Note, that the angular velocity of the gravitational center is equal to the platform frame, since a rigid body is assumed for the platform. As $\underset{\rightarrow}{\uparrow P}$ and the center of gravity usually do not coincide, the principle of angular momentum needs to be adjusted:

$$\boldsymbol{\Theta}_P\, \dot{\boldsymbol{\omega}}_P + \boldsymbol{\omega}_P \times (\boldsymbol{\Theta}_P\, \boldsymbol{\omega}_P) + m_P\, {}_P\boldsymbol{r}_S \times \ddot{\boldsymbol{r}}_P = \boldsymbol{\tau}_E + \sum_{i=1}^{m} {}_P\boldsymbol{r}_i \times \boldsymbol{f}_i. \tag{2.32}$$

Herein, the inertial tensor $\boldsymbol{\Theta}_P$ needs to be derived applying the Huygens-Steiner theorem:

$$\boldsymbol{\Theta}_P = \boldsymbol{\Theta}_S + m_P \, {}_P\tilde{\boldsymbol{r}}_S^{\mathrm{T}} \, {}_P\tilde{\boldsymbol{r}}_S. \tag{2.33}$$

${}_P\tilde{\boldsymbol{r}}_S$ is a skew symmetric cross product matrix[4] using the vector ${}_P\boldsymbol{r}_S = [{}_Pr_{S,x}, {}_Pr_{S,y}, {}_Pr_{S,z}]^{\mathrm{T}}$:

$${}_P\tilde{\boldsymbol{r}}_S = \begin{bmatrix} 0 & -{}_Pr_{S,z} & {}_Pr_{S,y} \\ {}_Pr_{S,z} & 0 & -{}_Pr_{S,x} \\ -{}_Pr_{S,y} & {}_Pr_{S,x} & 0 \end{bmatrix}. \tag{2.34}$$

Now eq. (2.31) is inserted into eq. (2.27) and eq. (2.32). Also, the external forces and torques acting onto the platform can be denoted as

$$\boldsymbol{w}_E = \begin{bmatrix} \boldsymbol{f}_E \\ \boldsymbol{\tau}_E \end{bmatrix}. \tag{2.35}$$

Using $\boldsymbol{A}^{\mathrm{T}}$ from eq. (2.20) as well as eqs. (2.27), (2.31), (2.32) and (2.35), it yields:

$$\begin{bmatrix} m_P\big(\ddot{\boldsymbol{r}}_P + \dot{\boldsymbol{\omega}}_P \times {}_P\boldsymbol{r}_S + \boldsymbol{\omega}_P \times (\boldsymbol{\omega}_P \times {}_P\boldsymbol{r}_S)\big) \\ \boldsymbol{\Theta}_P \, \dot{\boldsymbol{\omega}}_P + \boldsymbol{\omega}_P \times (\boldsymbol{\Theta}_P \, \boldsymbol{\omega}_P) + m_P \, {}_P\boldsymbol{r}_S \times \ddot{\boldsymbol{r}}_P \end{bmatrix} = \underbrace{\begin{bmatrix} \sum_{i=1}^{m} \boldsymbol{f}_i \\ \sum_{i=1}^{m} {}_P\boldsymbol{r}_i \times \boldsymbol{f}_i \end{bmatrix}}_{\boldsymbol{A}^{\mathrm{T}}\boldsymbol{f}} + \boldsymbol{w}_E. \tag{2.36}$$

To isolate the angular velocity, the following relation is used:

$$\dot{\boldsymbol{\omega}}_P \times {}_P\boldsymbol{r}_S = -{}_P\boldsymbol{r}_S \times \dot{\boldsymbol{\omega}}_P = -{}_P\tilde{\boldsymbol{r}}_S \, \dot{\boldsymbol{\omega}}_P. \tag{2.37}$$

Bringing together eqs. (2.36) and (2.37) as well as eqs. (2.5) and (2.6), it leads to:

$$\begin{aligned} &\underbrace{\begin{bmatrix} m_P \, \boldsymbol{I}_3 & -m_P \, {}_P\tilde{\boldsymbol{r}}_S \boldsymbol{\mathcal{H}} \\ m_P \, {}_P\tilde{\boldsymbol{r}}_S & \boldsymbol{\Theta}_P \boldsymbol{\mathcal{H}} \end{bmatrix}}_{\boldsymbol{M}(\boldsymbol{x}_P)} \underbrace{\begin{bmatrix} \ddot{\boldsymbol{r}}_P \\ \ddot{\boldsymbol{\Phi}} \end{bmatrix}}_{\ddot{\boldsymbol{x}}_P} + \dots \\ &+ \underbrace{\begin{bmatrix} m_P\Big((\dot{\boldsymbol{\mathcal{H}}}\dot{\boldsymbol{\phi}}) \times {}_P\boldsymbol{r}_S + (\boldsymbol{\mathcal{H}}\dot{\boldsymbol{\phi}}) \times \big((\boldsymbol{\mathcal{H}}\dot{\boldsymbol{\phi}}) \times {}_P\boldsymbol{r}_S\big)\Big) \\ \boldsymbol{\Theta}_P \dot{\boldsymbol{\mathcal{H}}}\dot{\boldsymbol{\phi}} + (\boldsymbol{\mathcal{H}}\dot{\boldsymbol{\phi}}) \times (\boldsymbol{\Theta}_P \boldsymbol{\mathcal{H}}\dot{\boldsymbol{\phi}}) \end{bmatrix}}_{\boldsymbol{K}(\boldsymbol{x}_P, \dot{\boldsymbol{x}}_P)} + \underbrace{(-\boldsymbol{w}_E)}_{\boldsymbol{Q}(\boldsymbol{x}_P, \dot{\boldsymbol{x}}_P)} = \boldsymbol{A}^{\mathrm{T}}\boldsymbol{f}. \end{aligned} \tag{2.38}$$

Herein, $\boldsymbol{I}_3$ is a 3×3 identity matrix. $\boldsymbol{M}$ is defined as mass matrix, $\boldsymbol{K}$ contains Coriolis and gyroscopic forces and $\boldsymbol{Q}$ all other applied external forces and torques, including weight and

[4] The cross product between two arbitrary vectors $\boldsymbol{a}, \boldsymbol{b} \in \mathbb{R}^3$ leads to the same result as a multiplication of $\boldsymbol{b}$ with the skew symmetric matrix $\tilde{\boldsymbol{a}}$, i.e. $\boldsymbol{a} \times \boldsymbol{b} = \tilde{\boldsymbol{a}}\boldsymbol{b}$ with $\tilde{\boldsymbol{a}} = \begin{bmatrix} 0 & -a_z & a_y \\ a_z & 0 & -a_x \\ -a_y & a_x & 0 \end{bmatrix}$.

disturbances. Note, that the inertia tensor needs to be transformed into the inertial frame using the rotation matrix ${}^{B}\boldsymbol{R}_{P}$:

$$ {}^{B}\boldsymbol{\Theta}_{P} = {}^{B}\boldsymbol{R}_{P}\, {}^{P}\boldsymbol{\Theta}_{P}\, {}^{B}\boldsymbol{R}_{P}^{\mathrm{T}}. \tag{2.39} $$

Equation (2.38) can also be written in short form as:

$$ \underbrace{\boldsymbol{M}(\boldsymbol{x}_P)\ddot{\boldsymbol{x}}_P + \boldsymbol{K}(\boldsymbol{x}_P, \dot{\boldsymbol{x}}_P) + \boldsymbol{Q}(\boldsymbol{x}_P, \dot{\boldsymbol{x}}_P)}_{-\boldsymbol{w}} = \boldsymbol{A}^{\mathrm{T}}\boldsymbol{f}, \tag{2.40} $$

which is typically expressed also in the following form:

$$ \boldsymbol{A}^{\mathrm{T}}\boldsymbol{f} + \boldsymbol{w} = \boldsymbol{0}. \tag{2.41} $$

If the robot's platform is at rest, the motion terms can be set to zero in order to determine a static force equilibrium. Note that gravitational forces and torques due to mass of the platform are included in $\boldsymbol{w}_E$. For a given trajectory, eq. (2.41) needs to be solved to determine feasible cable forces. This essential problem is addressed within Section 2.3. Note that a consideration of the pulley inertia is neglected in this work.

2.2.6 Cables

To ensure a proper modeling of a CDPR, it is necessary to consider the cables as they transmit the force between the end effector and the cable-drum. Depending on their material, length or tension, cables show different dynamic effects, which include e.g. sagging, vibration, creeping or elastic deformation. As displayed in [Pott, 2018], some or all effects of the above can be addressed within simulation. Depending on the chosen modeling approach, complexity and calculation time differ remarkably. As an example, a cable can be described as a unilateral constraint with ideal and delay free transmission of a pulling force from a cable drum to the robot's platform, which is the simplest approach.

A simple yet effective approach is the Kelvin-Voigt model[5] [Tempel, 2019], which will be utilized within this work. It is the most simple viscoelastic material model showing typical rubber properties, which is primarily elastic but has further resistance to fast deformation. This model employs a purely viscous damper and a purely elastic spring in parallel, neglecting cable masses. Consequently, the transmitted force depends solely on the cable's elongation and its time derivative. The eigendynamics of the cables are not considered. This approach can display a linear-elastic deformation of the cables and thus allows to represent

[5]The model is named after the British physicist and engineer Lord Kelvin and the German physicist Woldemar Voigt.

platform vibrations [Pott, 2018]. Still it is rather simple and efficient in calculation time. The approach is chosen because this work focuses damage prevention after a cable failure rather than a precise modeling of the failing cable. The cable tension f_i is modeled using a picewise defined function for each i^{th} cable:

$$f_i(\boldsymbol{x}_P, \theta_i, \dot{\boldsymbol{x}}_P, \dot{\theta}_i) = \begin{cases} k_{c,i}(l_{i,tot})\,\Delta l_i(\boldsymbol{x}_P, \theta_i) + d_{c,i}\,\Delta \dot{l}_i(\dot{\boldsymbol{x}}_P, \dot{\theta}_i) & \text{for } \Delta l_i > 0 \text{ and } k_{c,i}\Delta l_i > -d_{c,i}\Delta \dot{l}_i \\ 0 & \text{for } \Delta l_i \leq 0 \text{ or } k_{c,i}\Delta l_i \leq -d_{c,i}\Delta \dot{l}_i \end{cases} \tag{2.42}$$

The second case results since cables cannot push. Moreover, the spring force cannot be exceeded by a negative damping force. Thereby, pushing forces within the cable model are avoided when a cable is compressed.

It is well-known, that the cable stiffness $k_{c,i}$ is dependent on the total cable length $l_{i,tot}$ [Pott, 2018, Sturm, 2020]. Note that the part of the cable coiled on the drum is neglected here. The damper coefficient $d_{c,i}$ is assumed to be constant. $l_{i,tot}$ is a function of the cable length $l_{i,0}$ at the starting pose $\boldsymbol{x}_{P,0}$ and the cable that was wound on or unwound from the drum with radius $\rho_{d,i}$ and angle θ_i. $l_{i,0}$ contains the free cable length $||\boldsymbol{l}_i(\boldsymbol{x}_{P,0})||_2$ in starting position, the cable length between drum and deflection point of the cable $l_{d,i}$, which is constant for fixed pivoting pulleys and the piece of cable wrapped around the pulley.

$$l_{i,tot}(\theta_i, l_{i,0}) = \theta_i\,\rho_{d,i} + \underbrace{||\boldsymbol{l}_i(\boldsymbol{x}_{P,0})||_2 + l_{d,i} + (\beta_i + \frac{\pi}{2})\rho_i}_{l_{i,0}} \tag{2.43}$$

The cable length difference Δl_i describes whether a cable is slack or in tension:

$$\Delta l_i(\boldsymbol{x}_P, \theta_i) = (||\boldsymbol{l}_i(\boldsymbol{x}_P)||_2 + l_{d,i} + (\beta_i + \frac{\pi}{2})\rho_i) - l_{i,tot}(\theta_i, l_{i,0}). \tag{2.44}$$

Using this approach, the kinematic cable length at an arbitrary pose $\boldsymbol{x}_P$ is compared to the total cable length $l_{i,tot}$, which varies when the cable is wound or unwound. The approach to determine the cable velocity difference $\Delta \dot{l}_i$ is alike:

$$\Delta \dot{l}_i(\dot{\boldsymbol{x}}_P, \dot{\theta}_i) = \underbrace{(-\boldsymbol{A}\dot{\boldsymbol{x}}_P)_i}_{\dot{l}_i(\boldsymbol{x}_P, \dot{\boldsymbol{x}}_P)} - \dot{\theta}_i \rho_{d,i}. \tag{2.45}$$

To determine the cable velocity, eq. (2.21) is used. The angular velocity of the cable drum is $\dot{\theta}_i$. Note that the model holds true, since cable sagging is neglected and the cables are assumed to be straight lines under tension. Moreover, it is assumed that the cables are wound and unwound uniformly on the drum. Thereby, length variance in the cable from coiling under different tension levels is also neglected. For more comprehensive modeling approaches including hysteresis or cable sagging it is referred to [Merlet, 2015, Miermeister et al., 2015].

2.2.7 Drive Units

To conduct a modeling of the drive units, the rotational inertia $J_{d,i}$ for each unit i needs to be determined. It is assumed that the drive units for all cables are identical, since the use of equal components is common for CDPRs [Bruckmann, 2010]. Various drive unit designs are possible, e.g. the combination of a cable drum and a direct drive or a combination of drive, gear, cable drum and compensating coupling. Consequently, the rotational inertia needs to be determined for each individual component, which is usually done using data sheets and CAD models. Note that the inertia of the bearings is neglected here. For a direct drive with the motor inertia $J_{m,i}$ and the cable drum inertia $J_{w,i}$, this leads to

$$J_{d,i} = J_{m,i} + J_{w,i}. \tag{2.46}$$

In contrast for the unit with gearbox and coupling it yields

$$J_{d,i} = J_{m,i} {r_{g,i}}^2 + J_{g,i} {n_{g,i}}^2 + J_{c,i} + J_{w,i}. \tag{2.47}$$

Here, the rotational inertia is summarized on the side of the gear which carries the cable drum. $n_{g,i}$ is the gear ratio and $J_{g,i}$ the rotational inertia of the gear on motor side. The coupling's inertia is $J_{c,i}$. Assuming, that each cable has its own drive unit, the rotational inertia for all m drive units can be brought together in the diagonal matrix

$$\boldsymbol{J}_d = \begin{bmatrix} J_{d,1} & & \\ & \ddots & \\ & & J_{d,m} \end{bmatrix}, \quad 1 \leq i \leq m. \tag{2.48}$$

Now, the equations of motion for the drive system are derived. Let $\ddot{\boldsymbol{\theta}} \in \mathbb{R}^{m \times 1}$ be the vector of angular accelerations of all cable drums. To model frictional effects in each drive unit, a Stribeck curve is assumed, which is a well-known approach [Krämer and Kempkes, 2013, Ruderman, 2012, Stribeck, 1903]. The so-called Stribeck effect describes the transition between coulomb and viscous friction for low relative speeds between objects. It is characterized by the fact that after surpassing the breakaway force, the friction coefficient decreases first with increasing relative speed. Afterwards it starts to linearly increase. Since within this work, the Stribeck friction is mainly applied for rotating parts, the typical variables are expressed in terms of angular velocities and torques instead of linear velocities and forces. Let the Stribeck frictional torque $\boldsymbol{F}_F \in \mathbb{R}^{m \times 1}$, dependent on the current angular velocities $\dot{\boldsymbol{\theta}}$ be

$$\boldsymbol{F}_F(\dot{\boldsymbol{\theta}}) = \operatorname{sgn}(\dot{\boldsymbol{\theta}}) \left(F_c + (F_s - F_c) \cdot \exp\left(- \left| \frac{\dot{\boldsymbol{\theta}}}{\theta_s} \right|^{\epsilon} \right) \right) + F_v \cdot \dot{\boldsymbol{\theta}}. \tag{2.49}$$

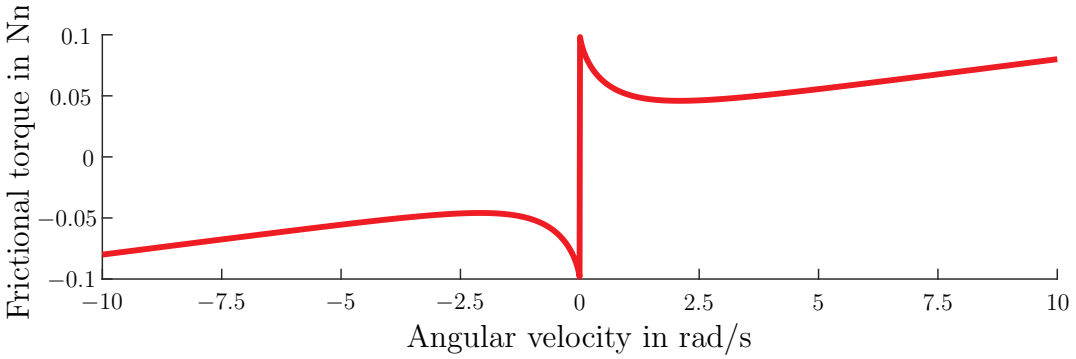

Figure 2.6: Stribeck curve with the arbitrary set of parameters $F_s = 0.1$ Nm, $F_c = 0.03$ Nm, $F_v = 0.005$ Nms/rad, $\epsilon = 0.75$, and $v_s = 0.6$ rad/s.

Here, the static friction is described by F_s, the sliding friction by F_c and the velocity proportional part of the viscous friction by F_v. The Stribeck rotational velocity is θ_s and the Stribeck form factor is ϵ. Figure 2.6 shows an exemplary Stribeck curve for an arbitrary set of parameters. Due to manufacturing tolerances, the friction in the drive units may vary significantly, even thou they are identically built. Therefore, it might be useful to identify the friction separately in each drive unit. A further approach for friction modeling, which is neglected here, is the so-called generalized Maxwell slip [Al-Bender et al., 2005].

Since the tensed cables connect the cable drums and the robot's platform, the cable forces $\boldsymbol{f}$ are also acting on the cable drums with the drum radii

$$\boldsymbol{\rho}_d = \begin{bmatrix} \rho_{d,1} & & \\ & \ddots & \\ & & \rho_{d,m} \end{bmatrix}, \quad 1 \leq i \leq m. \tag{2.50}$$

It is moreover assumed, that each motor controller can process a desired torque command with a dead time T_t and is able to produce it with a delay. This is represented using a PT1 System with the time constant T_1. The torques produced by the motor current controllers are denoted as $\boldsymbol{\tau}_c \in \mathbb{R}^{m\times 1}$. Finally, the equations of motion are given by

$$\boldsymbol{J}_d\,\ddot{\boldsymbol{\theta}} = \boldsymbol{n}_g\,\boldsymbol{\tau}_c - \boldsymbol{\rho}_d\,\boldsymbol{f} - \boldsymbol{F}_F(\dot{\boldsymbol{\theta}}). \tag{2.51}$$

$\boldsymbol{n}_g \in \mathrm{R}^{m\times m}$ is a diagonal matrix containing all gear ratios. For drive units without transmission, it is an identity matrix. For eq. (2.51), an ideal gear without losses is assumed.

2.2.8 Stiffness

For most robotic applications, position accuracy and tolerances are of major importance. As cable robots are subject to their cables' elasticity, the robot's stiffness for a given pose might

be of particular interest. A higher stiffness reduces elastic effects and supports more accurate operation and control of the robot, especially for large applications and non negligible elastic cables [Bruckmann and Boumann, 2021]. The stiffness is modeled using a spring equation

$$\delta \boldsymbol{w} = \boldsymbol{K}_s(\boldsymbol{x}_P)\delta \boldsymbol{x}_P. \tag{2.52}$$

Here, a platform displacement $\delta \boldsymbol{x}_P$ results in a reaction force $\delta \boldsymbol{w}$ and elastic cable deformations. The diagonal pose dependent stiffness matrix $\boldsymbol{K}_s(\boldsymbol{x}_P)$ can be computed by

$$\boldsymbol{K_s}(\boldsymbol{x}_P) = \underbrace{-\frac{\partial \boldsymbol{A}^{\mathrm{T}}}{\partial \boldsymbol{x}_P}\boldsymbol{f}}_{\boldsymbol{K}_g} + \underbrace{\boldsymbol{A}^{\mathrm{T}}\boldsymbol{K}_l\boldsymbol{A}}_{\boldsymbol{K}_c}, \tag{2.53}$$

according to [Hoevenaars, 2016, Reichert et al., 2015a]. $\boldsymbol{K}_g$ describes the so-called active stiffness of the system, while the passive stiffness is denoted by $\boldsymbol{K}_c$. The passive part describes the linear elastic behavior of the cables and might also include the stiffness of the winches' position controller, see Section 2.6. To obtain the diagonal matrix

$$\boldsymbol{K}_l = \begin{bmatrix} k_{c,1} & & \\ & \ddots & \\ & & k_{c,m} \end{bmatrix}, \quad \boldsymbol{K}_l \in \mathrm{R}^{m\times m}, \tag{2.54}$$

the stiffness of each cable $k_{c,i}$ needs to be determined. Contrarily to the passive stiffness, the active stiffness $\boldsymbol{K}_g$ does not depend on elastic effects like the cable or controller elasticity. Instead, this element describes the changes of the structure matrix $\boldsymbol{A}^{\mathrm{T}}$, when the platform is subject to a displacement $\delta \boldsymbol{x}_P$. Moreover, it is dependent on the cable forces which can be *actively* influenced by the drives, resulting in its name [Kock and Schumacher, 1998].

The opposite effect of the stiffness, see eq. (2.52), can be described by the compliance. Using the compliance matrix $\boldsymbol{C}_s$, which is the inverse of the stiffness matrix $\boldsymbol{K}_s$, the displacement for a given disturbance wrench can be calculated as

$$\delta \boldsymbol{x}_P = \boldsymbol{K}_s^{-1}\delta \boldsymbol{w} = \boldsymbol{C}_s\delta \boldsymbol{w}. \tag{2.55}$$

It might be of particular interest to homogenize the displacement since both translational and rotational motions might occur. This can be conducted using a diagonal homogenization matrix $\boldsymbol{J}_v$ according to [Nguyen and Gouttefarde, 2014, Stocco et al., 1998]

$$\boldsymbol{J}_v = \mathrm{diag}\left(1, 1, 1, j_x, j_y, j_z\right). \tag{2.56}$$

Herein, j_x, j_y and j_z can be understood as medium platform radii. They are computed using

the x-,y- and z-components of the m platform vectors ${}^P\boldsymbol{p}_i$ with $1 \leq i \leq m$:

$$j_x = \frac{1}{m}\sum_{i=1}^{m}\left|{}^P\boldsymbol{p}_{x_i}\right|, \quad j_y = \frac{1}{m}\sum_{i=1}^{m}\left|{}^P\boldsymbol{p}_{y_i}\right|, \quad j_z = \frac{1}{m}\sum_{i=1}^{m}\left|{}^P\boldsymbol{p}_{z_i}\right|. \tag{2.57}$$

The homogenized structure matrix now is

$$\boldsymbol{A}_h^{\mathrm{T}} = \boldsymbol{J}_v^{-1}\boldsymbol{A}^{\mathrm{T}}, \tag{2.58}$$

which can be used instead of $\boldsymbol{A}^{\mathrm{T}}$ in eq. (2.53), allowing to apply eq. (2.55) to obtain the homogenized displacement $\delta\boldsymbol{x}_{P,h}$.

2.3 Cable Force Calculation

One essential problem within the field of CDPRs is the solution of eq. (2.41) for a feasible cable force distribution $\boldsymbol{f}$ [Pott, 2018]. Herein, it is crucial to consider cable forces limitations: A lower limit $f_{\min}$ and an upper limit $f_{\max}$ are introduced for each i^{th} cable, such that $f_{\min} \leq f_i \leq f_{\max}$. The lower limit is intended to keep the cables tensed and to prevent them from sagging. Moreover, at least some tension is required to constrain the system since cables cannot push. The upper limit can be determined based on the available drive torques or the strength of the mechanical parts in order to prevent damages to the system.[6]

2.3.1 Geometrical Interpretation

A suitable way to determine cable force distributions is a geometrical interpretation of the mathematical problem [Verhoeven, 2006]: Inside the m-dimensional space of the cable forces, a hypercube[7] $\mathcal{C} \subset \mathbb{R}^m$ is formed by the cable force limits. Consequently, each cable's force limits introduce a set of delimiting hyperplanes to the cube, defined by $f_i = f_{\min} \vee f_i = f_{\max}, 1 \leq i \leq m$. Equation (2.41) is a linear system of n equations with m unknown variables. As this work deals mainly with the classes CRPM and RRPM (see Section 2.1) it can be assumed that $n < m$ always holds true. Consequently, eq. (2.41) is under-determined.[8] Hence, the redundancy $r = m - n$ of the robot defines the dimension of the solution space and $\boldsymbol{A}^{\mathrm{T}}$ does not have a square shape. To solve eq. (2.41) for $\boldsymbol{f}$, the Moore-Penrose-Pseudo-

[6] The determination of $f_{\max}$ can also be vice versa: The necessary maximum forces (e.g. to obtain a required workspace volume or to carry a certain load) may result from a task requirement. In this case, the drive capabilities as well as the strength of the mechanical parts are derived from $f_{\max}$.

[7] A hypercube is a m-dimensional analogue of a cube where $m = 3$.

[8] For systems with $n = m$ or $n > m$, it is referred to [Pott, 2018].

Inverse $\boldsymbol{A}^{+\mathrm{T}}$ can be used, which is calculated as follows:

$$\boldsymbol{A}^{+\mathrm{T}} = \boldsymbol{A}\big(\boldsymbol{A}^{\mathrm{T}}\boldsymbol{A}\big)^{-1}, \quad \boldsymbol{A}^{+\mathrm{T}} \in \mathbb{R}^{m\times n}. \tag{2.59}$$

Now, the solution of eq. (2.41) for $\boldsymbol{f}$ reads

$$\boldsymbol{f} = \underbrace{-\boldsymbol{A}^{+\mathrm{T}}\boldsymbol{w}}_{\boldsymbol{f}_0} + \boldsymbol{H}\boldsymbol{\lambda}. \tag{2.60}$$

The projection of the desired wrench $\boldsymbol{w}$ onto the solution space is $\boldsymbol{f}_0$ and $\boldsymbol{\lambda} \in \mathbb{R}^r$ is a vector of multipliers $[\lambda_1, \dots \lambda_r]$. $\boldsymbol{H} \in \mathbb{R}^{m\times r}$ is the kernel (or null space) of $\boldsymbol{A}^{\mathrm{T}}$, defined by

$$\boldsymbol{H} = \Big[\boldsymbol{h}_1, \dots, \boldsymbol{h}_r\Big], \tag{2.61}$$

with the vectors $\boldsymbol{h}_k$ solving the equation

$$\boldsymbol{A}^{\mathrm{T}}\boldsymbol{h}_k = 0, \quad 1 \le k \le r. \tag{2.62}$$

The columns of $\boldsymbol{H}$ span the r-dimensional solution space $\mathcal{S} \subset \mathbb{R}^m$ which contains all solutions of eq. (2.41). If now the solution space $\mathcal{S}$ intersects the hypercube $\mathcal{C}$ as shown in fig. 2.7, feasible cable force distributions, which lie within the cable force limits, exist in the intersection $\mathcal{F}$. The manifold containing all feasible cable force distributions and describing this intersection is denoted as

$$\mathcal{F} = \mathcal{C} \cap \mathcal{S} \neq \emptyset. \tag{2.63}$$

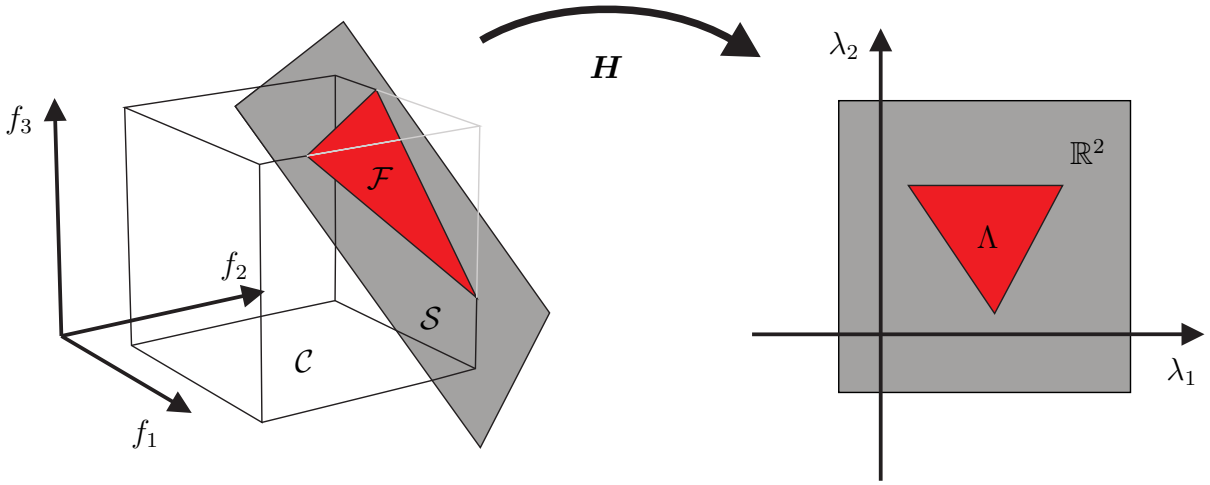

Figure 2.7: Visualization of solution space, cube, manifold and map for $r = 2$ and $m = 3$.

As long as $\mathcal{F}$ is nonempty for the given wrench $\boldsymbol{w}$, it forms a convex polytope[9] [Verhoeven, 2006] and the pose is called wrench-feasible. The multipliers $\boldsymbol{\lambda}$ form the polytope Λ as shown in fig. 2.7, leading to wrench-feasible solutions. Here, the null space $\boldsymbol{H}$ is used to transform between $\mathbb{R}^r$ and $\mathbb{R}^m$. Considering the given force limits when solving eq. (2.60), it yields

$$\begin{aligned} \boldsymbol{f}_{\min} \leq \boldsymbol{f}_0 + \boldsymbol{H}\boldsymbol{\lambda} \leq \boldsymbol{f}_{\max} \\ \Leftrightarrow \boldsymbol{f}_{\min} - \boldsymbol{f}_0 \leq \boldsymbol{H}\boldsymbol{\lambda} \leq \boldsymbol{f}_{\max} - \boldsymbol{f}_0. \end{aligned} \tag{2.64}$$

Herein, $\boldsymbol{f}_{\min}, \boldsymbol{f}_{\max} \in \mathbb{R}^{m\times 1}$ are the vector representation of the cable force boundaries. As stated above, the basis for the solution space is being formed by the null space of the structure matrix for $r > 0$. If now a feasible cable force distribution exists, the inner tension of the system can be modified within the cable force limits by adjusting $\boldsymbol{\lambda} \in \Lambda$.

2.3.2 Formulation as an Optimization Problem

Besides the geometrical interpretation of the cable-force distribution problem, other solution approaches exist, which differ in computation time, continuity along a given platform trajectory, force level, real-time capability or workspace coverage [Pott, 2018]. Another suitable method, is the consideration of the problem as an optimization problem [Bruckmann et al., 2006]. It can be expressed as follows:

$$\text{minimize} \qquad e(\boldsymbol{f}) = \|\boldsymbol{f} - \tilde{\boldsymbol{f}}\|_p = \sqrt[p]{\sum_{i=1}^{m}(f_i - \tilde{f})^p} \tag{2.65}$$

$$\text{with} \qquad f_{min} \leq f_i \leq f_{max} \tag{2.66}$$

$$\text{and} \qquad w_\gamma = -\sum_{i=1}^{m} A_{\gamma,i}^{\mathrm{T}} f_i \quad 1 \leq \gamma \leq n \tag{2.67}$$

Here $\tilde{\boldsymbol{f}} = \tilde{f} \cdot [1, \ldots, 1]^{\mathrm{T}} \in \mathbb{R}^{m\times 1}$ is the desired tension level of the cables. γ denotes the elements of $\boldsymbol{A}^{\mathrm{T}}$ and $\boldsymbol{w}$ which correspond to the degree of freedom of the platform. Depending on the choice of p, linear or nonlinear optimization problems can result. Choosing $p = 1$ [Oh and Agrawal, 2005] leads to a linear optimization problem of the form

$$\text{minimize} \quad e(\boldsymbol{f}) = \boldsymbol{c}^{\mathrm{T}}\boldsymbol{f} \tag{2.68}$$

$$\text{with} \quad \boldsymbol{N}\boldsymbol{f} \leq \boldsymbol{v} \tag{2.69}$$

$$\text{and} \quad \boldsymbol{Z}\boldsymbol{f} = \boldsymbol{z}. \tag{2.70}$$

[9] A polytope is a generalized polygon for an arbitrary number of dimensions.

In this case, the cost function is linear dependent on the forces, the constraint is linear as well. Choosing the weighting factor $\boldsymbol{c}^{\mathrm{T}} = [1, \ldots, 1] \in \mathbb{R}^{1\times m}$ is useful, since cables and drives are often equal parts with the same workloads. Matrix $\boldsymbol{N}$ and vector $\boldsymbol{v}$ describe eq. (2.66) while $\boldsymbol{Z}$ and $\boldsymbol{z}$ result from eq. (2.67).

As described by Bruckmann [Bruckmann, 2010], the solution of this problem might be computationally expensive but is real-time capable using linear programming. However, the computed cable forces along a platform trajectory can be discontinuous contrary to the nonlinear case [Verhoeven, 2006]. In the most simple nonlinear case, $p = 2$ is chosen which enables the formulation as a least squares problem [Bruckmann, 2010]:

$$\text{minimize} \quad e(\boldsymbol{f}) = \frac{1}{2}\boldsymbol{f}^{\mathrm{T}}\boldsymbol{I}_m\boldsymbol{f} + \boldsymbol{c}^{\mathrm{T}}\boldsymbol{f} \tag{2.71}$$

$$\text{with} \quad \boldsymbol{N}\boldsymbol{f} \leq \boldsymbol{v} \tag{2.72}$$

$$\text{and} \quad \boldsymbol{Z}\boldsymbol{f} = \boldsymbol{z}. \tag{2.73}$$

Matrix $\boldsymbol{I}_m \in \mathbb{R}^{m\times m}$ is an identity matrix, while $\boldsymbol{c}^{\mathrm{T}}$ can be set to zero. Equations (2.72) and (2.73) are analogue to eqs. (2.66) and (2.67). The optimization can be performed e.g. using an interior point [Waltz et al., 2006] or an active-set [Gouttefarde et al., 2015] algorithm. Despite the computational effort of the optimization, the application in real-time is generally possible for modern computer systems [Pott et al., 2009].

Further methods to compute cable forces from a given wrench are, for example, the Puncture Method [Müller et al., 2014], the Barycentric Method [Mikelsons et al., 2008] or the (Improved) Closed Form [Pott, 2014]. An excellent overview and the explanation of further methods is given in [Pott, 2018].

2.4 Workspace

The workspace is the space a robot manipulator can reach with its end effector. In principal, it can be determined kinematically. As defined by [Spong et al., 2005], the workspace is the total volume of all points that the end effector can reach while moving all joints within their limits. It is bounded by the geometry of the robot. Usual definitions are, however, often tailored to serial robots [Bruckmann, 2010]. Workspace definitions for parallel robots are given e.g. by Merlet [Merlet, 2010]. For parallel robots and especially CDPRs, a purely kinematic description might be insufficient [Pott, 2018]. Moreover, a simple graphical representation is not always possible. Consequently, special workspace definitions for CDPRs are necessary, which will be explained in the following.

2.4.1 Workspace Definitions for Cable Robots

As described previously, cables are assumed as unilateral constraints, unable to push. Mainly because of this characteristic, special workspace definitions are required [Bruckmann, 2010], which are given for example in [Bosscher et al., 2006, Ebert-Uphoff and Voglewede, 2004, Gouttefarde et al., 2006, Gouttefarde et al., 2007, Pott, 2018]. Based on the analogy of the unilateral cable constraints to gripping systems, the following types of workspaces are defined in [Ebert-Uphoff and Voglewede, 2004] for CDPRs as listed in [Bruckmann, 2010]:

- The *Wrench-Closure Workspace* ($\mathcal{WCW}$) is the workspace, which can be reached with positive cable tensions under arbitrarily high loads. It is also called *Controllable Workspace* ($\mathcal{CWS}$) and contains all platform poses where eq. (2.41) is fulfilled considering $\mathbf{0} \leq \boldsymbol{f} \leq \boldsymbol{\infty}$ for arbitrary $\boldsymbol{w}$.

- The *Wrench-Feasible Workspace* ($\mathcal{WFW}$) is a subset of the $\mathcal{WCW}$ and contains all poses where bounded cable tensions $\boldsymbol{f}_{\min} \leq \boldsymbol{f} \leq \boldsymbol{f}_{\max}$ can be found for a given limited wrench $\boldsymbol{w} \in [\boldsymbol{w}_{\min}, \boldsymbol{w}_{\max}]$.

- The *Static-Equilibrium Workspace* ($\mathcal{SEW}$) can be defined as set of poses which can be reached with feasible cable forces under the influence of gravity which acts on the platform and the payload.

- The *Dynamic-Equilibrium Workspace* ($\mathcal{DEW}$) is similar to the $\mathcal{SEW}$, adding the constraint that a certain platform acceleration $\ddot{\boldsymbol{x}}_P$ can be reached.

- The *Statically Stable Workspace* ($\mathcal{SSW}$) contains the set of poses, where an infinitesimal movement of the platform increases the system's potential energy.

- The *Reachable Workspace* ($\mathcal{REW}$) is the set of poses which can be reached kinematically, bounded by limited cable lengths.

Unless mentioned otherwise, the term workspace is used to reference the $\mathcal{SEW}$ within this work. Besides the aforementioned definitions, which are mainly related to positive and feasible cable tensions, the consideration of further criteria might be useful when analyzing a CDPRs workspace [Pott, 2018]:

- Singularities: Within a robot's workspace, singularities might occur, causing uncontrollable degrees of freedom. A workspace can be examined for possible singularities, e.g., by checking if the structure matrix at a given pose has a decrease in rank (i.e. $\operatorname{rank}(\boldsymbol{A}^{\mathrm{T}}) < n$). Supplementary information can be found in [Bruckmann, 2010, Pott, 2018].

- Collisions: Dependent on the robots pose, interferences in between parts of the robot itself or the environment might occur. Those interferences might be in between multiple cables, a cable and the platform, a cable and an obstacle or the platform and an obstacle [Blanchet and Merlet, 2014, Bury et al., 2019, Fabritius et al., 2018, Merlet, 2004a, Merlet and Daney, 2006, Nguyen and Gouttefarde, 2015, Perreault et al., 2010]. Generally, they are to be avoided. The robot's ability to complete its intended task without collisions must be considered during the robot's design process [Bruckmann et al., 2011] and motion planning [Bruckmann and Boumann, 2021, Herrmann et al., 2022]. Besides that, research work exists where collisions are caused intentionally, e.g. between cables and obstacles in order to extend the workspace of the CDPR [Rushton and Khajepour, 2021].

- Mechanical constraints: The bending radii of cables cannot be arbitrarily small, which needs to be taken into account when designing the mechanical parts of the cable guidance system (pulleys, cable anchor points at the platform, distances between cable deflections). Depending on the attachment of the cables at the mobile platform, the (constrained) mobility of the installed joint also needs to be considered.

2.4.2 Workspace Calculation

When considering the introduced workspace definitions for CDPRs, the question arises, how to calculate such workspaces in order to gain knowledge about an existing CDPR or while designing one. As summarized in [Pott, 2018], different approaches exist to determine the workspace of a cable robot, whereby a distinction can be made between three main concepts:

- Discretization methods: A discrete spatial grid is used and the workspace is investigated at a finite number of poses within this grid. A common approach is to investigate each point of this grid for a feasible cable force distribution (see eq. (2.41)) [Pusey et al., 2004]. This approach is wide-spread and straightforward to implement, however the determination of the exact workspace boundaries is inaccurate and no information about the space between the grid points is obtained.

- Continuous methods: Sets of poses are investigated for their belonging to the workspace. Each set (e.g. boxes, spheres or intervals) is usually described by a range of values. The sets can be successively split in order to determine the workspace more accurately [Bruckmann, 2010].

- Analytical workspace boundary determination: The $n-1$-dimensional boundary of a workspace might be computed analytically. For this, it is necessary to formulate a connection between the parameters of interest (e.g. wrench-feasibility) and the pose, which

is difficult in general. Even thou lengthy algorithms can be implemented in a computer program, mathematical tools cannot be applied in such situations [Pott, 2018].

Within this work, discretization methods are applied to obtain CDPR workspaces, since the ease of implementation outweighs the necessity to determine the exact boundaries.

2.5 Motion Planning

Planning the targeted movement of a robot is one of the fundamental problems in robotics [Siciliano and Khatib, 2008]. For a robot fulfilling a task, it is essential to move from one location to another whilst e.g. avoiding collisions with obstacles [Siciliano and Khatib, 2008, Spong et al., 2005]. Such movement can be planned within the robot's operational space or its configuration space.[10] A variety of well-known methods exist to plan a motion either on a pure geometric path using e.g. potential fields, probabilistic roadmaps or random motions [Spong et al., 2005] or along of a trajectory which e.g. contains also velocity or acceleration of a robot's platform or its joints. Within this work, only trajectory planning in the operational space is used. For further approaches to trajectory planning it is referred to [Gasparetto et al., 2015, Pham, 2015].

2.5.1 Polynomials

A well-known approach to describe the trajectory between two points are polynomials, parameterized with corresponding boundary conditions [Lalo, 2014, Spong et al., 2005, Sturm, 2020]. Let $\boldsymbol{x}_P(t_0)$ be the starting pose at the time t_0 and $\boldsymbol{x}_P(t_f)$ be the goal pose at the final time t_f. Since the robot should be at rest in both poses, the following boundary conditions arise:

$$\dot{\boldsymbol{x}}_P(t_0) = 0 \qquad \dot{\boldsymbol{x}}_P(t_f) = 0. \tag{2.74}$$

Now every degree of freedom $k = 1, \ldots, n$ is described separately by $x_{P,k}$ and can be considered individually. Above boundaries can for example be met using a polynomial of third order with the the time t:

$$x_{P,k}(t) = a_{3_k} t^3 + a_{2_k} t^2 + a_{1_k} t + a_{0_k}. \tag{2.75}$$

Here, the polynomials coefficients for the k^{th} degree of freedom are a_{0_k} up to a_{3_k}. However, for a third order polynomial, acceleration and jerk are discontinuous which may lead to vibrations and increased wear of components [Bruckmann and Boumann, 2021]. To account

[10] While the vector $\boldsymbol{q}$ contains all joint variables of one robot configuration, the configuration space is a set of all possible configurations [Spong et al., 2005].

for a continuous position, velocity, acceleration and jerk profile along the trajectory, septic polynomials can be chosen. Taking into account corresponding boundary conditions it yields

$$\boldsymbol{x}_P(t_0) = \boldsymbol{x}_{P,0} \qquad \dot{\boldsymbol{x}}_P(t_0) = 0 \qquad \ddot{\boldsymbol{x}}_P(t_0) = 0 \qquad \dddot{\boldsymbol{x}}_P(t_0) = 0 \tag{2.76}$$

$$\boldsymbol{x}_P(t_f) = \boldsymbol{x}_{P,f} \qquad \dot{\boldsymbol{x}}_P(t_f) = 0 \qquad \ddot{\boldsymbol{x}}_P(t_f) = 0 \qquad \dddot{\boldsymbol{x}}_P(t_f) = 0, \tag{2.77}$$

which can be represented using a polynomial of seventh order in the form of

$$x_{P,k}(t) = a_{7_k}t^7 + a_{6_k}t^6 + a_{5_k}t^5 + a_{4_k}t^4 + a_{3_k}t^3 + a_{2_k}t^2 + a_{1_k}t + a_{0_k}. \tag{2.78}$$

The derivatives to meet all boundary conditions are thus as follows

$$\dot{x}_{P,k}(t) = 7a_{7_k}t^6 + 6a_{6_k}t^5 + 5a_{5_k}t^4 + 4a_{4_k}t^3 + 3a_{3_k}t^2 + 2a_{2_k}t^1 + a_{1_k} \tag{2.79}$$

$$\ddot{x}_{P,k}(t) = 42a_{7_k}t^5 + 30a_{6_k}t^4 + 20a_{5_k}t^3 + 12a_{4_k}t^2 + 6a_{3_k}t + 2a_{2_k} \tag{2.80}$$

$$\dddot{x}_{P,k}(t) = 210a_{7_k}t^4 + 120a_{6_k}t^3 + 60a_{5_k}t^2 + 24a_{4_k}t + 6a_{3_k}. \tag{2.81}$$

To determine the polynomial coefficients efficiently for given boundary conditions as well as given t_0 and t_f, the problem can be expressed and solved in matrix form [Sturm, 2020]. Such continuously described trajectory between two points can be sampled cyclically in discrete time steps to serve as an input for robot motion control. A graphical presentation can be found in Section 4.3.2. For further information it is referred to [Spong et al., 2005].

2.5.2 Splines

While polynomials are well suited for point-to-point trajectory planning, the task may require to plan a movement along multiple points or robot configurations. A well-known approach is to use so-called via points [Spong et al., 2005] or way points [Siciliano and Khatib, 2008]. Each via point imposes additional constraints to the trajectory which can, for instance, be satisfied by using a polynomial of higher order. However, with increasing order for multiple via points, the computational costs for the determination of the coefficients rise. Moreover, a polynomial with high order may tend to oscillations between the via points. Alternatively, the trajectory can be split up into segments. Each segment is then represented by a lower order polynomial and connected at the via points, resulting in a spline. The constraints introduced by each via point ensure for a continuous transition in all time derivatives between the trajectory segments. Moreover, the determination of the polynomials' coefficients decays into solving multiple linear systems with lower dimension [Spong et al., 2005]. Within this work, the via points are also referred to as knots, see Section 6.2.

2.6 Model-Based Control

In general, various control algorithms may be applied for a CDPR. A pose control based on the kinematic robot models is common [Pott, 2018], also force control is feasible [Kraus, 2016, Mattioni et al., 2023, Reichert et al., 2014]. However, due to their heavy non-linear characteristics, a pose control of CDPRs is nontrivial. In [Reichert et al., 2015a, Reichert et al., 2015b], a suitable control approach is presented: A non-linear augmented PD controller, short APD controller. The controller's basis is formed by a PD control of desired cable lengths $\boldsymbol{l}_D \in \mathrm{R}^m$ and cable velocities $\dot{\boldsymbol{l}}_D \in \mathrm{R}^m$ in joint space. The latter can be derived from a trajectory using inverse kinematics. The desired pose and its derivatives at a discrete time step on the desired trajectory are denoted as $\boldsymbol{x}_D$, $\dot{\boldsymbol{x}}_D$ and so forth. Using drive unit measurements, the vectors of cable length errors $\Delta\boldsymbol{l} \in \mathrm{R}^m$ and velocity errors $\Delta\dot{\boldsymbol{l}} \in \mathrm{R}^m$ are determined according to eq. (2.44) and eq. (2.45). $\boldsymbol{K}_P \in \mathrm{R}^{m\times m}$ and $\boldsymbol{K}_D \in \mathrm{R}^{m\times m}$ are diagonal gain matrices. The required platform wrench $\boldsymbol{w}$, as introduced in eq. (2.38), is further included to complement the controller by a model-based feed forward path, which supports to cope for the robots nonlinearities. This yields the following controller law

$$\boldsymbol{w}_{\mathrm{APD}} = \underbrace{\boldsymbol{A}^{\mathrm{T}}(\boldsymbol{K}_P\,\Delta\boldsymbol{l} + \boldsymbol{K}_D\,\Delta\dot{\boldsymbol{l}})}_{\boldsymbol{w}_{\mathrm{PD}}} + \boldsymbol{w}. \tag{2.82}$$

The resulting wrench $\boldsymbol{w}_{\mathrm{APD}}$ is further used to compute cable force distributions $\boldsymbol{f}_D \in \mathrm{R}^m$ according to Section 2.3, which are converted to set-point torques $\boldsymbol{\tau}_D \in \mathrm{R}^m$ for the drives. The controller's structure is displayed by fig. 2.8. A brief discussion on the controller's parametrization and stability is given in [Hufnagel, 2014]. Within this work, the APD controller is referred to as conventional controller.

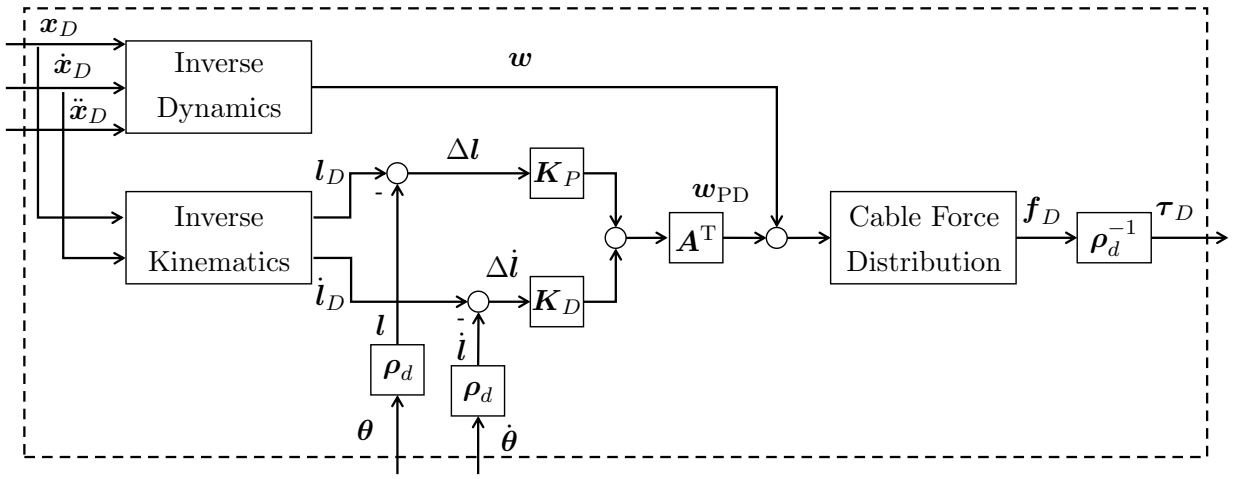

Figure 2.8: Diagram of the augmented PD controller based on [Reichert et al., 2015a, Boumann and Bruckmann, 2022].

Chapter 3

Strategies for Damage Avoidance After Cable Failure

This chapter introduces the strategies for damage avoidance after a cable failure developed and employed within this work. First, fundamental and mathematical considerations are conducted regarding the post-failure situation. Based on the theoretical background given in the previous chapter, algorithms are proposed to determine cable robot workspaces. This includes a consideration of pre- and post-failure workspace taking into account platform rotation if necessary. Two emergency strategies developed by the author are presented subsequently: The first strategy is based on a nonlinear model prediction in order to minimize the system's kinetic energy and thus stop unfavorable movement of the end effector. Furthermore, the strategy is extended by using movable deflection pulleys. The second strategy utilizes potential fields, which is a well-known robotic path planning method, for damage avoidance and robot guidance. Because of the emergency scenario, this strategy needs to be combined with a method to determine cable forces outside of the $\mathcal{WFW}$. Two methods for this purpose are presented: The first one is an optimization based approach, while the second method, developed by the author, relies on geometrical calculations within the space of cable forces and is non iterative.

3.1 Fundamental Considerations

As described in Section 1.2, a cable of a CDPR may fail in various cases, resulting in unfavorable or fatal consequences. Such can be mis- or uncontrolled movement [Boumann and Bruckmann, 2022], possibly leading to machine damage, loss of a carried payload, harm to workers or environmental damage. Therefore, it is crucial to have action strategies in place for such scenarios. CDPRs typically use multiple cables, and many prototypes are of the CRPM or RRPM type. Hence, if a cable fails, there will still be a robot with $m-1$ cables that can be influenced or constrained by the remaining cables, as assumed in the following.

In the event of a cable failure, the workspace of a CDPR may be significantly reduced [Boumann and Bruckmann, 2019a, Boumann and Bruckmann, 2019b]. Thus, it is advisable to consider the entire workspace when analyzing the CDPR, as cable failures can occur anywhere within it.[1] As a result, there is a high probability that the end effector will be outside the remaining workspace after a failure. No static force equilibrium is possible at such pose with the remaining cables. Of course, enabling the brakes (if available at the prototype) would be the most intuitive action. Yet under the influence of gravity the platform will inevitably start to move, i.e. even if the drives of the remaining cables are braked, some cables can get loose while the platform sways uncontrolled. Provided the robot stops without a crash, an automated restart will not be possible since the platform is still outside the workspace with some cables slack. Hence, a restart can only be done manually. Options would be to repair the robot within the braked stated, bringing the platform manually into the remaining workspace or bringing it manually to the ground for maintenance and repair. Depending on the surroundings, the given equipment, the size of the robot and the end effector's mass, this maneuver might be circumstantial and possibly dangerous for workers, as they might need to enter the robots workspace.[2] An automatic guidance to the post-failure workspace after a cable failure would clearly be the better option.[3] From there, the robot can automatically move into a desired pose or to the ground (if allowed by the remaining workspace) for repair. Beyond that, it could even continue fulfilling operations in the post-failure workspace using the remaining cables.

As discussed in [Boumann and Bruckmann, 2019a, Boumann and Bruckmann, 2019b], standard control approaches might fail in the situation of a cable failure when the robot is outside of its remaining workspace, leading to un- or miscontrolled movement of the platform [Boumann and Bruckmann, 2022], which will be further shown in Section 4.3.4 and Sec-

[1] Details on pre- and post-failure workspace are given in the upcoming section.

[2] Persons below hanging objects must be critically examined regarding working safety [DGUV, 2020].

[3] Note that besides using the remaining cables for an emergency strategy, the motor of the failed cable should be stopped to prevent the loose cable end from getting stuck or lashing.

tion 5.3.1. Existing strategies to react in case of a cable failure are discussed in Section 1.3.1. Many of these rely on trajectory planning, which might be computationally expensive. Since the robot is not within its original workspace, finding feasible trajectories into a well-chosen goal position within the post-failure workspace might become a complicated optimization problem [Passarini et al., 2019]. During computationally intensive operations, valuable time is lost while the platform may perform uncontrolled motion. Therefore, the intervention should be as fast and targeted as possible. For this purpose, two damage avoidance strategies are introduced in the upcoming sections, which are proposed and tested in simulation by the author in [Boumann and Bruckmann, 2019a, Boumann and Bruckmann, 2019b]. They do not require complex trajectory planning, but rather rely on reflexive actions. In practice, the control system also needs to reliably detect a cable failure in order to enable an emergency strategy. Therefore, the detection of cable failures at a given prototype is investigated in Section 5.1.3.

When studying cable failure, it is reasonable to consider only a few different cases of a failed cable: As CPDRs often own a symmetrical structure, the results can be transferred to the other cables in good approximation. In this work, a general distinction is made between the failure of an upper cable, i.e. a cable that goes from the top of the frame to the platform, and a lower cable, i.e. a cable that goes from the bottom of the frame to the platform. It is assumed that, due to the symmetrical structure of the prototypes studied, the results of these two cases can be transferred to all other cables.

For the failure of one cable, $m-1$ cables still exist, which leads to changes in the mathematical models: The structure matrix of the post-failure system is reduced by the column of the missing cable and will be denoted $\boldsymbol{A}^{\mathrm{T}*} \in \mathbb{R}^{n\times m-1}$ in the following. The remaining cable force distribution becomes $\boldsymbol{f}^* \in \mathbb{R}^{(m-1)\times 1}$ without the entry of the broken cable. Accordingly, the force boundaries become $\boldsymbol{f}^*_{\min}, \boldsymbol{f}^*_{\max} \in \mathbb{R}^{(m-1)\times 1}$. In the case of multiple cable failure, the above is adjusted correspondingly, i.e. for two failed cables $m-2$ cables remain, et cetera. As long as at least one cable remains, the platform can be influenced.

3.2 Determination of the Post-Failure Workspace

Understanding the shape of the workspace and its deformation after a cable failure is crucial to determining the probability that the platform will get outside the workspace after failure. In addition, this knowledge might be necessary to plan damage avoidance strategies. Thus, the pre-failure workspace (before a cable fails) and the post-failure workspace (after a cable fails) are defined as described in [Boumann and Bruckmann, 2021].

Within this work, the displayed workspaces are determined using discretization methods (see Section 2.4.2). The exact procedure is similar as described in

[Boumann and Bruckmann, 2021], which is based on [Bruckmann, 2010]: First, a discrete grid $\mathcal{G}$ is defined for poses $\boldsymbol{x}_P$ to be examined. The limits are set to

$$\boldsymbol{x}_P = \begin{bmatrix} r_x \\ r_y \\ r_z \\ \varphi \\ \vartheta \\ \psi \end{bmatrix} \in \begin{bmatrix} [r_{x,\min}, r_{x,\max}] \\ [r_{y,\min}, r_{y,\max}] \\ [r_{z,\min}, r_{z,\max}] \\ [\varphi_{\min}, \varphi_{\max}] \\ [\vartheta_{\min}, \vartheta_{\max}] \\ [\psi_{\min}, \psi_{\max}] \end{bmatrix}, \tag{3.1}$$

with $[r_{x,\min}, r_{x,\max}]$ being the limits for the x-component of the pose, et cetera. For each degree of freedom, a discretization step width is introduced as

$$\Delta\boldsymbol{x}_P = \Big[\Delta r_x, \Delta r_y, \Delta r_z, \Delta\varphi, \Delta\vartheta, \Delta\psi\Big]^{\mathrm{T}}, \tag{3.2}$$

with Δr_x being the step width for the x-component of the pose, et cetera. For the purpose of simple representation within this work, a grid $\mathcal{G}$ is described by

$$\mathcal{G} = \begin{bmatrix} [r_{x,\min}, r_{x,\max}], \Delta r_x \\ [r_{y,\min}, r_{y,\max}], \Delta r_y \\ [r_{z,\min}, r_{z,\max}], \Delta r_z \\ [\varphi_{\min}, \varphi_{\max}], \Delta\varphi \\ [\vartheta_{\min}, \vartheta_{\max}], \Delta\vartheta \\ [\psi_{\min}, \psi_{\max}], \Delta\psi \end{bmatrix}. \tag{3.3}$$

Within a workspace calculation, the grid is now sampled according to the step size in each DOF. The grid's physical units are m for position and rad for orientation. They will not be displayed further on for reasons of readability. At each pose, the inverse kinematics (see Section 2.2.2) is computed and eq. (2.41) is tried to be solved as an optimization problem in the least-squares sense, using an active set algorithm. For the calculation of static equilibrium forces, only the gravitational forces and torques are included within $\boldsymbol{w}$. Poses with feasible cable forces between $\boldsymbol{f}_{\min}$ and $\boldsymbol{f}_{\max}$ are saved into a set $\mathcal{G}_{\text{feasible}}$. For an eligible graphical representation of the feasible poses forming the workspace, a convex hull is created around $\mathcal{G}_{\text{feasible}}$ in Cartesian space, which is displayed with a triangular surface plot.

When determining the static equilibrium workspace with constant orientation, further called $\mathcal{SECOW}$), the grid is limited to the Cartesian space directions and φ, ϑ, ψ are set to zero, leading to the grid $\mathcal{G}_{\mathcal{SECOW}}$. The corresponding algorithm can be formulated as displayed in algorithm 1. As an example, it is now applied to the prototype CARLO (described in Section 1.1.3 and Section 6.1.4). First the regular (pre-failure) workspace is

Algorithm 1 Discrete determination of static equilibrium workspace with constant orientation $\mathcal{SECOW}$.

$\mathcal{G}_{\text{feasible}} \leftarrow \{\}$
for $r_x = r_{x,\min} : \Delta r_x : r_{x,\max}$ **do**
  for $r_y = r_{y,\min} : \Delta r_y : r_{y,\max}$ **do**
    for $r_z = r_{z,\min} : \Delta r_z : r_{z,\max}$ **do**
      Compute inverse kinematics with $\boldsymbol{x}_P = [r_x, r_y, r_z, 0, 0, 0]^{\mathrm{T}}$
      Compute cable forces $\boldsymbol{f}$
      if $\boldsymbol{f}_{\min} \leq \boldsymbol{f} \leq \boldsymbol{f}_{\max}$ **then**
        $\boldsymbol{r}_P = [r_x, r_y, r_z]^{\mathrm{T}}$
        $\mathcal{G}_{\text{feasible}} \leftarrow \mathcal{G}_{\text{feasible}} \cup \boldsymbol{r}_P$
      else
        $\mathcal{G}_{\text{feasible}} \leftarrow \mathcal{G}_{\text{feasible}}$
      end if
    end for
  end for
end for
Create convex hull around $\mathcal{G}_{\text{feasible}}$
Generate triangular surface plot

determined with all cables operational and the movable pulleys in their regular position, see [Bruckmann and Boumann, 2021], depicted in fig. 3.1a. If now a cable fails, the workspace can be reduced or deformed. For demonstration, the post-failure workspace is determined exemplarily for the failure of one of the upper cables of CARLO. As described in Section 3.1, the corresponding cable is excluded accordingly and algorithm 1 is performed resulting in fig. 3.1b. As can be seen from the figure, the remaining post-failure workspace is remarkably smaller, promoting the chance of the platform being outside of the workspace after cable failure. In this case, the platform will start to move, even if brakes are engaged for the remaining drives units. This clearly shows that a damage avoidance strategy is indispensable.

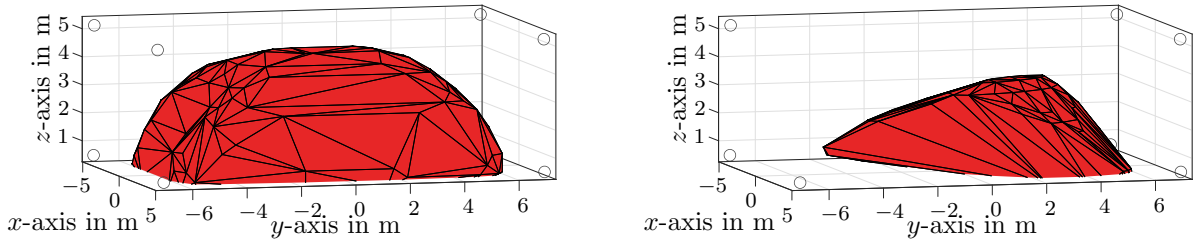

(a) Pre-failure workspace.

(b) Post-failure workspace, failure of cable 2.

Figure 3.1: Pre- and post-failure static equilibrium workspace with constant orientation of the prototype CARLO using the discrete Grid $\mathcal{G}_{\mathcal{SECOW}} = \begin{bmatrix} [-4, & [-6, & [0, & [0, & [0, & [0, \\ 4] & 6] & 5.2] & 0] & 0] & 0] \\ 0.25 & 0.25 & 0.325 & 0 & 0 & 0 \end{bmatrix}^{\mathrm{T}}$. Pulley positions indicated by circles in the corners.

In the context of damage avoidance strategies and recovery planning, it might be helpful to consider some platform rotation. Platform rotation can be bothersome, e.g. if a payload is being carried or if cable collisions are imminent, but it can increase the number of poses in which static equilibrium, i.e. a safe state, can be found. Thus, investigating the points on a discrete grid as shown in algorithm 1 for feasible cable forces in a rotated pose can be promising. The static equilibrium workspace with variable orientation is now referred to as $\mathcal{SEOW}$. As displayed in algorithm 2, each point on the spatial grid is investigated for a feasible cable force distribution using the angles φ, ϑ, ψ within their boundaries and the corresponding discretization step width. It can be noted that, as soon as any orientation with a feasible cable force distribution is found at a certain position, the loop is interrupted and the next position is investigated. The algorithm is chosen this way because the most useful information is whether there is a feasible orientation at a given position, not to gain knowledge about all feasible orientations at that position. Therefore, the information gain about all feasible orientations at that position is neglected. As a result, the computation time for the workspace is shorter compared to a study of all possible orientations. More-

Algorithm 2 Discrete determination of static equilibrium workspace with variable orientation $\mathcal{SEOW}$.

1: $\mathcal{G}_{\text{feasible}} \leftarrow \{\}$
2: **for** $r_x = r_{x,\min} : \Delta r_x : r_{x,\max}$ **do**
3: **for** $r_y = r_{y,\min} : \Delta r_y : r_{y,\max}$ **do**
4: **for** $r_z = r_{z,\min} : \Delta r_z : r_{z,\max}$ **do**
5: **for** $\varphi = \varphi_{\min} : \Delta\varphi : \varphi_{\max}$ **do**
6: **for** $\vartheta = \vartheta_{\min} : \Delta\vartheta : \vartheta_{\max}$ **do**
7: **for** $\psi = \psi_{\min} : \Delta\psi : \psi_{\max}$ **do**
8: Compute inverse kinematics with $\boldsymbol{x}_P = [r_x, r_y, r_z, \varphi, \vartheta, \psi]^{\mathrm{T}}$
9: Compute cable forces $\boldsymbol{f}$
10: **if** $\boldsymbol{f}_{\min} \leq \boldsymbol{f} \leq \boldsymbol{f}_{\max}$ **then**
11: $\boldsymbol{r}_P = [r_x, r_y, r_z]^{\mathrm{T}}$
12: $\mathcal{G}_{\text{feasible}} \leftarrow \mathcal{G}_{\text{feasible}} \cup \boldsymbol{r}_P$
13: **go to** 20
14: **else**
15: $\mathcal{G}_{\text{feasible}} \leftarrow \mathcal{G}_{\text{feasible}}$
16: **end if**
17: **end for**
18: **end for**
19: **end for**
20: **end for**
21: **end for**
22: **end for**
23: Create convex hull around $\mathcal{G}_{\text{feasible}}$
24: Generate triangular surface plot

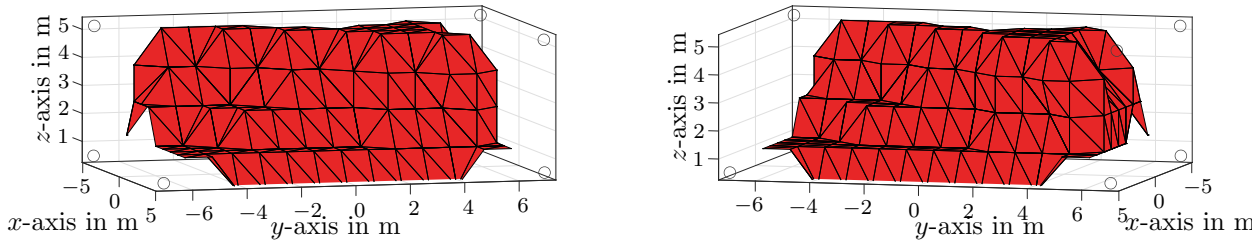

(a) View from left.

(b) View from right.

Figure 3.2: Post-failure static equilibrium workspace after failure of cable 2 with variable orientation using the discrete grid $\mathcal{G}_{\mathcal{SEOW}} = \begin{bmatrix} [-4, & [-6, & [0, & [-0.3, & [-0.3, & [-0.3, \\ 4] & 6] & 5.2] & 0.3] & 0.3] & 0.3] \\ 0.25 & 0.25 & 0.325 & 0.15 & 0.15 & 0.15 \end{bmatrix}^{\mathrm{T}}$. Pulley positions indicated by circles in the corners.

over, the three-dimensional representation of feasible poses is still appropriate and provides a comprehensive illustration if any (rotated) pose can be found on the spatial grid points within its boundaries where a static force equilibrium is possible. Using algorithm 2, the graphical representation fig. 3.2 can be obtained for the prototype CARLO allowing orientations according to the grid $\mathcal{G}_{\mathcal{SEOW}}$. In comparison to fig. 3.1b, it is obvious, that a feasible pose can be found at remarkably more positions if some rotation is allowed. Thus, chances are high that the platform must get in a slightly tilted pose to be stopped successfully and more easily.

In conclusion, it is likely that the end effector gets outside its workspace after a cable failure, leading to an inevitable movement of the platform. Consequently, damage avoidance strategies to guide the platform in a controlled manner into a static stable pose are required. Two strategies developed by the author are explained in the next sections.

3.3 Kinetic Energy Minimization Method

In the case of a cable failure, the end effector might get beyond its workspace (see Section 3.2). Consequently, common methods to calculate cable forces might fail [Boumann and Bruckmann, 2019a] and alternative approaches are required to control the platform in order to prevent damage. The author proposes two damage avoidance strategies in his work [Boumann and Bruckmann, 2019a], which will be broadly explained in the following. The main idea of the first approach presented is to minimize the kinetic energy of the system and hence the speed of the platform. If it can be stopped successfully with all cables in tension, it will automatically be in a static force equilibrium. This strategy is implemented using a nonlinear model predictive control approach.

3.3.1 Nonlinear Model Predictive Control Approach

Model-based predictive controls are the advanced control methods which are most widely used in industrial practice, which is shown by Quin and Badgwell [Qin and Badgwell, 2003]. Within literature it is also referred to as model predictive control or MPC for short. The field of application is versatile [Adamy, 2014] and application for CDPRs is common [Katliar et al., 2017]. Basically, model-based predictive control is a nonlinear control method, applicable to linear and nonlinear controlled systems. The function of a MPC is described in numerous sources, e.g. by Huang [Sunan et al., 2001], Camacho [Camacho, 2007], Grüne [Grüne, 2011] or Adamy [Adamy, 2014]. Within this work, the focus is on nonlinear model predictive control, which is denoted NMPC in the following. As displayed in fig. 3.3,

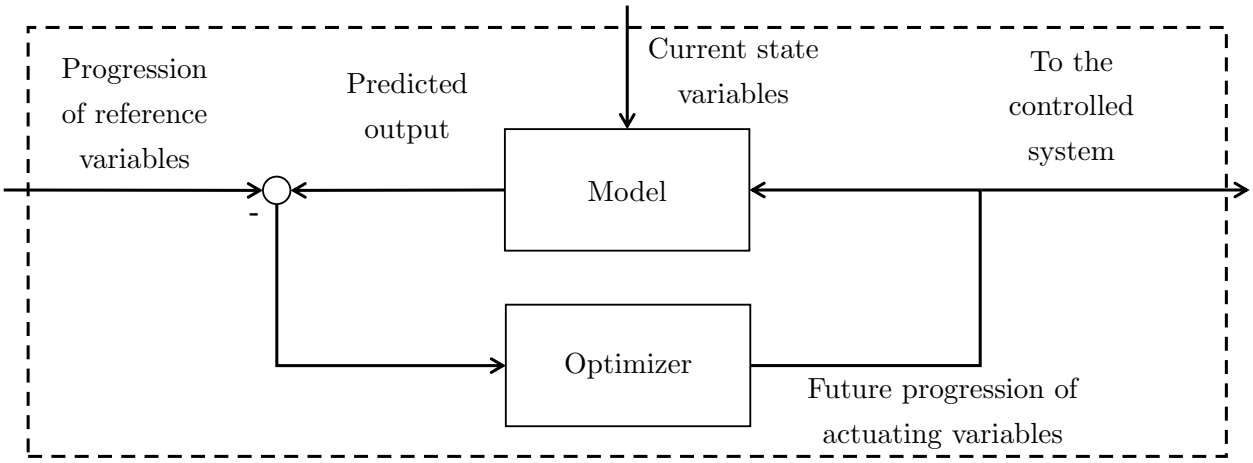

Figure 3.3: Structure of a model-based predictive control adapted from [Adamy, 2014].

the main idea of an MPC consists of a prediction based on a mathematical system model combined with an optimization of the future system behavior in order to receive an optimal control variable progression. This progression is generated online and can then be used to control the system. Adamy [Adamy, 2014] compares the predictive optimization process with the procedure of a chess player. The player evaluates a finite number of move sequences and afterwards decides on the best possible next move, which he then performs in reality.

The description of a system within the context of a NMPC can be continuous or discrete. Mostly, discrete or discretized models of the following form are used:

$$\boldsymbol{x}(k+1) = f\big(\boldsymbol{x}(k), \boldsymbol{u}(k)\big) \tag{3.4}$$

$$\boldsymbol{y}(k) = g\big(\boldsymbol{x}(k), \boldsymbol{u}(k)\big). \tag{3.5}$$

The system states at discrete points of time t_k, $k = 0, 1, ...$ are denoted $\boldsymbol{x}(k)$. Hence, at each point of time k a control variable $\boldsymbol{u}(k)$ can be assigned to influence the future behavior of the system states. The inputs $\boldsymbol{u}(k)$ can be used to control the progression of the system

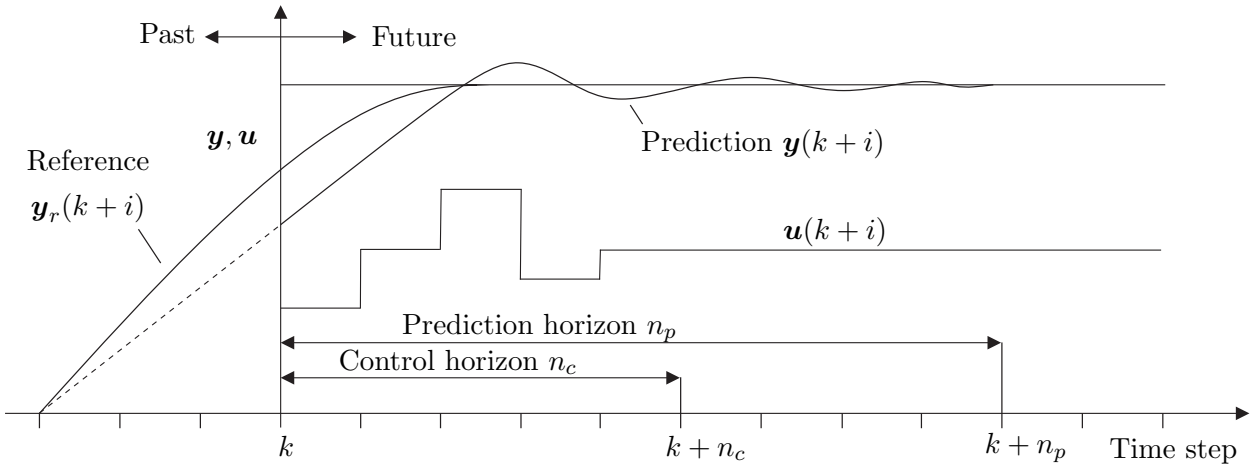

Figure 3.4: Time horizon of prediction and control variables adapted from [Adamy, 2014].

states or outputs along a reference trajectory $\boldsymbol{x}_\mathrm{r}(k)$, or $\boldsymbol{y}_\mathrm{r}(k)$ respectively. For the sake of simplicity, let the state variables be $\boldsymbol{x}(k) \in \boldsymbol{X} = \mathbb{R}$ and the control variables $\boldsymbol{u}(k) \in \boldsymbol{U} = \mathbb{R}$ for all $k \geq 0$ in the following. In the optimization process, the progression of control variables $\boldsymbol{u}(k+i)$ is varied for a finite number of steps to follow the desired reference trajectory. A quadratic cost function is often used to evaluate the optimization quality:

$$J = \sum_{i=1}^{n_p} \left\| \boldsymbol{R}\big(\boldsymbol{y}(k+i) - \boldsymbol{y}_r(k+i)\big) \right\|^2 + r_1 \sum_{i=i}^{n_c} \left\| \boldsymbol{u}(k+i-1) - \boldsymbol{u}(k+i-2) \right\|^2. \tag{3.6}$$

Here, $\boldsymbol{R}$ is a positive definite matrix, usually in diagonal shape and r_1 is a weighting factor for the control variable progression. The control horizon n_c contains the number of prediction steps in which the control variable progression $\boldsymbol{u}(k+i)$ is varied to optimize the cost function. The cost function is determined over the so-called prediction horizon with n_p steps. Both time horizons and the progression of the named variables is clarified in fig. 3.4. The first part of the cost function in eq. (3.6) evaluates the difference between the predicted and the reference system output. The second part compares the current and the previous control values in order to avoid discontinuities between two consecutive control values. After one optimization cycle, the calculated control values are fed into the system. The prediction and control horizon move one time step into the future. This type of procedure within an MPC is called moving horizon. Control deviations as well as disturbances can be taken into account through a recurring determination of the current system state, which can be done, e.g., by a measurement. In the case of non-measurable values, an observer for state estimation of $\tilde{\boldsymbol{x}}(k)$ might also be used [Busawon and Saif, 1999]. The resulting structure of the control loop including the optimizer and an observer is shown in fig. 3.5. In the nonlinear case, the calculation and optimization of control values is significantly more complex and computation extensive than in the linear case. Generally speaking, an optimization problem based on a

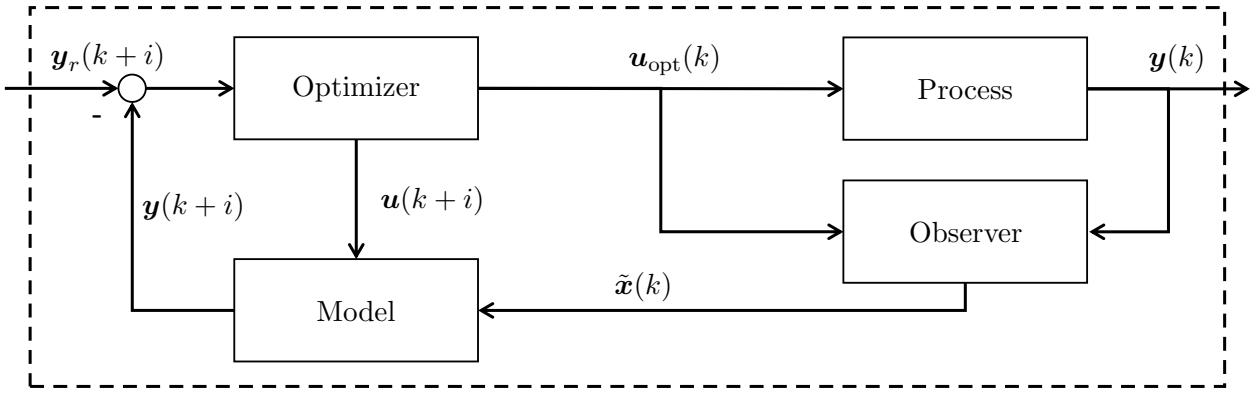

Figure 3.5: Structure of an NMPC control loop with state observer adapted from [Adamy, 2014].

nonlinear system dynamic is no longer convex [Adamy, 2014] and can have multiple local minima. Also the cost function value J is nonlinear dependent on the control values $\boldsymbol{u}(k+i)$. To solve the optimization problem, numerical optimizer can be used, e.g. according to [Coleman and Li, 1996], which follow an iterative scheme. The integration of the system over several time steps can be done with numerical methods like the Runge-Kutta or the Adams-Bashforth Method [Hairer et al., 1996, Hairer et al., 1993]. Solving such problems in real-time is one of the main challenges of MPC. Consequently, it is often used for slow control loops. Another challenge besides the real-time capability is that the assurance of the control loop's stability cannot be guaranteed due to the nonlinear dynamics. Often, it has to be evaluated experimentally. A good indication for evaluating the stability is provided by a monotonically or strictly monotonically decreasing value of the cost value J [Adamy, 2014]. Despite the computational effort of this control approach, its application is enabled for more dynamic systems in recent times, since the computing power of modern processor and computer technology is drastically increasing, see e.g. [Sieberg, 2021].

3.3.2 Application as a Damage Avoidance Strategy

One strategy to avoid damage after a cable failure in a CDPR is based on the aforementioned nonlinear model predictive control. The author develops and proposes this strategy in [Boumann and Bruckmann, 2019a]. The main idea is to minimize the kinetic energy of the system after a cable failure. The kinetic energy is dependent on the robot's velocity. Using a nonlinear dynamic robot model based on the explanations in Section 2.2.5, the NMPC is built up. Subsequently, the method predicts the system state utilizing the dynamic model to find set-point cable forces within feasible boundaries, which will minimize the kinetic energy of the platform (and thus its velocity). This necessarily leads to a stop of the system if the optimization is successful. Inherently, the end effector will be automatically within the

post-failure static equilibrium workspace if it is able to stop with the cables tensed. One major advantage of this method is that the final position does not need to be predefined. The method is developed as follows: First, the kinetic energy of the platform is given by

$$E_{\text{Kin}} = \frac{1}{2} m_P \dot{\boldsymbol{r}}_P^{\mathrm{T}} \dot{\boldsymbol{r}}_P + \frac{1}{2} \boldsymbol{\omega}_P^{\mathrm{T}} \boldsymbol{\Theta}_P \boldsymbol{\omega}_P, \tag{3.7}$$

assuming a rigid body. $\boldsymbol{\omega}_P$ is the angular velocity of the platform which is directly depending on $\dot{\boldsymbol{\Phi}}$ [Schramm et al., 2018], see eq. (2.5). Accordingly, the magnitude of $\dot{\boldsymbol{x}}_P$ must be minimized in order to minimize the kinetic energy. The system can be described by the nonlinear discrete state equations with the nonlinear system function $f\big(\boldsymbol{x}(k), \boldsymbol{u}(k)\big)$ which is based on eq. (2.38)

$$\begin{aligned} \boldsymbol{x}(k+1) &= f\big(\boldsymbol{x}(k), \boldsymbol{u}(k)\big) \\ \boldsymbol{y}(k+1) &= \boldsymbol{C}\, \boldsymbol{x}(k+1). \end{aligned} \tag{3.8}$$

Here, $\boldsymbol{x}(k)$ is the state vector of velocity and position, $\boldsymbol{y}(k)$ the output vector, $\boldsymbol{C}$ the output matrix and $\boldsymbol{u}$ the input vector. The state vector and the output vector are defined by

$$\begin{aligned} \boldsymbol{x}(k) =& [\, \dot{\boldsymbol{r}}_P^{\mathrm{T}}(k), \dot{\boldsymbol{\Phi}}^{\mathrm{T}}(k), \boldsymbol{r}_P^{\mathrm{T}}(k), \boldsymbol{\Phi}^{\mathrm{T}}(k) \,]^{\mathrm{T}} \\ \boldsymbol{y}(k) =& [\, \dot{\boldsymbol{r}}_P^{\mathrm{T}}(k), \dot{\boldsymbol{\Phi}}^{\mathrm{T}}(k) \,]^{\mathrm{T}}. \end{aligned} \tag{3.9}$$

Please note, that the output vector contains the system velocities. For a CDPR with $n = 6$, the output matrix is given by

$$\boldsymbol{C} = \begin{bmatrix} \boldsymbol{I}_3 & \boldsymbol{0} & \boldsymbol{0} & \boldsymbol{0} \\ \boldsymbol{0} & \boldsymbol{I}_3 & \boldsymbol{0} & \boldsymbol{0} \end{bmatrix}, \tag{3.10}$$

using the 3×3 identity matrix $\boldsymbol{I}_3$. The input vector is defined using the vector of remaining cable forces, i.e.

$$\boldsymbol{u}(k) = \boldsymbol{f}^*(k). \tag{3.11}$$

The nonlinear system function $f\big(\boldsymbol{x}(k), \boldsymbol{u}(k)\big)$ delivers $\boldsymbol{x}(k+1)$ which is the state vector in the next time step. This is implemented using numerical integration with a prediction step size of Δt_c, based on the Euler-Cromer Method [Cromer, 1981]:

$$\begin{aligned} \begin{bmatrix} \dot{\boldsymbol{r}}_P(k+1) \\ \dot{\boldsymbol{\Phi}}(k+1) \end{bmatrix} &= \begin{bmatrix} \dot{\boldsymbol{r}}_P(k) \\ \dot{\boldsymbol{\Phi}}(k) \end{bmatrix} + \begin{bmatrix} \ddot{\boldsymbol{r}}_P(k) \\ \ddot{\boldsymbol{\Phi}}(k) \end{bmatrix} \Delta t_c \\ \begin{bmatrix} \boldsymbol{r}_P(k+1) \\ \boldsymbol{\Phi}(k+1) \end{bmatrix} &= \begin{bmatrix} \boldsymbol{r}_P(k) \\ \boldsymbol{\Phi}(k) \end{bmatrix} + \begin{bmatrix} \dot{\boldsymbol{r}}_P(k+1) \\ \dot{\boldsymbol{\Phi}}(k+1) \end{bmatrix} \Delta t_c, \end{aligned} \tag{3.12}$$

with the acceleration derived from eq. (2.38)

$$\begin{bmatrix} \ddot{\boldsymbol{r}}_P \\ \ddot{\boldsymbol{\Phi}} \end{bmatrix} = \ddot{\boldsymbol{x}}_P = \boldsymbol{M}(\boldsymbol{x}_P)^{-1}\Big(\boldsymbol{A}^{\mathrm{T}*}\boldsymbol{f}^* - \boldsymbol{K}(\boldsymbol{x}_P, \dot{\boldsymbol{x}}_P) - \boldsymbol{Q}(\boldsymbol{x}_P, \dot{\boldsymbol{x}}_P)\Big). \tag{3.13}$$

Now a cost function J_{Ekin} can be set up using the prediction horizon n_p and the control horizon n_c. The cost function is minimized at each time step to generate set-point cable forces $\boldsymbol{f}^*$. Note, that the cable force limits $\boldsymbol{f}^*_{\mathrm{min}}$ and $\boldsymbol{f}^*_{\mathrm{max}}$ are taken into account. Consequently, the nonlinear optimization problem is constrained. Since the kinetic energy (and thus the velocity) should be minimized, the reference output $\boldsymbol{y}_r$ is set to zero. Hence, when the robot comes to a full stop and the cable forces remain constant, the function minimum will be obtained.

$$\begin{aligned} J_{\mathrm{Ekin}} = &\sum_{i=1}^{n_p} \big(\boldsymbol{y}(k+i) - \boldsymbol{y}_r(k+i)\big)^{\mathrm{T}} \boldsymbol{R} \big(\boldsymbol{y}(k+i) - \boldsymbol{y}_r(k+i)\big) + \dots \\ &\sum_{i=i}^{n_c} \big(\boldsymbol{f}^*(k+i-1) - \boldsymbol{f}^*(k+i-2)\big)^{\mathrm{T}} r_1 \big(\boldsymbol{f}^*(k+i-1) - \boldsymbol{f}^*(k+i-2)\big) \end{aligned} \tag{3.14}$$

With the parameters $\boldsymbol{R}$ and r_1, the optimization criteria can be weighted. Depending on r_1, varying cable forces between two time steps cause more or less costs. Therefore r_1 can be used to avoid discontinuities in the control values between two time steps. The elements of the diagonal matrix $\boldsymbol{R} = \mathrm{diag}(R_1, R_2, R_3, R_4, R_5, R_6)$ for $n = 6$, can be used to weight the importance of minimizing the velocity in each degree of freedom. For $R_3 = 2 \cdot R_1$ as an example, a deviation (platform movement) from the reference velocity (zero) in z-direction causes double the costs than the same deviation in x-direction. As a consequence, the optimization avoids movement of the platform in z-direction while it favors movement in x-direction. Such weightings might be used to enable evasive motion in some DOF, when movement in unfavorable DOF could lead to collisions (e.g. because of the platform moving towards the ground). The ratio between $\boldsymbol{R}$ and r_1 describes which of the multiple optimization goals is more important (constant forces or zero velocity). Ideally, both goals are achieved at the end of a damage avoidance scenario because they are not in opposition in static force equilibrium. A reasonable choice of the parameters can be determined experimentally or in simulation. The units of both parameters are chosen in such a way that J_{Ekin} becomes a unitless quantity. The resulting optimization problem is given by

$$\begin{aligned} \text{minimize} \quad & J_{\mathrm{Ekin}} \\ \text{with} \quad & \boldsymbol{f}^*_{\mathrm{min}} \leq \boldsymbol{f}^* \leq \boldsymbol{f}^*_{\mathrm{max}}. \end{aligned} \tag{3.15}$$

3.3.3 Extension with Movable Pivoting Pulleys

As explained in Section 1.1.3, some CDPR prototypes are equipped with movable pivoting pulleys allowing for a dynamic reconfiguration of the robot. In [Boumann and Bruckmann, 2021] the author demonstrates how the damage avoidance strategy based on a NMPC can be extended and enhanced using movable pivoting pulleys. In the following, this extension will be briefly described.

It is now assumed, that a prototype has pivoting pulleys which are actively movable in vertical direction. The movable pulleys are described with the parameters $\boldsymbol{s} = [s_1, \ldots, s_m]^{\mathrm{T}}$ for m cables. Here, each s describes the magnitude of the pulley movement of each pulley in z-direction. Consequently, the z-values of the corresponding $\boldsymbol{b}_i$ are changed, leading to a change of $\boldsymbol{B}$ over time according to the pulley movement. Consequently, all variables dependent on $\boldsymbol{B}$ are affected and thus change correspondingly. Note that only those elements are included in $\boldsymbol{s}$, for which the corresponding pulley is vertically movable. Now the input vector is extended to

$$\boldsymbol{u}(k) = [\boldsymbol{f}^{*\mathrm{T}}(k),\, \boldsymbol{s}^{\mathrm{T}}(k)]^{\mathrm{T}}. \tag{3.16}$$

This only holds true for failure of one of the cables without a movable pulley. Otherwise, the corresponding entry needs to be removed from $\boldsymbol{s}$, leading to $\boldsymbol{s}^*$. Since the pulley movement affects $\boldsymbol{B}$ and thus the structure matrix $\boldsymbol{A}^{\mathrm{T}*}$, the latter is now a function of values contained in the extended input within the optimization problem and eq. (3.13) is adjusted correspondingly. The pulley movement is weighted using the parameter r_2. The choice and scaling of the parameters is analog to Section 3.3.2. Now the extended cost function J_{EkinMov} can be set up as follows:

$$\begin{aligned} J_{\mathrm{EkinMov}} = &\sum_{i=1}^{n_p} \big(\boldsymbol{y}(k+i) - \boldsymbol{y}_r(k+i)\big)^{\mathrm{T}} \boldsymbol{R} \big(\boldsymbol{y}(k+i) - \boldsymbol{y}_r(k+i)\big) + \ldots \\ &\sum_{i=i}^{n_c} \big(\boldsymbol{f}^*(k+i-1) - \boldsymbol{f}^*(k+i-2)\big)^{\mathrm{T}} r_1 \big(\boldsymbol{f}^*(k+i-1) - \boldsymbol{f}^*(k+i-2)\big) + \ldots \\ &\sum_{i=i}^{n_c} \big(\boldsymbol{s}(k+i-1) - \boldsymbol{s}(k+i-2)\big)^{\mathrm{T}} r_2 \big(\boldsymbol{s}(k+i-1) - \boldsymbol{s}(k+i-2)\big). \end{aligned} \tag{3.17}$$

3.4 Potential Field Method

Besides the Kinetic Energy Minimization Method, the author presents a second strategy to avoid damage after a cable failure in [Boumann and Bruckmann, 2019a], which is based on potential fields. This method is a path planning method with the goal to avoid obstacles on the path of a robot. It will first be explained in general, followed by its application as a damage avoidance strategy.

The upcoming explanations of attractive and repulsive fields are based on the work of Spong [Spong et al., 2005] and consider potential fields within the operational space. The robot is treated as a point in the workspace and influenced by an artificial field $\boldsymbol{U}_{\text{pot}}$. This field $\boldsymbol{U}_{\text{pot}}$ is set up in a way that the robot will be pulled into its final position $\boldsymbol{r}_{P,\text{final}}$, while it is repelled from obstacle boundaries. Generally, the field $\boldsymbol{U}_{\text{pot}}$ is composed by one or more fields which can be attractive or repulsive. Let $\boldsymbol{U}_{\text{att}}$ be an attractive field and $\boldsymbol{U}_{\text{rep}}$ be an repulsive field, respectively. Then

$$\boldsymbol{U}_{\text{pot}}(\boldsymbol{r}_P) = \boldsymbol{U}_{\text{att}}(\boldsymbol{r}_P) + \boldsymbol{U}_{\text{rep}}(\boldsymbol{r}_P) \tag{3.18}$$

is a field whose potential is dependent on the position $\boldsymbol{r}_P$. In terms of field strength, the path planning can be viewed as an optimization problem with the goal of finding the local minimum of the resulting field strength [Spong et al., 2005]. One of the simplest algorithms to solve this problem is a gradient method: The composed virtual force acting on the robot is considered as negative gradient ∇ of the field $\boldsymbol{U}_{\text{pot}}$, which yields

$$\boldsymbol{F}(\boldsymbol{r}_P) = -\nabla \boldsymbol{U}_{\text{pot}}(\boldsymbol{r}_P) = -\nabla \boldsymbol{U}_{\text{att}}(\boldsymbol{r}_P) - \nabla \boldsymbol{U}_{\text{rep}}(\boldsymbol{r}_P). \tag{3.19}$$

Consequently, $\boldsymbol{F}(\boldsymbol{r}_P)$ is the virtual force which acts onto the platform in dependence of the current position $\boldsymbol{r}_P$ in order to move the robot according to the chosen potential fields.

3.4.1 Attractive Fields

As introduced, the method can include attractive and repulsive fields. As described in [Spong et al., 2005], an attractive field $\boldsymbol{U}_{\text{att}}$ should fulfill different requirements. First, it should be monotonically increasing with the distance to the final position $\boldsymbol{r}_{P,\text{final}}$. The most simple solution would be a field which is growing linear with the distance, called conic well potential. However, the gradient of such field is nonzero in its origin, which might cause stability issues since it causes a discontinuity in attractive forces at this location. Thus, a field is favored which is continuously differentiable. Hence, the attractive force decreases when the robot reaches $\boldsymbol{r}_{P,\text{final}}$. For this, the simplest approach would be a field which grows quadratically with the distance to the final position. Let $\rho_f(\boldsymbol{r}_P)$ be the Euclidean distance between $\boldsymbol{r}_P$ and $\boldsymbol{r}_{P,\text{final}}$, calculated as

$$\rho_f(\boldsymbol{r}_P) = \|\boldsymbol{r}_P - \boldsymbol{r}_{P,\text{final}}\|. \tag{3.20}$$

Thereupon, the quadratic field can be defined as

$$\boldsymbol{U}_{\text{att}}(\boldsymbol{r}_P) = \frac{1}{2}\zeta \rho_f^2(\boldsymbol{r}_P). \tag{3.21}$$

Using the parameter ζ, the effect of the attractive potential can be scaled. The gradient of the field $\boldsymbol{U}_{\text{att}}$ is given as

$$\nabla \boldsymbol{U}_{\text{att}}(\boldsymbol{r}_P) = \nabla \frac{1}{2}\zeta \rho_f^2(\boldsymbol{r}_P) = \zeta(\boldsymbol{r}_P - \boldsymbol{r}_{P,\text{final}}). \tag{3.22}$$

For the quadratic field, the attractive force $\boldsymbol{F}_{\text{att}}(\boldsymbol{r}_P) = -\nabla \boldsymbol{U}_{\text{att}}(\boldsymbol{r}_P)$ is a vector pointing towards $\boldsymbol{r}_{P,\text{final}}$. The magnitude of the attractive force is linear dependent on the distance of $\boldsymbol{r}_P$ to $\boldsymbol{r}_{P,\text{final}}$. It is to note, that while the attractive force converges towards zero in direction of $\boldsymbol{r}_P$ to $\boldsymbol{r}_{P,\text{final}}$, it also rises without a boundary, the more $\boldsymbol{r}_P$ moves away from the final position. As a consequence, attractive forces can be generated that may be considered too high. Therefore, a combination of a conic and a quadratic potential is suggested in [Spong et al., 2005]. For larger distances to $\boldsymbol{r}_{P,\text{final}}$, the conic potential is used, while the quadratic potential attracts the robot if $\boldsymbol{r}_P$ is near to $\boldsymbol{r}_{P,\text{final}}$. Such field can be defined using a distinction of cases:

$$\boldsymbol{U}_{\text{att}}(\boldsymbol{r}_P) = \begin{cases} \frac{1}{2}\zeta \rho_f^2(\boldsymbol{r}_P) & : \rho_f(\boldsymbol{r}_P) \leq d_b \\ d\zeta \rho_f^2(\boldsymbol{r}_P) - \frac{1}{2}\zeta d^2 & : \rho_f(\boldsymbol{r}_P) > d_b. \end{cases} \tag{3.23}$$

The resulting attractive force results in

$$\boldsymbol{F}_{\text{att}}(\boldsymbol{r}_P) = -\nabla \boldsymbol{U}_{\text{att}}(\boldsymbol{r}_P) = \begin{cases} -\zeta(\boldsymbol{r}_P - \boldsymbol{r}_{P,\text{final}}) & : \rho_f(\boldsymbol{r}_P) \leq d_b \\ -\dfrac{d\zeta(\boldsymbol{r}_P - \boldsymbol{r}_{P,\text{final}})}{\rho_f(\boldsymbol{r}_P)} & : \rho_f(\boldsymbol{r}_P) > d_b. \end{cases} \tag{3.24}$$

It is to note that the distinction of cases at the border $\rho_f(\boldsymbol{x}_P) = d_b$ produces equal forces in both cases, ensuring a smooth transition between both fields. The parameter d_b can be used to set the distance at which the stronger quadratic potential will act.

3.4.2 Repulsive Fields

A repulsive field also needs to meet requirements with respect to the robot movement, similar to an attractive field [Spong et al., 2005]. First, the robot should be repelled from an obstacle in a way, that a collision is impossible. Second, the robot's movement should not or only marginally be affected in greater distances to an obstacle. This can be achieved by defining a potential which declines to zero at a certain distance from the obstacle, while it rises towards infinity in the direction of the object boundaries. Let ρ_0 be the influence distance of an obstacle. For distances between the end effector and the obstacle larger than

ρ_0, the potential of the field does not affect the robot. This potential can be described by

$$\boldsymbol{U}_{\text{rep}}(\boldsymbol{r}_P) = \begin{cases} \frac{1}{2}\eta\left(\frac{1}{\rho_{\text{rep}}(\boldsymbol{r}_P)} - \frac{1}{\rho_0}\right)^2 & : \rho_{\text{rep}}(\boldsymbol{r}_P) \leq \rho_0 \\ 0 & : \rho_{\text{rep}}(\boldsymbol{r}_P) > \rho_0. \end{cases} \tag{3.25}$$

Here, $\rho_{\text{rep}}(\boldsymbol{r}_P)$ is the shortest distance in between $\boldsymbol{r}_P$ and the nearest boundary of the hindering obstacle, similar to eq. (3.20). The parameter η can be used to scale the influence of the field. Assuming an obstacle whose boundaries can be described by single convex regions, the corresponding repulsive force is given by the negative gradient of the repulsive field

$$\boldsymbol{F}_{\text{rep}}(\boldsymbol{r}_P) = \begin{cases} \eta\left(\frac{1}{\rho_{\text{rep}}(\boldsymbol{r}_P)} - \frac{1}{\rho_0}\right)\frac{1}{\rho^2_{\text{rep}}(\boldsymbol{r}_P)}\nabla\rho_{\text{rep}}(\boldsymbol{r}_P) & : \rho_{\text{rep}}(\boldsymbol{r}_P) \leq \rho_0 \\ 0 & : \rho_{\text{rep}}(\boldsymbol{r}_P) > \rho_0. \end{cases} \tag{3.26}$$

Let $\boldsymbol{o}_b$ be the point on the obstacle boundary, which is nearest to $\boldsymbol{r}_P$. Then the gradient of the distance to the nearest obstacle is given by

$$\nabla\rho_{\text{rep}}(\boldsymbol{r}_P) = \frac{\boldsymbol{r}_P - \boldsymbol{o}_b}{\|\boldsymbol{r}_P - \boldsymbol{o}_b\|}. \tag{3.27}$$

To avoid different obstacles, multiple repulsive fields might be defined.

3.4.3 Application as a Damage Avoidance Strategy

In general, the Potential Field Method can be utilized for robot path planning as described in the previous section. Of course, it can be also be applied for CDPRs as demonstrated in [Zi et al., 2015]. In [Boumann and Bruckmann, 2019a] the author proposes to apply this method as a damage avoidance strategy after a cable failure. The implementation shown here is furthermore based on work of the author presented in [Boumann et al., 2023].

The main idea is as follows: First, a goal pose within the post-failure workspace (as described in Section 3.2) is selected after a workspace analysis, which needs to be done carefully in advance of an emergency. In case of cable failure, the end effector should be pulled into this goal pose to bring it into a static force equilibrium and stop any movement. In comparison to the Kinetic Energy Minimization Method (see Section 3.3), a carefully chosen goal pose is crucial. For simplicity, position $\boldsymbol{r}_P$ and orientation $\boldsymbol{\Phi}$ are considered separately. The desired final position is $\boldsymbol{r}_{P,\text{final}}$ and the desired final orientation is $\boldsymbol{\Phi}_{\text{final}}$. The attractive force is given by $\boldsymbol{F}_{\text{att}}(\boldsymbol{r}_P)$, analogous to eq. (3.24), with the vector of scaling factors $\boldsymbol{\zeta}_r = \text{diag}(\zeta_x, \zeta_y, \zeta_y)$ and the border d_b. Furthermore, an attractive torque $\boldsymbol{\tau}_{\text{att}}(\boldsymbol{\Phi})$ is

introduced, dependent on $\boldsymbol{\Phi}$ and $\boldsymbol{\Phi}_{\text{final}}$. Here, only a quadratic potential is employed, see eq. (3.24), using the vector of scaling factors $\boldsymbol{\zeta}_{\Phi} = \text{diag}(\zeta_{\varphi}, \zeta_{\vartheta}, \zeta_{\phi})$. Accordingly, a parameter for a border does not apply in this case. To prevent platform collisions with obstacles, a robot frame or the ground, repulsive fields can be defined. In preliminary work of the author [Boumann and Bruckmann, 2019a], the ground is chosen to place a repulsive field for example. For each obstacle a separate repulsive field is introduced. Let $o \in \mathbb{R}$ be the number of repulsive fields. Then the virtual force acting onto the platform due to its position and the repulsive fields is given by

$$\boldsymbol{F}_{\text{rep}}(\boldsymbol{r}_P) = \sum_{i=1}^{o} \boldsymbol{F}_{\text{rep,i}}(\boldsymbol{r}_P). \tag{3.28}$$

It is to note, that each $\boldsymbol{F}_{\text{rep,i}}(\boldsymbol{r}_P)$ is given analogous to eq. (3.26) taking into account the influence distance for each field. The virtual force generated by the attractive and repulsive potential fields is included within the wrench $\boldsymbol{w}_E$. Moreover, a virtual damping onto the platform movement is introduced, which is proportional to the translational and rotational velocity. It is intended to introduce a stabilizing effect. To enable scaling of the damping for each individual DOF, the diagonal matrices $\boldsymbol{D}_1 = \text{diag}(D_{r,x}, D_{r,y}, D_{r,z})$ and $\boldsymbol{D}_2 = \text{diag}(D_{\varphi}, D_{\vartheta}, D_{\psi})$ are used. Considering all virtual forces and torques including external ones, eq. (2.35) yields

$$\boldsymbol{w}_E = \begin{bmatrix} \boldsymbol{f}_E \\ \boldsymbol{\tau}_E \end{bmatrix} + \begin{bmatrix} \boldsymbol{F}_{\text{att}}(\boldsymbol{r}_P) + \sum_{i=1}^{o} \boldsymbol{F}_{\text{rep,i}}(\boldsymbol{r}_P) \\ \boldsymbol{\tau}_{\text{att}}(\boldsymbol{\Phi}) \end{bmatrix} - \begin{bmatrix} \boldsymbol{D}_1 \dot{\boldsymbol{r}}_P \\ \boldsymbol{D}_2 \dot{\boldsymbol{\Phi}} \end{bmatrix}. \tag{3.29}$$

If now this wrench can be generated by the cables, the end effector will move according to the potential fields. Depending on the parameter choices and the end effector pose, which may be outside of the post-failure workspace, the wrench may vary drastically. Thus, eq. (2.41) might not be solvable with given force limits. Consequently, conventional methods to determine cable forces might fail [Boumann and Bruckmann, 2019a] and specialized methods are required which will be discussed in the next section.

3.5 Cable Force Calculation Outside the Wrench-Feasible Workspace

Besides leaving the static workspace, a CDPR may also get outside of the wrench-feasible workspace as stated previously. This may happen when using a haptic device [Côté et al., 2016] or after a cable failure [Boumann and Bruckmann, 2019a, Boumann and Bruckmann, 2020b, Boumann and Bruckmann, 2020a], for example. In such

cases, common methods to determine cable force distributions fail to operate as no feasible solution for eq. (2.41) exists [Boumann and Bruckmann, 2022]. Therefore, two methods to generate approximated but reasonable cable force distributions outside of the wrench-feasible workspace are now given.

3.5.1 Optimization-Based Approach

A method to determine cable force distributions as an optimization problem within certain force limits outside of the wrench-feasible workspace is proposed in [Côté et al., 2016]. First it is assumed that the robot is outside its $\mathcal{WFW}$. Changing the constraints of minimum and maximum cable forces in order to find feasible force distributions is no option. Therefore, eq. (2.41) needs to be relaxed adding a so called slack variable $\boldsymbol{\varsigma}$ to the equation. The resulting problem can be solved using quadratic programming as proposed in [Côté et al., 2016]. It is given as

$$\begin{aligned} \text{minimize} \quad & \boldsymbol{\varsigma}^{\mathrm{T}}\boldsymbol{W}_1\boldsymbol{\varsigma} + (\boldsymbol{f} - \widetilde{\boldsymbol{f}})^{\mathrm{T}}\boldsymbol{W}_2(\boldsymbol{f} - \widetilde{\boldsymbol{f}}) \\ \text{with} \quad & \boldsymbol{A}^{\mathrm{T}}\boldsymbol{f} + \boldsymbol{w} + \boldsymbol{\varsigma} = \boldsymbol{0} \\ & \boldsymbol{f}_{\min} \leq \boldsymbol{f} \leq \boldsymbol{f}_{\max}. \end{aligned} \tag{3.30}$$

With the weighting matrices $\boldsymbol{W}_1$ and $\boldsymbol{W}_2$, the solution can be adjusted. For $\boldsymbol{W}_1 < \boldsymbol{W}_2$ the solution will mainly tend to follow the target forces $\widetilde{\boldsymbol{f}}$. Otherwise, the resulting forces will more likely generate an approximation of the desired wrench. Using well chosen target forces, the solution can be adjusted, e.g. for low forces or high stiffness. In context of industrial real-time applications, the proposed iterative scheme might lead to problems, even if an optimization of this problem can be carried out computationally efficient as demonstrated in [Côté et al., 2016]. Consequently, a method might be preferable if it could offer a low and – most important – well defined number of calculation steps.

3.5.2 Nearest Corner Method

To the authors best knowledge, there is no existing method based on geometrical analysis offering a well-known number of calculation steps to determine cable forces outside of the wrench-feasible workspace. Thus, the author proposes the so-called Nearest Corner Method in [Boumann and Bruckmann, 2020a] and [Boumann and Bruckmann, 2020b], which is explained in the following.

If a situation occurs where the end effector of a CDPR gets outside of its $\mathcal{WFW}$, an optimization approach as outlined in the previous section is applicable. Usually, such algorithms employ iterative solvers which might affect their suitability in a real-time control system, since the calculation time is not well defined and may vary. The proposed Nearest Corner

Method offers a different approach: It is based on geometrical analysis within the space of cable forces and offers a well-defined number of calculation steps. The space of cable forces $\boldsymbol{f}$ can be represented using an orthogonal coordinate system as described in Section 2.3. Remember, the hypercube $\mathcal{C}$ contains all cable force distributions that are within the given limits $\boldsymbol{f}_{\min}$ and $\boldsymbol{f}_{\max}$ and thus can be produced by the robot. As an initial step, finding a solution to eq. (2.41) using a conventional method as described in Section 2.3 is always tried first. If this method fails, the platform seems to be outside of its $\mathcal{WFW}$ and the following steps of the Nearest Corner Method are considered:

For m cables, this hypercube has 2^m corners. Let those corners be denoted as $\boldsymbol{F}_{E,j}, j = 1, \ldots, 2^m$. In the following, it is assumed that the CDPR is of type CRPM or RRPM, i.e. $r = 1$ or $r = 2$. If the end effector is now within the $\mathcal{WFW}$ of the robot, a set of various cable force distributions $\mathcal{F}$ exist, which are solutions to eq. (2.41). Moreover, continuous solutions along a trajectory can be found and the methods discussed in Section 2.3 can be used. Still, if the CDPR gets outside of its $\mathcal{WFW}$, $\mathcal{F}$ is empty and these methods will fail to compute cable force distributions. This is due to the fact that, despite both the hypercube $\mathcal{C}$ and the solution space $\mathcal{S}$ exist, there is no intersection of them. In this situation there will be at least one corner of $\mathcal{C}$, which has the closest Euclidean distance to the solution space $\mathcal{S}$. Note that $\mathcal{S}$ might be a hyper straight line (for $r = 1$) or a hyperplane (for $r = 2$). Now, the corners $\boldsymbol{F}_{E,j}$ of $\mathcal{C}$ can be orthogonal projected onto $\mathcal{S}$ as depicted in fig. 3.6. The projected corners on the solution space are furthermore denoted $\boldsymbol{F}_{P,j}$. Based on the distances of the corners to the solution space, the nearest corner of $\mathcal{C}$ can be determined. The cable force distribution $\boldsymbol{f}$ at this corner is no solution to eq. (2.41), but it is an approximation in terms of the motion inducing parts of $\boldsymbol{f}$, which are $\boldsymbol{f}_0$. Moreover, it is compliant with the

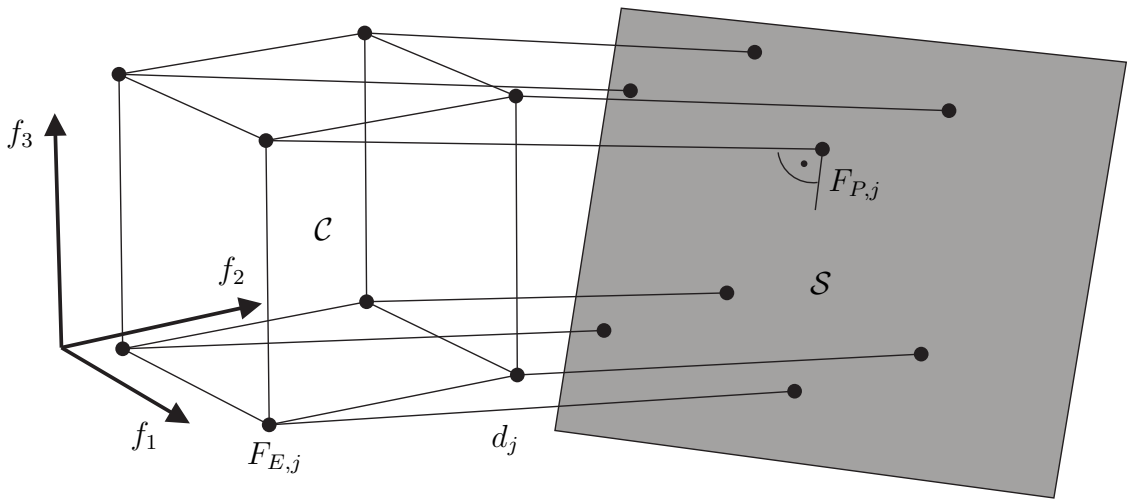

Figure 3.6: Projection of the corners of $\mathcal{C}$ onto the solution space $\mathcal{S}$ for an empty set of $\mathcal{F}$, example for $r = 2, m = 3$.

force boundaries and can thus be used for control purposes. However, the nearest corner might switch instantaneously when the system is in motion. Consequently, selecting only the nearest corner as a solution does not seem to make sense, since the resulting forces will be discontinuous when $\mathcal{S}$ travels. To ensure continuity of the resulting cable forces during robot motion, all corners of $\mathcal{C}$ are further considered. This is done by weighting the corners according to their Euclidean distance to $\mathcal{S}$. The distances between the projected forces $\boldsymbol{F}_{P,j}$ and the corners $\boldsymbol{F}_{E,j}$ are given by

$$d_{S,j} = ||\boldsymbol{F}_{P,j} - \boldsymbol{F}_{E,j}||, \quad 1 \leq j \leq 2^m. \tag{3.31}$$

A proper weighting g_j for each corner of $\mathcal{C}$ is obtained by using the summarized distance of all corners

$$L = \sum\nolimits_{j=1}^{2^m} d_{S,j}. \tag{3.32}$$

Based on this and using the exponential weight p, the weights are determined by

$$g_j = \Big(\frac{L}{d_{S,j}}\Big)^p. \tag{3.33}$$

With the exponential weight, the influence of the nearest corner with regard to all other corners can be adjusted. Using a higher weight for p, the nearest corner to $\mathcal{S}$ will more likely dominate all other corners, the closer it gets to the solution space. This shall ensure a continuous transition between force distributions outside and within the $\mathcal{WFW}$ if, at some point, $\mathcal{S}$ and $\mathcal{C}$ are about to intersect. In this situation, a force distribution on the boundaries of $\mathcal{C}$, e.g. at one corner, is about to become a valid solution to eq. (2.41). Using the sum of all weights

$$G = \sum\nolimits_{j=1}^{2^m} g_j, \tag{3.34}$$

the force distribution according to the Nearest Corner Method can be determined as

$$\boldsymbol{f} = \sum_{j=1}^{2^m} \big(\boldsymbol{F}_{E,j}\, \frac{g_j}{G}\big), \quad 1 \leq j \leq 2^m. \tag{3.35}$$

Summarizing, this resulting force distribution is feasible within the cable force limits and has minimal distance to the solution space $\mathcal{S}$. Thus, it is a suitable approximation that can be used for control purposes. A successful application of the method within simulation is done by the author for $r = 1$ after cable failure in [Boumann and Bruckmann, 2020a] and for $r = 2$ in [Boumann and Bruckmann, 2020b], including a demonstration of real-time feasibility.

Chapter 4

Simulative Studies of Damage Avoidance Strategies

This chapter deals with simulative studies of the damage avoidance strategies proposed in Chapter 3. First, the prototype SEGESTA is introduced, which is the basis for the simulations. In the upcoming chapter, it will also be used for experimental testing. A dynamic multibody simulation environment is set up based on the fundamentals given in Chapter 2, consisting of a robot platform, cables, drive units and a controller model. To identify model parameters of the cables and the drive units, two experiments are conducted. The pre- and post-failure workspace of SEGESTA is subsequently analyzed, based on the given set of parameters. Physically reasonable behavior of the multibody simulation framework is demonstrated using an example platform trajectory in the pre-failure workspace. Further, the event of a cable failure is simulated and the malfunction of the conventional APD controller is demonstrated. Building upon this, the damage avoidance strategies are implemented and thoroughly studied. Moreover, a fault tolerant APD controller and the usage of motor brakes are investigated. Finally, the results are summarized and discussed.

4.1 The SEGESTA Prototype

The SEGESTA prototype is the oldest among several CDPR prototypes, that have been established and operated by the Chair of Mechatronics, University of Duisburg-Essen, see

Section 1.1.3. Because of its size, the SEGESTA prototype is particular useful for prototype experiments, which is further discussed in Chapter 5. Moreover, it is available for experiments in the context of this thesis. Thus, it will be used as a basis for preliminary studies in simulation. Using simulations, the emergency strategies will be verified in a first step. Furthermore, possible limitations, restrictions, and hurdles in implementing emergency strategies within prototype hardware can be studied.

The SEGESTA prototype is operated with $m = 8$ cables and has $n = 6$ degrees of freedom, resulting in a kinematic redundancy of $r = 2$. Based on the definitions given in Section 2.1, SEGESTA is a RRPM with 3R3T motion patterns. If a cable fails, the redundancy is reduced to $r = 1$ and the prototype becomes a CRPM with $m = 7$ cables. In case of multiple cable failures, SEGESTA would even become an IRPM. As displayed in [Reichert et al., 2015a, Reichert et al., 2015b], the prototype can also be operated with 10 cables and $r = 4$, using counter weights and additional drives for energy or stiffness optimization. Note that this case is not considered here. Highly dynamic direct drives power the winches, which are winding up and down the synthetic fiber cables made of Dyneema. Each cable is deflected by two pulleys until it enters the robot's workspace. The second pulleys are pivoting. The cable guidance systems are equipped with cable force measurement sensors to determine the current cable forces. Moreover, the drives are equipped with high resolution encoders to measure the winch angles and velocities. More details to the cables and the drive units are given in the upcoming sections. To control the motors and to retrieve sensor data, SEGESTA has a `BECKHOFF` PLC using TwinCAT 3. All control algorithms are integrated within the PLC, which is running on a 2 kHz control frequency. This yields to a calculation time for all mathematical problems of 0.5 ms per cycle.

According to Chapter 2, most of the parameter values necessary to set up a simulation of SEGESTA based on the modeling equations are given in table 4.1. They are obtained from data sheets, CAD drawings and physical measurements on the prototype. Not all parameters are explicitly stated in matrix or vector form, since many equal parts are used.

$\boldsymbol{B} = \begin{bmatrix} 0.74 & -0.734 & 0.74 & -0.74 & 0.734 & -0.74 & 0.74 & -0.74 \\ -0.679 & -0.6425 & -0.679 & -0.679 & 0.6425 & 0.679 & 0.679 & 0.679 \\ 0 & 0.0975 & 1.007 & 1 & 0.0975 & 0 & 1.007 & 1.007 \end{bmatrix}$ m	$f_{\min} = 15$ N $\quad f_{\max} = 150$ N
$\boldsymbol{P} = \begin{bmatrix} 0.04 & -0.04 & 0.0375 & -0.0375 & 0.04 & -0.04 & 0.0375 & -0.0375 \\ 0 & 0 & -0.0375 & -0.0375 & 0 & 0 & 0.0375 & 0.0375 \\ 0.035 & 0.035 & -0.035 & -0.035 & 0.035 & 0.035 & -0.035 & -0.035 \end{bmatrix}$ m	$\boldsymbol{\Theta}_S = \begin{bmatrix} 0.0002 & 0 & 0 \\ 0 & 0.0002 & 0 \\ 0 & 0 & 0.0002 \end{bmatrix}$ kg m^2
$\boldsymbol{R}_{D_1} = \text{diag}(-1, 1, -1) = \boldsymbol{R}_{D_2} \quad \boldsymbol{R}_{D_3} = \text{diag}(1, 1, 1) = \boldsymbol{R}_{D_4}$	$\rho = 0.009$ m $\quad {}_P\boldsymbol{r}_S = [0, 0, -0.5]^{\mathrm{T}}$ mm
$\boldsymbol{R}_{D_5} = \text{diag}(1, -1, -1) = \boldsymbol{R}_{D_6} \quad \boldsymbol{R}_{D_7} = \text{diag}(-1, -1, 1) = \boldsymbol{R}_{D_8}$	$m_P = 0.125$ kg $\quad l_d = 0.275$ m

Table 4.1: Parameters of the SEGESTA prototype.

4.2 Simulation Environment

Before applying and validating the proposed emergency strategies (see Chapter 3) on the SEGESTA prototype, simulative studies are carried out within this chapter in order to verify and test the strategies.

As commonly known, a simulation has many advantages: The implementation, verification and testing of the strategies can be done without risk of damage and in a reproducible manner. Moreover, numerous tests to investigate on the strategies' behavior or parameter dependencies can be carried out in short times and automatically. Finally, the functioning controller implementation containing the emergency strategies can be transferred onto the prototype for application and further testing, minimizing possible implementation issues. Needless to say, a simulation also has its limitations: The reality can only be represented to a certain extent and the calculation time might strongly depend on the level of detail and the modeling assumptions, leading to an inevitable trade-off. Furthermore, modeling errors and incorrect modeling assumptions might lead to results that are far apart from reality. Nonetheless, the situation of a cable failure might be dangerous, see Section 1.2, so preliminary simulative studies of the situation and the proposed damage avoidance strategies are highly reasonable before implementation and testing on a prototype.

In order to perform realistic simulative experiments, a dynamic multibody simulation environment is set up, based upon the presented modeling fundamentals in Chapter 2. This environment and its parametrization are described within this section. The simulation's structure is based upon work published by the author in [Boumann and Bruckmann, 2022]. To obtain a reasonable trade-off between calculation time, implementation effort, traceability and realistic results, the following design choice are made:

- Despite existing software for dynamic multibody simulations with predefined mechanical parts, such as `ADAMS` [Hexagon AB, 2023], `DYMOLA` [Dassault Systèmes, 2023] or `Simscape` [The MathWorks, Inc., 2023d], the simulation is set up using `Simulink` [The MathWorks, Inc., 2023e] and the model equations are implemented manually to obtain full control and traceability of the model.

- A simple and straightforward cable modeling approach is chosen, as explained in Section 2.2.6. Even thou, more complex and realistic cable models exist within literature [Merlet, 2015, Miermeister et al., 2015], their parametrization can be challenging. Moreover, simple cable models result in shorter calculation times, which is beneficial when carrying out numerous simulations. Still, a representation of the cable dynamics is provided with the chosen approach [Pott, 2018].

- In order to represent the drive dynamics and the interaction between drives and cables, a model of the drive units is included, as given in Section 2.2.7.

- The pulleys are modeled kinematically, i.e. a dynamic modeling and thus inertia about the rotating and pivoting axes are neglected. To reflect their influence on the cable forces remotely, the simulated friction in the drive units is increased by a factor.

Based on the design choices and the associated simplifications, it is to assume that the simulation results will not exactly correspond to reality. However, the simulation environment must only be able to reasonably approximate reality in order to serve its purpose. If so, the robot simulation is then used to investigate the behavior and functionality of the damage avoidance strategies prior to prototype implementation and testing. A brief alignment with the results obtained from prototype experiments is conducted in Chapter 5.

Most of the required model parameters can be obtained from table 4.1. Measurements to identify the cable parameters (stiffness and damping) and the drive unit parameters (friction, drive latency) are performed subsequently. Note that also different CDPRs can be represented with the proposed simulation if the parameters are given, see Section 6.3.

4.2.1 Simulation Structure

Analog to the author's publication [Boumann and Bruckmann, 2022], the simulation structure consists of a controller model and models of the physical elements, as depicted in fig. 4.1. Both parts are built upon the fundamentals that are given in Chapter 2. The resulting environment is used to carry out simulative experiments in this thesis. The simulation's two main parts (controller and physical elements) are allocated with differing sample times of fixed step widths. Based on reality, the controller models are calculated with 2 kHz, which equals a step width of 0.5 ms. The physical parts, including drive units, cables and the robot's

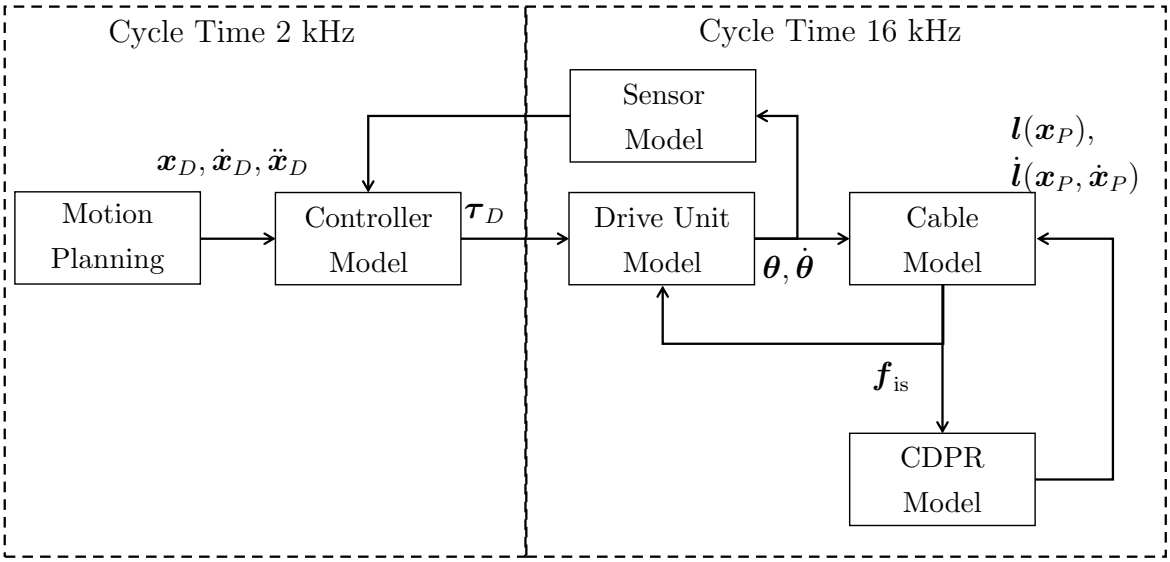

Figure 4.1: System structure of the simulation environment with two differing sample times.

platform, are sampled with 16 kHz. The higher sample frequency is aligned to typical clock frequencies of motor current controllers. Further, it is intended to create an adequate representation of the physics and a smaller integration step size usually benefits the simulation stability [Zapolsky and Drumwright, 2015].

From motion planning, see Section 2.5, a desired trajectory given by $\boldsymbol{x}_D$, $\dot{\boldsymbol{x}}_D$, $\ddot{\boldsymbol{x}}_D, \in \mathbb{R}^{n\times 1}$ is generated and fed to the controller, according to Section 2.6. $\boldsymbol{\theta} \in \mathbb{R}^{m\times 1}$ are the winch angles, resulting from movement of the drive units, assuming one drive per cable. Accordingly, the winch velocities are $\dot{\boldsymbol{\theta}} \in \mathbb{R}^{m\times 1}$. Both values are routed through a sensor model and used as a feedback in the controller. A first order lowpass filter with a time constant of 0.002 s is used to represent the sensors. The setpoint torques $\boldsymbol{\tau}_D \in \mathbb{R}^{m\times 1}$ are generated by the controller and fed to the simulated drives. For cable force calculation, an active-set algorithm is employed which aims at producing minimal cable forces. The internal drive controllers accelerate the winches according to eq. (2.51), depending on the torque command, the current cable forces $\boldsymbol{f}_{\text{is}} \in \mathbb{R}^{m\times 1}$ and the appearing friction. Numerical integration finally leads to $\dot{\boldsymbol{\theta}}$ and $\boldsymbol{\theta}$.

The current cable forces $\boldsymbol{f}_{\text{is}}$ result from the cable model according to eq. (2.42). Depending on the current kinematic cable lengths and velocities $\boldsymbol{l}$, $\dot{\boldsymbol{l}}$ received from the inverse kinematics at the current pose as well as $\dot{\boldsymbol{\theta}}$ and $\boldsymbol{\theta}$, the cable forces are determined.[1]

Using $\boldsymbol{f}_{\text{is}}$ and the current structure matrix, forces and torques at the platform exerted by the cables are determined. Therefrom, the platform acceleration is obtained using eq. (2.38). In analogy to the drives, velocity and position of the platform result from numerical integration. Then the structure matrix, kinematic cable lengths, and velocities are re-calculated at each time step using the platform position and velocity and the inverse kinematics with pulley based cable guidance, see Section 2.2. The numerical integration of the system states, such as platform velocity or winch angles, is carried out time-discretely using the trapezoidal integration method while a Runge-Kutta solver is chosen for the whole simulation.

The initial states, depending mainly on the starting pose of the platform, are computed once before a simulation is started. Initially, all parts are at rest. To avoid instability, the platform pose is fixed for a short time period until the cable forces have built up. This initialization process and a sample trajectory are shown in fig. 4.8. The upcoming sections present the experimental parameter identification of cables and drives.

[1] A simple example is assumed for explanation: First, let the platform be fixed. Second, the cable damping is neglected. If now a motor unwinds, the cable will be slack and no force can be transmitted. If the motor winds up the cable, it gets tensed and forces are transmitted according to the cable elongation.

4.2.2 Cable Parametrization

As discussed in Section 2.2.6, several modeling approaches exist for cables that differ in complexity, calculation effort and accuracy. For the simulation at hand, modeling of the cables as a spring damper system is chosen, which is a very simple yet efficient and straightforward approach. The stiffness is variant and depending on the cable length. For parametrization of the cable model, two approaches are conceivable:

- Obtaining the parameters from literature or manufacturer data, if available, or
- carrying out experiments and deriving the parameters from the measurements.

For the first approach, specifications from different manufacturers for synthetic fiber cables can be found: The cables used within the SEGESTA prototype are of the type D-Pro by `Liros` with a diameter of 1 mm. In manufacturer data of the company [LIROS GmbH, 2023b], working strain is defined as the elongation at the working point. The working point is set at 30% of breaking load f_b which is 1950 N for 1 mm diameter, according to the given catalog data. At the working point, the manufacturer states that the elongation e_c is below 1% [LIROS GmbH, 2023a], which is fairly imprecise. Still, this point can be used as a linearization point. Therefrom, the length dependent stiffness $k_{c,i}(l_i)$ for the i^{th} cable can be derived:

$$k_{c,i}(l_i) = \frac{0.3 f_b}{e_c \, l_i}. \tag{4.1}$$

However, other manufacturers also use the breaking point for linearization and specify the percentage of breaking strain at breaking load, as discussed in [Bruckmann and Boumann, 2021]. A different approach to determine the cable stiffness is presented in [Pott, 2018]: Using the Young's modulus for the cable material E_c and the cross section of the cable A_c, the stiffness can be determined as

$$k_{c,i}(l_i) = \frac{E_c \, A_c}{l_i}. \tag{4.2}$$

Still, this approach requires information about E_c that is not available in [Pott, 2018]. In all cases, no statement regarding the cable's damping is given. Consequently, experiments are required to obtain information on the cable damping and the working elongation. For parameter identification from the experiment's measurement, eq. (4.1) is used.

A possible experimental setup to determine cable stiffness and damping is presented in [Sturm, 2020], see fig. 4.2a: A cable is mounted to a fixed force sensor on one side and attached to a motorized cable drum on the other side. Using the drive, a force input is given to the cable and both the force and the winch states are measured. Parameter identification from a given experiment leads to a stiffness of 24 320 N/m and a damping of 58.42 Ns/m with

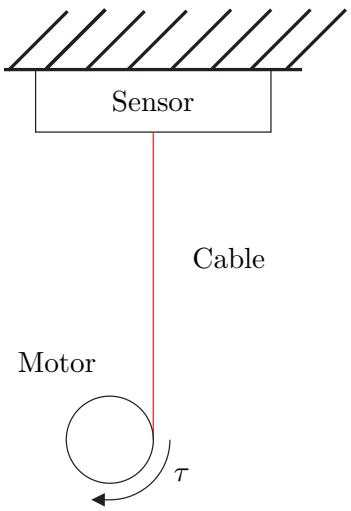

(a) Setup according to [Sturm, 2020].

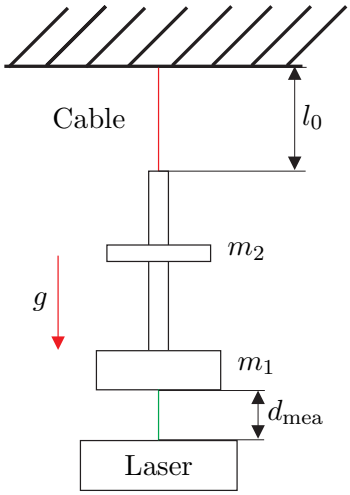

(b) Setup used within this work.

Figure 4.2: Experimental setups for cable parameter identification.

a cable length of 1.615 m using a `Liros` D-Pro cable with 3 mm diameter [Sturm, 2020]. To exclude the drive dynamics from the experiment, a different setup is used within this work, as depicted in fig. 4.2b. One cable end is fixed to a suspension which is assumed to be neglectible stiff. On the second cable end, a hanging weight with the mass m_1 is attached. The geometrical shape of the weight allows for a second weight with the mass m_2 to be mounted. The second weight can slide along the first weight. For experiments, it can be lifted manually and dropped, creating an impulse to excite the system. Without m_2, the cable has an initial length of l_0. The dynamic movement in cable direction is measured using a laser distance sensor, mounted below the hanging weight. The measured distance is d_{mea}. Since the system is capable of pendulum motion due to the chosen setup, it is attempted not to excite the system perpendicular to the cable while conducting the experiment. Due to the very simple nature of the experiment, measurement inaccuracies are neglected. A model featuring a spring, a mass and a damper is set up in simulation to approximate the parameters. The simulated system is excited with an impulse according to the experiment and the mass's movement is traced. Manual parameter matching leads to the results shown in fig. 4.3. Using the experiment's parameters $m_1 = 5$ kg, $m_2 = 0.5$ kg and $l_0 = 2.23$ m, a good quality fit is reached with an elongation at the working point of $e_c = 1.15\%$ and a cable damping of $d_c = 45$ Ns/m. This leads to cable stiffness of $k_c(l_0) = 22\,787$ N/m.

Besides the motion in cable direction, the measured data shows additional effects: A high frequent motion can be observed that is likely due to transverse motion of the cable and weight, as well as rotation of the weights. In the first part of the experiment, until 0.4 s, the effect of cable elongation predominates. Frequency, displacement and damping of the oscillation seem to match between simulation and experiment. All subsequent residual

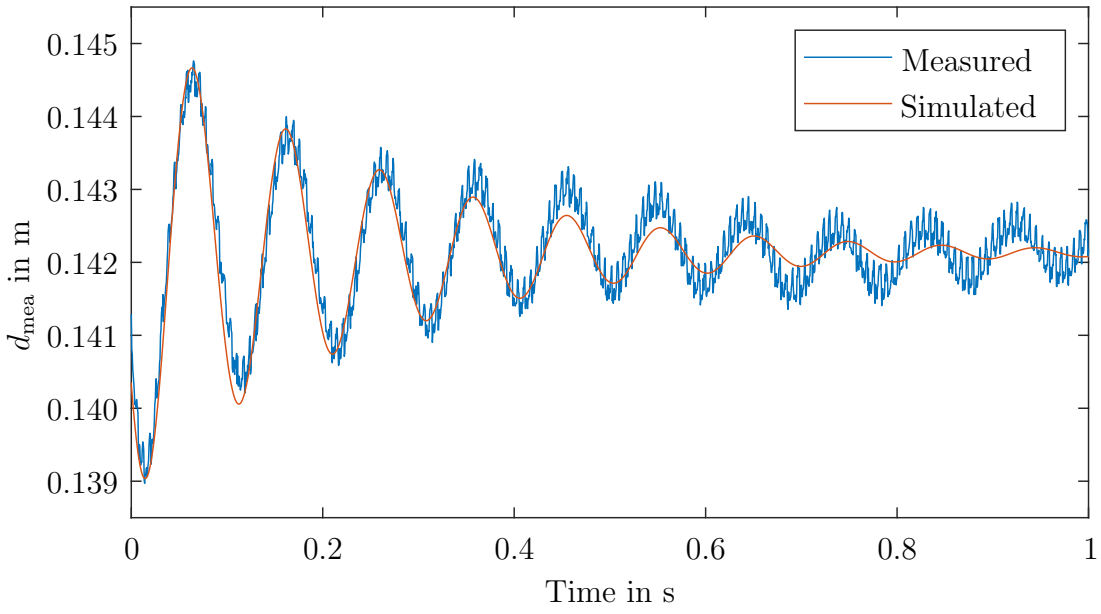

Figure 4.3: Comparison of measured and simulated movement of the cable and the masses. The distance in simulation is related to the laser sensor's point of measurement.

motion, seen especially from ~ 0.6 s, is probably pendulum motion. Thus, it is neglected within parameter matching. Further, it is to note that the magnitude of the found parameters are congruent to the measurement presented in [Sturm, 2020]. The working elongation of 1.15% is slightly higher than specified by the manufacturer ($< 1\%$). It is assumed that this divergence is caused by the cable's age.

Summing up, a good quality fit of the experiment can be achieved using the chosen cable model with the identified parameter values. Accordingly, these values will be employed to parametrize the cables within the cable robot simulation model. However, it is to note that with the observed perturbating motion in the experiment, the results of the parameter identification are naturally subject to inaccuracy.

4.2.3 Drive Unit Parametrization

Similar to the cables, some of the drive unit parameter values will be determined by experiment. This accounts in particular for friction. The motor used are of the type AM8031 by the manufacturer `BECKHOFF` [Beckhoff Automation GmbH & Co. KG, 2023]. Relevant parameters for the simulation are: $\rho_d = 0.015$ m, $J_d = 2.250 \cdot 10^{-4}$ kg m^2, $T_t = 0.25$ ms, $T_1 = 0.4291$ ms. They are well-known from data sheets, CAD drawings and physical measurements on the prototype. As equal parts are used, not all parameters are explicitly stated in matrix or vector form. It is assumed that the powerful direct drives of SEGESTA are neglectible stiff. Thus, linear elastic deformation of the drive unit is omitted within the sim-

ulation. The drive unit model is integrated into the simulation based on the fundamentals given in Section 2.2.7. A delay of T_t is assumed until the motor controller processes the set-point command coming from the CDPR controller. Due to the limited resolution of the data type, the set-point command is previously discretized with a resolution of 0.1%. To determine the resulting acceleration of the winch, eq. (2.51) is rearranged for $\ddot{\boldsymbol{\theta}}$. With the current cable forces $\boldsymbol{f}_{\text{is}}$, the drum radii $\boldsymbol{\rho}_d$ and the frictional torques $\boldsymbol{F}_F(\dot{\boldsymbol{\theta}})$, $\ddot{\boldsymbol{\theta}}$ can be determined and integrated to $\dot{\boldsymbol{\theta}}$ and $\boldsymbol{\theta}$, respectively. The frictional torques $\boldsymbol{F}_F(\dot{\boldsymbol{\theta}})$ are calculated based on the identified friction parameters and eq. (2.49).

Now to identify the occurring friction within the drive units of SEGESTA, the following experiment is conducted using one motor: First, the corresponding cable is disconnected at the cable drum to allow for free turning of the chosen winch. For simplicity, the friction in the whole investigated drive unit is analyzed without considering its components individually. Starting with the motor at rest, the set torque is increased step-wise by the smallest possible increment, which is determined by the resolution of the set-point signal. It is assumed that the motor sufficiently delivers the set torques. After each increment, the drive is checked to see if it overcomes static friction and starts moving. Once this is the case, the resulting drive velocity is recorded. It is to note that using this approach, the transition phase between adhesion and sliding is not supervised. To obtain more data points, the set torque is incremented for a few more steps while recording the velocities. The same experiment is conducted in the opposite drive direction, using negative set torques. Figure 4.4 shows the measured data. Now, it is referred to eq. (2.51). No cable is attached, therefore $\boldsymbol{\rho}_d \boldsymbol{f}$ is zero. For continuous speeds that set in $\ddot{\boldsymbol{\theta}}_D$ is zero as well. Hence, the torques generated by

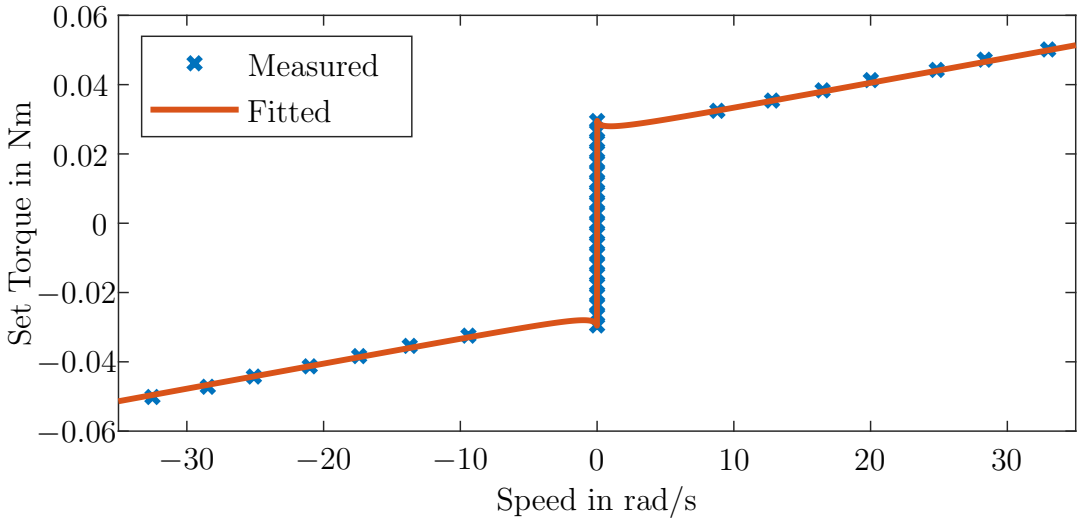

Figure 4.4: Measured motor speed and set torque, fitted by a friction curve with $F_s = 0.03$ Nm, $F_c = 0.026$ Nm, $F_v = 7.25e-04$ Nms/rad, $\epsilon = 0.5$, and $\theta_s = 0.75$ rad/s.

the motor equal the friction torques at the measured points and the measured data can be used to determine the friction within the investigated drive unit. Applying a friction model according to eq. (2.49), which is based on Stribeck, Coulomb and viscous components, leads to a good quality fit, see fig. 4.4. Using the identified parameters, the friction of each drive unit within simulation is parametrized. For simplicity, it is assumed that each drive unit in simulation has the same friction characteristics. The experiment is repeated using a second motor to verify that no motor with particularly high or low friction was chosen for the experiment. Further, a linear slope is included between the values at -0.05 rad and 0.05 rad to achieve a continuous transition of frictional torques trough a drive standstill.

Furthermore, it is to mention that the double deflection within the cable guidance system also imposes friction to the system, which is not measured or identified within this work. Also the masses and dynamics of the pulleys are neglected. To reflect this effects within the simulation, the identified frictional torque within the drive unit is simply doubled in amount, leading to $F_s = 0.06$ Nm, $F_c = 0.052$ Nm and $F_v = 0.0015$ Nms/rad. A more sophisticated approach to consider these effects can be found in [Miyasaka et al., 2015].

4.3 Simulative Studies

In this section, simulative studies are carried out using the established and parameterized simulation. First, the pre- and post-failure workspace of SEGESTA are analyzed. Second, example trajectories without cable failure are performed to demonstrate physically meaningful behavior of the simulation. Based on this, the malfunction of the selected conventional controller is demonstrated in a test scenario that simulates a cable failure. Subsequently, the author's damage avoidance strategies after cable failure introduced in Chapter 3 are implemented and thoroughly tested for different scenarios.

4.3.1 Workspace Analysis

Initially, the workspace of the SEGESTA prototype in the given configuration using the parameters from table 4.1 is determined. Based on the obtained shape and size of the workspace, the impact of cable failure can be emphasized. Figure 4.5 displays the static equilibrium workspace with constant (zero) orientation ($\mathcal{SECOW}$) from two point of views with all $m = 8$ cables in operation, thus its pre-failure. The workspace is computed on a discrete grid according to the algorithms introduced in Section 3.2. As fig. 4.5 shows, a major part of the area in between the pulleys belongs to the $\mathcal{SECOW}$. Besides minimum and maximum cable forces, the workspace's volume and especially its shape depend on the chosen configuration of $\boldsymbol{B}$ and $\boldsymbol{P}$. Resulting from the configuration, the workspace is approximately symmetrical about the x- and y-axis. Due to construction space restrictions, the positions

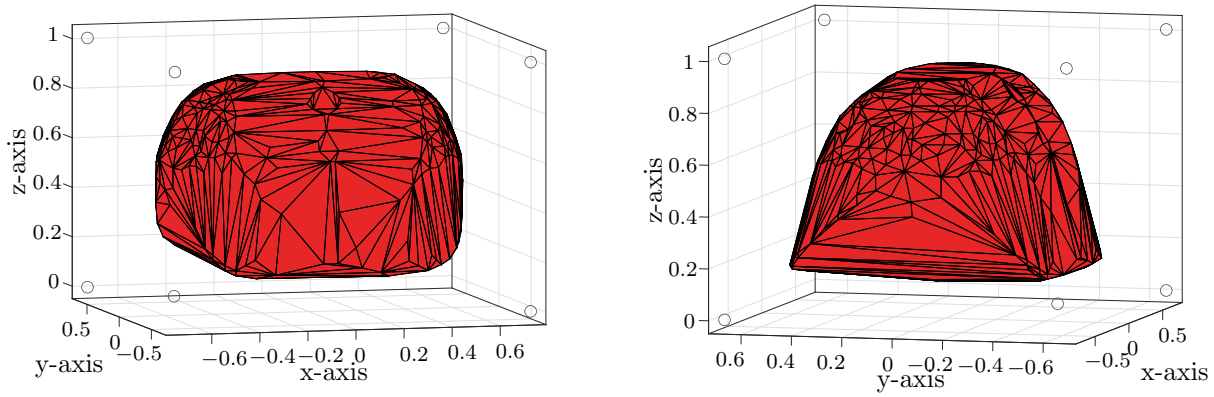

(a) View from front.

(b) View from side.

Figure 4.5: $\mathcal{SECOW}$ of SEGESTA using the grid $\mathcal{G}_{\mathcal{SECOW}} = \begin{bmatrix} [-0.625, & [-0.625, & [0.100, & [0, & [0, & [0, \\ 0.625] & 0.625] & 0.900] & 0] & 0] & 0] \\ 0.02 & 0.02 & 0.02 & 0 & 0 & 0 \end{bmatrix}^{\mathrm{T}}$. Pulley positions indicated by circles in the corners.

of the pulleys are not exactly opposite, see table 4.1. Thus, the workspace is not perfectly symmetrical.

Now, if a cable fails, the workspace size and shape change, as discussed in Section 3.2. Note that due to the high degree of symmetry of SEGESTA, it is only distinguished between the failure of a lower and an upper cable in the following. Figure 4.6 displays the $\mathcal{SECOW}$ after cable failure of a lower cable (number 2) and an upper cable (number 4), thus it is the post-failure workspace. The figure depicts that the impact of a cable failure on the workspace is dramatic. While the workspace is nearly halved for the failure of an upper cable, no $\mathcal{SECOW}$ remains for the failure of a lower cable. As elaborated in Section 3.2, a static force equilibrium at the platform might be possible at additional poses, if changes in platform orientation are considered. Therefore, the static equilibrium orientation workspace ($\mathcal{SEOW}$) for failure of both cables is determined based on algorithm 2 and displayed in fig. 4.7. Considering platform rotations up to ± 0.3 rad per axis (which equals $\sim \pm 17$ °), as given in $\mathcal{G}_{\mathcal{SEOW}}$, enlarges the post-failure workspace remarkably. Thus, there are a variety of poses in which the platform can reach a static force equilibrium if it is slightly tilted. Especially the case for lower cable failure demonstrates that a consideration of platform tilting is inevitable. As long as the platform does not tip over, this is considered acceptable. Otherwise, there is a risk of collisions in between cables or loss of payload in practical scenarios. Overall, the post-failure workspaces for a lower and an upper cable failure show that there is a high risk that the platform will be outside the post-failure workspace when the failure occurs. Consequently, damage avoidance strategies are required to bring the platform into a statically stable pose as the platform will inevitably start to move. Further discussion

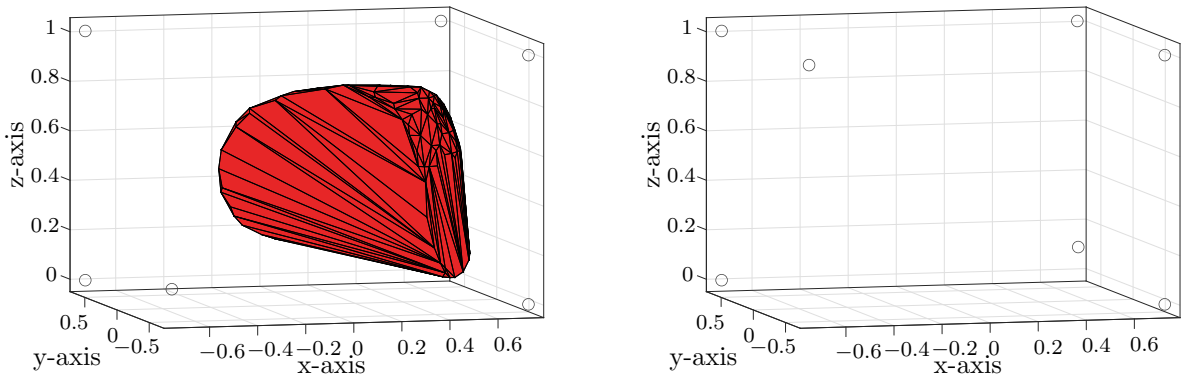

(a) Failure of cable 4 (coming from above)

(b) Failure of cable 2 (coming from below)

Figure 4.6: Post-failure $\mathcal{SECOW}$ of SEGESTA (static equilibrium constant orientation workspace), using the grid $\mathcal{G}_{\mathcal{SECOW}} = \begin{bmatrix} [-0.625, & [-0.625, & [0.100, & [0, & [0, & [0, \\ 0.625] & 0.625] & 0.900] & 0] & 0] & 0] \\ 0.02 & 0.02 & 0.02 & 0 & 0 & 0 \end{bmatrix}^{\mathrm{T}}$. Pulley positions indicated by circles in the corners. Failed cable indicated by left out pulley.

on this can be taken from Chapter 3.

In addition to the above, another conceptual idea is proposed: The fact that the post-failure workspace reduction can vary massively depending on the failed cable gives the impression that there may be configurations of $\boldsymbol{B}$ and $\boldsymbol{P}$ that are more or less likely to lose workspace post-failure. Consequently, it is proposed to develop algorithms for CDPR design that incorporate failure resistance criteria in terms of workspace retention after failure. Developing such algorithms will be part of future work.

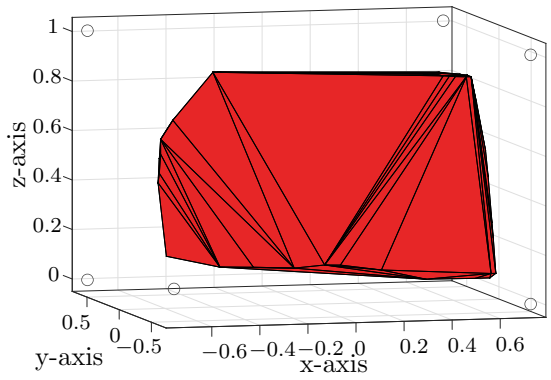

(a) Failure of cable 4 (coming from above), view from front.

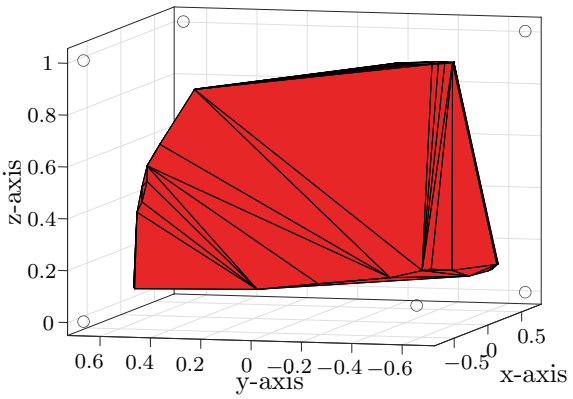

(b) Failure of cable 4 (coming from above), view from side.

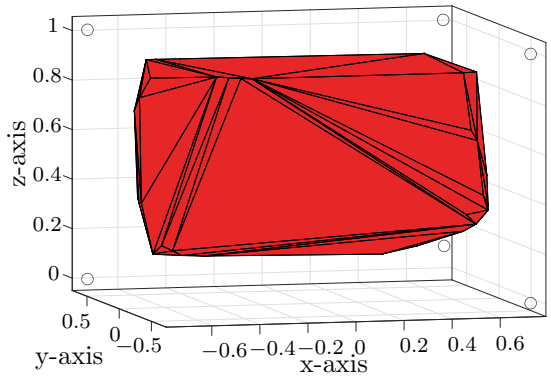

(c) Failure of cable 2 (coming from below), view from front.

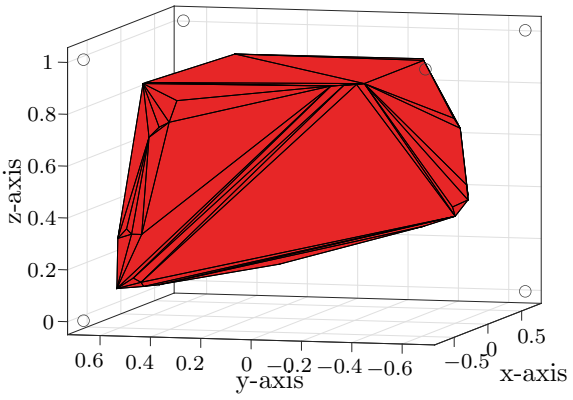

(d) Failure of cable 2 (coming from below), view from side.

Figure 4.7: Post-failure $\mathcal{SEOW}$ of SEGESTA (static equilibrium orientation workspace), using the grid $\mathcal{G}_{\mathcal{SEOW}} = \begin{bmatrix} [-0.625, & [-0.625, & [0.100, & [-0.3, & [-0.3, & [-0.3, \\ 0.625] & 0.625] & 0.900] & 0.3] & 0.3] & 0.3] \\ 0.02 & 0.02 & 0.02 & 0.15 & 0.15 & 0.15 \end{bmatrix}^{\mathrm{T}}$. Pulley positions indicated by circles in the corners. Failed cable indicated by left out pulley.

4.3.2 Example Trajectory Without Cable Failure

In order to demonstrate physically reasonable behavior of the multibody simulation framework, an example platform trajectory through the workspace of SEGESTA without cable failure is performed and analyzed. Before any test, the simulation needs to be initialized. Within the initialization phase, which is displayed in fig. 4.8, the platform is spatially constrained at the chosen starting pose $[-0.2\ \text{m}, -0.2\ \text{m}, 0.2\ \text{m}, 0\ \text{rad}, 0\ \text{rad}, 0\ \text{rad}]^{\mathrm{T}}$ to enable a seamless numerical transient process of the system. The cable length in the workspace with $\boldsymbol{\theta} = \mathbf{0}$ corresponds to the initial cable length $\boldsymbol{l}_0$. Thus $\Delta\boldsymbol{l} = \mathbf{0}$, i.e. the cables are not in tension and do not transmit forces initially. Note that all elements of $\boldsymbol{K}_P$ are set to 8000 N/m and all elements of $\boldsymbol{K}_D$ to 50 Ns/m. Since the controller requests desired cable forces converted to $\boldsymbol{\tau}_D$, the drive units accelerate until they reach a torque equilibrium, which can be seen from $\boldsymbol{\theta}$ and $\dot{\boldsymbol{\theta}}$. This imposes a steep buildup of the cable forces $\boldsymbol{f}_{\text{is}}$, reaching up to ~ 135 N in cable 5, which stabilizes shortly after the transient process, reaching the desired cable forces $\boldsymbol{f}_D$. This can be seen in particular observing the vector of cable force errors $\Delta\boldsymbol{f} = \boldsymbol{f}_{\text{is}} - \boldsymbol{f}_D$ in fig. 4.12 within the first seconds. When the cable forces are settled, the platforms spatial constraint is released using a linear fade after 1 s. From $\ddot{\boldsymbol{r}}_P$ in fig. 4.8, it can be seen that the platform is subject to a short vibration when releasing. Nonetheless,

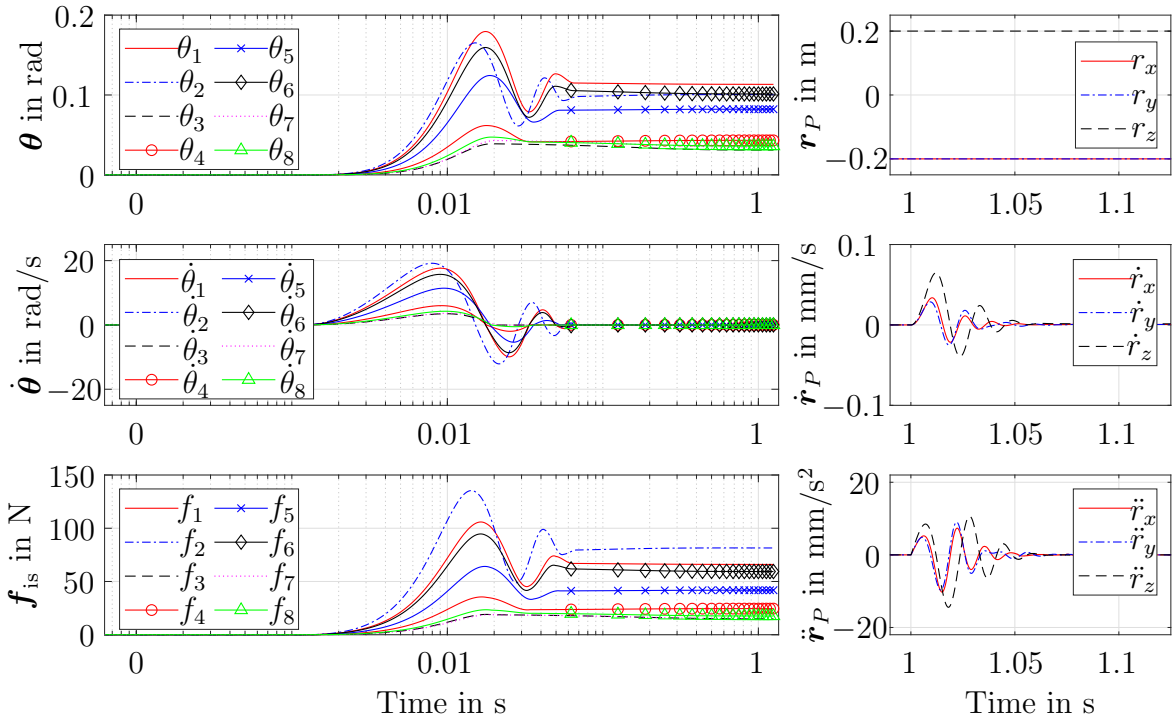

Figure 4.8: Initialization phase of the simulation. Left: Motor angles $\boldsymbol{\theta}$, angular velocities $\dot{\boldsymbol{\theta}}$ and current cable forces $\boldsymbol{f}_{\text{is}}$ with logarithmic time scaling. Right: Platform position $\boldsymbol{r}_P$ and its time derivatives.

the platform movement is inhibited by the controller after ~ 0.05 s with maximum platform velocity below 0.1 mm/s in magnitude and accelerations below 0.02 m/s^2 in magnitude. The highest magnitude in acceleration can be observed in z-direction, which can be attributed to gravitational forces. When releasing the platform, changes in cable forces, drive unit angles and velocities are not significant. This might be due to the relatively low platform mass. For the sake of readability and since the information value is minor, the platform orientation and its derivatives are not shown here. Finally, the simulated system is in control and fully operational. As the initialization phase is similar for each experiment, it will not be displayed further on. After the initialization, an experiment can be started, which might be the execution of a platform trajectory or a cable failure scenario.

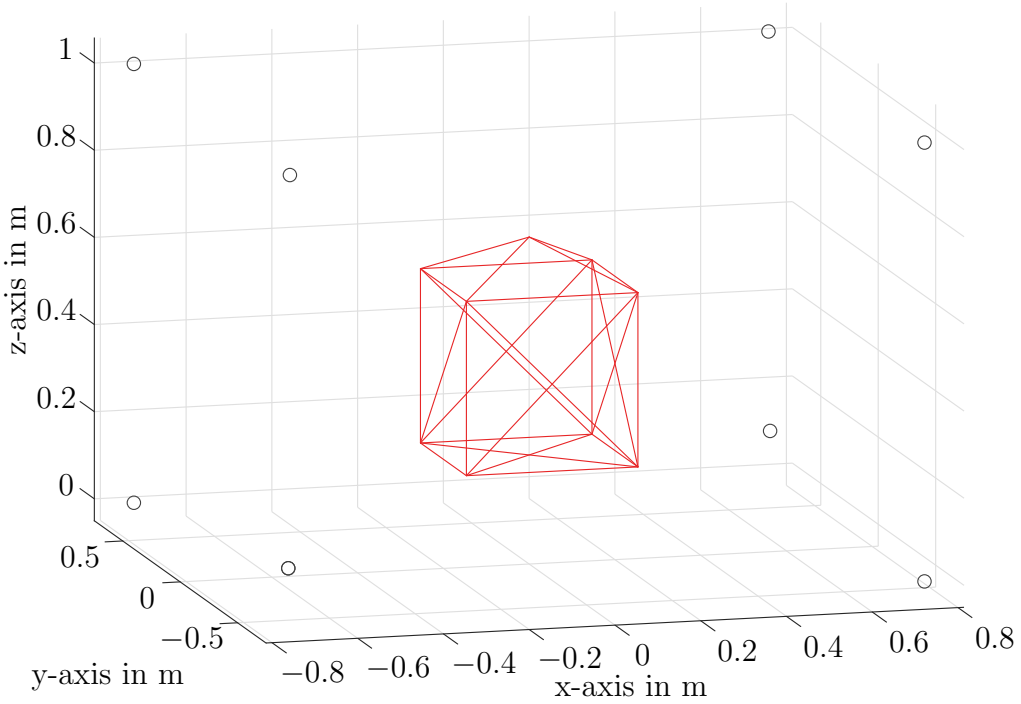

Figure 4.9: Spatial path of the example trajectory trough the workspace of SEGESTA, indicated by red lines. Circles indicate the pulley positions.

Here, an example trajectory without cable failure is now executed. The platform trajectory includes several poses with constant (zero) orientation, i.e. $\varphi_D, \vartheta_D, \psi_D = 0$ rad, throughout the workspace of SEGESTA, as shown in fig. 4.9. At each pose, the platform is at rest, i.e. $\dot{\boldsymbol{x}}_D, \ddot{\boldsymbol{x}}_D, \dddot{\boldsymbol{x}}_D = \mathbf{0}$. Note, that $\boldsymbol{x}_D = [\boldsymbol{r}_D^{\mathrm{T}}, \boldsymbol{\Phi}_D^{\mathrm{T}}]^{\mathrm{T}} = [r_{D,x}, r_{D,y}, r_{D,z}, \varphi_D, \vartheta_D, \psi_D]^{\mathrm{T}}$, et cetera for the time derivatives. In between those poses, polynomials of seventh order according to Section 2.5.1 are used to define the trajectory segments with the boundary conditions given above. The resulting desired platform trajectory is displayed in fig. 4.10. On position level, the platform is moved in between -0.2 m and 0.2 m in x- and y-direction

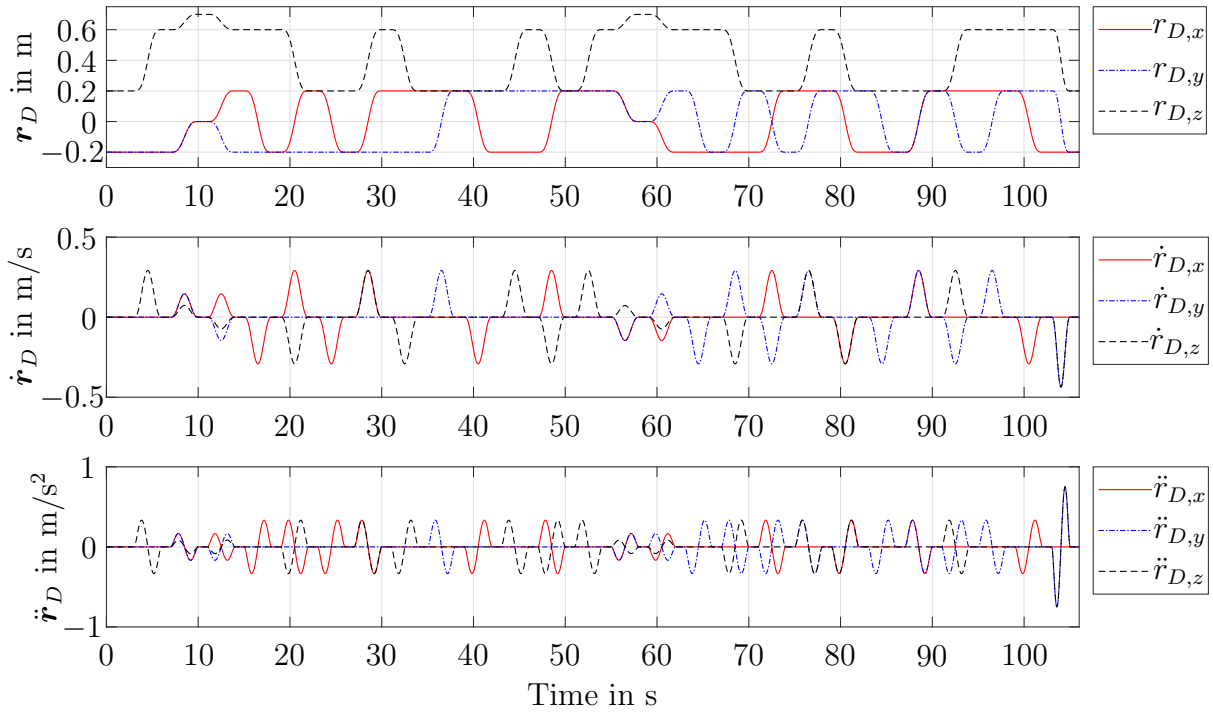

Figure 4.10: Desired example trajectory over time. Note that $\boldsymbol{\Phi}_D, \dot{\boldsymbol{\Phi}}_D, \ddot{\boldsymbol{\Phi}}_D = 0$ for all time steps, wherefore they are not displayed.

and in between 0.2 m and 0.6 m in z-direction. The absolute velocities go up to 0.4 m/s and the acceleration reaches 0.75 m/s^2. The progression over time shows a continuous transition between all poses down to acceleration level, which also implicates that no discontinuities occur in the platform jerk.

To asses the ability of the simulated system and the controller to follow this desired trajectory, the trajectory tracking error $\boldsymbol{x}_{\text{err}}$ is now defined. With the given pose $\boldsymbol{x}_P$ and the desired pose $\boldsymbol{x}_D$, the error

$$\boldsymbol{x}_{\text{err}} = \boldsymbol{x}_P - \boldsymbol{x}_D = [\boldsymbol{r}_{P,\text{err}}^{\text{T}}, \boldsymbol{\Phi}_{\text{err}}^{\text{T}}]^{\text{T}} \tag{4.3}$$

can be formulated, where $\boldsymbol{r}_{P,\text{err}} = [r_{x,\text{err}}, r_{y,\text{err}}, r_{z,\text{err}}]^{\text{T}}$ and $\boldsymbol{\Phi}_{\text{err}} = [\varphi_{\text{err}}, \vartheta_{\text{err}}, \psi_{\text{err}}]^{\text{T}}$. The determination and the naming are analogous for the error's time derivatives. Figure 4.11 shows the occurring trajectory tracking errors. On position level, the errors stay below 2.5 mm absolute deviation in position and 0.02 rad in orientation, which indicates adequate performance of the position controller. However, the errors $\dot{\boldsymbol{x}}_{\text{err}}, \ddot{\boldsymbol{x}}_{\text{err}}$ in velocity and acceleration are respectively higher with spikes at each point-to-point segment of the trajectory. For the velocity $\dot{\boldsymbol{r}}_{P,\text{err}}$, the spikes reach 18 mm/s absolute error as well as 0.5 rad/s for the angular velocity $\dot{\boldsymbol{\Phi}}_{\text{err}}$. On acceleration level, the absolute deviation even reaches 2.1 m/s^2 and 55 rad/s^2, which is fairly high. Nonetheless, the controlled system seems to stay stable. Presumably,

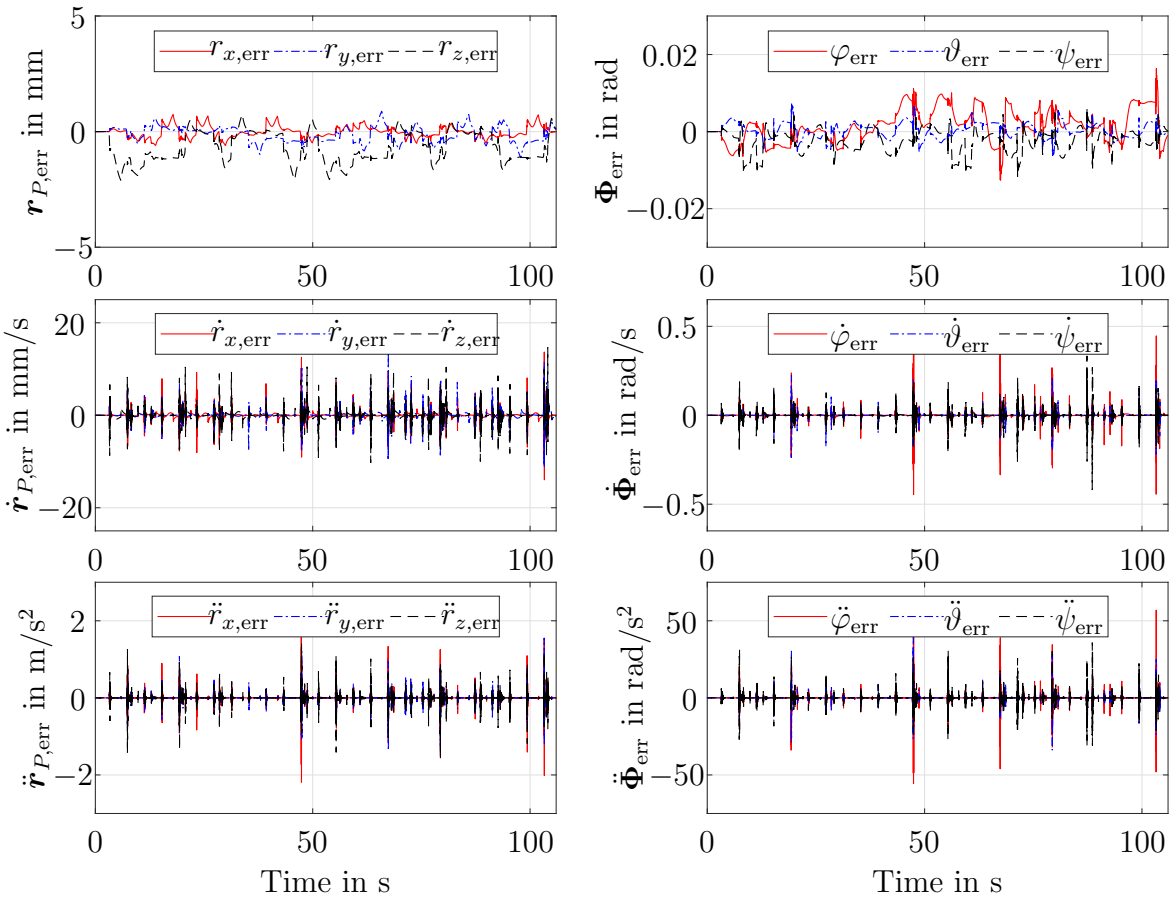

Figure 4.11: Trajectory tracking errors and their time derivatives for the example trajectory.

these high deviations on acceleration level may be connected to physical effects, which are modeled but not covered by the employed APD controller. Two contributing effects can be named: First, the drive units inertia needs to be accelerated and decelerated. Second, the systems friction opposes the winch movement. Both effects relate in particular to dynamic states of the system and they are not covered by feed forward terms in the control, see Section 2.6. Consequently, deviations are expected within the cable forces, especially while the system is in motion. Figure 4.12 confirms this assumption. The errors in cable forces $\Delta \boldsymbol{f}$ range from ± 7 N with some spikes up to ± 12 N. Remarkably, the errors almost drop to zero each time the trajectory pauses between two points, see also fig. 4.10. The desired forces $\boldsymbol{f}_D$ stay well within the given force limits of 15 N and 150 N, implying correct function of the APD controller. Taking into account figs. 4.9 and 4.10, it can also be observed that, depending on direction of movement, a different set of cables is too lose or too tensed respectively. As there is no cable force control loop employed, this is not unexpected. All cables stay in tension throughout the example trajectory. However, the current forces $\boldsymbol{f}_{\mathrm{is}}$ sometimes fall below the minimum desired cable force. The lowest cable force occurring throughout the

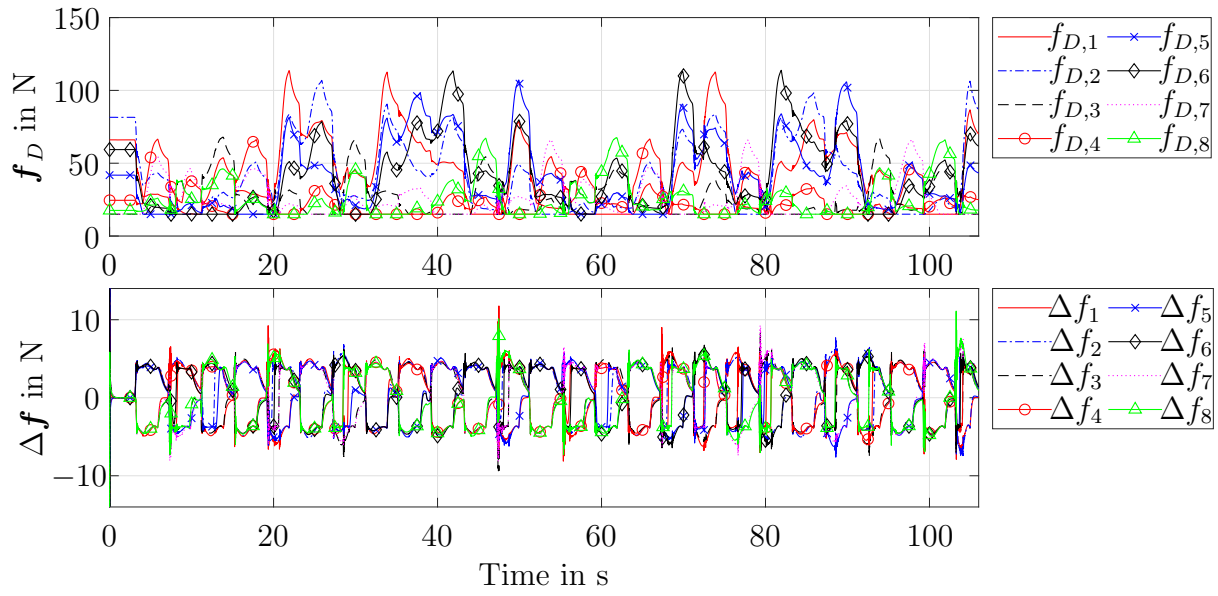

Figure 4.12: Desired cable forces $\boldsymbol{f}_D$ and error $\Delta\boldsymbol{f}$ throughout the example trajectory.

trajectory is 7.3908 N in cable 1. Thus, the chosen $f_{\min}$ prevents the cables from sagging.

To investigate further on the occurring spikes within $\ddot{\boldsymbol{x}}_{\text{err}}$, a close up of a trajectory segment in between 39 s and 40 s is given in fig. 4.13. The segment displayed is a movement in x-direction, see also fig. 4.10. At 39 s, the desired trajectory starts, which can be seen from $\ddot{r}_{D,x}$. After 0.19 s, $\ddot{r}_{D,x}$ already is -50 mm/s^2 and $\dot{r}_{D,x}$ is -3 mm/s. However, the motor does not yet turn, as can be seen from θ, presumably due to the given reasons (inertia and friction). The error between $r_{D,x}$ and $r_{P,x}$ increases during this phase, leading to changing outputs $\boldsymbol{\tau}_D$ caused by the APD controller. At $\sim$ 39.2 s, the generated torques by the motor controllers $\boldsymbol{\tau}_c$ overcome the remaining torques (see eq. (2.51)) and start to accelerate the drive units, which now break free, see $\boldsymbol{\theta}$. This leads to an abrupt acceleration of the whole system because of its parallel structure, with a maximum (undesired) acceleration $\ddot{r}_{P,y}$ of -0.38m/s^2. Since all drive units and cables are coupled at the platform, they highly influence each other in motion. With the example at hand, it is clearly apparent that the spikes displayed in fig. 4.11 can be attributed to this effect.

In summary, it can be stated that the simulation and the controller work and the simulated system behaves physically reasonable. Thus, the simulation is considered valid and suitable as a basis for further investigations within this thesis. Further, a feed forward control of drive unit inertia and system friction seems reasonable. This is omitted here, as it is not within the scope of this work.

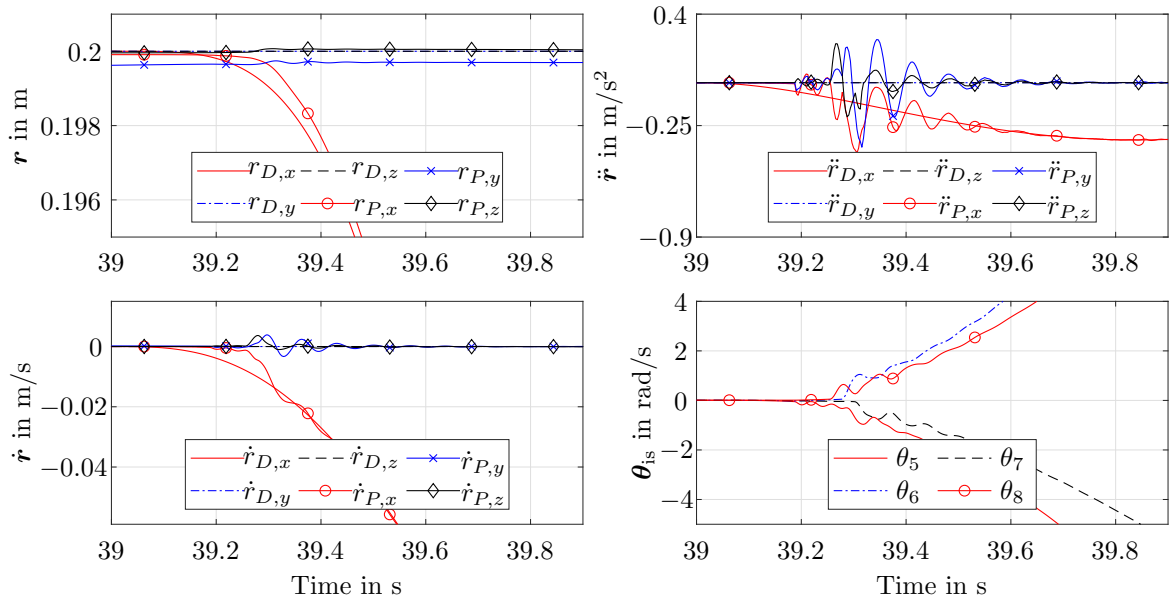

Figure 4.13: Close up of a trajectory segment. Comparison of the desired and actual platform positions $\boldsymbol{r}_D$ and $\boldsymbol{r}_P$ and their time derivatives. Drive unit angles $\boldsymbol{\theta}$ exemplary for units 5 to 8.

4.3.3 Cable Failure Simulation Procedure

At each experiment, the simulation is newly started and the platform is initialized at the chosen pose. Note that the initialization phase as shown in Section 4.3.2 will not be displayed further on. The event of cable failure is now used as temporal reference point. The cable failure is simulated by instantaneously setting the cable force to zero for the affected cable and keeping it there. Thus, from there on, no more intervention of this cable on the platform is possible. To assess how the system behaves and whether damage is caused, the following further assumptions are made:

- It is assumed that damage occurs, when the platform reaches or crosses the robot's frame. The frame is assumed to be a cuboid, defined by the outer coordinates of the pulley positions $\boldsymbol{B}$. For simplicity, the boundaries of the platform are defined by a sphere with the radius $p_r = \max(j_x, j_y, j_z)$, see eq. (2.57), which yields 0.0387 m here. Thus, the following conditions are derived:

$$r_x - p_r \leq \min(\boldsymbol{B}, x) \vee r_x + p_r \geq \max(\boldsymbol{B}, x) \tag{4.4}$$
$$r_y - p_r \leq \min(\boldsymbol{B}, y) \vee r_y + p_r \geq \max(\boldsymbol{B}, y) \tag{4.5}$$
$$r_z - p_r \leq \min(\boldsymbol{B}, z) \vee r_z + p_r \geq \max(\boldsymbol{B}, z). \tag{4.6}$$

  If one of those conditions are met, a collision is assumed.

- Further, it is assumed that damage occurs when one of the platform angles in $\boldsymbol{\Phi}$ exceeds $[-90; 90]^\circ$ (which equals $[-1.57; 1.57]$ rad). In this case, it can be presumed that a collision in between two cables has happened[2] or that a hypothetically carried load is lost. Note that collisions between cables and platform or in between cables are not explicitly checked here. Approaches for the detection of such collisions can be found in [Blanchet and Merlet, 2014, Bury et al., 2019, Fabritius et al., 2018, Merlet, 2004a, Merlet and Daney, 2006, Nguyen and Gouttefarde, 2015, Perreault et al., 2010] as well as in Section 6.2 and [Herrmann et al., 2022].

If one of these cases is detected, the simulation is terminated and labeled as failed. For successful simulations, it is checked whether all elements of the final platform velocity $\dot{\boldsymbol{x}}_P$ are below 0.1 m/s or 0.02 rad/s, respectively. If applicable, it can be assumed that the platform has stopped within the simulated time frame. Otherwise, it is still moving, which is also considered as a failure for simplicity. A simulation time of 2 s after cable failure has found to be suitable for the scenarios presented here.

4.3.4 Behavior of a Conventional Controller

In order to demonstrate the necessity of damage avoidance strategies after a cable failure, the behavior of the conventional APD controller is investigated in cable failure scenarios. In work of the author [Boumann and Bruckmann, 2022], this is done for a simple system with $m = 4$ cables and $n = 2$ DOF. Here, it will be tested using the introduced structure simulating the SEGESTA prototype with a pre-failure degree of redundancy $r = 2$.

APD Controller Without Failure Detection Outside of the Post-Failure Workspace For the experiments in this section, it is assumed that the cable failure is not detected and hence the control strategy is not changed after cable failure. Now a first scenario is considered as displayed in fig. 4.14. The platform's initial pose is $[-0.385, -0.025, 0.460]^\mathrm{T}$ m and $[0, 0, 0]^\mathrm{T}$ rad, which is outside of the post-failure workspace (see fig. 4.6), cable 4 fails. The controller fails to rescue the platform and the simulation is aborted at 0.05 s after cable failure. As $\boldsymbol{f}_D$ show, the controller still tries to set forces for the failed cable, since it misses knowledge about the cable failure. Of course, this results in movement of the associated drive unit, which increases the controller's errors, resulting in undesired behavior, since all control errors contribute to the desired platform wrench (see eq. (2.82)). Due to the system's parallelism, this also affects all other drives, leading to

[2] A collision in between cables does not necessarily lead to system failure. Under certain conditions it can be tolerated or planned [Otis et al., 2009]. Nonetheless, it is defined as undesired here and considered as a fault, since it promotes rolling over of the platform.

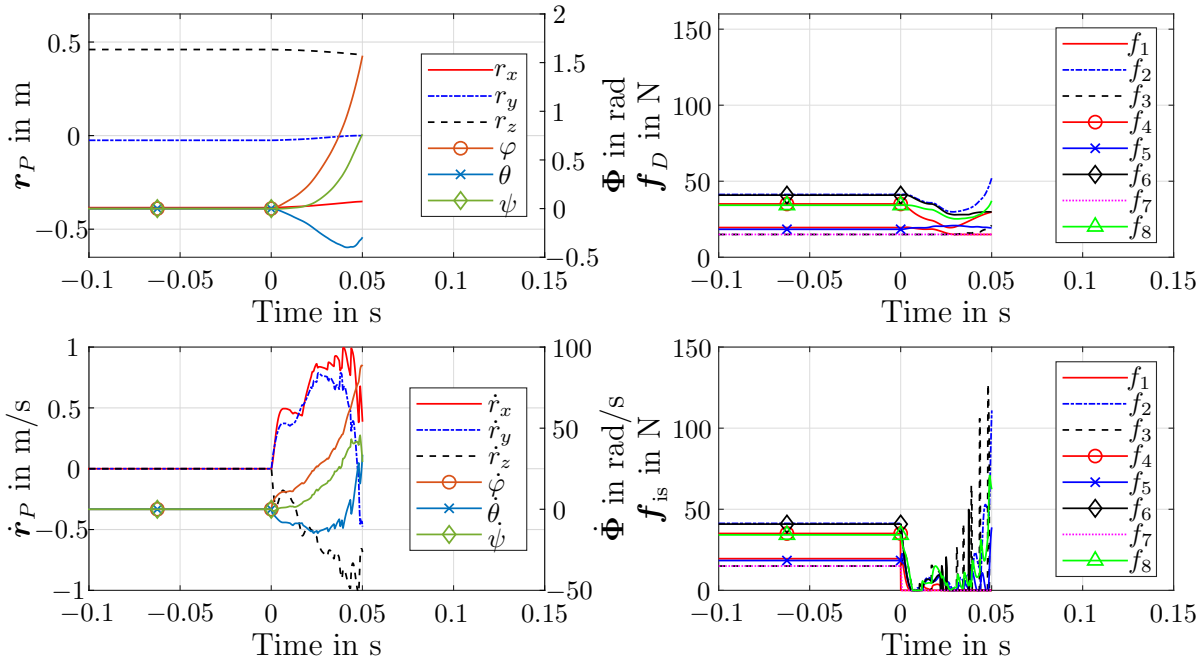

Figure 4.14: Cable failure scenario of cable 4 outside of the post-failure workspace using the conventional APD controller. Time scale aligned with event of cable failure. Top left: Pose of the platform; Top right: Desired cable forces; Bottom left: Velocity of the platform; Bottom right: Actual cable forces.

cables going slack and back in tension. This results in increasing cable forces as the motors accelerate and build up energy when torque is commanded without tensioned cables. Figure 4.14 displays an abruptly increasing speed after cable failure with particularly high rotational velocity leading to tipping over of the platform about the x-axis, which terminates the scenario. Generally, the outcome is as expected, since the starting pose is outside of the post-failure workspace and the controller does not anticipate the failure.

APD Controller Without Failure Detection Inside of the Post-Failure Workspace
When the platform is inside the post-failure workspace, the controller might be able to stabilize it after failure, which is tested within a second scenario, see fig. 4.15. Here, the platform's initial position is $[0.255, 0.075, 0.220]^{\mathrm{T}}$ m, all other parameters remain equal. With ~ 0.16 s, the simulation runs longer than the first scenario until it fails. However, also in this case the controller tries to utilize the defect cable, see f_4 in $\boldsymbol{f}_D$. After ~ 0.7 s, several cables reach $f_{\max}$. Comparable to the first scenario, undesired platform motion cannot be avoided. Although the cables do not get slack, undesired velocity builds up anyway. With a rotational maximum speed of 50 rad/s about the x-axis, e.g., this is not as high as in the first scenario (88 rad/s). Also, the speed does not increase abruptly. Nonetheless, the platform still tips over about the x-axis, leading to a failure of the simulation.

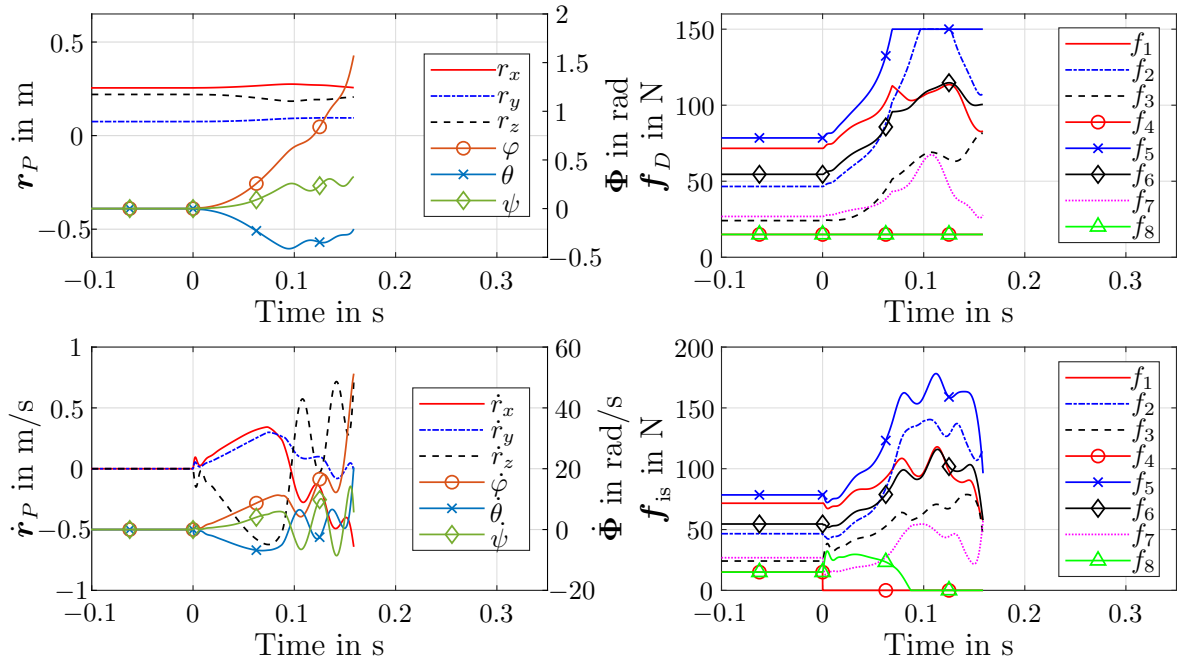

Figure 4.15: Cable failure scenario of cable 4 inside of the post-failure workspace using the conventional APD controller. Time scale aligned with event of cable failure. Top left: Pose of the platform; Top right: Desired cable forces; Bottom left: Velocity of the platform; Bottom right: Actual cable forces.

APD Controller Without Failure Detection in Multiple Scenarios The two previous scenarios suggest that it is barely possible to stabilize the platform after undetected cable failure using the conventional APD controller. To verify this hypothesis, multiple simulations are now carried out, covering the whole workspace. Based on fig. 4.5, 1649 feasible poses of the grid $\mathcal{G}_{\mathcal{SECOW}}$ have been extracted, which serve as simulation inputs. For each pose, two cable failure scenario are simulated, each for a failure of cable 4 and cable 2 respectively. The results are displayed in fig. 4.16. The color of the associated poses indicates, whether the simulation is failed. For both the failure of cable 4 and 2, the APD controller fails to stabilize the platform after cable failure in nearly all cases. Accordingly, the hypothesis can be confirmed. A few rare cases can be found, where the controller manages to stabilize the platform (0.06 % for cable 4 and 0.79 % for cable 2). This is considered serendipity here, due to a pose, which might be especially insensitive against platform tilting, when the corresponding cable fails and moreover possibly due to frictional forces. Those special cases are not further considered here. Investigation of such effects will be part of future work. In most of the cases where the controller fails, the simulation is terminated due to tipping over, as displayed by the red dots. No cases occur, where the robot's boundaries are violated, e.g. due to the platform falling down. Presumably, this is due to the low platform mass in comparison to the cable force boundaries. Especially for the failure of cable 2, some poses

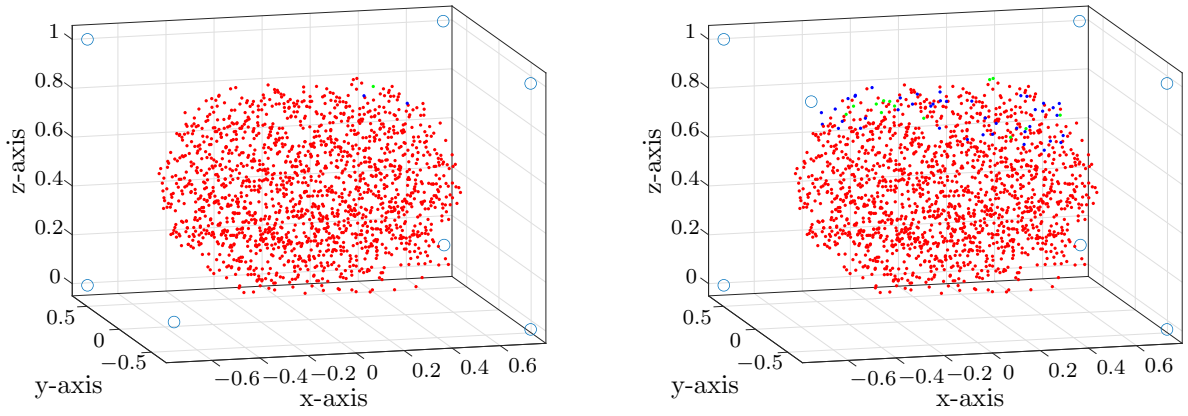

(a) Failure of cable 4 (coming from above). 1646 red dots, 0 magenta dots, 2 blue dots, 1 green dot.

(b) Failure of cable 2 (coming from below). 1593 red dots, 0 magenta dots, 43 blue dots, 13 green dots.

Figure 4.16: Multiple cable failure scenarios covering the pre-failure workspace using the conventional APD controller, 1649 poses per simulation series. Red dot: Simulation terminated due to tipping over; Magenta dot: Simulation terminated due to platform collision; Blue dot: Platform still moving at end of simulation; Green dot: Simulation successful, platform stopped and stabilized. Pulley positions indicated by blue circles in the corners, pulley of failed cable not displayed.

also exist at which the system does not fail within the simulation time, but the platform also cannot be braked. As this occurs rarely, it is not further investigated here.

In conclusion, it can be stated that the conventional APD controller is not able to ensure a stabilization of the platform after cable failure, not even within the post-failure workspace, as long as the failure remains undetected. Hence, it is examined in the following, how the APD controller performs after cable failure if the failure is detected and considered.

APD Controller With Failure Detection Inside of the Post-Failure Workspace
It is now assumed, that the cable failure is detected as soon as it occurs.[3] Hence, the missing cable is removed from $\boldsymbol{A}^{\mathrm{T}}$, as described in Section 3.1. Moreover, the missing cable is neglected within $\Delta\boldsymbol{l}$ and $\Delta\dot{\boldsymbol{l}}$. As for this example, a robot with $r = 1$ remains after cable failure, the APD controller can still be applied without restriction. Presumably, the APD controller with failure detection might be able to stabilize the platform after cable break, if it is within the post-failure workspace. Thus, the second scenario described in the paragraph above, with the platform's initial position of $[0.255, 0.075, 0.220]^{\mathrm{T}}$ m, is investigated first. Except from the adjustment of the controller, all parameters and the scenario remain equal. Figure 4.17, displays the experiment's results. As expected, the controller successfully stabilizes the platform after cable failure. At the event of cable break, an impulse, as

[3]Details on cable failure detection and application on a prototype is described within Chapter 5.

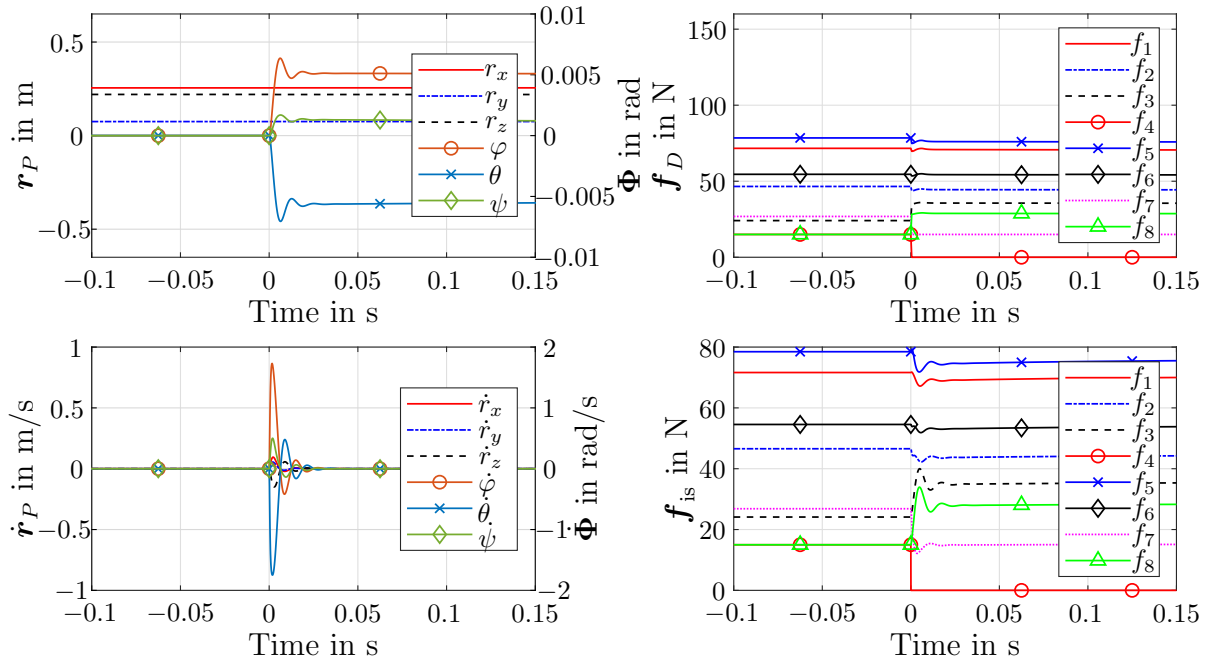

Figure 4.17: Cable failure scenario of cable 4 inside of the post-failure workspace using the APD controller with failure detection. Time scale aligned with event of cable failure. Top left: Pose of the platform; Top right: Desired cable forces; Bottom left: Velocity of the platform; Bottom right: Actual cable forces.

also seen in the previous experiments, is introduced to the system, leading to a maximum velocity of -0.15 m/s in z-direction and a maximum angular velocity of 1.7 rad/s about the x-axis in particular. However, the adjusted controller is able to regulate it after 0.03 s. With a small offset of ~ 0.005 rad about x- and y-axis, the platform pose is maintained. The set forces $\boldsymbol{f}_D$ change abruptly when changing from 8 to 7 cables within the APD, which presumably contributes to the impulse at the platform due to the stored energy within the tensed cables. To avoid this effect, a fade could be introduced in between both modes using e.g. polynomials, which is, however, not further investigated here. The desired force for the defect cable is set to zero in order to avoid winding of the corresponding motor, possibly leading to lashing of the cable end in reality.

APD Controller With Failure Detection Outside of the Post-Failure Workspace
Now the scenario with starting pose $[-0.385, -0.025, 0.460]^{\mathrm{T}}$ m and $[0, 0, 0]^{\mathrm{T}}$ rad is considered in fig. 4.18, the platform is outside of the post-failure workspace. The course of the experiment is quite similar to fig. 4.14. However, the controller now does realize that the platform is outside of the post-failure workspace at 0 s, leading to $f_4 = 0$ and all remaining forces in $\boldsymbol{f}_D$ equal $f_{\min}$. Thus it takes 0.02 s longer until the simulation is terminated due to tipping over about the x-axis. Due to the low $\boldsymbol{f}_D$, all cables get slack momentarily after

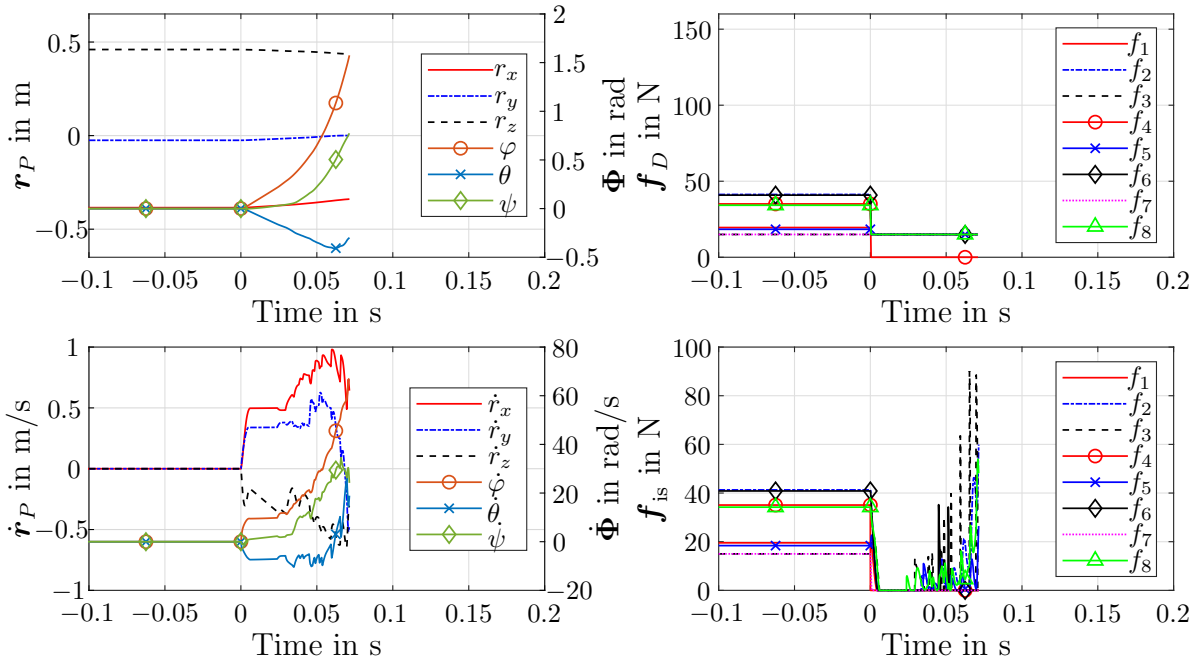

Figure 4.18: Cable failure scenario of cable 4 outside of the post-failure workspace using the APD controller with failure detection. Time scale aligned with event of cable failure. Top left: Pose of the platform; Top right: Desired cable forces; Bottom left: Velocity of the platform; Bottom right: Actual cable forces.

0 s. The maximum platform velocity ($\sim$ 1 m/s along x) and maximum rotational velocity ($\sim$ 65 rad/s about x-axis) are a little lower. The magnitude of the velocity resulting from the impulse after cable failure is almost equal in all DOF. The failure of the simulation is as expected, since the platform is outside of the post-failure workspace and besides the failure detection, there is no dedicated strategy to bring the platform back into the workspace. Naturally, the APD controller cannot stabilize it at a pose that does not belong to the $\mathcal{SEW}$. This is clearly shown in fig. 4.19.

APD Controller With Failure Detection in Multiple Scenarios Analogous to fig. 4.16, the results of a series of simulations covering the pre-failure workspace are displayed for the failure of cable 4 and 2. Especially for the failure of cable 4, the similarity to the post-failure workspace displayed in fig. 4.6a is remarkable. 76 % of the feasible poses (green) are part of the post-failure $\mathcal{SECOW}$ and 100 % of the non-feasible poses (red+blue+magenta) are also not part of the post-failure $\mathcal{SECOW}$. For the remaining feasible poses, the simulation is successful as the final pose after stabilization is within the $\mathcal{SEOW}$ or the stabilization is supported due to the systems friction. The opposite applies for the non-feasible poses. For the failure of cable 2, the assessment of the poses' post-failure workspace membership is not possible in this form, as the post-failure $\mathcal{SECOW}$ is empty in

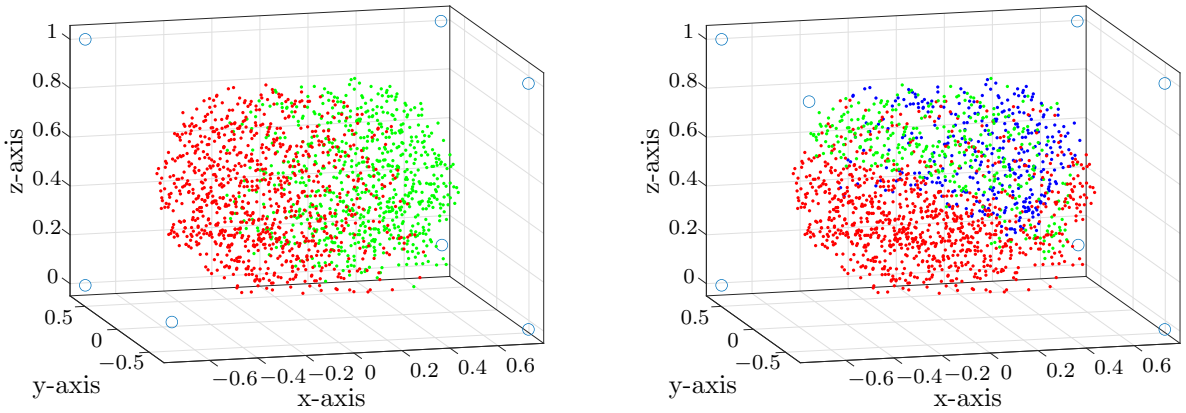

(a) Failure of cable 4 (coming from above). 920 red dots, 0 magenta dots, 0 blue dots, 729 green dots.

(b) Failure of cable 2 (coming from below). 965 red dots, 0 magenta dots, 340 blue dots, 344 green dots.

Figure 4.19: Multiple cable failure scenarios covering the pre-failure workspace using the APD controller with failure detection, 1649 poses per simulation series. Red dot: Simulation terminated due to tipping over; Magenta dot: Simulation terminated due to platform collision; Blue dot: Platform still moving at end of simulation; Green dot: Simulation successful, platform stopped and stabilized. Pulley positions indicated by blue circles in the corners, pulley of failed cable not displayed.

this case, see fig. 4.6b. Nonetheless, fig. 4.7 indicates that static force equilibrium is possible for several poses considering little deviation in platform orientation. This seems to be the case for the feasible poses (green). Remarkably, a lot of cases occur, where the platform does not crash but also does not get stabilized and stopped within the simulation time (blue). It seems likely that static force equilibrium would be possible but is not reached as the controller tries to maintain the starting pose with an orientation of $[0, 0, 0]^{\mathrm{T}}$ rad. Roughly, the area of green and blue dots is is similar to the area of the $\mathcal{SEOW}$ in fig. 4.7, which supports this assumption.

Summing up the findings from this section, it is clearly evident that dedicated strategies to rescue the platform into the post-failure workspace and stabilize it there after cable failure are indispensable. The simulative results support the theoretical considerations and assumptions given in Section 3.1 regarding post-failure behavior of a CDPR and the necessity of damage avoidance strategies, in particular for redundant CDPRs. Moreover, it has been shown that a detection of the cable failure is essential. Note, that further investigations on the influence of different initial states, such as varying orientation or velocity at the event of cable failure are part of future work.

Further, it is noticeable that the actual cable forces $\boldsymbol{f}_{\mathrm{is}}$ in fig. 4.14 and fig. 4.18 show high force peaks when transiting in between tension and slackness. This effect might be due to the chosen (simple) model of the simulated cable and could differ remarkably from reality.

A material model that might be more suitable is presented in [Flores et al., 2012] by Flores. Here, a hysteresis damping is introduced to account for energy dissipation. Consideration of this approach is also part of future work.

4.3.5 Kinetic Energy Minimization Method

As displayed in the previous section, it has been shown that damage avoidance strategies after cable failure are necessary when the platform gets outside of the post-failure workspace. Hence, the first emergency strategy developed by the author [Boumann and Bruckmann, 2019a], as elucidated in Section 3.3, is now implemented in the presented simulation of SEGESTA and thoroughly tested. It aims at minimizing the platform's kinetic energy to cause a full stop within the post-failure workspace. In underlying work of the author, it is applied within very simple simulations of planar and spatial redundant CDPRs, see e.g. [Boumann and Bruckmann, 2019a, Boumann and Bruckmann, 2020b, Boumann and Bruckmann, 2021, Boumann and Bruckmann, 2022]. The emergency strategy is implemented as displayed in fig. 4.20, altering the structure from fig. 4.1. For the simulation, it is assumed that the event of cable failure is detected immediately. This information is then processed and the conventional APD controller gets bypassed. The desired forces $\boldsymbol{f}_D$ calculated in the last cycle before failure serve as a warm start for this emergency strategy, which is optimization-based. As displayed in eq. (3.14) and fig. 4.20, this emergency controller requires information about platform velocity and pose. For simplicity, an ideal pose measurement is assumed here. The implementation of this measurement on the prototype is

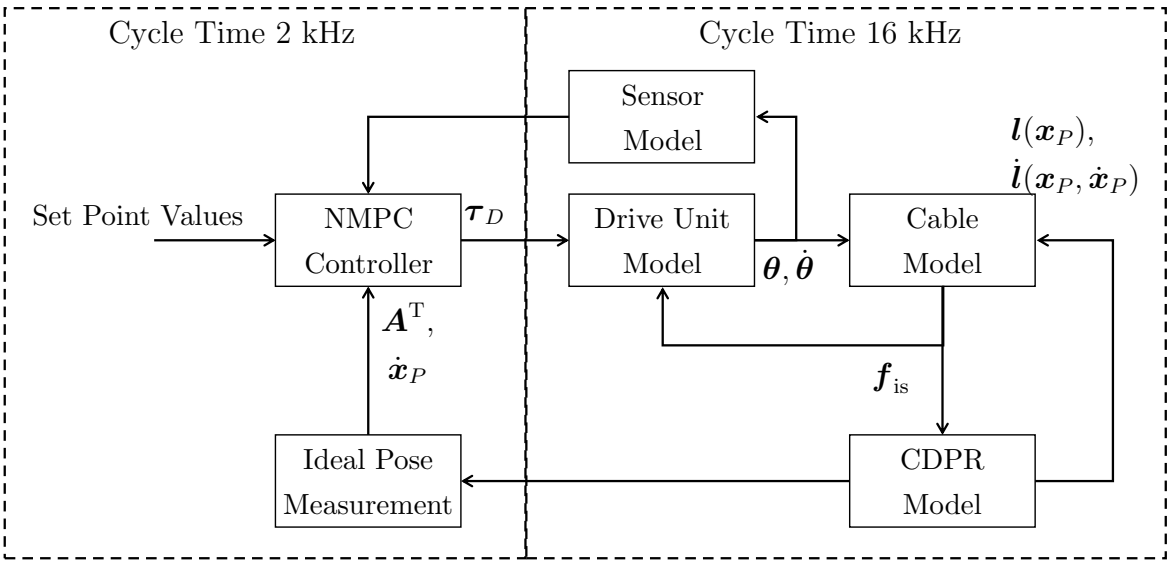

Figure 4.20: System structure with implementation of the Kinetic Energy Minimization Method in closed loop.

described in Section 5.2.1. After the event of cable failure, desired cable forces $\boldsymbol{f}_D$ are calculated by the emergency controller by minimizing the optimization problem eq. (3.15) with a desired reference velocity of $\boldsymbol{y}_r = \mathbf{0}$ in order to minimize Cartesian and angular velocity of the platform. The desired forces are converted to torques and commanded to the drive units, which are not affected by the failed cable. It is to note that the emergency controller based on an NMPC offers the possibility of predicting complex model behavior – which might also include drive units or frictional effects – over various time steps. Nonetheless, it is assumed that a shortage in available computation time will occur on prototype hardware[4], as a control frequency of 2 kHz is desired and the algorithm is based on an optimization approach. For these reasons, a rather simple model solely based on eq. (2.38) is employed within this work. In addition, the control and prediction horizon are set to $n_p = n_c = 1$ using a moving horizon. Besides an expected reduction in computing time, this is supposed to generate cable forces which stop the platform as best as possible directly within the next time step. `MATLAB`'s `fmincon()` is used to solve the optimization problem eq. (3.15), employing sequential quadratic programming (SQP) [Schittkowski and Zillober, 2005]. SQP can be considered state of the art in methods for nonlinear programming [The MathWorks, Inc., 2023a]. Various examples show that it can be applied in real-time for CDPRs, depending on the available computational power [Côté et al., 2016, Pott, 2018]. To constrain the time requirement of the optimization enabling real-time application, the maximum number of iterations is limited[5] to 50.

Kinetic Energy Minimization Method Outside of the Post-Failure Workspace I For a first experiment, the initial conditions as used for fig. 4.14 are employed with the initial pose $[-0.385, -0.025, 0.460]^{\mathrm{T}}$ m and $[0, 0, 0]^{\mathrm{T}}$ rad, which is outside of the post-failure workspace. Here, the conventional APD controller with failure detection still fails, see fig. 4.18. The weights $\boldsymbol{R} = \mathrm{diag}(1, 1, 1, 100, 100, 1)$ and $r_1 = 0.1$ are chosen. A high weight of 100 is assigned to suppress rotation about the x- and y-axis, as this appears to be critical in the previous experiments. The weight r_1 is chosen rather low to enable rapid intervention of the controller by quick adjustment of the cable forces. The remaining weights are chosen as 1, primarily since a balancing Cartesian movement of the platform is desired and the platform needs to build up speed in order to get back into the post-failure workspace. Figure 4.21 displays the experiment. Unfortunately, it turns out that analog to the experiment displayed in fig. 4.18, the platform cannot be stabilized with the aid of the emergency controller used and the chosen parameters. In comparison to fig. 4.18, noticeably

[4]The calculation times of the implementation are investigated in Section 5.2.

[5]Limiting the number of maximum iterations is a common approach towards real-time applicability. It aims at achieving similarly long maximal calculation times per optimization cycle. At the end of each optimization, the best obtained solution is fed to the system, see [Adamy, 2014].

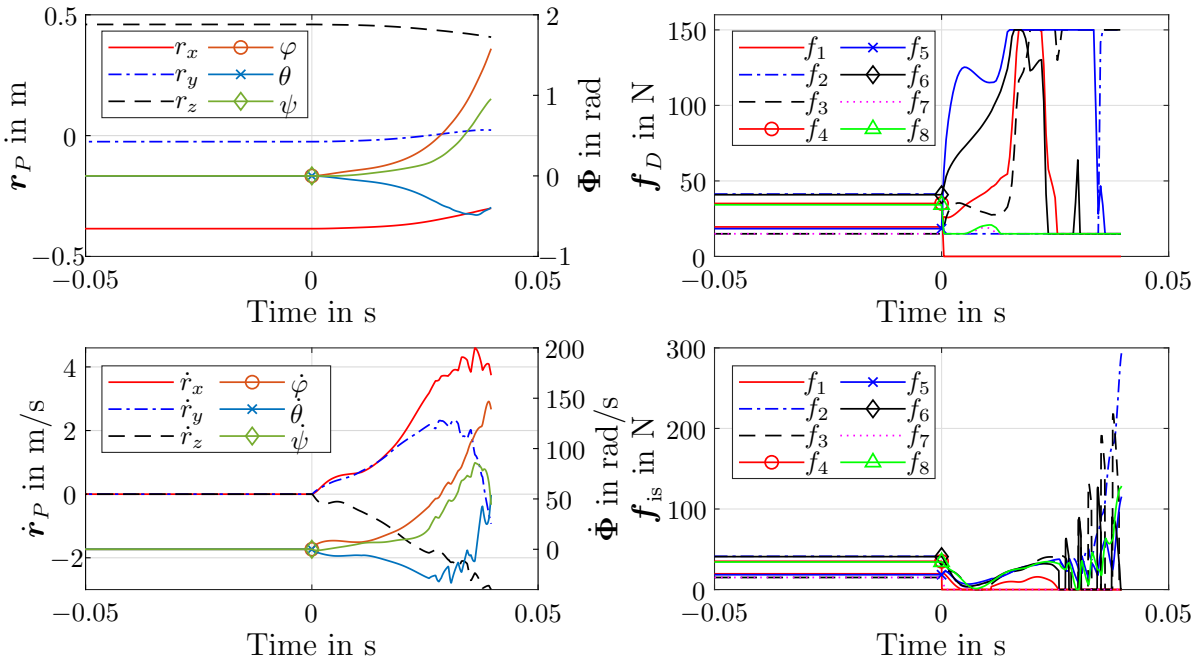

Figure 4.21: First cable failure scenario of cable 4 outside of the post-failure workspace using Kinetic Energy Minimization Method. Time scale aligned with event of cable failure. Top left: Pose of the platform; Top right: Desired cable forces; Bottom left: Velocity of the platform; Bottom right: Actual cable forces.

higher velocities in x- (max. 4.5 m/s) and y-direction (max. 2.3 m/s) can be observed. This indicates that the controller pulls the platform towards the post-failure workspace and tries to perform a balancing Cartesian movement, as desired by the weights set. However, the platform still tips over about the x-axis, which cannot be prevented by the controller, leading to simulation failure after ~ 0.4 s. The progression of $\boldsymbol{f}_D$ displays that the controller demands high forces for several cables and tries to rapidly intervene, which was desired by the choice of r_1. Nonetheless, those forces are not reached, potentially because the simulated drive units are not able to accelerate quick enough at the event of cable failure. In addition, it is to note that there is no closed loop force control using $\boldsymbol{f}_{\text{is}}$. However, nearly all cables can be prevented from getting slack during the first 0.025 s. At 0.034 s, the controller changes $\boldsymbol{f}_D$ rapidly from $f_2 = f_{\min}$ and $f_5 = f_{\max}$ to $f_2 = f_{\max}$ and $f_5 = f_{\min}$, leading to strong acceleration of drive unit 5 that produces a force peak of ~ 300 N in cable 2, when it gets in tension. As elaborated in the previous section, such force peaks might differ from reality due to the simple material model. Summing up, the platform cannot be stabilized and rescued within the given scenario using the given parameters, even thou the emergency strategy shows the right trend. The ill success of the emergency strategy in this scenario might have various reasons: Either the controller might be parametrized sub-optimal for the scenario, or the scenario in general has poor opportunities for a stabilization. The tipping over of the

platform seems to be a remarkable problem. It might be promoted due to the low weight and inertia of the platform in combination with high cable forces and the kinematic configuration defined by $\boldsymbol{B}$ and $\boldsymbol{P}$. This again emphasizes the consideration of the conceptual idea of cable failure resistant CDPR design, as discussed in Section 4.3.1, for future work.

Kinetic Energy Minimization Method Outside of the Post-Failure Workspace II Now a second experiment, see fig. 4.22, is conducted with a different initial position outside of the post-failure workspace at $[-0.025, -0.165, 0.16]^{\mathrm{T}}$ m. The APD controller even with failure detection fails to stabilize the platform at this initial position, see fig. 4.19. Using the proposed emergency controller, the platform is guided back into the post-failure workspace and stabilized. Analog to the previous experiment, mainly speed in x- and y-direction is built up to perform a balancing movement. After 0.63 s, both Cartesian and angular velocity can be controlled to the desired value $\boldsymbol{y}_r = \boldsymbol{0}$ while the platform comes to rest at $[0.319, 0.247, 0.198]^{\mathrm{T}}$ m and $[0.395, -0.274, -0.031]^{\mathrm{T}}$ rad. The maximum tilting of 0.541 rad about the x-axis and -0.477 rad about the y-axis during motion is acceptable. The controller is able to keep all cables in tension after cable failure, except from cable 7. At 0.066 s, it also gets back in tension abruptly, leading to a momentary vibration which is smoothed out quickly. The experiment demonstrates that cases of cable failure exist, where

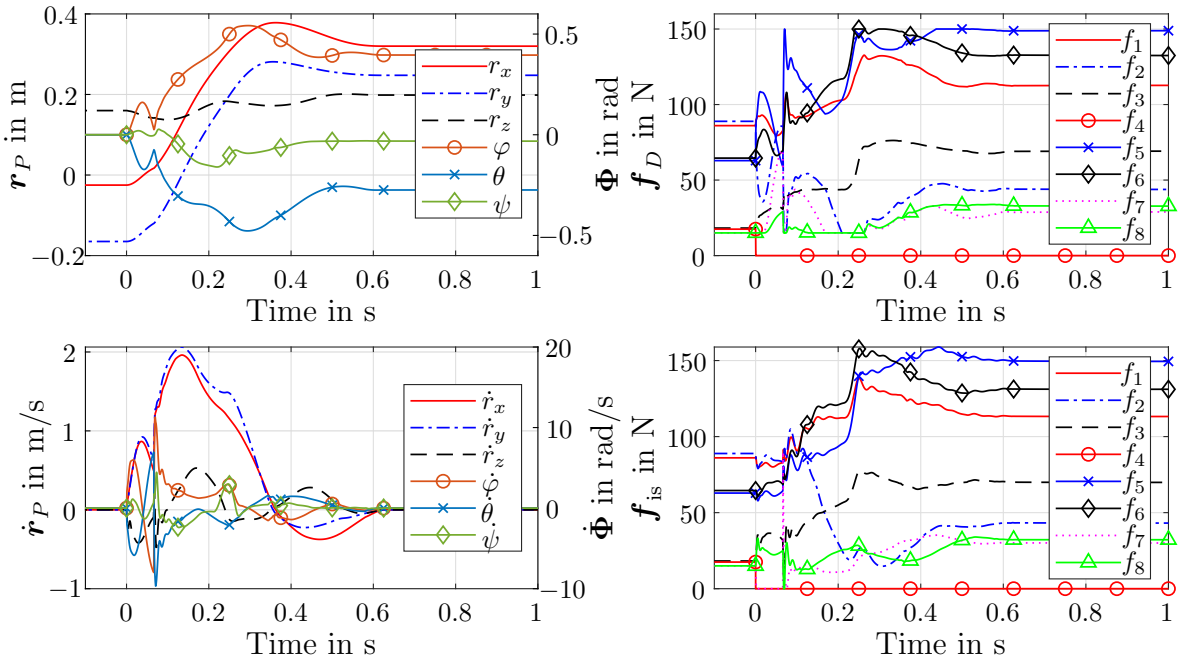

Figure 4.22: Second cable failure scenario of cable 4 outside of the post-failure workspace using Kinetic Energy Minimization Method. Time scale aligned with event of cable failure. Top left: Pose of the platform; Top right: Desired cable forces; Bottom left: Velocity of the platform; Bottom right: Actual cable forces.

the conventional controller fails to stabilize the platform even with failure detection, but it can be guided back into the post-failure workspace and stabilized there using the proposed emergency controller based on minimization of kinetic energy. This can be considered as a first success of this work and substantiates the feasibility of the approach.

Kinetic Energy Minimization Method in Multiple Scenarios Nonetheless, it is also shown that the emergency strategy might fail with specific parametrization and initial states. Consequently, the whole pre-failure workspace is now investigated, analog to fig. 4.19, for failure of cable 4 and 2, using constant controller parametrization of $\boldsymbol{R}$ and r_1. The results are displayed in fig. 4.23. For both the failure of cable 4 and 2, numerous successful simulations can be recognized with the given parameter setting. For failure of cable 4, 901 out of 1649 simulations are successful, which is an improvement of $\sim 24\%$ compared to fig. 4.19. For failure of cable 2, the results display an even greater improvement of $\sim 204\%$ in comparison to fig. 4.19, 1047 out of 1649 simulations are successful. Still there are regions, especially towards the pre-failure workspace boundaries, where the strategy fails. As this may be due to the given robot parameters in conjunction with those of the strategy, parameter studies are carried out in the following.

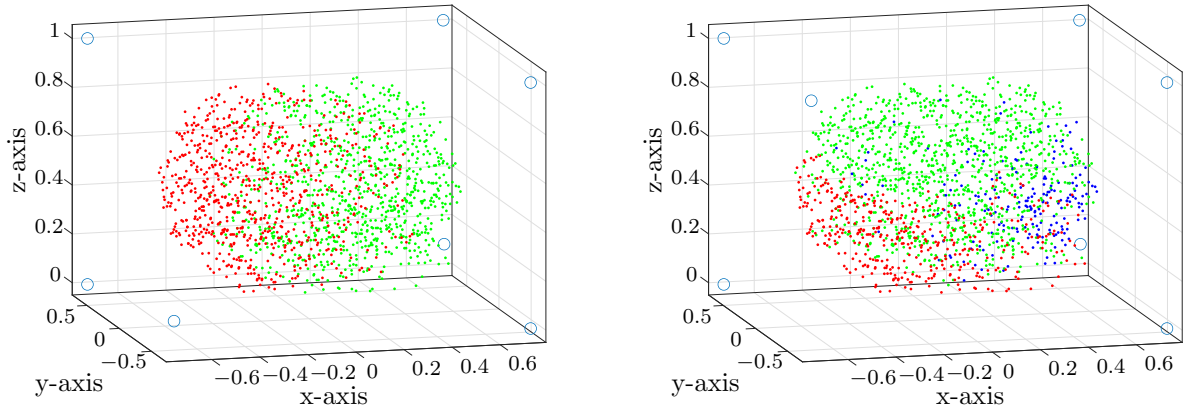

(a) Failure of cable 4 (coming from above). 748 red dots, 0 magenta dots, 0 blue dots, 901 green dots.

(b) Failure of cable 2 (coming from below). 411 red dots, 0 magenta dots, 191 blue dots, 1047 green dots.

Figure 4.23: Multiple cable failure scenarios covering the pre-failure workspace using Kinetic Energy Minimization Method, 1649 poses per simulation series. Red dot: Simulation terminated due to tipping over; Magenta dot: Simulation terminated due to platform collision; Blue dot: Platform still moving at end of simulation; Green dot: Simulation successful, platform stopped and stabilized. Pulley positions indicated by blue circles in the corners, pulley of failed cable not displayed.

Kinetic Energy Minimization Method - Parameter Study of r_1 First, it is investigated if adjusting the controller weights leads to the expected behavior of the algorithm (and thus of the robot). Initially, the parameter r_1 is considered in more detail. It reflects how strong the algorithm tends to change control variables, which are the desired cable forces in this case. Different parameters are set for r_1 and the simulation behavior is explored. The weighting matrix $\boldsymbol{R}$ is set to $\boldsymbol{R} = \mathrm{diag}(1, 1, 1, 1, 1, 1)$, the starting pose is $[-0.005, -0.095, 0.54]$ m and $[0, 0, 0]$ rad, cable 2 fails. This example is chosen, as it reveals the parameter influences of the Method more effectively. Figure 4.24 displays the results. As expected, it can be observed that the controller is allowed to rapidly change the control variables $\boldsymbol{f}_D$ with lower weights of r_1 and vice versa for higher values of r_1. The optimization

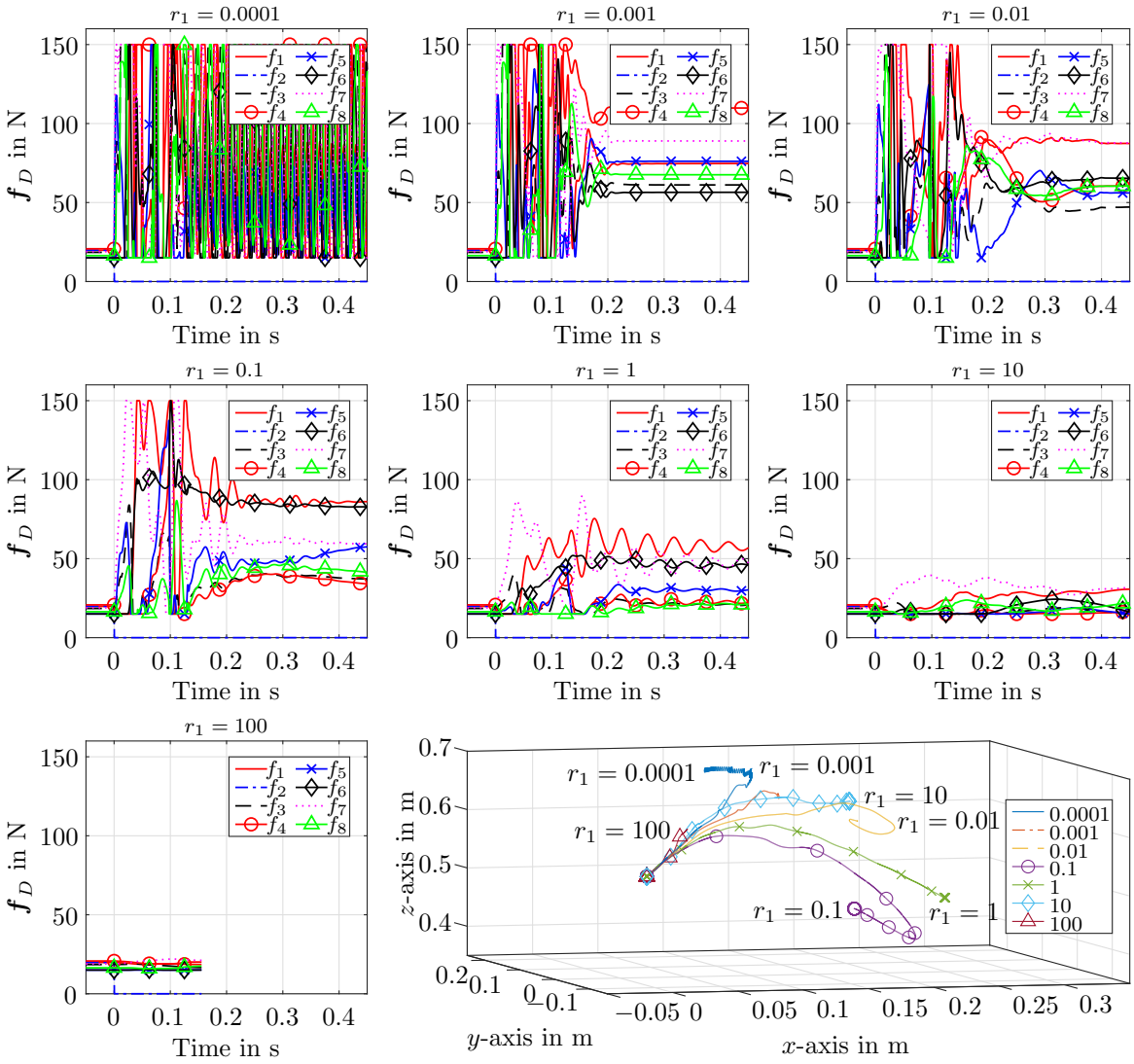

Figure 4.24: Investigation on parameter r_1 in a cable failure scenario using Kinetic Energy Minimization Method, cable 2 fails. Progression of the control variables $\boldsymbol{f}_D$ for different values of r_1 and spatial representation of the according platform movement (bottom right).

constraints of minimum and maximum forces are respected at all times by the algorithm. In between $r_1 = 0.001$ and $r_1 = 1$, the algorithm seems to perform quite well and the platform can be stopped after less than 0.5 s in all cases. The lower r_1 is, the faster the platform is brought to rest (which is not explicitly displayed in fig. 4.24). This behavior seems to be correct, since the weighting for reaching the target velocity $\boldsymbol{y}_r = \mathbf{0}$ is higher or at least equal to having constant control variables $\boldsymbol{f}_D$ in those cases. Additionally, with a lower weight of r_1, the algorithm can intervene more rapidly, while the forces get more smooth with rising weight. For higher weights of r_1, $\boldsymbol{f}_D$ is hardly adjusted (see $r_1 = 10$), leading to almost invariant control variables at $r_1 = 100$. This is due to the fact that the cost function value J_{Ekin} is easy to minimize for the optimizer by choosing rather constant forces and ignoring the predicted velocity with such weighting parameters, possibly getting stuck in a local minimum. At $r_1 = 100$, this leads to a premature termination of the simulation after 0.15 s due to tipping over of the platform. Likewise, in the opposite direction, a very low value of $r_1 = 0.0001$ leads to an extremely nervous behavior of the algorithm, causing massive and lasting platform vibration that cannot be flattened by the controller. Depending on how strong the controller can intervene, the platform's trajectory also differs of course, as displayed on the bottom right of fig. 4.24. Summing up, the selection of the weight r_1 results in expected behavior of the algorithm. Very low ($r_1 < 0.001$) or very high values ($r_1 > 10$) with respect to $\boldsymbol{R}$ do not appear useful, as they lead to unsuccessful experiments in this case. Of course, choice of the weighting parameters for the optimization is always a trade-off in between the individual optimization goals, which are in this case: continuous force versus zero predicted velocity.

Kinetic Energy Minimization Method - Parameter Study of $\boldsymbol{R}$ Based upon the study of the first parameter r_1, the parameter $\boldsymbol{R}$ is now investigated. The weighting of the control variables is set to $r_1 = 1$ and $\boldsymbol{R} = \text{diag}(R_1, 1, 1, 1, 1, 1)$ is chosen. Exemplarily for $\boldsymbol{R}$, R_1 is now varied between 0.001 and 1000, all other parameters remain equal. The results are displayed in fig. 4.25. In between $R_1 = 0.001$ and $R_1 = 1$, the platform's trajectory is barely affected by parameter changes of R_1. Weights for R_1 lower than the remaining parameters of $\boldsymbol{R}$ and r_1 promote more movement in x-direction, if movement in the remaining DOF can be avoided, which can be observed from fig. 4.25. Vice versa accounts for higher weights of R_1. Since the trajectory still moves primarily in x-direction with $R_1 = 1$, it can be assumed that this stabilizing movement seems to be generally favorable for the optimizer with the given initial pose and the remaining cables. Once the weighting parameter gets $R_1 = 10$ or $R_1 = 100$, movement in x-direction is stronger avoided. While the platform moves 0.295 m through the workspace in x-direction for $R_1 = 1$, it only moves 0.096 m for $R_1 = 100$. In these cases, the optimizer tends to surrogate the motion in x-direction by balancing movement in

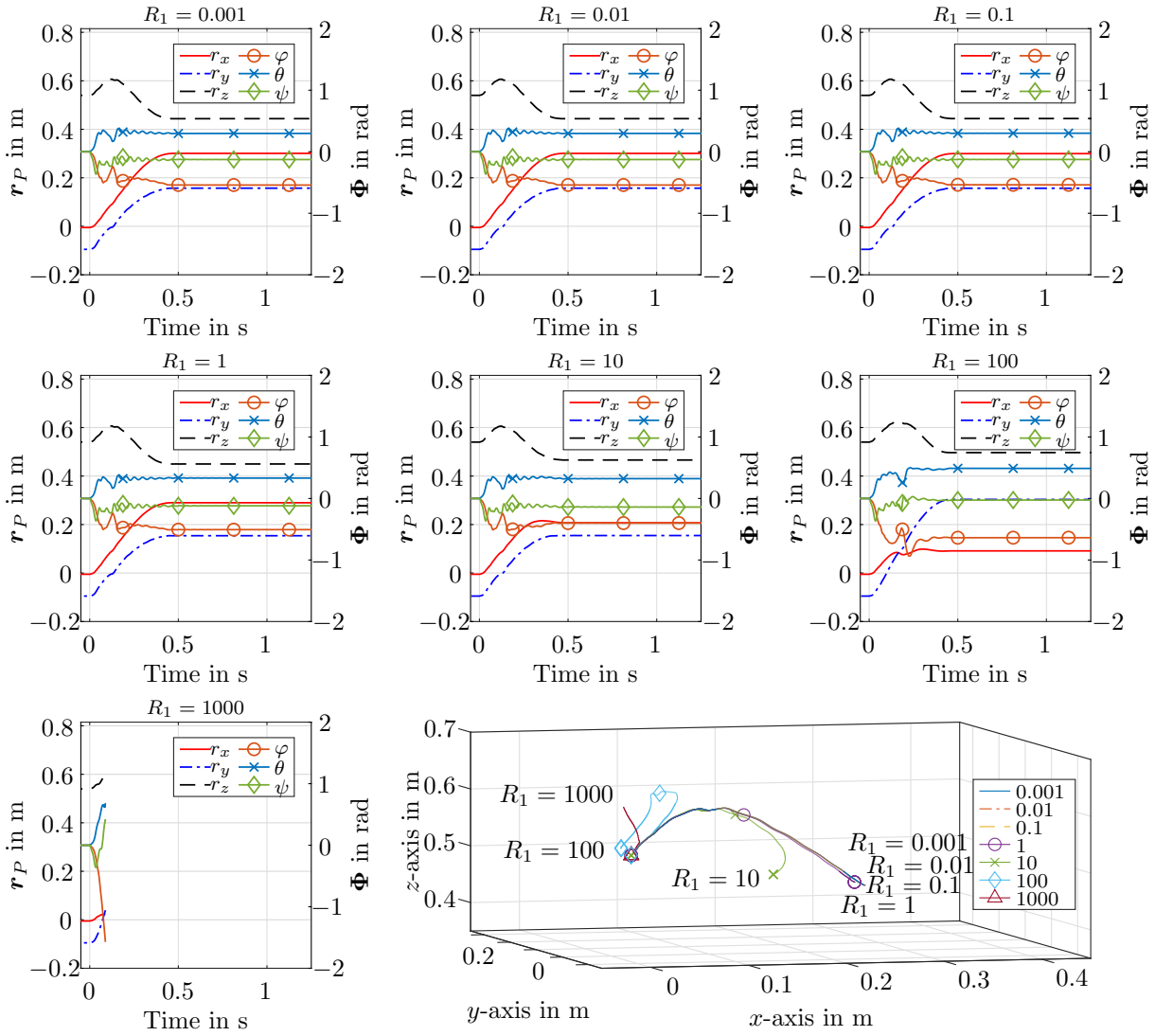

Figure 4.25: Investigation on parameter R_1 in a cable failure scenario using Kinetic Energy Minimization Method, cable 2 fails. Progression of position $\boldsymbol{r}_P$ and orientation $\boldsymbol{\Phi}$ for different values of R_1 and spatial representation of the according platform movement (bottom right).

y-direction to stabilize and stop the system. For a very weight of $R_1 = 1000$, the optimizer attempts to suppress movement in x-direction so strongly that the platform tips over and the simulation is terminated. Consequently, too high weights of R_1 with respect to $\boldsymbol{R}$ and r_1 do not appear useful. Summing up, it can be stated that adjustment of the weight R_1 affects the optimization and the robots trajectory as expected. It is assumed, that the same accounts for the remaining parameters of $\boldsymbol{R}$.

Kinetic Energy Minimization Method - Parameter Study of $n_{\max}$ Based upon the previous consideration of the weights used within the optimization's cost function J_{Ekin}, the performance of the optimization algorithm in general should also be examined. This is

of particular interested, since a proper minimization of the cost function during the rescue scenario needs to be ensured. Otherwise, the optimization goals might not be reached, which would lead to malfunction of the damage avoidance strategy. As stated before, the optimizer employed in the previous experiments is set up using `MATLAB`'s `fmincon()` with a SQP-algorithm and a number $n_{\max}$ of 50 iterations. Besides that, the remaining optimization options are set to default values, see [The MathWorks, Inc., 2023b]. It is now investigated in one example, how the algorithm behaves with different $n_{\max}$. The results are shown in fig. 4.26. From the number of used iterations per calculation cycle n_{iter} it can be observed that

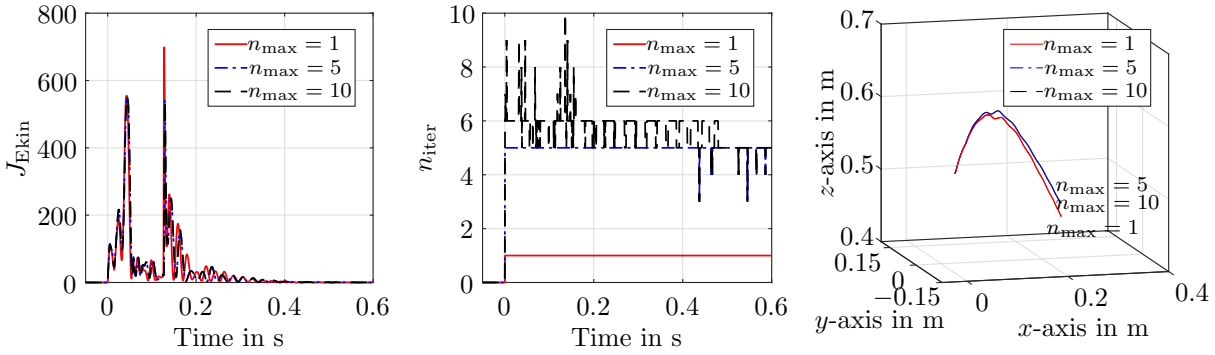

Figure 4.26: Investigation on the SQP-algorithm used within the Kinetic Energy Minimization Method in a cable failure scenario, cable 2 fails. Cost function values J_{Ekin}, number of iterations used per optimization cycle n_{iter} and spatial path of the platform for different numbers of maximum iterations $n_{\max}$.

$n_{\max} = 10$ iterations are sufficient to obtain the best-possible cost function values in the given example. For $n_{\max} = 1$ and $n_{\max} = 5$, the optimizer has to exploit the maximum number of iterations in each cycle, leading to a premature abortion of the SQP-Algorithm in those cases. This does not apply for $n_{\max} = 10$. Here, the border is only reached once at 0.136 s. The values of J_{Ekin} over time are quite similar for all $n_{\max}$ and the distinctive profile of minimum and maximum values follows the same trend. However, in between $n_{\max} = 1$ and $n_{\max} = 5$, the maximum values are mostly higher. Especially the peak at ~ 0.128 s has a difference in value of ~ 150. This indicates that worse optimization results are obtained due to premature abortion for $n_{\max} = 1$, which is as expected. For the spatial path of the platform, this leads to slight differences and the final position in between $n_{\max} = 1$ and $n_{\max} = 5$ differs by $[0.0013, 0.0011, -0.0185]^{\text{T}}$ m and $[0.0766, -0.0372, -0.024]^{\text{T}}$ rad. Nonetheless, it is to note that the platform can be successfully stabilized even with $n_{\max} = 1$. The differences in between $n_{\max} = 5$ and $n_{\max} = 10$ are barely visible. The maximum difference in J_{Ekin}, e.g., is only 0.1146 at 0.1285 s, where J_{Ekin} is approximately 550. For a number of maximum allowed iterations greater than $n_{\max} = 10$, the results and the optimization steps taken per cycle do not change anymore. For the sake of clarity, this is not displayed in fig. 4.26. Thus it can be assumed that with $n_{\max} = 50$, which was chosen for the preliminary experiments,

the optimizer should have enough capacity to properly minimize J_{Ekin} at its best. Moreover, it is indicated that $n_{\max}$ could be reduced while maintaining sufficient optimization results, if calculation time issues arise on the prototype hardware. Considering the course of J_{Ekin}, it is to note that the values do not constantly decrease during the rescue scenario, which might be useful to assess the methods stability (see Section 3.3). As the platform is outside of the post-failure workspace at the start of the experiment, it needs to build up speed in some DOF to find its way back into the workspace, in order to get stabilized there. With a prediction and control horizon of $n_p = n_c = 1$, this fact cannot be reflected within the values of J_{Ekin}. Thus, they may rise during the procedure. To consider the whole rescue scenario within the cost function, n_p and n_c need to be increased and a receding horizon might be used. Naturally, this results in a more computational expensive method. Investigation on this is part of future work.

Kinetic Energy Minimization Method - Parameter Study of Platform Mass and Inertia As the preliminary experiment in fig. 4.26 has shown, it can be assumed that with $n_{\max} = 50$, the optimizer works properly and adjustments will not change the failed cases (see fig. 4.23). This suggests that the scenario is rather hard to rescue, since the robot tends to tip over easily with the given parameters, especially towards the workspace boundaries. To assess this assumption, the platform mass and inertia are now increased by the factor four and the simulation experiment from fig. 4.23 is repeated. Figure 4.27 displays the results. Of course, it is to note that also the shape and volume of the pre- and post-failure workspace change slightly with different platform mass and inertia. Hence, the comparability, especially towards the conventional controller scenario, is not necessarily given. Nonetheless, the change in workspace seems to be minor: It is not observed in simulation, that the platform crashes prior to the event of cable failure at the whole outer workspace region. Furthermore, the experiment substantiates the assumption that the robot might be more easy to rescue in this case, as the platform's tendency to tilt declines with the parameter changes. Compared to fig. 4.23, a simulation failure due to tipping over only occurs in 515 cases (versus 748 cases) for the failure of cable 4 and in 276 cases (versus 411 cases) for the failure of cable 2. Additionally for cable 4, nine cases occur where the platform collides with an assumed frame (magenta dots), indicating that the simulation now runs long enough for those cases to happen instead of premature termination due to tipping over. For the failure of cable 2, a large amount of cases arise (1096), where the platform is still moving at the end of the simulation. Presumably, a higher platform mass and inertia might lead to slower stopping of the platform. Therefore, the experiment is repeated with a doubled simulation time of 8 s, leading to 277 red dots, 0 magenta dots, 131 blue dots and 1241 green dots. This demonstrates that the platform can be stopped and stabilized in a lot of cases that do not

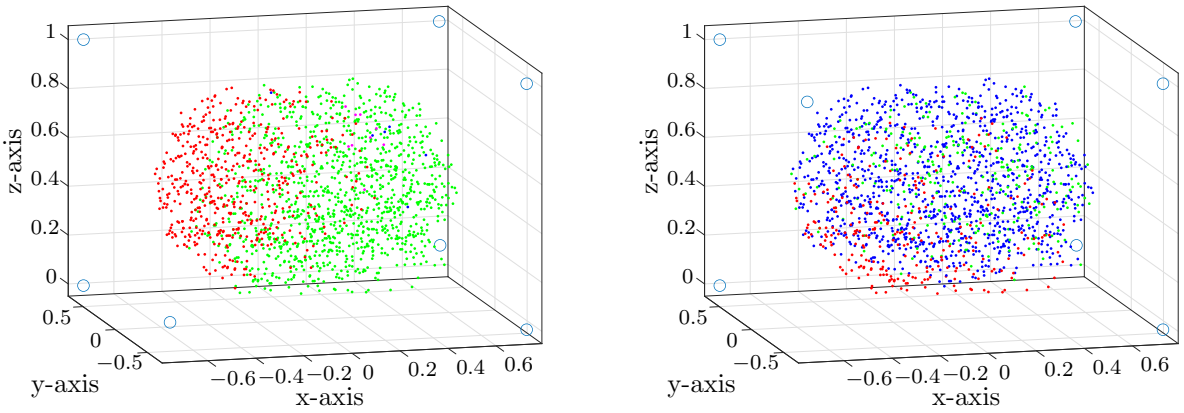

(a) Failure of cable 4 (coming from above). 515 red dots, 9 magenta dots, 6 blue dots, 1119 green dots.

(b) Failure of cable 2 (coming from below). 276 red dots, 0 magenta dots, 1096 blue dots, 277 green dots.

Figure 4.27: Multiple cable failure scenarios covering the pre-failure workspace using Kinetic Energy Minimization Method, 1649 poses per simulation series. Platform mass and inertia increased by factor four. Red dot: Simulation terminated due to tipping over; Magenta dot: Simulation terminated due to platform collision; Blue dot: Platform still moving at end of simulation; Green dot: Simulation successful, platform stopped and stabilized. Pulley positions indicated by blue circles in the corners, pulley of failed cable not displayed.

lead to tipping over, even after longer simulation duration. Accordingly, the method seems to perform quite well in the cable failure scenarios, especially if the platforms tendency to tip over is reduced by increasing mass and inertia.

Conclusion on the Kinetic Energy Minimization Method Summing up the results from this section, it can be stated that the emergency strategy based on minimization of the platform's kinetic energy is proven to work in the proposed simulation of the SEGESTA prototype. The weighting parameters $\boldsymbol{R}$ and r_1 influence the methods outcome as expected and can be used to adjust the optimizer's solution, e.g. for less movement in a DOF or a smoother course of the desired cable forces $\boldsymbol{f}_D$. In comparison to a scenario without damage avoidance strategy, using a conventional APD controller even with failure detection, the method enables a platform rescue in $\sim 24\%$ (failure of cable 4) or $\sim 204\%$ (failure of cable 2) more cases, dependent on the failed cable. Still cases occur, especially at the workspace boundaries, where the method cannot prevent the platform from tipping over, leading to a simulation failure. It is indicated, that those cases are hard to rescue in particular and that the method performs even better if the platform's tendency to tip over after cable failure is reduced by increasing mass and inertia. But even then, cases remain, where the platform cannot be recovered after a cable failure, using the proposed methods with the given parameter setting. Moreover, finding a proficient set of weighting parameters has shown to

be crucial and might be complex. Thus, investigation on simplification or automation of parameter setting is part of future work. Furthermore, the method can be adjusted and examined using a larger prediction and control horizon. Lastly, the cost function could be extended by a position control part to consider obstacles within the workspace, a desired goal pose or a trajectory tracking, for example.

4.3.6 Potential Field Method

A further strategy for damage avoidance after cable failure considered within this work is based on the usage of potential fields in the workspace. The strategy, as introduced in Section 3.4, is now implemented and extensively tested within the simulation framework based on the SEGESTA prototype. By using potential fields that imprint virtual forces and torques onto the robot's platform, it shall be guided towards a pose within the post-failure workspace after cable failure, where it should be brought into a static force equilibrium. For avoidance of obstacles or contact with the robot's frame, e.g., repulsive fields can be added. Moreover, virtual damping can be utilized to restrict the robots translational and rotational velocity. The emergency strategy is implemented as depicted in fig. 4.28. To calculate the virtual wrench resulting from the potential fields and the damping factors, the algorithm requires knowledge on platform pose and velocity. Analog to Section 4.3.5, ideal pose measurement, instantaneous cable failure detection and bypassing of the conventional controller are assumed. According to the chosen potential fields, the platform should be guided into the goal pose $\boldsymbol{x}_{P,\text{final}}$, using the desired cable forces $\boldsymbol{f}_D$ calculated by the method. To solve for $\boldsymbol{f}_D$ outside of the $\mathcal{WFW}$, the Nearest Corner Method, see Section 3.5.2, is

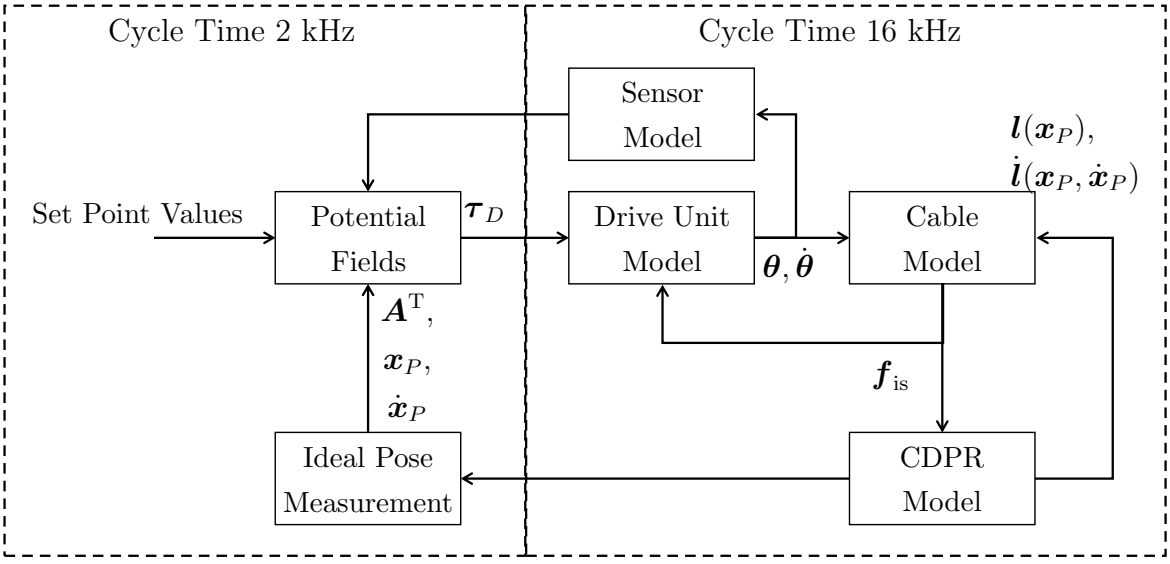

Figure 4.28: Structure with implementation of the Potential Field Method in closed loop.

employed. The so-called Puncture Method [Müller et al., 2014] is set as a standard method to check for feasible solutions first. Both Methods are based on geometrical calculations within the space of cable forces and do not rely on an iterative structure, which might be beneficial in terms of real-time application on prototype hardware.

Potential Field Method Outside of the Post-Failure Workspace I For a first experiment, the initial conditions are set equal as in fig. 4.21 and fig. 4.14 ($\boldsymbol{r}_P = [-0.385, -0.025, 0, 460]^{\mathrm{T}}$ m, $\boldsymbol{\Phi} = [0, 0, 0]^{\mathrm{T}}$ rad, cable 4 fails). An attractive field is placed with its origin at the goal pose $\boldsymbol{r}_{P,\mathrm{final}} = [0.375, 0.25, 0.2]^{\mathrm{T}}$ m and $\boldsymbol{\Phi}_{\mathrm{final}} = [0, 0, 0]^{\mathrm{T}}$ rad, which is well within the post-failure workspace. The field strength is set to $\boldsymbol{\zeta}_r = 950 \cdot \mathrm{diag}(1, 1, 1)$ 1/m and $\boldsymbol{\zeta}_\Phi = 60 \cdot \mathrm{diag}(1, 1, 1)$ 1/rad. The border d_b on position level is set to 0.25 m. For virtual damping, the parameter $\boldsymbol{D}_1 = 25 \cdot \mathrm{diag}(1, 1, 1)$ Ns/m and $\boldsymbol{D}_2 = 0.25 \cdot \mathrm{diag}(1, 1, 1)$ Nms/rad are set. Initially, no repulsive field is used. The exponential weight of the Nearest Corner Method is set to $p = 16$. Figure 4.29 shows the results. Even thou, $\boldsymbol{f}_D$ is different to fig. 4.21, the damage avoidance strategy is not able to guide the system into a stable pose without tipping over about the x-axis. The course of $\boldsymbol{x}_P$ and $\dot{\boldsymbol{x}}_P$ as well as of $\boldsymbol{f}_{\mathrm{is}}$ is quite similar to fig. 4.21, the simulation is aborted after ~ 0.03 s. This substantiates once again, that it is rather difficult to avoid tipping over at this pose with the given robot parameters.

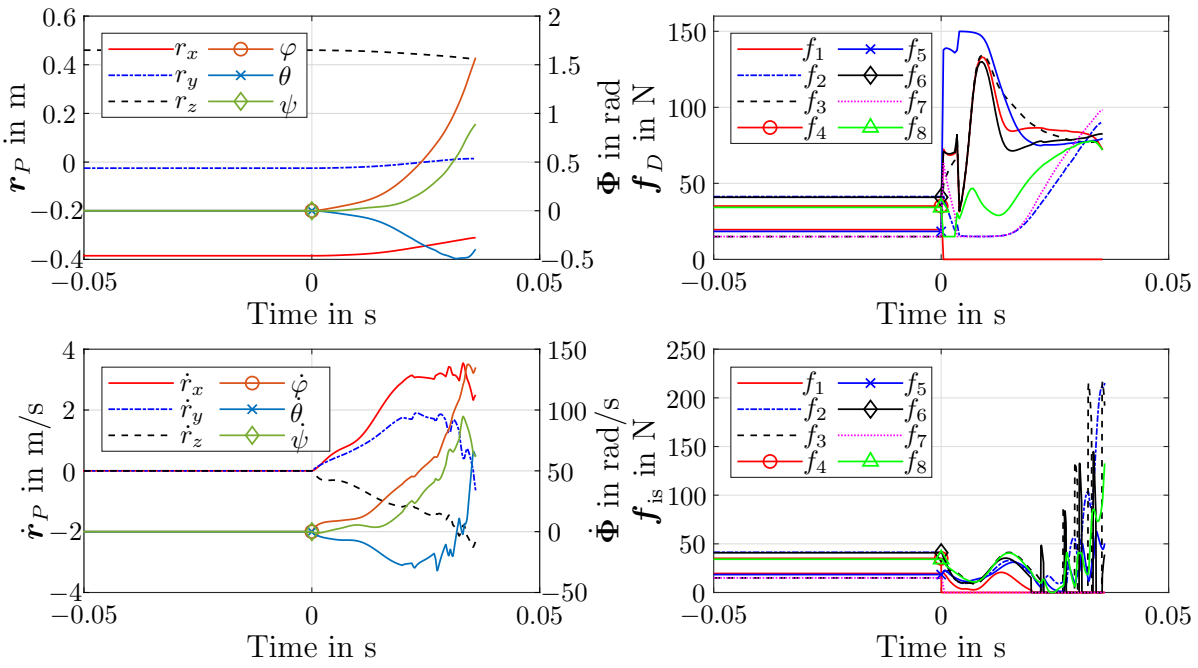

Figure 4.29: First cable failure scenario of cable 4 outside of the post-failure workspace using Potential Field Method. Time scale aligned with event of cable failure. Top left: Pose of the platform; Top right: Desired cable forces; Bottom left: Velocity of the platform; Bottom right: Actual cable forces.

Potential Field Method Outside of the Post-Failure Workspace II With the same initial conditions as fig. 4.22 ($\boldsymbol{r}_P = [-0.025, -0.165, 0.16]^{\mathrm{T}}$ m, $\boldsymbol{\Phi} = [0, 0, 0]^{\mathrm{T}}$ rad, cable 4 fails), a second experiment is carried out. Once more, it is to note that the conventional APD controller, even with cable failure detection, fails to stabilize the platform at that pose. The goal position $\boldsymbol{r}_{P,\mathrm{final}}$ as well as all other parameters of the potential fields remain equal. Figure 4.30 displays a successful rescue maneuver of the platform using potential fields after cable failure. After ~ 0.65 s, the platform stopped and stabilized without collision or tipping over. The goal pose, where the potential field's origin is set, is reached with an offset of $[0.0183, 0.0144, 0.0736]^{\mathrm{T}}$ m and $[0.062, -0.0837, -0.001]^{\mathrm{T}}$ rad. The offset remains, as the proposed method does not have an integral control part, which might be part of future work. The progression of $\boldsymbol{f}_D$ show that the method produce continuous desired cable forces within the given force boundaries. Displayed especially in the first 0.1 s after cable failure, the method can adjust the cable forces rapidly to intervene immediately, if necessary. Similar to fig. 4.22, cable 7 gets slack after the event of cable failure and creates a momentary vibration when getting back in tension abruptly. Away from this, $\boldsymbol{f}_{\mathrm{is}}$ show that the cables can mostly be kept under tension. The experiment demonstrates, that the platform can be stabilized and guided back into the workspace at a pose, where the conventional controller fails. This result is similar to the first proposed method, emphasizing the feasibility of the approach.

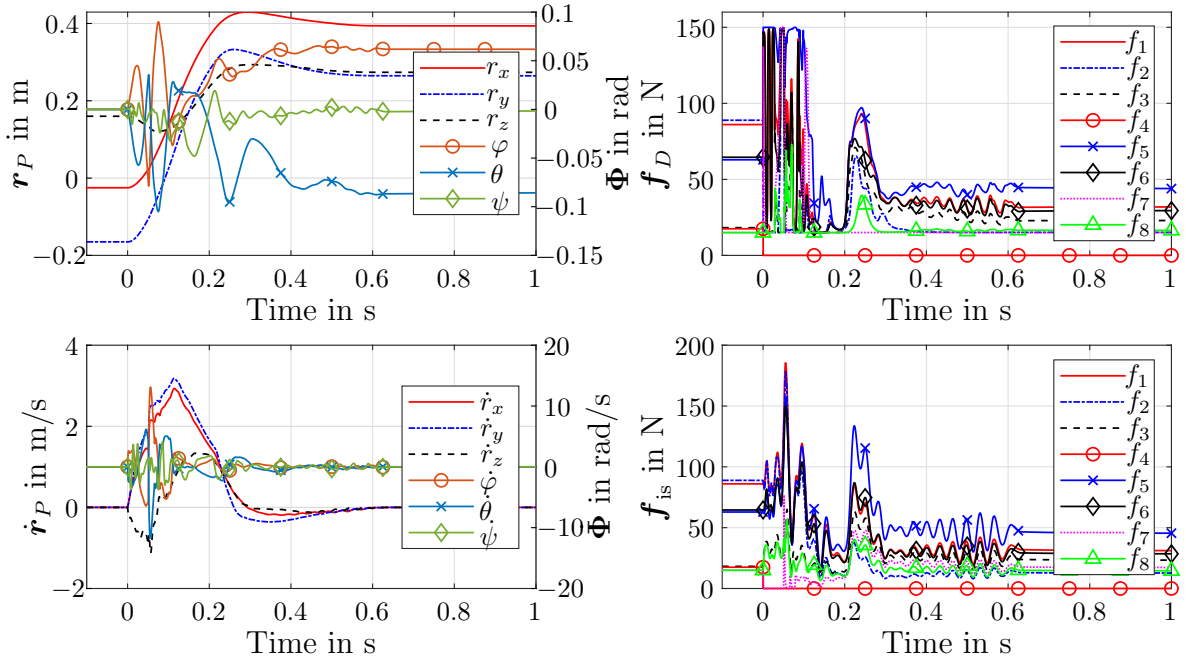

Figure 4.30: Second cable failure scenario of cable 4 outside of the post-failure workspace using Potential Field Method. Time scale aligned with event of cable failure. Top left: Pose of the platform; Top right: Desired cable forces; Bottom left: Velocity of the platform; Bottom right: Actual cable forces.

Potential Field Method in Multiple Scenarios Similar to Section 4.3.5, the method is now examined throughout the whole pre-failure workspace of the SEGESTA prototype to identify its feasibility for different poses. For the failure of cable 4, the potential field is placed at $r_{P,\text{final}} = [0.2, 0.1, 0.4]^{\text{T}}$ m and $\mathbf{\Phi}_{\text{final}} = [0, 0, 0]^{\text{T}}$ rad, inside of the post-failure $\mathcal{SECOW}$. For the failure of cable 2, respectively, it is placed at $r_{P,\text{final}} = [0.175, 0.115, 0.58]^{\text{T}}$ m and $\mathbf{\Phi}_{\text{final}} = [0, 0, -0.15]^{\text{T}}$ rad, which is within the post-failure $\mathcal{SEOW}$, according to fig. 4.7. For both cases, $p = 30$ is set to allow for a stronger intervention of the rescue method, see Section 3.5.2. All other parameters remain equal to fig. 4.30. For the failure of cable 4, 832 out of 1649 simulations are successful, which is an improvement of $\sim$ 14 % compared to fig. 4.19. Still, in comparison to fig. 4.23, the improvement is a little lower. For failure of cable 2 in comparison to fig. 4.19, 628 simulations are successful, which is a greater improvement of $\sim$ 85 %. However, a number of 1020 aborted simulations due to tipping over is comparable to the results of fig. 4.19 (965 of 1649). As fig. 4.31 shows, still regions exist where this emergency strategy fails, similar to fig. 4.23. Nonetheless, the results depict a vast improvement, when using one of the proposed emergency strategies. In comparison between fig. 4.31 and fig. 4.23, different poses can be found where a recovery of the platform is possible after cable failure. It can be assumed that the feasible regions are dependent on a certain parameter setting. Especially for the Potential Field Method, the chosen goal

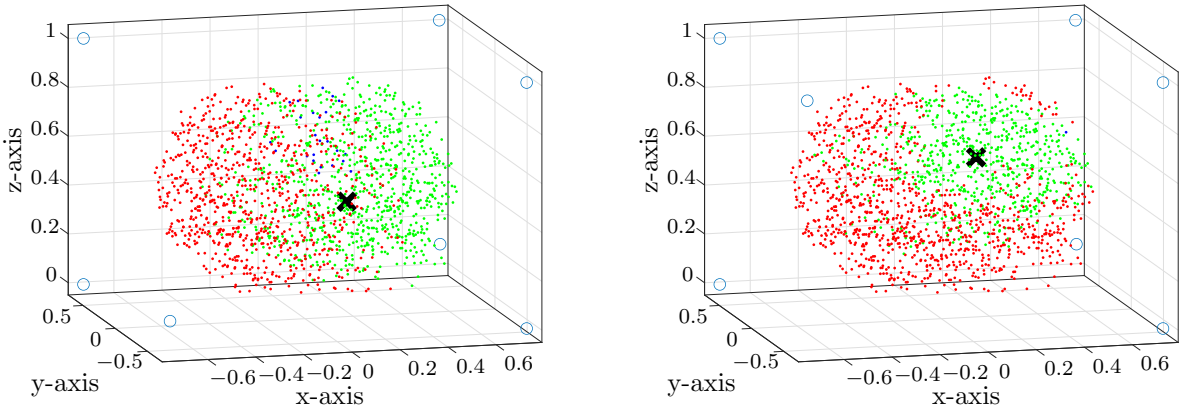

(a) Failure of cable 4 (coming from above). 794 red dots, 0 magenta dots, 24 blue dots, 831 green dots.

(b) Failure of cable 2 (coming from below). 1020 red dots, 0 magenta dots, 1 blue dots, 628 green dots.

Figure 4.31: Multiple cable failure scenarios covering the pre-failure workspace using Potential Field Method, 1649 poses per simulation series. Red dot: Simulation terminated due to tipping over; Magenta dot: Simulation terminated due to platform collision; Blue dot: Platform still moving at end of simulation; Green dot: Simulation successful, platform stopped and stabilized. Pulley positions indicated by blue circles in the corners, pulley of failed cable not displayed. A black cross indicates the origin of the attractive potential field.

pose $\boldsymbol{x}_{P,\text{final}}$ might be essentially determining whether the platform can be recovered from a certain initial pose. Also the remaining parameters might lead to differences in the results. Therefore, parameter studies are carried out in the following, in analogy to Section 4.3.5.

Potential Field Method - Parameter Study of $\boldsymbol{r}_{P,\text{final}}$ First, the chosen goal position $\boldsymbol{r}_{P,\text{final}}$ is varied in four examples while $\boldsymbol{\Phi}_{\text{final}} = [0, 0, 0]^{\text{T}}$ rad. All resulting $\boldsymbol{x}_{P,\text{final}}$ are within the post-failure workspace. The remaining initial conditions are set as in fig. 4.30, cable 4 fails. For all chosen different goal positions, the platform is pulled into the according direction as desired, which is displayed in fig. 4.32. In the examples, the platform is always recovered and stabilized successfully in less than 0.6 s. During the recovery process, the method always delivers forces $\boldsymbol{f}_D$ within the given boundaries. However, the intervention of the method directly after cable failure is very extreme in all cases. The position of $\boldsymbol{r}_{P,\text{final},3}$ seems to be in a region, where the methods provokes a larger compensatory movement to prevent the platform from tipping over. Basically, the method seems to follow the different goal positions. Still, for three of the cases, the chosen goal pose is only reached with a remarkable residual error in pose. This may be due to the setting of $p = 16$. It can be assumed that the desired $\boldsymbol{w}_E$ is not generated in a sufficient approximation by the remaining cables after

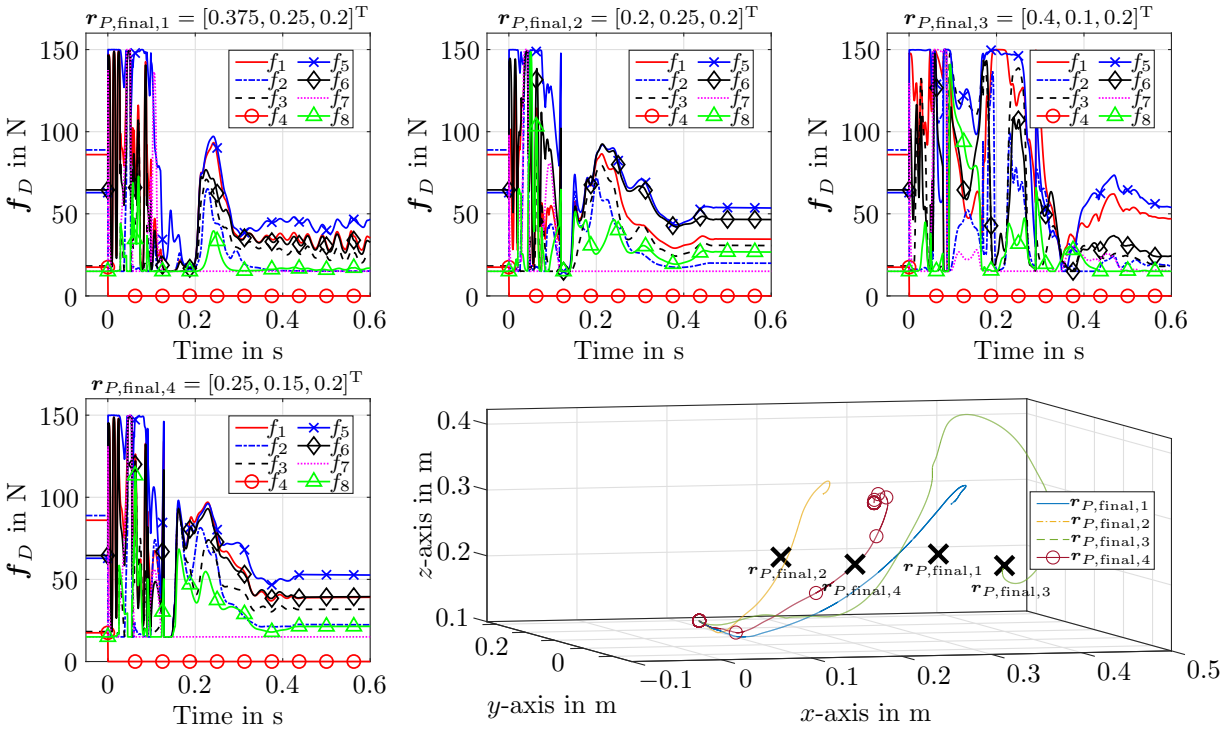

Figure 4.32: Investigation on parameter $\boldsymbol{r}_{P,\text{final}}$ in a cable failure scenario using Potential Field Method, cable 4 fails. Progression of the control variables $\boldsymbol{f}_D$ for different values of $\boldsymbol{r}_{P,\text{final}}$ and spatial representation of the according platform movement (bottom right). Goal positions marked by black crosses.

failure, as the solution is not near enough to the borders of the feasible hypercube $\mathcal{C}$, see Section 3.5.2. Further, the Potential Field Method does not employ an integral control part.

Potential Field Method - Parameter Study of p Consequently, the influence of the parameter p within the Nearest Corner Method is now investigated. The remaining parameters are still chosen as in fig. 4.30. Figure 4.33 displays seven examples for different settings of the parameter p. Based on the progressions of $\boldsymbol{f}_D$, it can be recognized that very small values of p ($1, 2$ and 4 in this example) lead to desired forces that tend very strongly to the middle of $\mathcal{C}$. Following the method's description in Section 3.5.2, this is expected. In the

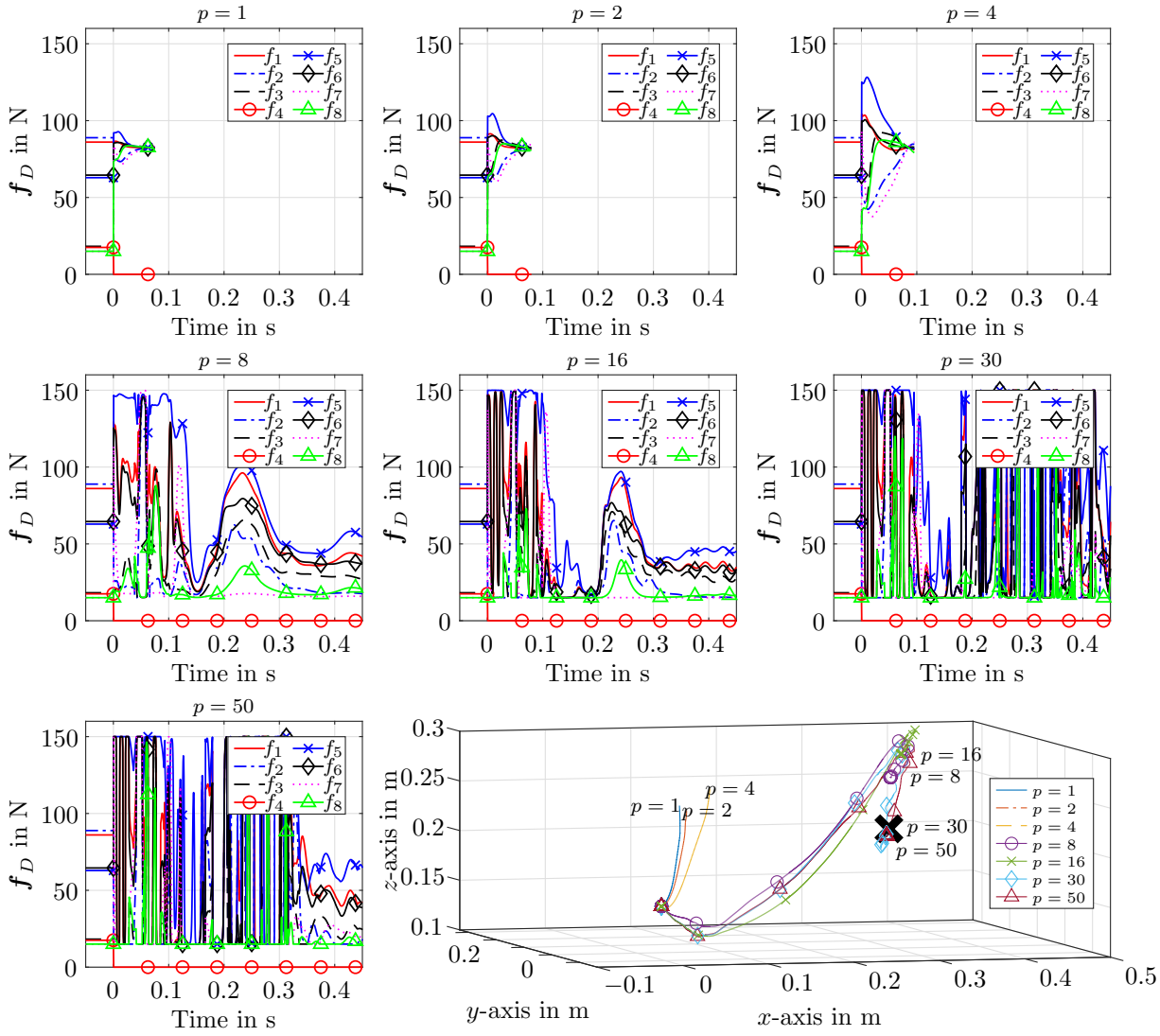

Figure 4.33: Investigation on parameter p in a cable failure scenario using Potential Field Method, cable 4 fails. Progression of the control variables $\boldsymbol{f}_D$ for different values of p and spatial representation of the according platform movement (bottom right). Goal position marked by black cross.

given cases, the platform is not pulled towards the given goal pose (see fig. 4.33, bottom right) and the simulations are prematurely aborted due to tipping over of the platform. With increasing p, the method is able to intervene more strongly. A value of $p = 8$ is shown to be sufficient to rescue the platform in this example. Still, the residual pose error is remarkable. The courses of $\boldsymbol{f}_D$ for $p = 30$ and $p = 50$ show that with larger values of p, the intervention of the method gets more extreme and the desired forces are change rapidly and often in between the given cable force limits. Still, the limits of $f_{\min}$ and $f_{\max}$ are respected at all times. Even thou the method sets the desired forces very aggressively for those values of p, the goal pose is reached with a negligible pose error in these cases. Note that even higher values of p are not displayed here, as they lead to an overshooting that also causes the platform to tip over, which terminates the simulation. Of course, a rapid intervention with extreme cable forces might be necessary after a cable failure. Still, an intervention, as extreme as displayed for $p = 30$ and above, might be troublesome for real hardware in terms of stability, longevity and the prevention of further cable failures. It can be stated that in the event of cable failure, the rescue and stabilization of the platform is more important than reaching a goal pose with minimal offset. Hence, $p = 16$ is set in the following simulations and further investigations on the influence of the remaining parameters on the rescue scenarios are done.

Potential Field Method - Parameter Study of $\boldsymbol{\zeta}_\Phi$ Now it is examined, how the orientation of the platform can be influenced by the parameter $\boldsymbol{\zeta}_\Phi$, which is varied in between $1 \cdot \mathrm{diag}(1, 1, 1)$ and $200 \cdot \mathrm{diag}(1, 1, 1)$. The results are displayed in fig. 4.34. A very small gain ($1 \cdot \mathrm{diag}(1, 1, 1)$) cannot prevent the platform from tipping over, leading to premature termination of the simulation. It can be recognized, that the spatial path is going directly towards the goal pose and nearly no balancing movement is done. The same vice versa accounts for too high gains ($200 \cdot \mathrm{diag}(1, 1, 1)$ in this example), where the platform does not move towards the goal pose at all and enters a region, where tipping over cannot be averted. For a value of $5 \cdot \mathrm{diag}(1, 1, 1)$, the platform tilts strongly about the x- (up to ~ 1 rad) and y-axis (up to ~ -0.9 rad) during the rescue procedure but is stabilized at the end. With rising gain of $\boldsymbol{\zeta}_\Phi$, the tilting during the recovery gets drastically reduced, leading to a maximal rotation of ~ 0.07 rad about the x-axis and ~ -0.1 rad about the y-axis for $\boldsymbol{\zeta}_\Phi = 50 \cdot \mathrm{diag}(1, 1, 1)$. For gains of 10 and 75, $\boldsymbol{\Phi}$ can be brought to approximately $[0, 0, 0]^\mathrm{T}$ rad leading to a negligible pose error towards the end of the simulation. Interestingly, for a gain of 50, the platform gets in a state with a remarkable residual error of $[0.0196, 0.0145, 0.0737]^\mathrm{T}$ m and $[0.0733, -0.101, -0.0017]^\mathrm{T}$ rad at the end of the recovery. For $\boldsymbol{\zeta}_\Phi = 100 \cdot \mathrm{diag}(1, 1, 1)$, the system seems to get marginally stable with an undamped bounded oscillation, mainly rotating about the z-axis. Hence, the best value of $\boldsymbol{\zeta}_\Phi$ presumably is between 50 and below 100 for the scenario and the parameter setting given. Depending on the chosen gain, the

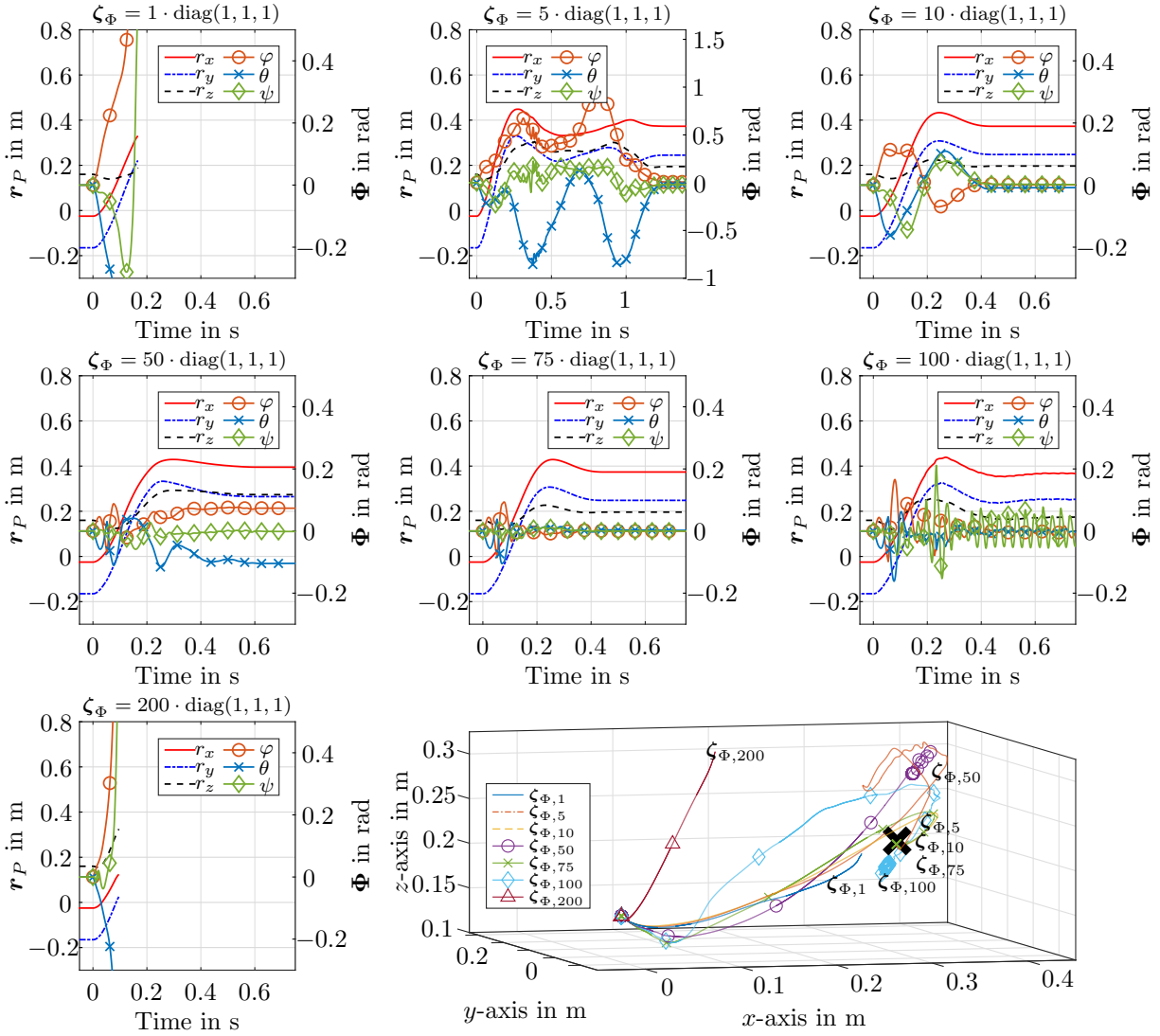

Figure 4.34: Investigation on parameter $\boldsymbol{\zeta}_\Phi$ in a cable failure scenario using Potential Field Method, cable 4 fails. Progression of position $\boldsymbol{r}_P$ and orientation $\boldsymbol{\Phi}$ for different values of $\boldsymbol{\zeta}_\Phi$ and spatial representation of the according platform movement (bottom right). Goal position marked by black cross.

spatial path of the platform towards the goal, while performing balancing movements to prevent tilting, may differ.

Potential Field Method - Parameter Study of $\boldsymbol{D}_1$ The parameters for virtual damping are investigated in the next experiment, exemplary by the means of the Cartesian damping $\boldsymbol{D}_1$. All other parameters remain as set for fig. 4.30. The platforms position $\boldsymbol{r}_P$ and velocity $\dot{\boldsymbol{r}}_P$ as well as the platforms spatial paths for varying values of $\boldsymbol{D}_1$ are displayed in fig. 4.35. For a value of $0.1 \cdot \mathrm{diag}(1,1,1)$, the maximum velocities of $\dot{\boldsymbol{r}}_P$ range from -2 m/s up to 4 m/s, leading to a circular movement around the goal position before reaching it after

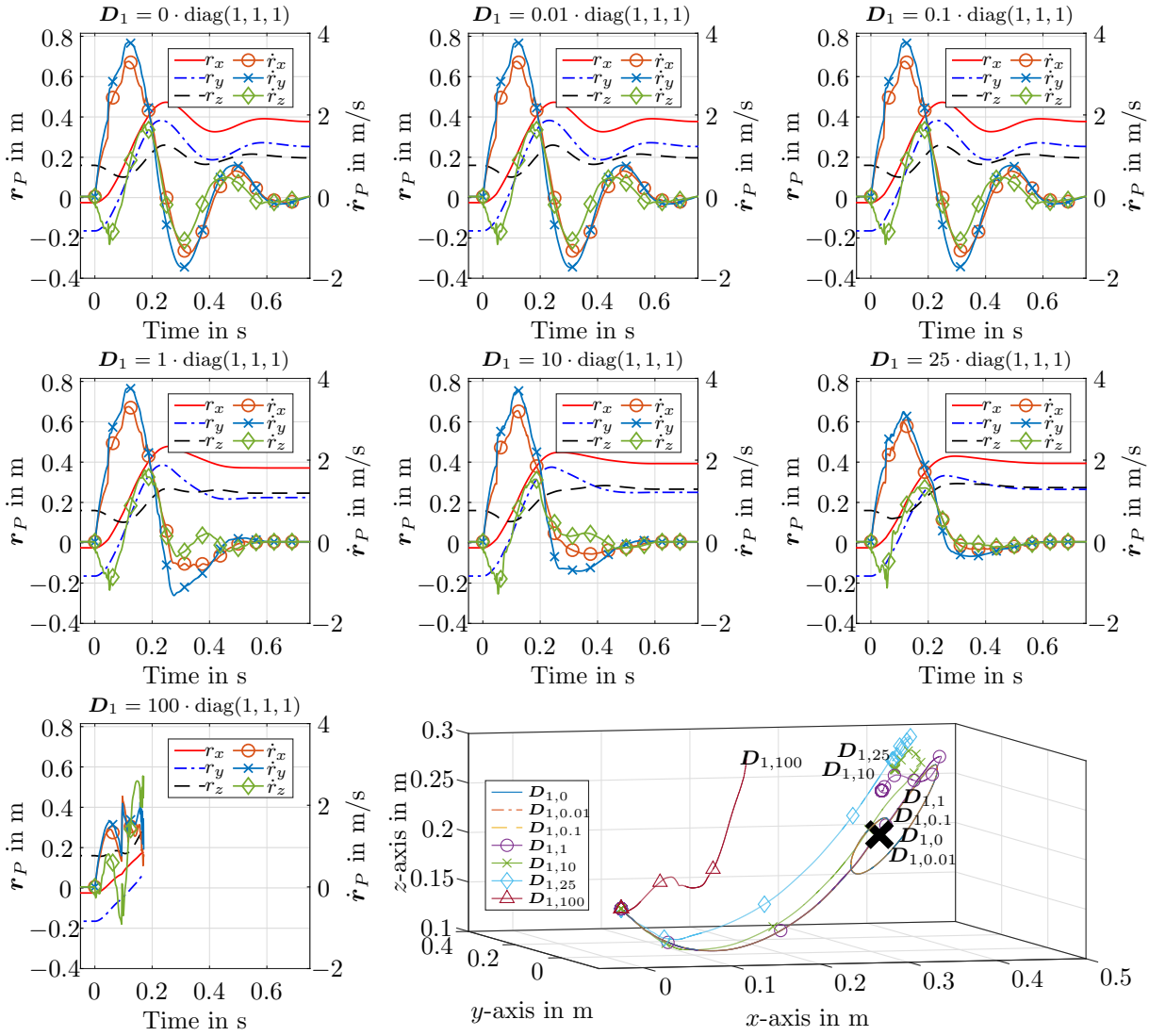

Figure 4.35: Investigation on parameter $\boldsymbol{D}_1$ in a cable failure scenario using Potential Field Method, cable 4 fails. Progression of position $\boldsymbol{r}_P$ and velocity $\dot{\boldsymbol{r}}_P$ for different values of $\boldsymbol{D}_1$ and spatial representation of the according platform movement (bottom right). Goal position marked by black cross.

~ 0.7 s. For lower values of D_1 down to 0, this behavior does not change. Hence, omitting the Cartesian virtual damping does not lead to failure within this scenario. Nevertheless, $\dot{\boldsymbol{r}}_P$ is damped more strongly with increasing values of $\boldsymbol{D}_1$ up to 25, which is expected. Due to the faster stopping of the platform, the residual pose error at the end of the rescue movement increases though. With a too high damping of $\boldsymbol{D}_1 = 100 \cdot \mathrm{diag}(1,1,1)$, the platform does not move properly towards the goal pose, tips over and causes a simulation abortion. This experiment indicates that the Cartesian virtual damping represented by the parameter $\boldsymbol{D}_1$ might be reduced to improve the residual pose error. Nevertheless, a trade off between lower maximum velocities, faster stopping and less residual pose error after the recovery procedure

results. For future work, it might be useful to consider both the potential field's gain and the virtual damping gain simultaneously, since pose and velocity are physically connected.

Potential Field Method - Study of the Nearest Corner Method Lastly, it is examined if and how the switch of the Nearest Corner Method to the conventional chosen method for calculating cable force distributions affects the desired cable forces $\boldsymbol{f}_D$. For this purpose, the examples using $\boldsymbol{D}_1 = 0.1 \cdot \mathrm{diag}(1,1,1)$ and $\boldsymbol{D}_1 = 1 \cdot \mathrm{diag}(1,1,1)$, displayed in fig. 4.35 are chosen for demonstration. Figure 4.36 visualizes the desired cable forces $\boldsymbol{f}_D$ and the time frames where the Nearest Corner Method is active. As depicted in fig. 4.35, the platform reaches the goal pose during the recovery process for $\boldsymbol{D}_1 = 0.1 \cdot \mathrm{diag}(1,1,1)$, while a residual offset remains for $\boldsymbol{D}_1 = 1 \cdot \mathrm{diag}(1,1,1)$. This is reflected within the active force calculation method. In both cases, it is switched to the Nearest Corner Method as soon as the cable failure occurs and the platform gets out of the post-failure workspace. For the first case, the platform enters the $\mathcal{WFW}$ after ~ 0.17 s. From there on, the desired cable forces are produced using the Puncture Method and the platform is stopped after ~ 0.7 s. For the second case ($D_1 = 1 \cdot \mathrm{diag}(1,1,1)$), however, the platform leaves the $\mathcal{WFW}$ again at 0.2 s, switching back to the Nearest Corner Method. Since the platform comes to rest in a static force equilibrium after ~ 0.6 s with a remarkable residual pose error,

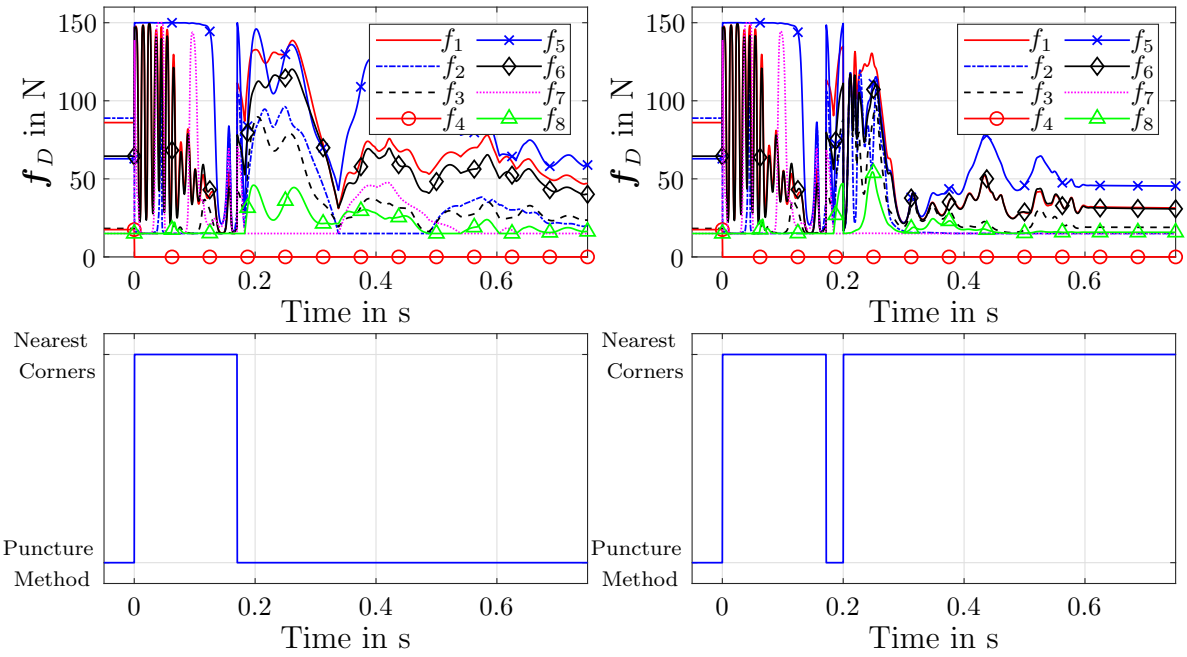

Figure 4.36: Investigation on $\boldsymbol{f}_D$ and switch of the Nearest Corner Method in a cable failure scenario using Potential Field Method, cable 4 fails. Progression of desired cable forces $\boldsymbol{f}_D$ (top) and switch of Nearest Corner Method (bottom). Left side: $\boldsymbol{D}_1 = 0.1 \cdot \mathrm{diag}(1,1,1)$, right side: $\boldsymbol{D}_1 = 1 \cdot \mathrm{diag}(1,1,1)$.

the wrench generated by the potential field remains so high that it is not feasible within the cable force limits, causing the Nearest Corner Method to stay active. Note that this is possible due to the systems frictional forces. However, it can be observed for both cases that the forces $\boldsymbol{f}_D$ rapidly go from one boundary to the other to some extent, when the method switches. The continuity in forces when entering the $\mathcal{WFW}$ is discussed by the author in [Boumann and Bruckmann, 2020b]: Generally, the calculated cable forces are continuous for a continuously moving solution space $\mathcal{S}$. Of course, when $\mathcal{S}$ start or stops to intersect the hypercube $\mathcal{C}$ and thus the robot enters or leaves the $\mathcal{WFW}$, a crucial point occurs. The solution of the Nearest Corner Method converges towards the edges or corners of $\mathcal{C}$ for exponential weights $p \to \infty$. If now the preceding force distribution method for feasibility checking covers the whole workspace, both methods should provide an equal cable force distribution at the moment of intersection. Consequently, the transition in between both methods is continuous in this case. For the experiment at hand and especially for application in a real system, a weight of ∞ is neither useful nor feasible. Thus, small discontinuities may occur. As the observed effect is not minor, the main cause might attributed to the usage of the Puncture Method. This method does not offer a full workspace coverage as stated in [Pott, 2018]. Hence, the method switch might lead to discontinuous cable forces distributions when the platform already entered the $\mathcal{WFW}$. For future work, methods covering the full workspace such as the Barycentric Method [Mikelsons et al., 2008], the Improved Closed Form [Pott, 2014] or the Improved Puncture Method [Müller et al., 2015] should be employed. Nevertheless, the rescue scenarios work using the proposed methods despite of the identified discontinuity and a successful rescue scenario on a real prototype is presented by the author in [Boumann et al., 2023], using the same methods.

Conclusion on the Potential Field Method In summary, the emergency strategy using potential fields and the Nearest Corner Method is shown to work within the proposed simulation of the SEGESTA prototype. The experiments demonstrate that the given parameters influence the method's (and thus the platform's) behavior as expected during a rescue movement after cable failure. Using the potential field's scaling factors $\boldsymbol{\zeta}_r$ and $\boldsymbol{\zeta}_\Phi$ and the virtual damping $\boldsymbol{D}_1$, $\boldsymbol{D}_2$, the resulting wrench at the platform can be tuned for desired platform motion. Moreover, the exponential weight p can be adjusted for a more rapid intervention of the method or for cable forces $\boldsymbol{f}_D$ closer to $\boldsymbol{f}^*_{\min} + (\boldsymbol{f}^*_{\max} - \boldsymbol{f}^*_{\min})/2$. In comparison to the method presented in Section 4.3.5, this emergency strategy offers more parameters to adjust the solution, thus it is more complex to handle. Note that no investigation on the usage of repulsive fields or the parameter d_b has been done here. In comparison to a scenario without damage avoidance strategy using a conventional controller even with failure detection, the method based on potential fields leads to a successful rescue in ~ 14 % more cases for failure

of cable 4 and $\sim$ 85 % more cases for failure of cable 2. However, the improvement is not as high compared to the results using the Kinetic Energy Minimization Method. Especially towards the pre-failure workspace borders, tipping over of the platform after cable failure cannot be prevented in most of the poses, which might be due to the method's parameter set and the robot's parameters in combination. This effect has already been examined in the previous section. As the parameter studies show, finding an optimal set of parameters is crucial. Investigation on simplification and automation of proficient parameter setting is part of future work. The continuity of the Nearest Corner Method when entering the $\mathcal{WFW}$ must be observed when conducting experiments on real hardware. Ensuring continuity for all cases is part of future work. Further conceivable approaches to future improvement of the method might be the usage of repulsive fields for undesired high platform angles or the utilization of quadratic and conic potentials to control the platform orientation. An additional approach might be the employment of different parameter sets for different poses when the cable fails. Bringing together the results from the previous section and this one, it can be recognized that for the given scenario using a simulation of the SEGESTA prototype, initial poses within the pre-failure workspace exist where both proposed methods fail to recover the platform and avoid tipping over. A further approach in the event of a cable failure might be the usage of motor brakes for the remaining drive units. Hence, in the following it is briefly investigated in simulation if motor brakes can be used with sufficient results in the event of cable failure.

4.3.7 Motor Brakes

Intuitively, a highly reasonable intervention in the event of a cable failure might be the usage of motor brakes on the drive units connected with the remaining cables. It is to note that some CDPR prototypes are missing operational brakes, which includes the SEGESTA prototype. Nonetheless, it is assumed that the simulated prototype has operational brakes, which can set still the drive units instantaneously. This is obtained within simulation by simply freezing the current winch angles and setting the winch velocities to zero at the event of cable failure. As stated in Chapter 3, the platform will necessarily start to move after a cable failure if it gets outside of the post-failure workspace, even if the brakes are engaged. This is verified in the following, studying the subsequent motion.

Using Motor Brakes In- and Outside of the Post-Failure Workspace The first experiment displayed in fig. 4.37 compares the platform movement and the occurring cable forces for two initial poses after failure of cable 4 using motor brakes. One of the poses is outside of the post-failure workspace ($[-0.385, -0.025, 0.046]^{\mathrm{T}}$ m and $[0, 0, 0]^{\mathrm{T}}$ rad), while the other one is within the post-failure workspace ($[0.375, 0.25, 0.2]^{\mathrm{T}}$ m and $[0, 0, 0]^{\mathrm{T}}$ rad).

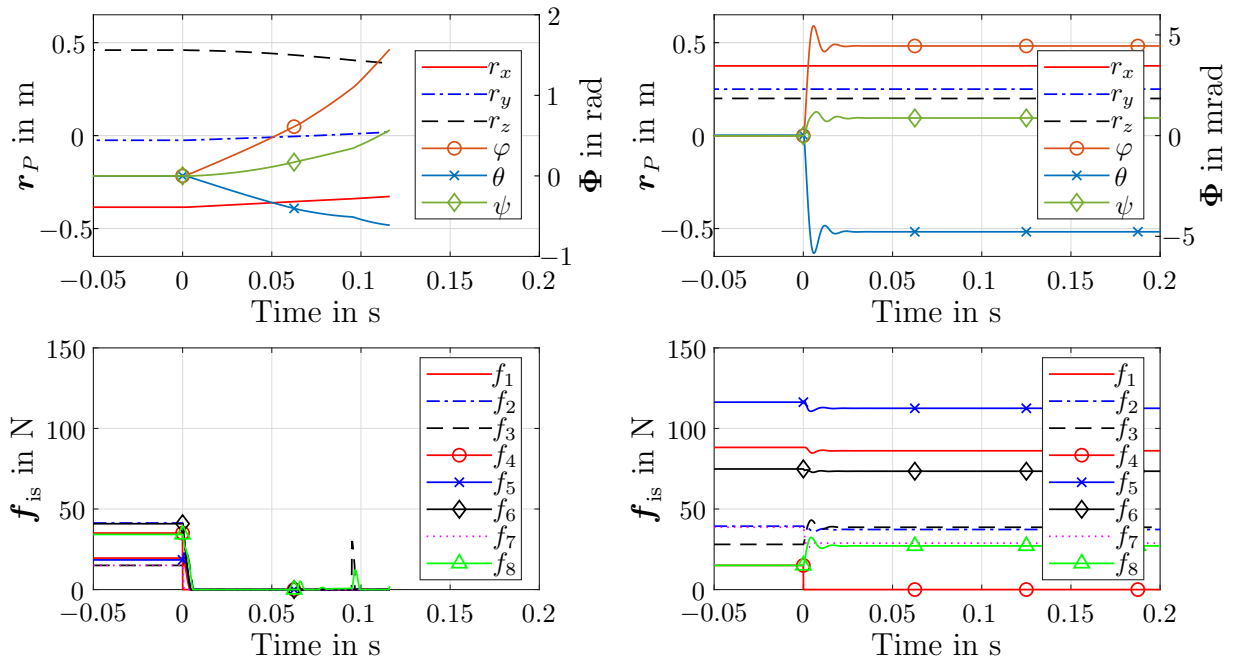

Figure 4.37: Two cable failure scenarios of cable 4 using motor brakes. Left: outside of the post-failure workspace; Right: inside of the post-failure workspace. Time scale aligned with event of cable failure. Top: Poses of the platform; Bottom: Actual cable forces.

As expected, the platform starts to move outside of the post-failure workspace, despite using brakes for the remaining cables. It starts to tilt, the cables get slack and the simulation is terminated after 0.12 s. Inside of the post-failure workspace, the platform tilts only negligible below 5 mrad and is properly constrained by the remaining braked cables. The cable forces only change minor. This behavior within the post-failure workspace is also as expected. It is to note that the results are idealized, as an operational brake has delay times in real hardware.

Using Motor Brakes in Multiple Scenarios Consequently, the behavior when using brakes is now investigated throughout the whole pre-failure workspace for the failure of cable 4 and 2. The results are depicted in fig. 4.38. For the failure of cable 4, in 842 out of 1649 simulations the platform can be stabilized using brakes. This result is superior to the usage of the conventional APD controller with failure detection, comparable to the Potential Field Method and inferior to the Kinetic Energy Minimization Method. Thus, braking seems to be a reasonable option if no emergency strategy is employed. For the failure of cable 2, the platform is only stabilized in 277 of the simulations. This result is inferior to both emergency strategies and the conventional controller with failure detection. However, the platform has residual movement in a significant number of 1096 simulations. It is to note that a vast amount of the dissipation in simulation is calculated within the drive units since

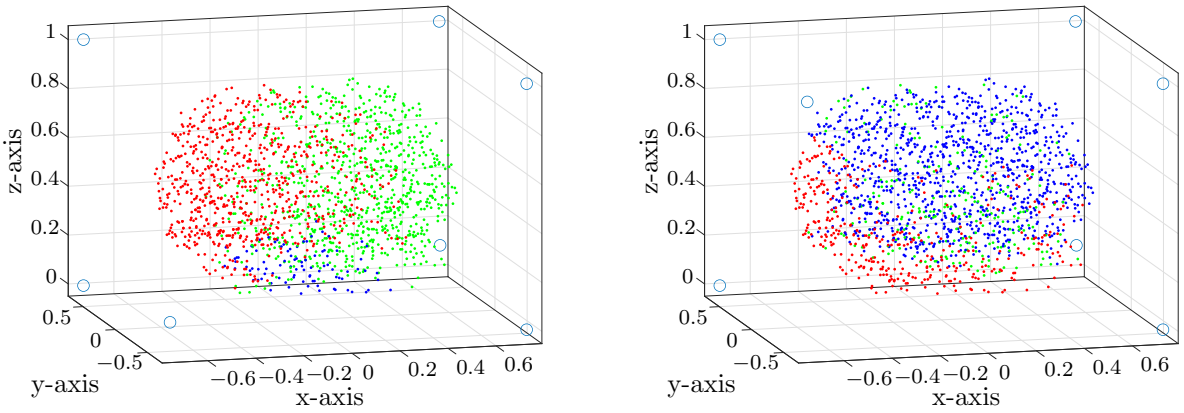

(a) Failure of cable 4 (coming from above). 716 red dots, 0 magenta dots, 91 blue dots, 842 green dots.

(b) Failure of cable 2 (coming from below). 276 red dots, 0 magenta dots, 1096 blue dots, 277 green dots.

Figure 4.38: Multiple cable failure scenarios covering the pre-failure workspace using motor brakes, 1649 poses per simulation series. Red dot: Simulation terminated due to tipping over; Magenta dot: Simulation terminated due to platform collision; Blue dot: Platform still moving at end of simulation; Green dot: Simulation successful, platform stopped and stabilized. Pulley positions indicated by blue circles in the corners.

pulley friction is not explicitly modeled here, which is part of future work. Hence, if the drive units are braked, these effects are omitted, possibly leading to longer residual movement of the platform. It can be assumed that a lot of the 1096 cases would be stopped more quickly and possibly stabilized, in reality. With this fact in mind, braking the drive units after cable failure seems like a very sound option. Nonetheless, it is inferior to the usage of an emergency strategy in several cases, especially outside of the post-failure workspace for failure of cable 4. Finally, it seems to be impossible to recover the platform after cable failure at some poses, particularly towards the workspace borders.

4.4 Conclusion and Discussion

Within this chapter, simulative studies of damage avoidance strategies have successfully been carried out. First, the SEGESTA prototype was introduced, serving as a basis to set up a simulation environment. Design choices have been made and justified with respect to the level of detail, the modeled and the neglected effects in simulation. A simulation structure based on work of the author has been introduced featuring models of a controller, drive units, cables and the CDPR platform. Using measurements on real hardware, the cables and the drive units were parametrized. For the SEGESTA prototype, the pre- and post-failure $\mathcal{SECOW}$ and $\mathcal{SEOW}$ for failure of one upper cable (number 4) and one lower cable (number

2) were calculated and displayed. An example trajectory through the pre-failure workspace was demonstrated to verify physically reasonable behavior of the simulation structure. To assess the simulations behavior after cable failure, criteria have been formulated to characterize a failed simulation, e.g. due to tipping over of the platform and vice versa for successful simulations. The conventionally used APD controller was shown to massively malfunction after cable failure. Assuming a detection of the failure, the APD controller can stabilize the platform after cable break in various cases, mainly within the post-failure workspace. Both emergency strategies as described in Chapter 3 were integrated and successfully tested. They both show a remarkable improvement in terms of platform recovery with regards to the conventional controller. The Kinetic Energy Minimization Method can recover the platform after failure of cable 2 from ~ 204 % more poses than the conventional controller with failure detection. For the Potential Field Method, the results shows slightly less improvement. This could be due to the more diverse setting options and the greater amount of the parameters. Most of the adjustable parameters in both methods have been exemplarily examined to demonstrate their desired effect and to define useful ranges for their values. However, carrying out detailed stability considerations of the proposed methods is part of future work. For both methods, potentials for further improvement have been emphasized. This accounts in particular for finding optimal parameter sets. Moreover, the continuity in cable forces when entering the $\mathcal{WFW}$ while using the Nearest Corner Method within the Potential Field Method might be an open issue within the implementation. Besides the vast improvement demonstrated by the emergency strategies, it was also displayed that the platform can not be prevented from tipping over with the given methods at some poses, particularly towards the workspace boundaries. Assuming ideal braking of the remaining drive units, it was also demonstrated that braking is a very reasonable option in case of cable failure, even thou it is inferior to the proposed emergency strategies in several cases.

Finally, it is to note that the results from this section are mostly limited to the investigated SEGESTA prototype. Moreover, the results can only be as realistic as the simulation allows with the given assumptions and simplifications. Rather than reproducing reality exactly, the simulation was intended to behave physically meaningful in order to give indication on the functionality of the emergency strategies. As this has been shown to the author's best knowledge, this section is considered as successfully completed. The upcoming chapter will provide insights on the accuracy of the real world representation. Accordingly, the logical next step is to implement the emergency strategies within a prototype and test them in a real world environment, which is presented in the next section. Ultimately, it is also conceivable to use the proposed emergency strategies for regular CDPR control.

Chapter 5

Validation on the SEGESTA Prototype

Within this chapter, the author's damage avoidance strategies after cable failure are validated on real hardware using the SEGESTA prototype. In order to enable the experiments on the prototype, some preparatory work has to be implemented beforehand: Based on a thorough requirement analysis, a decoupling device is developed, integrated and tested to mimic the failure of a cable at the platform. As some robot parameters are changed due to the device and safety limitations, the pre- and post-failure workspaces are updated. If a failure occurs, it needs to be detected to use any emergency strategy. Thus, an easy and fast failure detection algorithm, based on the available measurements, is introduced and demonstrated. The emergency strategies are implemented considering real-time constraints. Moreover, the applied forward kinematic algorithm to estimate pose and velocity after the cable failure is described, which serves as an input for the proposed emergency strategies. Finally, experiments on the prototype are conducted and compared to the simulation results.

5.1 Test Enabling and Preparation

Based upon the simulative experiments shown in Section 4.3, the logical next step to validate the proposed damage avoidance strategies are tests on real hardware. The SEGESTA prototype is particular suitable for algorithm tests and sandbox experiments due to its size and

platform mass. Therefore, potential damage that could be caused by malfunction or while experiments is comparably lower than for other prototypes. Moreover, it can be operated, troubleshooted and monitored by one single person. Nonetheless, it offers all the required hardware components and a versatile applicability as already discussed in Section 4.1. In order to increase operator safety, the system is encased by polycarbonate sheets[1]. They prevent objects like the end effector from exiting the robot frame (e.g. after a cable failure experiment), to avoid harm to the operator. Further, the operator is inhibited to reach into the robots workspace while the system is in operation. Summing up, the SEGESTA prototype is the ideal choice for first tests on real hardware of the damage avoidance strategies proposed by the author. First results on prototype tests of the author's strategies are published in [Boumann et al., 2023].

5.1.1 Development of a Cable Decoupling Device

In order to investigate the CDPR behavior after a cable failure, a method or device is necessary to evoke or mimic this particular situation. To unwind cable from the motor in order to loose tension and emulate a cable failure is one option [Boschetti et al., 2021]. Still, the unwound and loose cable might have an influence on the robot platform. While performing a damage avoidance maneuver, the loose cable might also get stuck at some part of the robot. For these reasons, this approach is neglected.

Instead, a device to decouple a cable from the end effector of the SEGESTA prototype is developed and integrated, as demonstrated in underlying work of the author [Boumann et al., 2023]. When developing a mechatronic system in general, the German norm VDI 2206 [VDI/VDE, 2021] can serve as an excellent guideline in the development process, ensuring a sufficient management and implementation of the requirements. The requirements for the device can be found as follows: First and foremost, the maximum cable forces of SEGESTA (150 N) need to be withstood by the device without failing. This is required to prevent the system from undesired failures. Additionally, the device needs to function with minimal tension on the corresponding cable (15 N) when triggered. After the decoupling, the mechanical connection between the corresponding cable and the end effector needs to be completely dissolved to ensure that it is no longer influenced by the decoupled cable. In order to investigate on failure of an upper and a lower cable, see Section 3.2, the device generally needs to allow for a decoupling of both. A short modification time to fulfill one or the other is conceivable. Lastly, it is also required, that the device is actuated and can be triggered automatically, so that no possibly harmful manual intervention within the workspace is needed.

[1]Polycarbonates are characterized by high stiffness, hardness and impact resistance. Additionally, they are good insulators against electrical voltage [Caseri, 2009].

Subsequently, demands can be placed on the device, which are not essential but favorable. Since it can be assumed that a lot of tests need to be done with the device, several demands result: The end effector with the decoupling device mounted should still fit into its set-down position. Otherwise, an initial calibration of the robot and thus its proper operation is not possible. If necessary, minor adjustments can be done at the set-down position. Establishing the connection between device and end effector as well as between cable and device should be easy and quick, in order to keep the setup time low. When decoupling the cable, it should ideally not be damaged. To maintain the given dynamic capability of the robot, the device should be as lightweight as possible. Moreover, the lower the masses of the platform are, the lower the risk of hazardous collisions is in case of failed experiments. Nevertheless, an increased mass and inertia may also be beneficial to avoid tipping over of the platform, see fig. 4.27.

No.	Type	Specification
1	$\mathcal{R}$	Maximum cable force of $f_{\max} = 150$ N must be withstood.
2	$\mathcal{R}$	Functionality with minimal tension $f_{\min} = 15$ N must be given.
3	$\mathcal{R}$	Any mechanical connection between the decoupled cable and the end effector must be resolved after decoupling.
4	$\mathcal{R}$	Device needs to decouple either a lower or an upper cable at the end effector.
5	$\mathcal{R}$	The decoupling needs to be actuated and triggered by a signal.
6	$\mathcal{D}$	The end effector with decoupling device should fit into its set-down position.
7	$\mathcal{D}$	The device should be connectable easily and quickly to the end effector.
8	$\mathcal{D}$	The cable to be decoupled should be connectable easily and quickly.
9	$\mathcal{D}$	The cable should not be damaged while decoupling.
10	$\mathcal{D}$	The Device should be as lightweight as possible.
11	$\mathcal{D}$	Ideally no mass should stay at the cable end when it gets decoupled.
12	$\mathcal{D}$	The device should fit in the outer end effector measurements ($8 \times 7.5 \times 7$ cm).
13	$\mathcal{D}$	The end effector should be altered as little as possible. This counts especially for the position of the cable attachment points $\boldsymbol{P}$.
14	$\mathcal{D}$	The decoupling principle should be easy to upscale for larger prototypes.
15	$\mathcal{D}$	Multiple cables can be decoupled at once.
16	$\mathcal{D}$	The trigger signal should be integrated into the existing `BECKHOFF` PLC.
17	$\mathcal{D}$	A feedback (open/closed) of the decoupling device is given back.
18	$\mathcal{D}$	The Device should be easy to repair.
19	$\mathcal{D}$	The Device should have low maintenance.

Table 5.1: Requirements ($\mathcal{R}$) and Demands ($\mathcal{D}$) for a cable decoupling device for the SEGESTA prototype.

At the same time, ideally no mass should be fixed to the cable end where it is disconnected, to avoid harm from lashing. To obtain a preferably homogeneous inertia tensor and to keep a symmetrical end effector design, the decoupling device should be placed inside the outer measurements of SEGESTA's platform. Those are roughly $8 \times 7.5 \times 7$ cm. Furthermore, ideally no or at least only minor (geometrical) modifications should be done at the end effector. This applies in particular for the coordinates of the cable attachment points in order to maintain the robot design and the corresponding properties (e.g. workspace shape, dynamic capability, et cetera). In future, further testings of damage avoidance strategies after cable failure using larger prototypes are conceivable. Therefore, it would be highly reasonable, if the decoupling principle is easy to upscale. Also the possibility of decoupling multiple cables would be a useful feature. Including the trigger signal into the consisting `BECKHOFF` PLC would allow for ease of use as well as a feedback of the decoupling device's state. If, however, the decoupling device has a malfunction, it should be easy to repair and moreover, it should have low maintenance. The requirements ($\mathcal{R}$) and demands ($\mathcal{D}$) for the device are collected in table 5.1.

Based upon the raised requirements and demands, the following solution as depicted in fig. 5.1 is developed: The main part of the decoupling device consists of an electromagnetic lock, which can be bought off the shelf. The lock, as depicted in fig. 5.1a, is actuated using a linear solenoid actuator with a voltage of 12 V DC and a current of 2 A. When triggered, the solenoid contracts and rotates the first hook, enabling the second hook to move. The second hook carries the cable to be decoupled, which is attached using a loop, tied with a bowline, at the cable end. In closed state, the loop cannot slip of the hook. As soon as the first hook is opened, the torsion spring attached to the second hook forces it to tilt, enabling the cable loop to slip of, as long as it is at least minimally tensed. Afterwards, the cable can slide along a rounded deflecting guidance until it exits the end effector and is fully decoupled. The status of the lock (open/closed) can be fed back using the installed limit switch. After an experiment, the cable can be reattached easily and quickly by placing the loop back on the hook and closing the lock by pushing against the hook, e.g. with a metal rod. The lock has a size of $73 \times 66 \times 13$ mm, which is within the outer diameter of SEGESTA's platform. It can be attached to either the base or the top plate of the end effector using three M4 mounting holes. For that purpose, both plates are slightly enlarged and newly manufactured. The set-down position also requires marginal adjustment to fit the platform. The lock attached to the bottom of the platform is depicted in fig. 5.1b. The solenoid is powered by an external supply, controlled by an optocoupler that galvanically isolates the `BECKHOFF` PLC. The optocoupler is triggered from the PLC using an analog output clamp of the type EL 4031. Moreover, the lock's status feedback is recorded using an analog input clamp of the the type EL 3062.

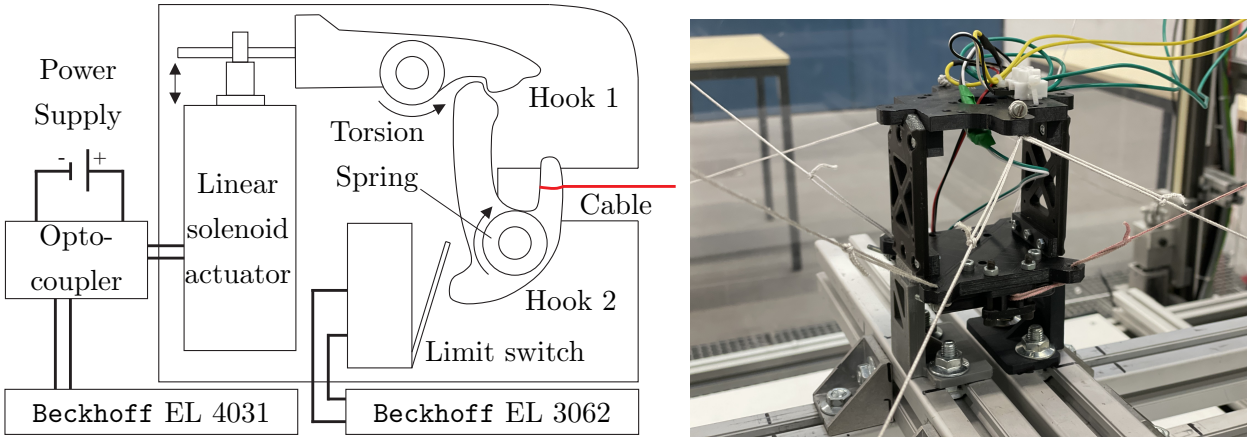

(a) Principal illustration of the decoupling device. (b) Device mounted in bottom position.

Figure 5.1: A cable decoupling device to mimic cable failure at the SEGESTA prototype.

As the end effector is marginally adjusted, the parameter changes yield: $m_{P,N} = 0.262$ kg, $\boldsymbol{P}_N = \begin{bmatrix} 45 & -45 & 35 & -35 & 45 & -45 & 35 & -35 \\ 0 & 0 & -35 & -35 & 0 & 0 & 35 & 35 \\ 35 & 35 & -35 & -35 & 35 & 35 & -35 & -35 \end{bmatrix}$ mm, ${}_P\boldsymbol{r}_{S,B} = [-4.4, 3.3, -30.5]^{\mathrm{T}}$ mm, and ${}^P\boldsymbol{\Theta}_{S,B} = \begin{bmatrix} 6.13 & 0.06 & -0.56 \\ 0.06 & 6.05 & 0.41 \\ -0.56 & 0.41 & 2.42 \end{bmatrix} \cdot 10^{-4}$ kg m^2, for the decoupling device in the bottom position. For the device in top position it yields: ${}_P\boldsymbol{r}_{S,T} = [-4.4, 3.3, 31.3]^{\mathrm{T}}$ mm, and ${}^P\boldsymbol{\Theta}_{S,T} = \begin{bmatrix} 6.13 & 0.06 & 0.56 \\ 0.06 & 6.05 & -0.41 \\ 0.56 & -0.41 & 2.42 \end{bmatrix} \cdot 10^{-4}$ kg m^2. As the changed parameter alter the robot's workspace, it is determined again in Section 5.1.2.

Based on the developed decoupling device, the (theoretical) fulfillment of the requirements and demands can be analyzed. Its functionality is demonstrated within the experiments further on, as well as in [Boumann et al., 2023]. Based on the manufacturer information, the lock can withstand a pulling force of 150 kg, which surpasses $f_{\max}$ roughly by factor ten. All other load carrying additional parts are manufactured out of the same material as the previous end effector, which has proven to withstand $f_{\max}$ for years. In the practical tests further on, no damage is observed within the material. Thus, the first requirement is considered fulfilled. As the ejection of the mechanical lock is supported by a spring, the cable is practically thrown out. This mostly works seamlessly in tests, even with $f_{\min} = 5$ N [Boumann et al., 2023], fulfilling the second requirement. However, as depicted e.g. in fig. 5.6, the cable might get stuck at the hook in rare cases. Improvement is part of future activities. Due to the provided cable guidance with rounded corners, further snagging of the cable is avoided and not emerged within the experiments. Therefore, also the third requirement is considered fulfilled. As the decoupling device can be mounted in a lower and an upper position on the end effector, including the possibility of taking up different cables, the fourth requirement is met. As described within the solution development, the lock is actuated using an electromagnet, triggered by a signal from the BECKHOFF PLC. Thus, requirement five and demand 16 are met. Since the lock fits the outer measures of the end

effector, it can still be placed properly within its set-down position, even thou both have been changed marginally, meeting demand six, twelve and thirteen. With three screws, the lock can be connected and disconnected very fast and easy in both mounting positions, thus demand seven is fulfilled. As described above, the cable can quickly be reattached by manually placing the loop back on the hook and closing the lock within seconds, thus demand eight is also met, enabling fast and efficient test series. By using a loop at the cable end, tied with a bowline, and rounded cable guidance, demand nine is fulfilled and wear at the cable is minimized. Moreover, the corresponding winch is stopped as soon as the cable failure is detected, to ensure the cable end does not snag within the robot's frame. Comparing m_P and $m_{P,N}$, it is obvious, that the platform mass is nearly doubled. Still, the absolute increase in mass is very low compared to $f_{\max}$. Thus, demand ten is not met to all extends. Nonetheless, demand eleven is fulfilled as no additional mass remains at the cable end, inhibiting lashing of the cable end after decoupling. The very simple operating principle consists mainly of the linear solenoid actuator, hooks, torsion springs and a cable guidance. This allows for effective scaling of the device, enables tests for larger prototypes and fulfills demand 14. The single components are very common and thus available in larger size and for higher forces. However, the device will most likely need to be self-built instead of using an off the shelf lock. Decoupling multiple cables at once is possible in general as, e.g., two cables can be fitted through the cable guidance and attached at the hook simultaneously. Thus, demand 15 can be considered as met. However, as multiple cable failure is not considered within this work, this aligns with future activities. As the lock's status feedback can be recorded and fed into the PLC using an analog input terminal, demand 17 is fulfilled, see fig. 5.3. The device consists mainly of the electromagnetical lock, which is an off the shelf component and can be replaced easily. This also accounts for standard parts like nuts and screws. The remaining parts are manufactured using 3D-printing. Thus, all parts of the device are easy and fast to replace, meeting demand 18. Finally, the number of used parts is very low. This accounts in particular for parts in motion. Moreover, the manufacturer states a mechanical life time of $> 10^6$ cycles. Therefore, a high level of maintenance is not expected and demand 19 is also fulfilled. Summing up, all requirements and mostly all demands are met, enabling series of cable failure and recovery tests at the SEGESTA prototype.

5.1.2 Workspace with Parameter Adjustment

As can be seen from the previous section, the parameters of the end effector carrying the decoupling device change slightly. Furthermore, the parameter set is dependent on the device's mounting position. Moreover, in the simulative studies, displayed for example in fig. 4.14 and fig. 4.18, it can be observed that high force peaks in $\boldsymbol{f}_D$ reaching $f_{\max}$ might cause even higher cable forces $\boldsymbol{f}_{\text{is}}$, exceeding the boundary $f_{\max}$. This may possibly lead to

further failure on the prototype hardware. Thus, for the cable failure experiments within this work, the maximum cable force is precautionary restricted to 75 N for reasons of safety. With the adjusted parameters, the pre- and post-failure workspaces are determined once again, analog to Section 4.3.1. Note that knowledge on the workspace is crucial for setting initial poses as well as goal positions for the emergency strategies.

First, the situation with the decoupling device mounted at the platform's bottom is considered. Figure 5.2a and fig. 5.2b display the workspace pre- and post-failure of cable 4. After failure of cable 4, the workspace is nearly halved, similar to Section 4.3.1. Note that for the failure of cable 2, the $\mathcal{SECOW}$ is also empty, thus it is not displayed. To determine the $\mathcal{SECOW}$, the same grid $\mathcal{G}_{\mathcal{SECOW}}$ as used in Section 4.3.1 is employed. Comparing fig. 5.2a with fig. 4.5, it can be recognized that the pre-failure workspace is already diminished. Only $\sim$ 46 % of the previous workspace remains due to the parameter adjustments. As mass and inertia of the platform are comparably low with regard to $f_{\min}$, the main cause of the workspace reduction is presumably within the lowered maximum cable force. Of course, a static force equilibrium is still possible at more poses, if the platform may be slightly tilted. In analogy to Section 4.3.1, the $\mathcal{SEOW}$ for failure of both the cables 4 (from above) and 2 (from below) is shown in figs. 5.2c to 5.2f. Here, the same grid $\mathcal{G}_{\mathcal{SEOW}}$ is employed as well. With the considered platform rotation about all axes, the post-failure workspace is also noticeably extended here. As stated above, the influence of the decoupling device's weight and inertia is minor with regards to the cable forces. As a consequence, the feasible poses within the pre- and post-failure workspace turn out to be alike for the given grids, if the decoupling device is mounted at the top position. Therefore, they are not displayed separately here.

Summing up, the evaluation of the pre- and post-failure workspace after parameter adjustment provides a basis for the upcoming experiments. Primarily due to the reduced maximum cable force, the workspace volume is decreased. Still, the results demonstrate that a static force equilibrium and thus a possible safe state after cable failure exist for a variety of poses. Subsequently, suitable initial and goal poses for the upcoming cable failure experiments can be determined. It is to be expected, that platform tilting is inevitably, especially for the failure of cable 2, since the $\mathcal{SECOW}$ is empty in this case. However, as long as the platform tilting does not exceed certain limit, it can be considered non-critical.

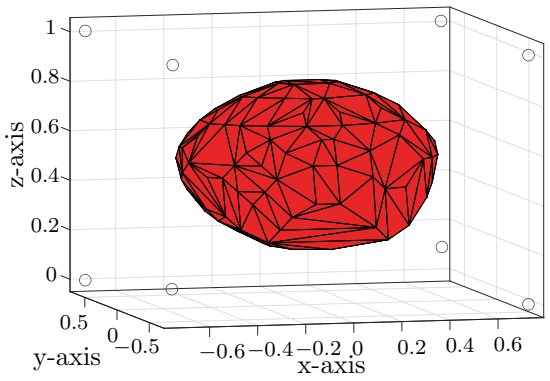

(a) Pre-failure $\mathcal{SECOW}$, all cables in operation. View from front.

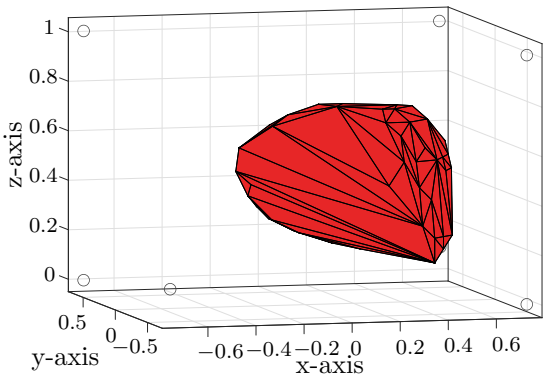

(b) $\mathcal{SECOW}$ post-failure of cable 4 (from above), view from front.

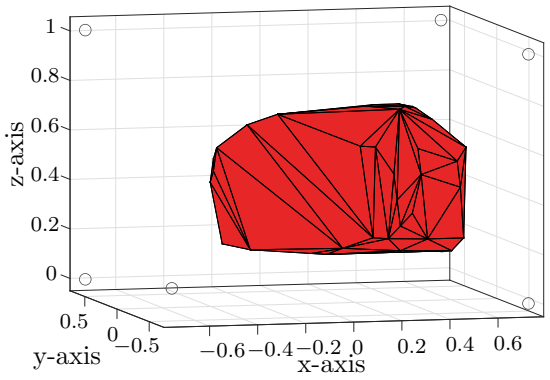

(c) $\mathcal{SEOW}$ post-failure of cable 4 (from above), view from front.

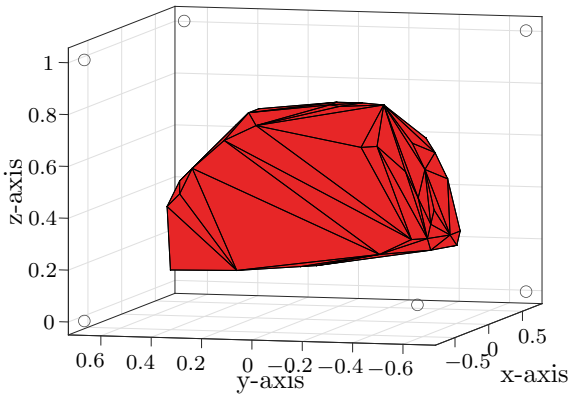

(d) $\mathcal{SEOW}$ post-failure of cable 4 (from above), view from side.

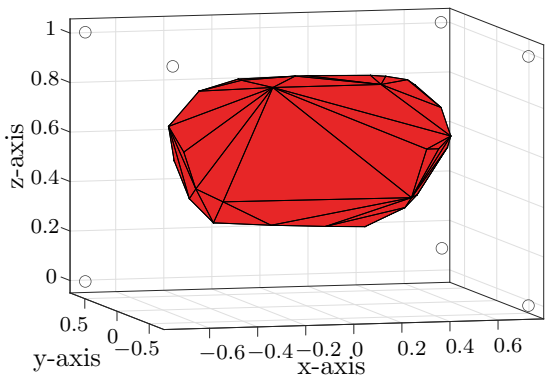

(e) $\mathcal{SEOW}$ post-failure of cable 2 (from below), view from front.

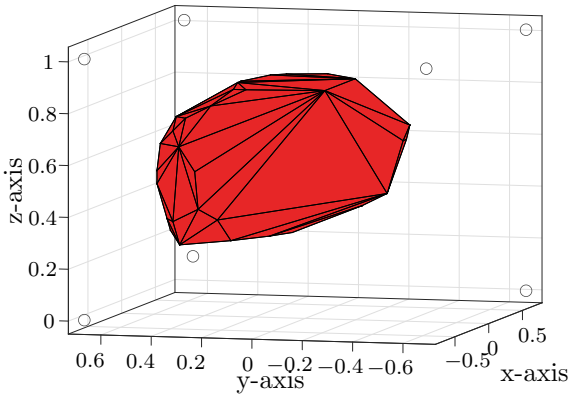

(f) $\mathcal{SEOW}$ post-failure of cable 2 (from below), view from side.

Figure 5.2: Pre- and post-failure $\mathcal{SECOW}$ (static equilibrium constant orientation workspace) and $\mathcal{SEOW}$ (static equilibrium orientation workspace) of SEGESTA with decoupling device mounted in bottom position. Pulley positions indicated by circles in the corners. Failed cable indicated by left out pulley.

5.1.3 Detection of Cable Failures

In order to avoid damage caused by mis- or uncontrolled robot movement after a cable failure, this incident needs to be detected. For diagnosis and fault-tolerant control, it is referred to [Blanke et al., 2006]. Only with a fault detection on prototype hardware, the control can be switched to emergency mode in order to avoid damage to the system and use, e.g., one of the proposed emergency strategies. To detect the cable failure, it is conceivable to either use the system's inherent measurements or to use an external measurement device, e.g. a camera based system. For this work, only the inherent measurements will be considered. The developed failure detection algorithm is presented by the author in [Boumann et al., 2023] in short form and will be derived and explained extensively in the following.

First, the measurements that lead to a reliable identification of a cable failure need to be identified out of the available ones. Both single measurements as well as a combination of them might be useful. The following signals are primarily measured within the prototype hardware:

- The current forces within the tensed cables
- The current angles of the motors
- The current velocities of the motors

Using the measured values, the cables' lengths and velocities are determined, see Section 2.2.6. By further processing the signals, additional information can be obtained. This includes, e.g.:

- Errors in cable lengths and velocities (using inverse kinematics)
- Pose and velocity of the platform (using forward kinematics)
- Pose, velocity, acceleration and forces at the platform (using state observers)

The given signals and information are now examined for their suitability to detect cable failures: Obviously, the measured cable force is a strong indicator for an issue, as soon as a measured cable force falls below $f_{\min}$. But besides a cable failure, this might also happen selectively if the platform collides with an object or if the cable gets slack momentarily during extreme fast motion. Thus, the sole cable force measurement with the first criterion $f < f_{\min}$ is not sufficient. Also, the measurements of angles and velocities of the motors do not provide helpful indication on cable failure without any information on proximity to or deviation from a desired value. A motor winding up the cable, e.g., would be perfectly normal in operation. However, if no platform movement is desired, the motor should be at rest while providing the cable force. Note that the motors are assumed to be torque controlled. If now a cable

fails, the motor would accelerate unintentionally, as it would try to provide the set-point torque (and thus force), leading to a significant error in motor velocity and winding up of the winch. Building upon this, the second criterion $\dot{\theta} > 0$ is introduced.

Naturally, the measured velocity is subject to noise, which would lead to erroneously failure detection when the platform is at rest. This might be resolved by using a certain threshold value or by combining it with the first criterion. If the motor winds up and the cable is not tensed when the platform is at rest, a disconnection between platform and cable is highly probable. Besides being at rest, the platform might be also in motion while either winding or unwinding of the cable is required, dependent on the direction of platform movement. If winding up is required, which is considered first, the second criterion will be active in all cases. If at one point the platform is accelerated too much due to imperfect control, the winding cable still might get slack for an instant. Thus, a third criterion is required to meet this circumstance.

In the described case, the considered cable would probably be too long rather than being too short. If the cable is too short, but the motor still winds up the cable while it is slack, it is most probably disconnected from the platform, leading to the third criterion $\Delta l < 0$.

Note that obviously, a too short cable alone is not sufficient to detect a cable failure. A combination of all three criteria would also detect the failure if the platform is at rest, since the cable would also get too short if the motor winds up in this situation. For a platform motion, where unwinding of the cable is required, the combination of all three criteria should also work. However, if the cable gets disconnected from the platform and slack, the according winch would still have unwinding movement due to its inertia. Only after a certain time, the winch will be decelerated, start to wind up and thus fulfilling the second criteria, possibly causing the failure detection to be slow in that case, which is suboptimal. Nonetheless, the combination of the three criteria for cable failure detection is promising, even thou it is very primal. A cyclical examination of all three conditions is implemented within the PLC of SEGESTA. As soon as all criteria hold true simultaneously for one cable, the control assumes a cable failure and switches to emergency mode. It is to note that only the first failed cable is detected. Detection of multiple cables is part of future work. As presented by the author in [Boumann et al., 2023], this failure detection algorithm appears to work. This is demonstrated more detailed in the following example:

First, the robot is moved to the pose $[0, 0, 0.5]^{\mathrm{T}}$ m and $[0, 0, 0]^{\mathrm{T}}$ rad, which is within the pre-failure but outside of the post-failure workspace. Afterwards, when the platform is at rest, the decoupling device is triggered and cable 4 is detached. In fig. 5.3, the progression of $\Delta \boldsymbol{l}$, $\dot{\boldsymbol{\theta}}$, $\boldsymbol{f}_{\mathrm{is}}$ and the three criteria leading to the cable failure detection are displayed. Moreover, the decoupling device's feedback (close/open) is depicted. Note that after successful detection, the control is switched to Potential Field Method, which is not further displayed.

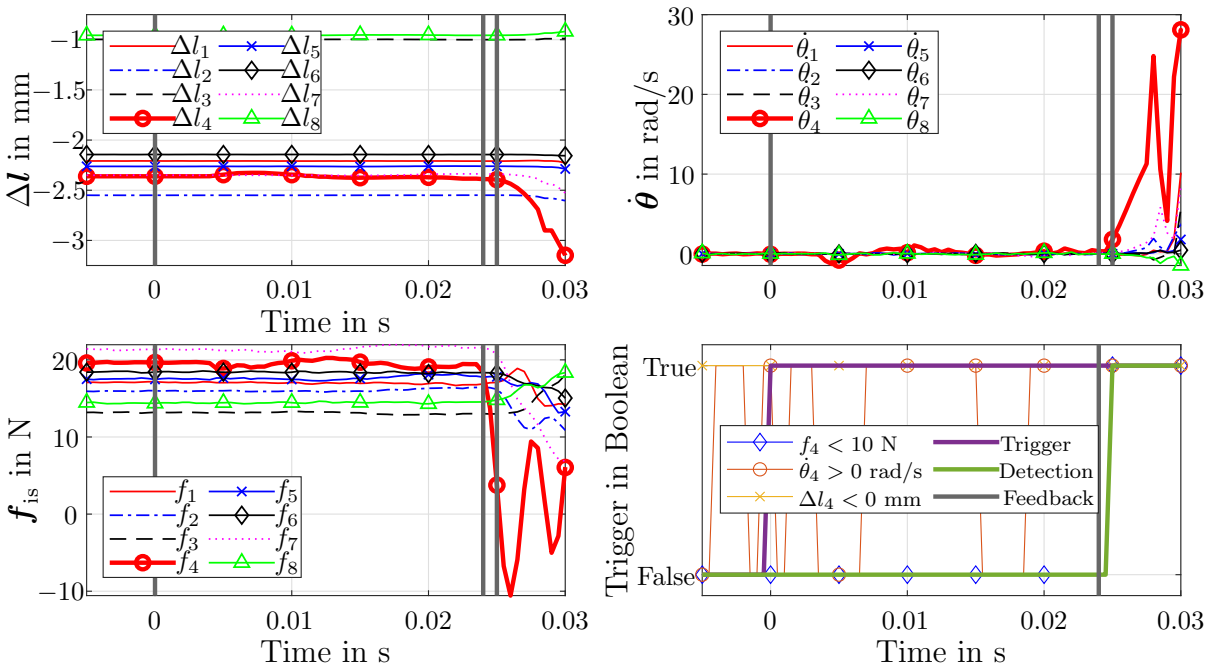

Figure 5.3: Cable failure detection, time scaling adjusted to decoupling device trigger. Detached cable 4 is highlighted. Vertical grey lines represent the trigger, the feedback and the failure detection signal.

After the decoupling device is triggered at 0 s, a delay time of 24 ms can be recognized until it opens, which is determined based on its feedback signal. The delay is presumably due to the electrical circuit and the device's actuator. Afterwards $\Delta\boldsymbol{l}$, $\dot{\boldsymbol{\theta}}$ and $\boldsymbol{f}_{\text{is}}$ start to change remarkably. The detached cable immediately starts to slip out of the platform, causing f_4 in $\boldsymbol{f}_{\text{is}}$ to decrease. After 1 ms, this cable's force drops below 10 N, which is used as a threshold value, while cable and platform disconnect. At the same moment, the associated motor starts to wind up the cable as expected, leading to a rising motor velocity θ_4. This is also reflected within the increasing cable length error Δl_4 of the affected cable. Thus, all three criteria behave as expected in the experiment. With all criteria fulfilled, the failure detection algorithm detects the failure fast and efficiently after 1 ms.

However, a few point are to be emphasized and discussed: It is to note that f_4 in $\boldsymbol{f}_{\text{is}}$ gets negative and oscillates about 0 N since the force sensor, attached to the pivoting pulley mounting, presumably receives a backlash due to the dissolved constraint of the cable. This leads to vibration before settling at 0 N. It is also remarkable that the motor velocity is noisy while the system is at rest, leading to a repetitive toggle of the second criteria. Moreover, the cable length error is negative permanently, as the platform reaches its desired pose with a remaining steady state offset, causing the third criteria also to be active permanently. Thus, the failure detection may be slower in different cases. Furthermore, a sound threshold for both criteria or the incorporation of the gradients to cope for those effects would be

highly reasonable to optimize the algorithm. Still, finding well suited threshold values and evaluating further criteria requires deeper investigation and extensive testing. Thus, it is part of future activities. The high speed of the detection may also allow for repeated and redundant checks to increase the success rate and avoid erroneously failure detection.

Summing up, it can be stated that the primal cable failure detection algorithm is proven to successfully detect the failure at a very high speed. Within the experiments described in the upcoming sections, the algorithm provides correct failure detection in all cases. Nonetheless, the algorithm also appears to rarely detect a non existent cable failure while the system is in regular operation and the platform is in motion. Presumably, all three conditions are met when heavy platform vibration occurs during the movement. A verification of this assumption and more extensive testing of the algorithm is part of future work. The same accounts for further improvement of the proposed failure detection algorithm. Besides using external measurements, e.g. a camera system, different approaches for improvement are conceivable: For the most simple approach, the algorithm could wait for the conditions to hold true over a certain amount of time before reporting a cable failure. This might support to eliminate influences coming from imperfect control and thus false failure reporting. However, in case of a failure, the detection would be retarded by the waiting time, while un- or miscontrolled platform movement might happen. As mentioned above, more sound threshold values for the second and thirds criteria could be employed. Whether this remarkably increases the required detection time needs to be investigated. Moreover, the results of a forward kinematic algorithm or a state observer could be integrated into the algorithm. For this, it must be examined how those algorithms behave in the event of a cable failure, in order to investigate if and how the failure is detectable within the data. Of course, algorithms based on artificial intelligence might be well suited for data-based failure detection. Finally, since a lot of the CDPRs introduced in Section 1.1 possess a cable force measurement directly at the platform in contrast to the SEGESTA prototype, it is also to be examined in future activities how such force measurement signals react in case of cable failure.

5.2 Implementation of Emergency Strategies

To test the proposed emergency strategies on the SEGESTA prototype, they need to be implemented into the real-time controller. In particular, the calculation times of the methods must be checked to ensure that the system's 2 kHz control cycle is maintained. As both methods rely on a forward kinematic algorithm to incorporate platform pose and velocity, this algorithm is considered first from a cable failure perspective. With respect to fig. 4.20 and fig. 4.28, it is to note that the ideal pose measurement used in simulation is replaced by a forward kinematic solution for both strategies, which is implemented on the prototype.

5.2.1 Forward Kinematics

As Section 4.3 shows, knowledge on the platform's pose and velocity is crucial for both proposed emergency strategies. With all cables in operation, the SEGESTA prototype has a redundancy of $r = 2$. Thus, after single cable failure, $r = 1$ remains and the forward kinematic algorithm introduced in Section 2.2.4 is still applicable. As soon as the event of cable failure is detected, see Section 5.1.3, the number of equations is reduced to $m - 1$, omitting the failed cable and the corresponding equation. Thus, the vector of cable lengths derived by angular motor encoder measurements $\boldsymbol{l}_\theta$ is reduced to $\boldsymbol{l}_\theta^* \in \mathbb{R}^{(m-1)\times 1}$. For the optimization problem, this yields

$$\upsilon(\boldsymbol{l}_\theta)^* = \min_{\boldsymbol{x}_e^*} \sum_{i=1}^{m-1} \Upsilon_i^2(\boldsymbol{x}_e^*, \boldsymbol{l}_\theta^*). \tag{5.1}$$

Using the pose estimation $\boldsymbol{x}_e^*$, the estimated structure matrix $\boldsymbol{A}_e^{T*}$ is calculated using inverse kinematics. Moreover, an estimation on the platform velocity $\dot{\boldsymbol{x}}_e^*$ is calculated using motor velocity measurement and $\boldsymbol{A}_e^{T*}$, referring to eq. (2.21). Numerical derivation of the pose estimation would be also conceivable. As the used forward kinematic algorithm is well-known and state of the art [Pott, 2018], its real-time capability is neither questioned, nor further investigated. The estimated parameters $\boldsymbol{x}_e^*$, $\dot{\boldsymbol{x}}_e^*$ and $\boldsymbol{A}_e^{T*}$ serve as an input for the emergency strategies. As detected within the simulations in Section 4.3, it can be expected that cables might get slack momentarily. Of course, this might influence the quality of the estimation obtained from forward kinematics. As long as the cable slackness is only momentarily and the deviation on cable length is tolerable, this merely results in minor error of the estimation, presumably. However, this needs to be considered. Finally, the quality of the forward kinematic estimation in particular after cable failure needs to be verified using external measurements, which is part of future activities. The same accounts for pose estimation in non-redundant CDPRs or after multiple cable failure. From here, the conceptual idea of a fault tolerant forward kinematic algorithm can be raised. A corresponding algorithm should cover the case that the CDPR changes, e.g. from redundant to non redundant after cable failure or due to massive cable slackness. This might, e.g., be implemented by supporting the forward kinematic with a Kalman filter: The platform movement might be predicted using the measured cable forces or by integration of an inertial measurement device. Further investigation of such algorithm is part of future work.

5.2.2 Kinetic Energy Minimization Method

Since the Kinetic Energy Minimization Method in the current implementation relies on numerical optimization to obtain cable forces, it is to be viewed critically with regards to

real-time. As described in Section 4.3.5, sequential quadratic programming, which can be considered state of the art, is used to solve the nonlinear constraint problem eq. (3.15). Thus, a sufficient calculation time might be obtained as other examples show [Côté et al., 2016]. Moreover, the number of iterations is constrained, leading to a suboptimal NMPC with similar computational costs per time step. To test the computational efficiency, the algorithm is compiled using `Simulink` in `MATLAB` R2021b. The execution is carried using an `Intel` CPU i7-1065G7 with 1.3 GHz on a Windows 10 System. The scenario as described in fig. 4.22 is used to measure the computation time per cycle step. Figure 5.4 displays the resulting

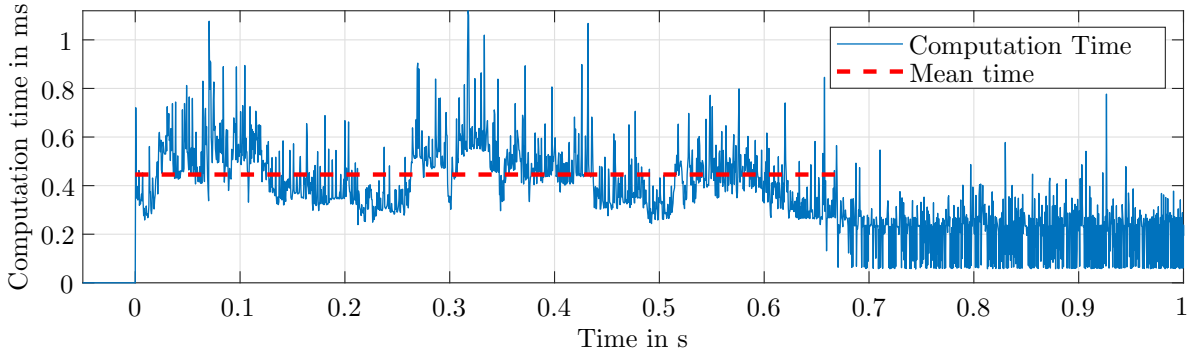

Figure 5.4: Computation time of the Kinetic Energy Minimization Method during a rescue maneuver.

computation time throughout the rescue maneuver used by the Kinetic Energy Minimization strategy. After roughly 0.67 s, the platform is rescued. From the event of cable failure until the platform is stabilized, a mean computation time of 0.4456 ms is determined for the algorithm. Per cycle, the computation time ranges from 0.25 ms at its lowest up to slightly above 1 ms at its highest. Considering the mean computation time, a cycle time of 2 kHz could be fulfilled by the algorithm, whereas the maximum computation time values might cause cycle time violations. However, it is to note that the number of iterations is set to $n_{\max} = 50$ in the given example. As fig. 4.26 shows, $n_{\max}$ can be reduced while maintaining a good quality solution. With $n_{\max} = 5$, the mean computation time drops to 0.2982 ms in the same experiment. In addition to that, the clock frequency of the used CPU with 1.3 GHz is comparably low to the one of SEGESTA with 2.4 GHz. Summarizing, it is expected, that the algorithm can be applied on the PLC without major computation time issues. This is verified in the upcoming experiment section, where no real-time violations are observed on the prototype.

5.2.3 Potential Field Method

Similar to the experiments in Section 4.3.6, the Nearest Corner Method is employed to determine cable forces outside of the $\mathcal{WFW}$ when applying the Potential Field Method. The

computational efficiency and real-time capability of the algorithm is demonstrated for a simple planar CDPR model in previous work of the author [Boumann and Bruckmann, 2020b]. For application on the prototype, of course the model with $m = 8$, $n = 6$ and $r = 2$ yields more computation effort. To investigate on the real-time capability of the algorithm, the same hardware as in Section 5.2.2 is employed. The scenario as described in fig. 4.36 on the left side ($\boldsymbol{D}_1 = 0.1 \cdot \mathrm{diag}(1, 1, 1)$) is used to measure the computation time. Figure 5.5

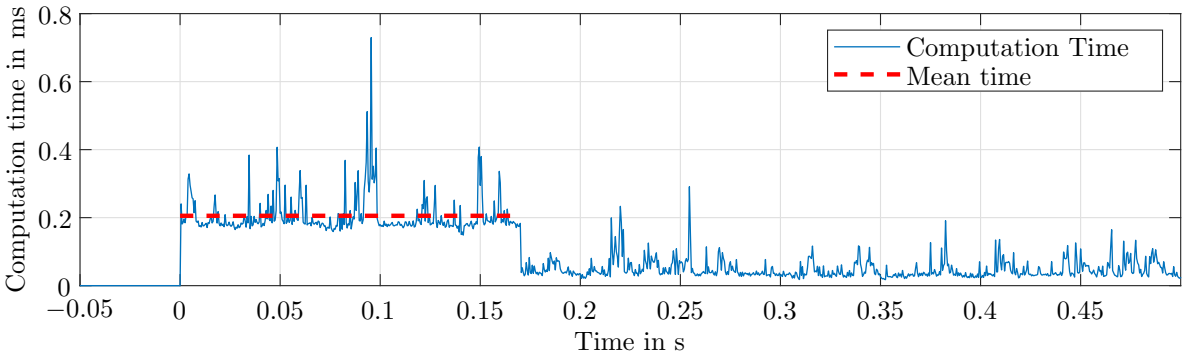

Figure 5.5: Computation time of the Potential Field Method using the Nearest Corner Method during a rescue maneuver.

displays the resulting computation time throughout the rescue maneuver required by the Potential Field Method using the Nearest Corner Method and the Puncture Method. After $\sim$ 0.17 s, the platform enters the $\mathcal{WFW}$ and the Puncture Method gets active. For this first time frame, a mean computation time of 0.2054 ms is found. The computation times per cycle range from $\sim$ 0.18 ms at its lowest up to some peaks of $\sim$ 0.4 ms, one peak at $\sim$ 0.5 ms and one maximum outlier of $\sim$ 0.75 ms. The decreasing computation time at the return of the robot back into its $\mathcal{WFW}$ after 0.17 s (see fig. 4.36 and fig. 5.5), depicts the computational costs of the Puncture Method alone, which requires fewer resources. Apart from one outlier, the methods are well within the required cycle time of 2 kHz, even with less powerful hardware than the prototype PLC of SEGESTA. With the same arguments as in Section 5.2.2, no computation time issues are expected for application of the method on the prototype and no real-time violations are observed when conducting experiments in the upcoming section.

5.3 Experiments on the SEGESTA Prototype

With all the preliminary work completed, experiments can now be carried out on the SEGESTA prototype to prove the applicability of the author's emergency strategies after cable failure on a real CDPR. Naturally, the amount of experiments done in simulation (see Section 4.3) is not feasible on the prototype. Thus, only a selection of experiments

is shown and discussed here. Due to parameter changes (decoupling device, precautionary safety limitation of $f_{\max}$, alteration of the workspace), the simulative experiments are not fully replicable. Moreover the prototype does not possess motor brakes, which is why the scenario displayed in Section 4.3.7 cannot be examined here. For all experiments it is to note that $\boldsymbol{f}_{\text{mea}}$ corresponds to the measured cable forces using the force sensors of SEGESTA. Furthermore, the estimated values $\boldsymbol{r}_{P,e}^{*}$, $\boldsymbol{\Phi}_{e}^{*}$ and their derivatives correspond to the pose estimation based on eq. (5.1). To validate the functionality of the emergency strategies, it suffices to address failure of cable 4 (from above) on the prototype. Failure of cable 2 (from below) is neither displayed nor investigated here.

5.3.1 Cable Failure without Failure Detection

First, the outcome of a cable failure on the SEGESTA prototype without any fault detection or safety mechanism is examined, based on the simulation in Section 4.3.4. Different from there, the starting position is set to $\boldsymbol{r}_P = [0.255, 0.075, 0.5]^{\mathrm{T}}$ m, as the platform cannot be moved below 0.38 m in z-direction due to constructive constraints by the set down position, see fig. 1.4, which was neglected in simulation. The chosen pose is within the post-failure $\mathcal{SECOW}$, see fig. 5.2. From there, the decoupling device is triggered at 0 s and the experiment's outcome is shown in fig. 5.6. Similar to fig. 5.3, the same delay can be observed before the device reacts and loosens the cable (see $\boldsymbol{f}_{\text{mea}}$). Until ~ 0.1 s, the decoupled cable

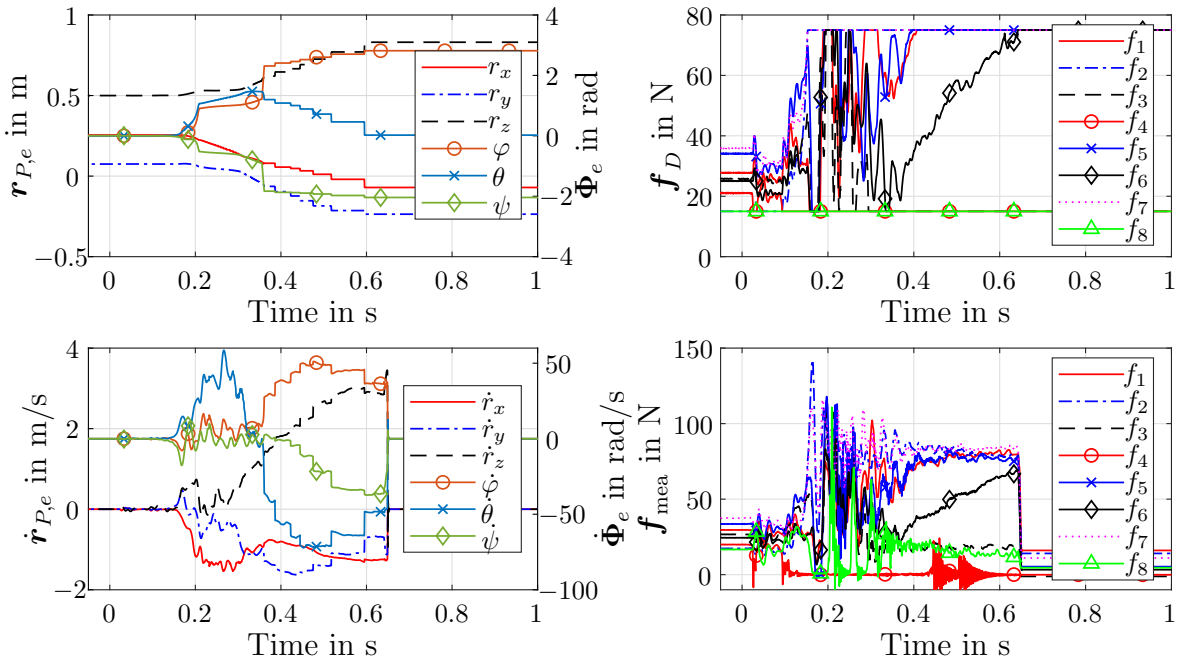

Figure 5.6: Cable failure scenario of cable 4 at SEGESTA inside of the post-failure workspace without failure detection. Time scale aligned with event of cable failure.

appears to get stuck at the platform, keeping the control and the pose stable. Afterwards, the cable is separated from the platform and the measured force for cable 4 drops down to 0 N. As there is no failure detection, the motor belonging to the decoupled cable is not stopped (see $\boldsymbol{f}_D$), while all remaining cables erroneously accelerate the platform drastically. Also, the failed cable is not excluded from the forward kinematic algorithm and the pose and velocity estimation in fig. 5.6 do not match with reality, as the algorithm tries to incorporate the decoupled cable that is getting wound up rapidly. Evaluating the experiment visually, the platform movement qualitatively is quite alike to the simulation depicted in fig. 4.15: Tipping over about positive x-axis, slight rotation about negative y- and positive z-axis, movement in positive x- and y-directions and in negative z-direction. Comparing $\boldsymbol{f}_D$, experiment and simulation are also quite similar: The commanded forces for cables 4 and 8 are both at $f_{\min}$ while all other forces increase towards $f_{\max}$. However, the maximum cable force is reached faster in simulation, even thou $f_{\max}$ was halved for the prototype experiments. This indicates more inert behavior of the reality, possibly due to unmodeled effects like pulley inertia within the simulation. It is to note that the simulation is stopped after 0.16 s due to tipping over after cable decoupling. Thus the remaining experiment is not comparable. The controller causes heavy vibration to the platform subsequently, as can be seen from $\boldsymbol{f}_{\text{mea}}$. The measured force peaks range up to 142 N in cable 2, which almost exceeds the lowered $f_{\max}$ by factor 2. Accordingly, the safety limitation of the maximum cable force for prototype experiments is very appropriate. In between 0.4 and 0.6 s, the decoupled cable is tugged through the pivoting and the deflecting pulley, exciting heavy vibrations in the guidance and force measurement mechanism. After ~ 0.64 s the emergency stop is pushed manually due to safety reasons. The motor power is disconnected and further uncontrolled movement or vibration excitation are inhibited, preventing the prototype from damage. The platform settles in a pose, where it is held due to system friction. Note that a heavier platform would fall down without motor brakes.

Summing up, the experiment's results are very comparable to the simulation qualitatively, even with slightly different upper cable force boundary, starting pose, platform mass and platform inertia. As expected, uncontrolled erroneously platform movement results without failure detection, even thou the platform is within the post-failure workspace after cable decoupling. This underlines the necessity of cable failure detection and emergency strategies, as proposed by the author.

5.3.2 Conventional Controller with Failure Detection

As presented simulatively in Section 4.3.4, the APD controller with failure detection should be able to stabilize the platform after cable failure if it is within the post-failure workspace. Thus, this scenario is tested now. A scenario with the platform outside of the post-failure

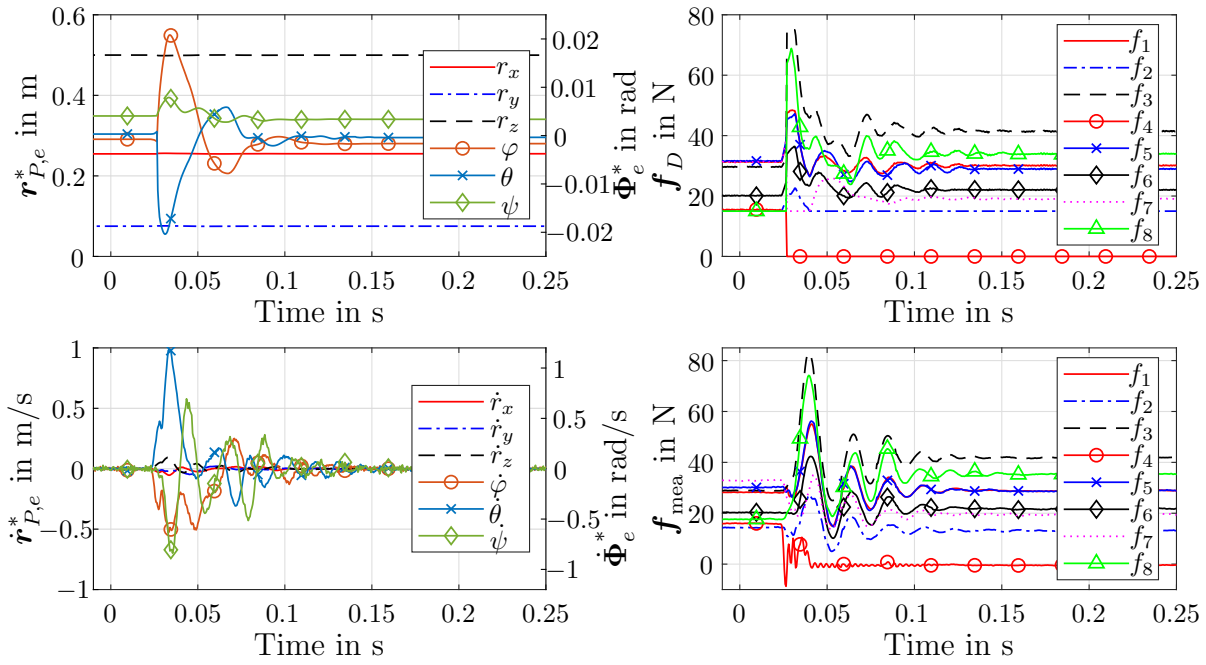

Figure 5.7: Cable failure scenario of cable 4 at SEGESTA inside of the post-failure workspace with failure detection. Time scale aligned with event of cable failure.

workspace is neglected here, since the approach is expected to fail in this case, see fig. 4.19. First, the platform is moved to the same starting pose as in the previous experiment, see fig. 5.6. Then, the outcome of the experiment, incorporating failure detection, is depicted in fig. 5.7. As expected, the approach can successfully stabilize the platform and keep it in place after cable failure. Due to the cable decoupling along with the changing set-point force distribution for seven cables, the platform is deflected and some vibration is introduced. However, the controller can successfully suppress and stabilize this after ~ 0.16 s. Nearly no Cartesian movement can be observed from the forward kinematic, which is equal to the simulation. The platform tilts barely noticeable (maximal ~ 0.021 rad about x-axis and ~ -0.02 rad about y-axis), which is align with the visual evaluation of the experiment. In comparison to the simulation experiment, see fig. 4.17, the residual angular offset is almost fully compensated according to the forward kinematic estimation. Also, the directions of angular movement are equal. The magnitude of rotation is higher in this experiment, while the maximal rotational velocities are only half as high, which may be due to higher platform mass and inertia caused by the decoupling device. Commanded and measured forces are remarkably higher in the prototype experiments and the residual vibration is lasting longer (~ 0.16 s versus ~ 0.03 s). Presumably, the change in cable force distribution after failure detection is more remarkable for the chosen pose, which differs in z-component from the simulative experiment. The root cause may as well be within the chosen (simple) cable model in simulation or the neglected dynamic pulley modeling.

In summary, the experiments in simulation and on the SEGESTA prototype are strongly comparable in this case, even thou the parameters and the evaluated pose differ slightly, as explained in the previous section. The successful prototype experiment provides a strong indication that the tested approach is highly suitable if the platform remains within the post-failure workspace after a cable failure.

5.3.3 Kinetic Energy Minimization Method

In analogy to Section 4.3.5, it is now investigated how the proposed Kinetic Energy Minimization Method performs in a cable failure scenario outside of the post-failure workspace on the SEGESTA prototype. The first successful applicability is demonstrated by the author in [Boumann et al., 2023]. The experiment's initial conditions are chosen equivalent to the simulation displayed in fig. 4.22 with some minor adjustments: The starting position is adjusted upwards in z-direction (see Section 5.3.1) and set to $\boldsymbol{r}_P = [-0.025, -0.165, 0.5]$, which is also outside of the post-failure $\mathcal{SECOW}$. The weighting parameters $r_1 = 10$ and $\boldsymbol{R} = \mathrm{diag}(1, 1, 5, 100, 100, 1)$ are chosen. Mainly, r_1 is weighted much higher in relation compared to the simulations. That is because the control was found to overdrive more easily on the prototype. Note that a lower $r_1 = 0.12$ is chosen in [Boumann et al., 2023], but with remarkably smaller weights chosen for $\boldsymbol{R}$ in relation. Possible causes for this have to be considered in future activities, as discussed in the upcoming conclusion. Furthermore, the weighting against movement in z-direction is increased by a factor of five, which shall prevent the platform from loosing to much height.

The experiment is displayed in fig. 5.8. The platform can be successfully stopped 1.339 s after cable failure at $[0.0886, -0.1242, 0.4387]^{\mathrm{T}}$ m and $[0.9957, -0.7474, 0.5568]^{\mathrm{T}}$ rad. No external collision is experienced, neither with the ground, nor with the set down position. Note that this resting pose is not contained in fig. 5.2c, as the orientation is higher than considered within the tested grid $\mathcal{G}_{\mathcal{SECOW}}$. Similar to fig. 5.6, the measured cable forces are remarkably higher than the commanded in this experiment, which could also be seen in some of the previous simulations, e.g. in fig. 4.14 and fig. 4.18. Thus, the safety limitation of $f_{\max}$ appears to be highly reasonable in order to prevent further failure. However, this was not witnessed within the corresponding simulation experiment displayed in fig. 4.22. In further comparison, even the rough stopping after ~ 0.75 s takes longer than fully stopping the system in simulation (0.63 s). Also the platform tilting cannot be suppressed as effectively. The absolute maximum estimated rotational velocity of ~ 22 rad/s about the z-axis is higher while the maximal Cartesian velocity of ~ 1.04 m/s along the y-axis is smaller. The tilting directions about x and y-axis are equal while the magnitude is higher, especially about the z-axis according to the forward kinematic estimation. This is despite a strong weighting against rotation about these axes. However, the simulation experiments displayed, that

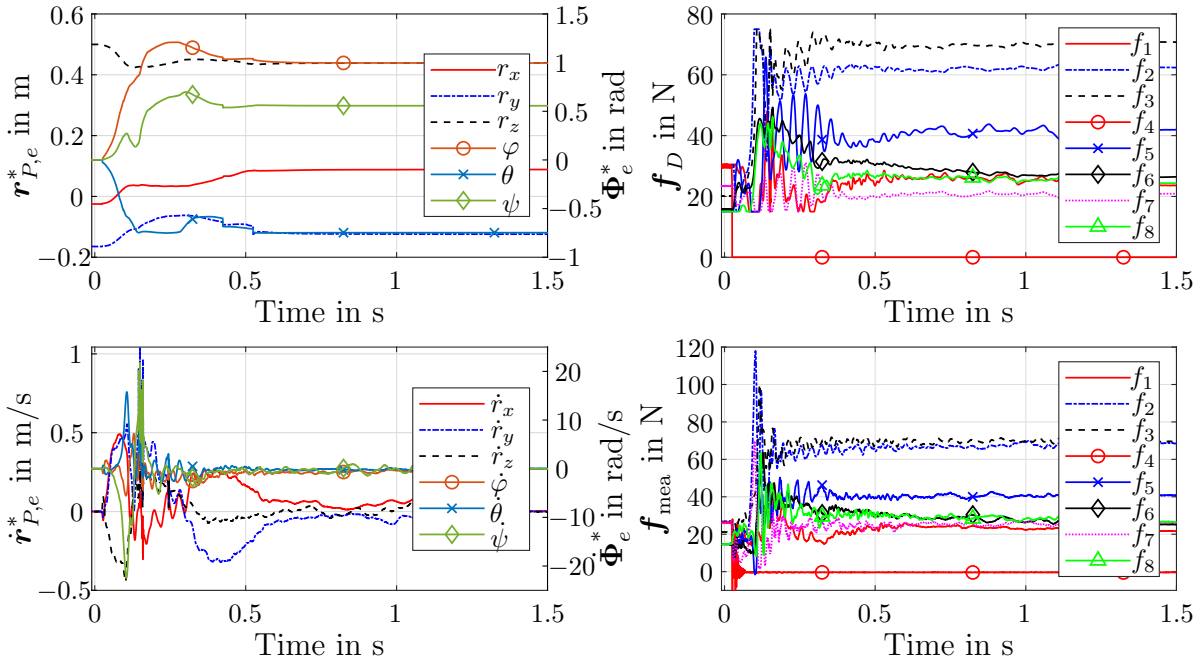

Figure 5.8: Cable failure scenario of cable 4 at SEGESTA outside of the post-failure workspace using Kinetic Energy Minimization Method. Time scale aligned with event of cable failure.

the platform tends strongly to tip over after cable failure. Thus, the previously described findings are reasonable. Desired compensatory movement in x and y-direction can also be witnessed, whereby this is more significant in the simulation. Also, a bit of movement in z-direction occurs. The controller is able to keep all cables in tension, despite one instant where cable 5 gets slack at ~ 0.1 s. More vibration is experienced within $\boldsymbol{f}_{\text{mea}}$ in comparison to the simulation which is align to Section 5.3.2.

Pictures taken from a video of the experiment are shown in fig. 5.9. It is to note that punctual cable folding can be observed visually during the experiment when the platform strongly tilts, see fig. 5.9b. This does not prevent the method from successfully rescuing the platform, see fig. 5.9c. However, it might influence the accuracy of the forward kinematic solution, which has to be investigated in future activities. To emphasize that the strategy is really accountable for the platform stabilization, the system is switched off. This leads to a descent of the platform, see fig. 5.9d.

In summary, this prototype experiment is not as comparable to the simulation as the one described in Section 5.3.2. Nevertheless, it shows some very similar trends and behavior. As previously discussed, some parameters differ from the simulation, which could provide an explanation. Presumably, the main cause is within the two major differences: First the forward kinematic algorithm is incorporated now within the control whereas an ideal pose measurement was assumed in simulation. Second, $f_{\max}$ was reduced for safety reasons, which

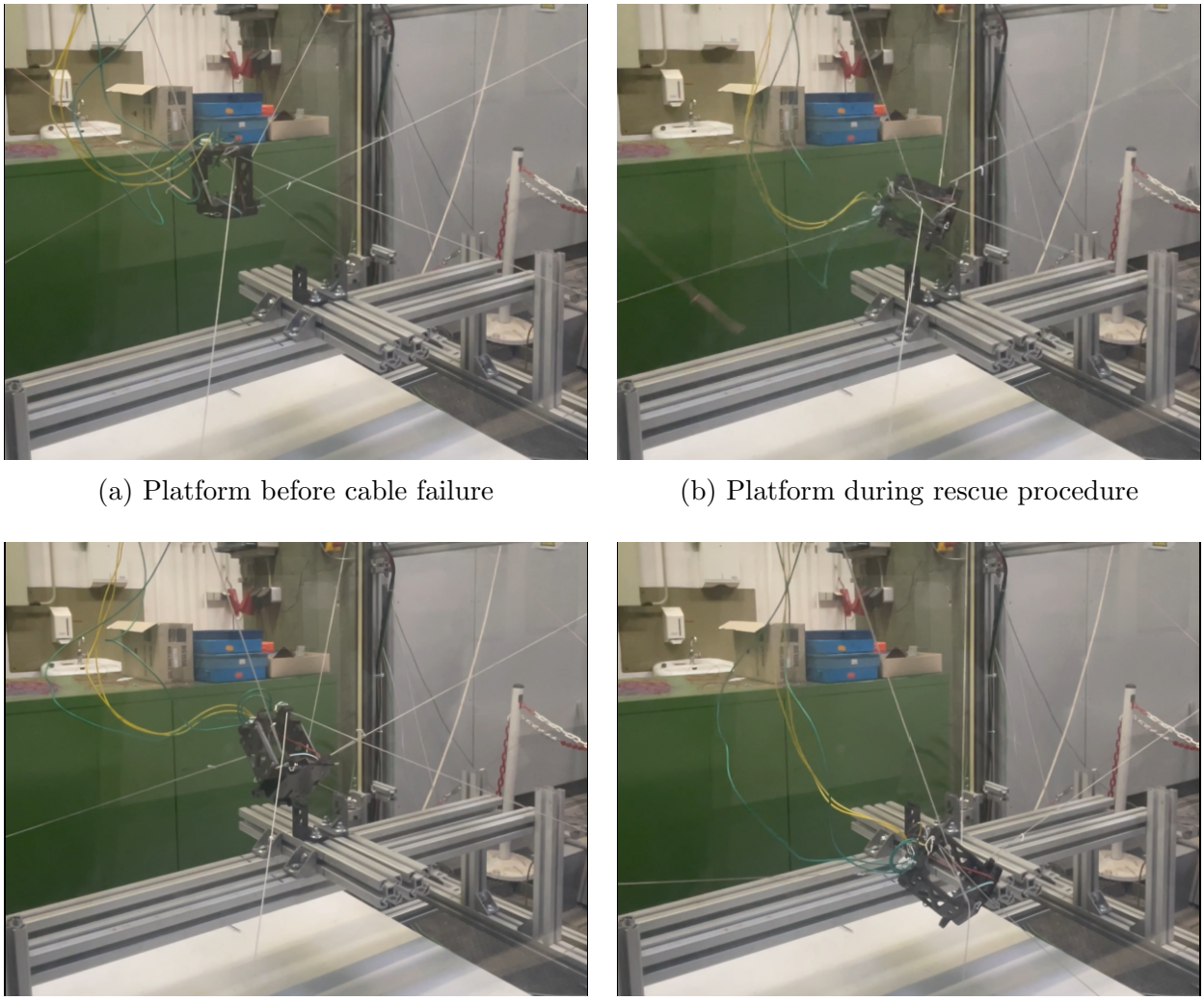

(a) Platform before cable failure

(b) Platform during rescue procedure

(c) Platform in safe pose after rescue

(d) Cables loose after switching off the system

Figure 5.9: Pictures of SEGESTA during rescue after failure of cable 4 outside of the post-failure workspace using the Kinetic Energy Minimization Method.

decreases the emergency strategy's margin and room for maneuver. However, the simulation could provide a suitable indication for feasibility and parametrization of the method, leading to a successful demonstration of the method here and in [Boumann et al., 2023]. A parameter study of the emergency strategy is omitted here, since it has already been carried out in simulation.

5.3.4 Potential Field Method

Now, the second proposed emergency strategy is tested at the SEGESTA prototype. To recreate the simulation experiment, the method's parameters are set equal to fig. 4.30. Due to constructive constraints, see Section 5.3.1, the same starting pose as Section 5.3.3 is chosen. Adapted from fig. 4.31a, $\boldsymbol{r}_{P,\text{final}} = [0.2, 0.1, 0.5]^{\text{T}}$ is set. Note that this first experiment is only

discussed briefly and not represented graphically. Using the Potential Field Method after cable failure, the platform is successfully pulled into the given goal pose and stopped there. However, it tips over along the path ($\varphi \approx 90°$), which also leads to cable folding. Considering fig. 4.31a, this is no surprise, as the starting pose is already at the border of the feasible region in simulation and the main reason for unfeasibility is tipping over of the platform. For the prototype experiments, the feasible region may be smaller as $f_{\max}$ is reduced for safety reasons, which narrows the emergency strategy's margin. Yet, the strong tendency of the platform to tip over, which was witnessed in the simulative experiments, can be verified here.

Now the initial position is marginally adjusted in x-direction to $\boldsymbol{r}_P = [0.025, -0.165, 0.5]^{\mathrm{T}}$ and the experiment is repeated. Figure 5.10 depicts the results. The platform is successfully brought to the goal pose after $\sim$ 0.48 s with a residual estimated offset of $[-0.0018, 0.0013, -0.0022]^{\mathrm{T}}$ m and $[-0.0018, -0.0011, 0.0026]$T rad, no collision is experienced. The algorithm stays well within the force boundaries and keeps all cables in tension during the rescue despite cable 7, which gets slack momentarily two times, between $\sim$ 0.04 s and $\sim$ 0.08 s after cable failure. Similar to the previous experiment, the measured forces range higher than the commanded. The maximum force occurring is $\sim$ 102 N at 0.066 s in cable 3. Despite start and goal position have been adjusted, still the experiment shown in fig. 4.30 is the most comparable. The platform is rescued even faster than in simulation (0.65 s). However, the distance traveled is also longer in simulation. The residual position

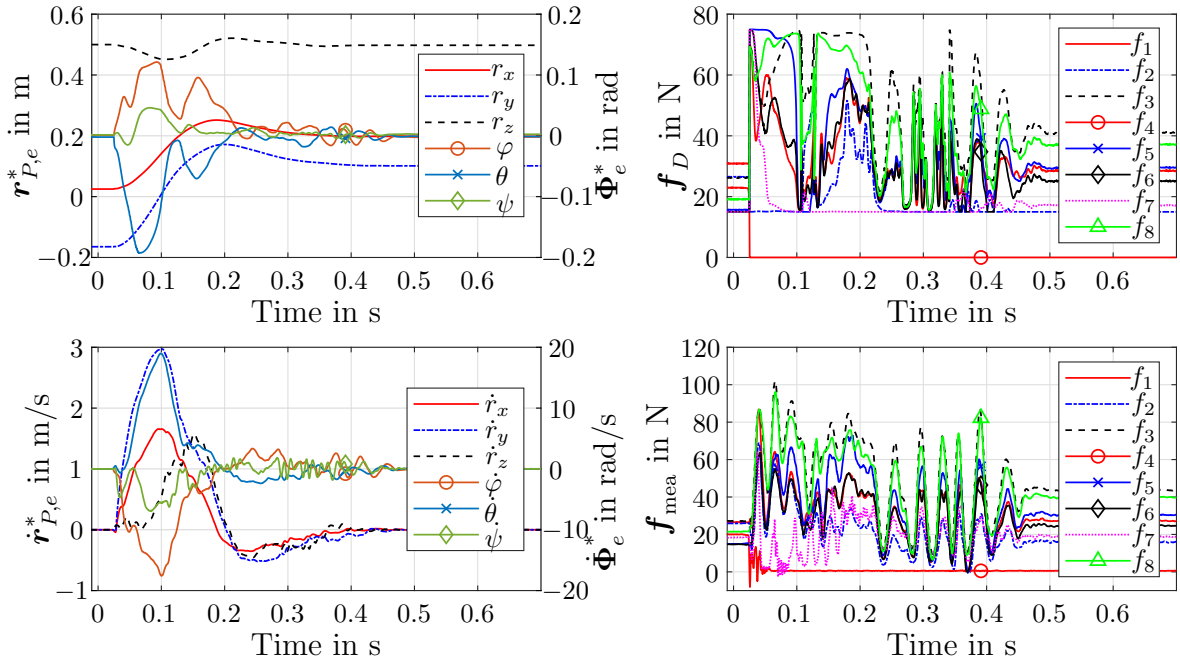

Figure 5.10: Cable failure scenario of cable 4 at SEGESTA outside of the post-failure workspace using Potential Field Method. Time scale aligned with event of cable failure.

offset in the experiment is smaller in magnitude by one decimal place, while the offset in orientation is within the same magnitude. The maximal Cartesian velocity of ~ 2.97 m/s can be found in y-direction and is at a comparable value in both the experiment and the simulation. The maximal rotational velocity of ~ 18.95 rad/s about the y-axis in the experiment is higher, which is analog to the previous section. Aside from that, different cables are the most tense. This is probably due to the changed direction from start to goal position. In the experiment, the most tense cables are number 3 and 8 (cable 5 and 7 in the simulation). The method's continuity when entering the post-failure $\mathcal{WFW}$ is comparable to the simulation experiment shown in fig. 4.36. Similar peaks appear at ~ 0.105 s and ~ 0.127 s. This does not prevent the method from successfully guiding the platform. However, it should be addressed in future activities, employing a cable force distribution algorithm with full workspace coverage, see Section 4.3.6. In analogy to the previous section, fig. 5.11 displays pictures of the experiment. Note that unfortunately, the image detail and angle are different. After successful rescue, see fig. 5.11b and fig. 5.11c, the system is also switched off for demonstration purposes. It can be noted that the platform descents as well (see fig. 5.11d), which emphasizes its previous stabilization by the emergency strategy.

Summing up, the experiment reveals similar tendencies as the simulation. The previous section's conclusions regarding parameter adjustments, the forward kinematic algorithm and $f_{\max}$ also apply. The same accounts for the simulations' indication for experiment feasibility and suitable parametrization. Also, this emergency strategy is successfully demonstrated here, as well as in [Boumann et al., 2023]. Analogous to the previous section, further parameter studies are neglected.

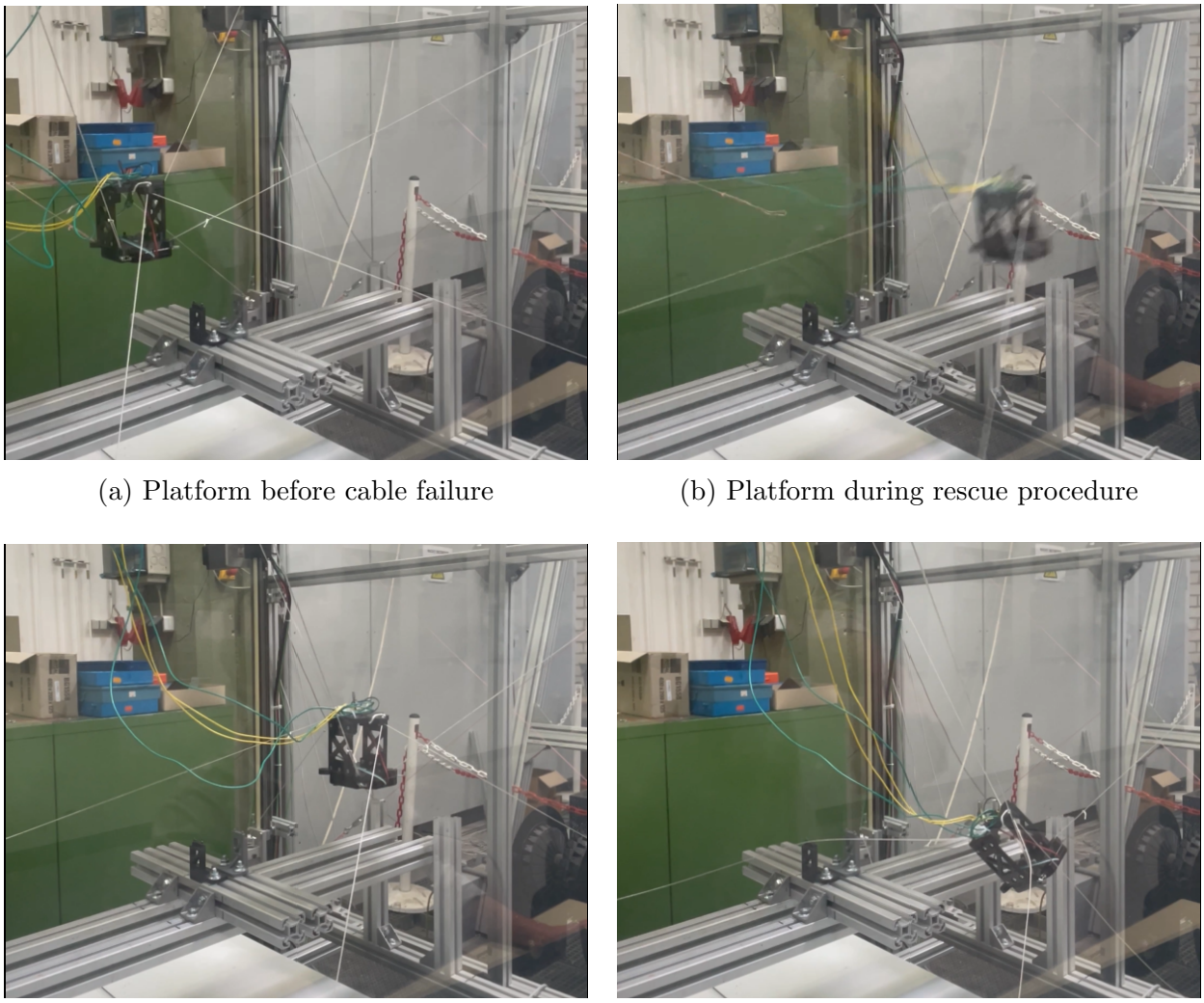

(a) Platform before cable failure

(b) Platform during rescue procedure

(c) Platform in safe pose after rescue

(d) Cables loose after switching off the system

Figure 5.11: Pictures of SEGESTA during rescue after failure of cable 4 outside of the post-failure workspace using the Potential Field Method.

5.3.5 CDPR Operation After Cable Failure

In the previous, it was elaborated how to stabilize the platform after cable failure if it is within the post-failure workspace, or how to guide it there if it is outside before. In both cases, the platform is in a rested and stable pose afterwards, assuming the rescue strategy is successful. Then, despite one missing cable, still a controllable robot remains, which may wait for maintenance or continue operation with a reduced set of cables as claimed by the author in [Boumann et al., 2023]. This is now demonstrated on the SEGESTA prototype for the example given in fig. 5.7 with $r = 1$ after cable failure. Figure 5.12 shows the experiment. It is to note that for enhanced readability, the time axes are separated to display the relevant data segments. In between, waiting times occur due to manual operation of the system including goal pose setting. The data marginally differs between the axes separations as some long

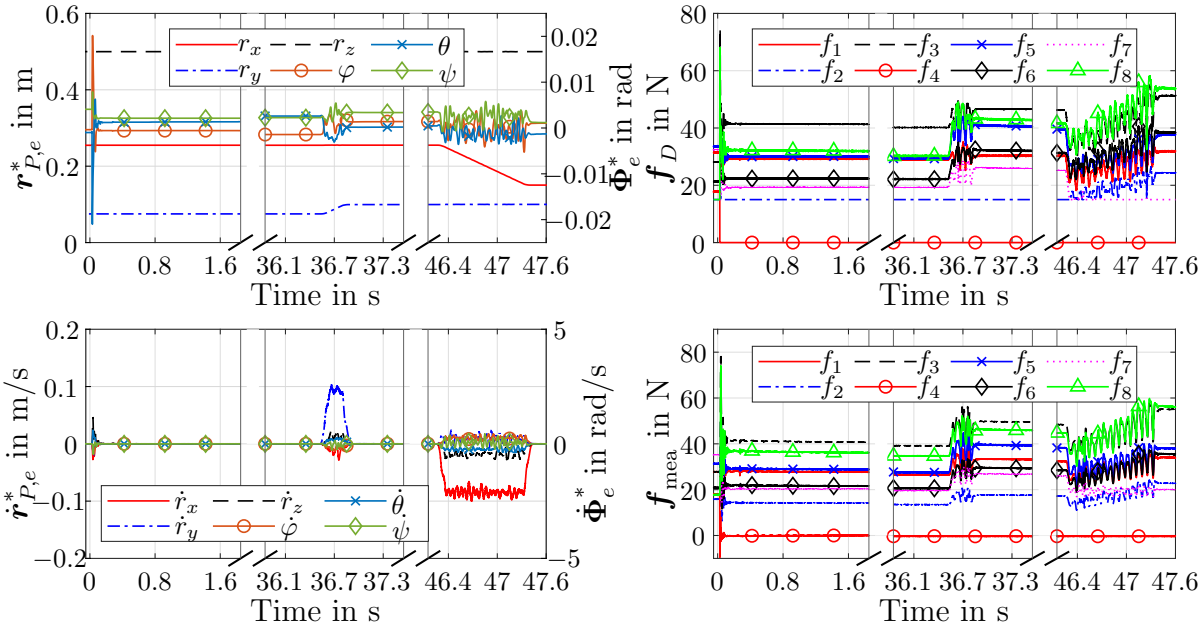

Figure 5.12: Cable failure scenario of cable 4 at SEGESTA inside of the post-failure workspace with failure detection and operation after rescue. Time scale aligned with event of cable failure.

time effects still take place within the system, such as cable creeping, presumably. After the platform is stabilized and remains at a rested pose within the post-failure workspace, two different poses within it are exemplarily approached (one movement in y-direction, one in negative x-direction). In contrast to Section 4.3.2, a trajectory generation with constant velocity phase is utilized here [Lemmen et al., 2019], with a desired directional velocity of 0.1 m/s per axis. In this experiment, the robot is already in conventional control with given trajectory planning after rescue. Merely the robot control is in seven cable mode as described in Section 4.3.4. The experiment shows that the two poses ($[0.255, 0.1, 0.5]^{\mathrm{T}}$ m and $[0.15, 0.1, 0, 5]^{\mathrm{T}}$ m, both with an orientation of $[0, 0, 0]^{\mathrm{T}}$ rad) can be approached successfully with negligible offset. During the movement, the platform is subject to vibrations, which, however, can be attributed to a loss of symmetry of the robot, stick slip effects due to the low velocity and an improvable control in general.

If now in contrast, the platform gets outside of the post-failure workspace after cable breakage and is brought back afterwards, using e.g. one of the author's proposed approaches, the control system and trajectory planning needs to be changed back to a regular state, in order to continue operation as demonstrated above. As this is technically feasible, it is no longer demonstrated here.

5.4 Conclusion and Discussion

Within this chapter, the validation of the proposed emergency strategies has successfully been conducted on the SEGESTA prototype. To enable tests, a device was developed and integrated, which mimics a cable failure by decoupling a cable. Various requirements and demands on the device were set and fulfilled. For safer testing, the upper force boundary $f_{\max}$ was decreased. Subsequently, the pre- and post-failure workspaces were determined again. To enable emergency strategies after cable failure, a simple, yet effective and fast failure detection algorithm was introduced and tested.

The emergency strategies, as described in Chapter 3 and studied in Chapter 4, were integrated into the PLC, considering their real-time feasibility in particular. To provide platform position and velocity data, a forward kinematic algorithm considering the failed cable was implemented. With the methods implemented on the prototype, experiments were conducted to validate their applicability and functionality.

In a first step, the conventional control system's malfunction without cable failure detection was demonstrated. Subsequently, the conventional controller extended by failure detection was proven to stabilize the platform, if it is within the post-failure workspace. For cases outside of the post-failure workspace, both proposed emergency strategies have been applied and validated in two exemplary scenarios. In those scenarios, as well as in work of the author presented in [Boumann et al., 2023], the methods have been proven to work on the SEGESTA prototype. They can successfully guide the platform back into the post-failure workspace and bring it to a statically stable pose without external collisions in the chosen scenarios.

Various findings that stand out from the experiments shall be stated and discussed: The decoupling device has proven to work reliable and repeatable. However, the cable rarely got stuck at the hook of the device, which should be optimized. The failure detection algorithm works seamless and reliable. It did not miss to detect any cable decoupling. However, a false detection might appear if strong platform vibration occurs during regular operation, revealing potential for improvement. Within the validation, only a few experiments have been considered to show the functionality of the emergency strategies. Of course, this needs to be tested more extensively. To enable for testing in a broader workspace, constructive changes may be applied to the current prototype, e.g. lowering the set down device in position. Moreover, the emergency strategies may be improved as already discussed in Section 4.4, featuring e.g. a position control loop for the model predictive approach, a cable force distribution covering the whole $\mathcal{WFW}$ for the Nearest Corner Method, or approaches to find universally applicable parametrization of the methods to reduce parameter sensitivity. To address rising computational effort of the model predictive approach, methods as presented in [Graichen and Käpernick, 2012, Graichen and Kugi, 2010] may be considered. It should

be noted that poor parameter settings of the emergency strategies can lead to dysfunctionality. This may even result in prototype damage, especially if no other safety mechanisms are installed, such as an emergency shutdown or brakes. Furthermore, the general safety and validity of the strategies have to be verified in future activities, including also a thorough stability analysis. It has been shown that the measured cable forces in cable failure scenarios may exceed the commanded ones remarkably. On the other hand, lowering the upper cable force boundary $f_{\max}$ decreases the feasible workspace. An advisable trade off would be an immediate restriction of $f_{\max}$ within the rescue maneuver, as soon as a cable failure is detected. The feasibility of this trade off needs to be verified.

Despite some differences between the prototype experiment and the simulation (parameter adjustments due to decoupling device and working safety, incorporation of pose estimation based on forward kinematic algorithms), the latter still provides a suitable indication on parametrization of the emergency strategies and a comparable dynamic behavior as well. However, due to the differences, a one-to-one comparison between simulation and prototype experiment was not possible. Still, the simulation is highly suitable to improve the proposed methods and develop further emergency strategies in future work, e.g. data driven approaches based on artificial intelligence.

Some effects that occurred in the prototype experiments, such as stronger vibrations or higher cable forces, reveal improvement potential of the simulation concerning the real world representation. This affects, e.g., the very simple cable model and a missing dynamic pulley model. Of course, adding more effects and higher complexity to the simulation environment will most likely increase computing times, which needs to be considered. In the experiments, cable folding was experienced for platform orientations in a smaller interval than $[-90; 90]^\circ$. Therefore, the assumption defined in Section 4.3.4 needs to be adapted, ideally by incorporating algorithms for the detection of self collisions. To substitute the ideal pose measurement, the forward kinematic algorithm may also be incorporated within the simulation. Furthermore, it can be assessed how the algorithm is affected if cables get slack momentarily. Since cable folding cannot always be suppressed, it should also be studied if and how this effect can be integrated into the pose and velocity estimation. To study the accuracy of this estimation based on the forward kinematic algorithm, an external measurement device, such as a camera or laser tracker, could be used. Finally, the platform of the SEGESTA prototype appears to tip over very easily. Thus, the conceptual idea of failure resistant design, as discussed in Section 4.3.1, should be considered.

Chapter 6

Cable Robots for Automation in Construction – Practical Examples

In this chapter, the application of robots – and especially cable robots – for automation in construction is focused. The construction industry, especially in Germany, suffers from labor shortage and a low degree of automation, which can be addressed using robots. Well-known approaches for robotized construction are described and basics on Building Information Modeling (BIM) are presented. A toolchain to generate robot inputs from BIM data for automated masonry is shown. Two cable robot prototypes developed within the research group are presented and briefly explained, addressing large scale 3D-printing of concrete elements as well as automated masonry. Based on BIM data and robot models, a framework for trajectory planning and optimization in automated masonry tasks is described, showing exemplary results. Finally, cable failure in an automated masonry process using a cable robot is considered in simulation and the proposed emergency strategies are applied. Moreover, reconfiguration of movable pivoting pulleys is utilized to counteract in case of cable failure.

6.1 Robotic Approaches for Construction

As mentioned within the state of the art, see Section 1.1, CDPRs own outstanding properties that qualify them in particular for the application in construction tasks. These advantages consist of a huge and adjustable workspace through the use of cables, the opportunity to

carry large payloads as well as their lightweight design and setup. They are very modular and it is conceivable to mount them to a climbing framework to serve multiple storeys [Bruckmann et al., 2016, Bruckmann and Boumann, 2021]. The robot frame can be chosen according to the desired building geometry and the robot's platform may navigate over the whole construction site. Finally, multiple cables and a proper choice of mechanical components and motorization allow for payloads up to tons [Pott, 2018].

6.1.1 Robotized Construction

The construction industry, especially in Germany, suffers from shortage of qualified labors. At the same time, the construction industry is one of the least automated fields, revealing high potentials for the integration of robots and automation into the processes [Bruckmann et al., 2016, Roske et al., 2021a]. The state of the art in robotized construction features numerous projects and approaches to automate construction processes. Thus, only a small selection can be briefly presented here. Nevertheless, credit is due to all concerned.

The focus of the given projects and solutions is usually on the implementation of isolated steps in the construction process of structures. Early projects such as ROCCO (RObot assembly system for Computer integrated COnstruction) [Andres et al., 1994, Spath et al., 1994] and BRONCO [Bock and Linner, 2016, Pritschow et al., 1994, Pritschow et al., 1998] have been carried out in the 1990s, using conventional industrial robots. To cope for their limited range, they might be combined with mobile platforms [Bonwetsch, 2015, Helm, 2014, Helm et al., 2012]. Still, such systems suffer from limited payload and vertical range. Furthermore, mobile platforms, especially on rough and complex terrain, are rather slow and navigation challenges have to be solved [Dörfler et al., 2016, Sandy et al., 2016].

There are also existing solutions on the market, such as the Semi-Automated Mason (SAM), offered by the American company `Construction Robotics LLC`, employing a conventional serial robot on a mobile platform [Bock and Linner, 2016]. It is to note that the system is only semi-automated, requiring a human bricklayer whose productivity, however, is enhanced by a factor of five.

Another system offered by the Australian company `Fastbrick Robotics` is HadrianX [FBR Ltd, 2023]. It features a very long robot arm with a mounted conveyor belt to transport bricks to the end effector. Still, according to [Brehm, 2019], the bricks are bonded with glue, which causes issues in material recycling. The number of storeys is also restricted due to the robot's workspace and the large arm tends to oscillate, which needs to be compensated. Finally, the payload is limited and the robot cannot handle heavy construction elements.

A further research project proposes the so-called Wallbot [Zickler R, 2021], which also aims at automating the masonry process. It consists of a mobile platform and a conventional

industrial robot. Thus, it is also confronted with proper movement and navigation on the construction site.

Besides automating masonry work, companies also aim at automating further work on site, such as Hilti's Jaibot [Hilti Deutschland AG, 2023], which supports workers by drilling holes in walls and ceilings.

A fundamentally different approach are mobile automated factories, such as SMART (Shimizu Manufacturing System by Advanced Robotics Technology) [Maeda, 1994], developed in the 1990s and employing a 1200 t platform. Further projects are BIG CANOPY (Big Canopy Automation System for High-Rise Reinforced Concrete Buildings) and ABCS (Automated Building Construction System) [Ikeda and Harada, 2006, Wakisaka et al., 2000], which unite automated and conventional processes to realize large steel constructions, recently using moving platforms [Arshad, 2012]. Such factories differ for each construction project and need to be changed individually. As their mass and complexity lead to high efforts in setup and dismantling, they are primarily economic for high-rise buildings.

Recently, the trend has also gone to 3D-printing of concrete, which is being investigated in a large number of projects by a wide variety of players and robotic systems. Examples include the company Vertico [Vertico, 2023], which offers solutions for concrete printing and is involved in robotic 3D-printing of concrete building components for residential buildings in Saudi Arabia [Alabbasi et al., 2023]. In addition, the company Peri should be mentioned, which realized the first 3D-printed residential building in Beckum, Germany [Weger et al., 2021]. While Vertico employs conventional industrial robots, Peri uses a large gantry system manufactured by the company Cobod [Cobod International A/S, 2023].

In addition to construction, the renovation or dismantling of structures should also be considered. The project Bots2Rec, for example, introduced various mobile robotic units for automated removal of asbestos contamination on construction sites [Detert et al., 2017].

As an alternative, the conventional robot systems are opposed by cable-driven parallel robots, which can be used versatile due to their advantages. [Shahmiri and Gentry, 2016] present details of suitable construction processes using cable robots and discuss the specific requirements. Besides general transportation tasks as displayed in [Lytle et al., 2008], contour crafting was focused in [Williams et al., 2008a, Williams et al., 2008b], investigating also economical feasibility [Bosscher et al., 2007]. The CDPR CoGiRo has been utilized to investigate on additive manufacturing for construction in practical full-scale demonstrations [Izard et al., 2018]. In Stuttgart, the CaRo Printer has been developed and tested [Pott et al., 2019], which, however, was not used for construction tasks. Additive and subtractive construction processes using cable robots have been investigated in the EU project Hybrid INDustrial CONstruction (HINDCON) [Papacharalampopoulos et al., 2020]. At the same time, a CDPR for the installation of facade modules has been implemented success-

fully in the EU project HEPHAESTUS [Iturralde et al., 2022, Iturralde et al., 2020]. Besides these tasks, CDPRs have been proposed for automated masonry construction, e.g. in [Bruckmann et al., 2016, Moreira et al., 2015, Sousa et al., 2016, Vukorep, 2017], while first experiments were limited to small scales, e.g. using wooden bricks [Fingrut et al., 2019, Wu et al., 2018]. Finally, the research group in which the author is located also developed two cable robot prototypes for different tasks on the construction site, which are presented in Section 6.1.3 and Section 6.1.4.

6.1.2 Building Information Modeling (BIM)

To employ robots or automation systems on a construction site, data is required to decide on the robot's or system's actions and movements. Digital building construction data for this purpose can be made available, using building models according to Building Information Modeling (BIM). BIM describes a software based method for interconnected planning, construction and management of buildings by digitally modeling and combining all relevant building data. Thus, BIM models can provide all required information such as geometry data of masonry, from which the necessary robot movements can be derived [Borrmann et al., 2018, Bruckmann and Boumann, 2021, Sacks et al., 2018]. Additionally, those models can be used for monitoring and maintenance purposes after building completion. Recent trends include 4D and 5D modeling, monitoring using artificial intelligence and sustainability aspects [Pfeil, 2023, Pfeil and Kemand, 2023].

In own publications of the author [Boumann et al., 2020a, Boumann et al., 2020b, Bruckmann and Boumann, 2021], a software framework based on BIM Data is developed to simulate and optimize an automated masonry process using a CDPR or load sharing drones [Herrmann, 2023, Herrmann et al., 2022], see Section 6.2. Thus, a broader insight on masonry and simulation using BIM is given hereafter.

In recent years, fundamental steps have been taken to incorporate masonry into BIM standards at the material level. The requirements to define masonry are described by [Gentry, 2013]. As part of the Building Information Modeling for Masonry (BIM-M) initiative, these requirements are developed into appropriate levels of detail (LOD) for specific purposes within a Masonry Unit Definition (MUD) model by [Cavieres et al., 2016]. A neutral data structure for automated generation of a masonry model on material level was employed by [Mousavian and Gentry, 2014]. Simulation approaches to model and optimize the logistics on size are introduced by [He and Wu, 2012, RazaviAlavi and AbouRizk, 2017]. This is further elaborated by [Astour and Franz, 2014], performing an optimization of site layouts with a focus on the use of a tower crane using agent systems. It is based on geometry data from BIM models. Spatial demands of construction processes are simulated by [Marx and König, 2013], using BIM models in order to identify overlaps. In

[Wang et al., 2015], a site layout optimization algorithm for tower cranes and material deposit is combined with BIM.

At the author's institute, a toolchain was developed to generate robot input data for automated masonry processes based on a BIM model in IFC format of a building to be constructed [Gifary, 2020, Lou, 2021]. The Industry-Foundation-Classes (IFC) are open data formats for the exchange of BIM data, standardized in DIN EN ISO 16739 [DIN EN ISO, 2021]. Various data formats might be used, such as the STEP Physical Format (SPF or IFC-SPF) based on the ISO 10303-21 standard [ISO, 2016] or the XML format (IFC-XML) defined by ISO 10303-28 [ISO, 2007]. Within the toolchain, a layered construction of the building is assumed using interlocking masonry. First, the BIM model of the building is converted from IFC STEP format into a BREP model (boundary representation) using IfcOpenShell [Krijnen, 2023]. Secondly, cross sections of the building are created, each representing one layer of masonry units. Afterwards, the segments to be erected are extracted considering their edges. Those segments are subsequently filled by cuboid masonry units that comply with predefined standard formats. Using calcium silicate units, those might be e.g. 6DF or 9DF [Rich, 2014]. Filling all segments over all layered cross sections, various rules are followed. Besides ensuring a robotically compatible laying sequence of the masonry units to avoid collisions between a gripper and the erected masonry, the required overlap within the masonry is also respected. This also applies to the connection of intermediate walls. Moreover, lintels for doors and windows are considered. The algorithm is furthermore able to cut masonry units, if a wall segment cannot be filled using regular units. In the last step, the coordinates of all units to be placed with respect to a chosen building frame are written into an excel file, serving as interchange format. Finally, the outputted file contains all target coordinates for each building element to be gripped, transported and set down by the robot and serves as input for a prototype (see Section 6.1.4), as well as for a simulation and optimization of robot trajectories (see section 6.2). The process is exemplified in fig. 6.1. For more details on the algorithm it is referred to [Gifary, 2020, Lou, 2021].

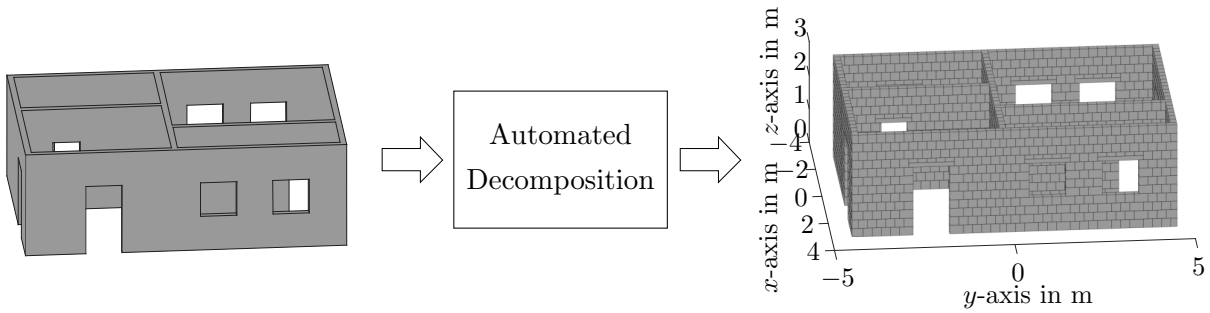

Figure 6.1: Automated decomposition of an IFC BIM model for masonry data.

6.1.3 A Cable Robot for Automated 3D-Printing of Concrete Elements - The Bauhaus Experiment

On the occasion of the 100th anniversary of the Bauhaus University of Weimar (2019), a cable robot for automated large scale 3D-printing of concrete was developed, installed and demonstrated by the team to which the author belongs during the process of this work. It was the first time that concrete facade elements were manufactured by a cable robot, which was publicly shown in a live demonstration to a large audience [Bauhaus-Universität Weimar, 2023]. The project and the system, as depicted in fig. 6.2, will be briefly explained within this section. Further details can be found in [Hahlbrock et al., 2022]. Credits are due to all people involved, supporters and sponsors. The cooperating team consisted out of three groups originating from different universities, namely the Professorship for Theory and History of Design at the Bauhaus-University Weimar, the Professorship for Digital Methods in Architecture at the University of Applied Sciences Dortmund and the Professorship for Mechatronics at the University of Duisburg-Essen. A digital toolchain was developed, which allowed for flexible integration of different robots [Bauhaus-Universität Weimar, 2023] to extrude cementitious material according to a precise digital blueprint.

Within the project, 115 carbon-reinforced concrete facade panels have been produced, as depicted in fig. 6.2. In order to 3D-print such parts robotically, the material to be processed must meet various requirements: It must allow for a stable aggregation, yet be soft enough to

Figure 6.2: A CDPR for concrete 3D-printing, facade elements installation and test specimen.

be conveyed via a pump. Furthermore, it must harden quickly enough to bear the loads of the layers placed on top, while at the same time bonding properly with it. The chosen material TF10 CARBOrefit® FINE CONCRETE [PAGEL Spezial-Beton GmbH & Co. KG, 2019] was taken as a basis and adjusted with an industry partner to meet the requirements. Using a screw pump, the material was then carried to the printing head, attached as a robotic tool at the CDPRs platform.

As depicted in fig. 6.2, the cable robot was installed outdoors into an existing steel frame for the exhibition in July 2019. It featured an approximate build space of 35 m^3, using eight cables driven by servo motors and connected via EtherCat to a `BECKHOFF` PLC. All components were designed to withstand a load of 2500 N per cable, for which the high-performance material Dyneema was chosen with a diameter of 6 mm. Moreover, options for easy steel frame attachment were integrated for the drive units and the pulleys. Using a model based control scheme, the robot was able to precisely follow a given trajectory. To enable the digital production toolchain, also a G-Code[1] interface was provided.

The design of the facade system was realized using an algorithmic approach in Rhinoceros and Grasshopper [McNeel and Associates, 2023]. Based on the position of the facade panels relative to a viewer, different shapes were automatically generated and converted into paths that were transferred to the robot. The geometry of the panels consisted of rectangular spirals with a panel size of 590 × 590 × 32mm. In addition to the production of facade elements, tests with several layers on top of each other were also carried out to test the material and to check whether the printing of larger structures is generally possible, see fig. 6.2. As a result of the project, multiple surfaces of the steel structure have been covered with the computationally designed arrangement of the 115 facade elements.

The project has successfully demonstrated a novel approach in robotic construction featuring computational design and a fabrication method, which can be implemented using a 3D-printing cable robot. Such robot allows for new opportunities in on-site fabrication of individualized parts. Moreover, the realization of accents and customizations while building construction is conceivable, leveraging architectural potentials. Within the funding "Langfristige experimentelle Untersuchung und Demonstration von automatisiertem Mauern und 3D-Druck mit Seilrobotern" by the Ministry of Regional Identity, Communities and Local Government, Building and Gender Equality of the Land of North Rhine-Westphalia, further aspects of the technological development are addressed, featuring e.g. an automated and integrated printing head (see fig. 6.2, top left) as well as further experiments.

[1] G-Code is a standardized data format, typically applied within CNC-machines and 3D-printing. Usually it can be derived from CAD/CAM data [Stark, 2022].

6.1.4 A Cable Robot for Automated Masonry Construction

A cable robot for the application in automated construction was developed by the team to which the author belongs within the AiF-IGF funded project "Entwicklung von Seilrobotern für die Erstellung von Kalksandstein-Mauerwerk auf der Baustelle". The scope of the project was to prove the applicability of cable robots for automated construction of masonry according to a digital building plan, using conventional calcium silicate units and thin bed mortar. The developed **ca**ble **r**obot for **l**arge scale applicati**o**ns was given the name CARLO, to which it is referenced further on. Furthermore, the development of the system and infrastructure was also supported in the project "Langfristige experimentelle Untersuchung und Demonstration von automatisiertem Mauern und 3D-Druck mit Seilrobotern" by the Ministry of Regional Identity, Communities and Local Government, Building and Gender Equality of the Land of North Rhine-Westphalia. Credits are due to all people involved in the project and to all supporters and sponsors.

As masonry is one of the most established construction processes, a broad expertise was required. Thus, the project team was formed out of four institutions covering various work packages. The cable robot including a fully automated gripper tool was developed by the team within the Professorship for Mechatronics at the University of Duisburg-Essen. The Institute for Applied Building Research in Weimar designed and built a machine for automated mortar application to masonry units and for handing them over to the cable robot. The Professorship for Construction Operations and Management at the University of Duisburg-Essen took care on building design, digital building plans and together with the German Calcium Silicate Research Association e. V. ensured that the implementation meets the requirements of construction sites, building materials and the established norms and procedures.

The system at the facility in Duisburg as depicted in fig. 6.3 is extensively presented in various publications, e.g. [Heidel et al., 2022, Roske et al., 2021a, Roske et al., 2021b], thus it will only be briefly described here. Whereas the long term strategy aims at full automation of the masonry or even the whole construction process, only a semi-automated plant could be realized within the project due to the given resources. While all of the mortar application and masonry process is automated using the mortar application machine and the cable robot, only the feeding of the masonry units into the system needs to be done manually. Afterwards, the machine applies mortar to the calcium silicate unit and hands it over to the cable robot at a defined position, which can be adjusted in height with the rising building. Finally, the cable robot places the unit at the position defined by the digital building plan. The $9 \times 6 \times 3$ m large building, planned within the project, was processed according to the BIM toolchain described in Section 6.1.2, to generate the input data for the robot system. The robot can carry a weight up to 80 kg with a speed up to several meters

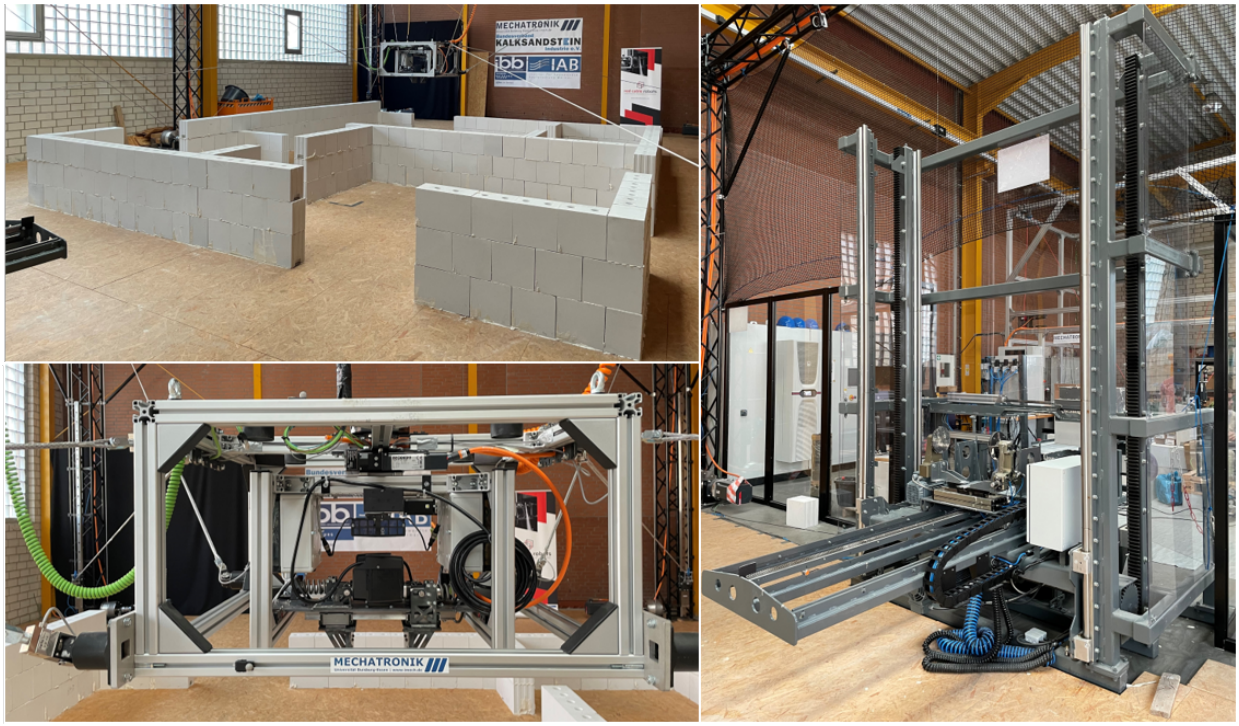

Figure 6.3: The CDPR for automated masonry construction CARLO and the mortar plant.

per second, allowing also for the transfer of lintels. Furthermore, the end effector owns some outstanding features: A passively secured gripper system can hold the payload even in case of power failure. Several laser sensors ensure accurate positioning as well as proper gripping and placing of the masonry units, obtaining an accuracy relative to the erected masonry of 5 mm in first tests [Heidel et al., 2022]. Also the cable forces are measured at the cable attachment points.

To allow the robot to climb in the frame as the building grows, sliding pulleys were implemented for system reconfiguration. The four lower pulleys are movable in vertical direction on linear slides to enable collision avoidance in the construction process. During system design, a digital twin and a digital toolchain were generated [Roske et al., 2021a, Roske et al., 2021b]. Dynamic simulations have been conducted to estimate power consumption and system speed in order to identify optimal robot parameters as well as optimal workspace dimensions. As a result, according motor and gear combinations were chosen. Using the data, the automated building construction was simulated. Trajectories with assured collision freedom (cables, platform with gripper and erected building) were calculated for each building element [Boumann et al., 2020a, Bruckmann and Boumann, 2021], which will be described further in the next section. Derived from this, an augmented reality application was developed to visually control the process on the construction site and strengthen acceptance [Lemmen et al., 2022]. Using models of energy consumption, see Section 6.2, as well as cost estimations, the economic feasibility was analyzed [Bruckmann and Boumann, 2021,

Herrmann et al., 2022]. Besides conventional manual workers, the system was also compared to a system of load sharing drones for masonry unit transportation in [Herrmann et al., 2022].

Due to its impact onto the construction industry, public interest on the system was exceptional and it was presented to broad public audiences at numerous occasions. One noteworthy event was the visit by the Federal Minister for Housing, Urban Development and Construction of the Federal Republic of Germany, Klara Geywitz, in the summer of 2022 [BMWSB, 2022].

In ongoing activities, a motion capturing system is tested for increased positioning accuracy. Furthermore, the project "Auf dem Weg zur digitalen Bauausführung: Automatisierung des Rohbaus mit Seilroboter-Technik", funded by the Ministry of Regional Identity, Communities and Local Government, Building and Digitalization of the Land of North Rhine-Westphalia, currently investigates on the construction of intermediate ceilings using the cable robot CARLO. [Jeziorek et al., 2023] describes first concepts that have been developed. Moreover, it is planned to optimize the masonry process using CARLO in terms of speed and accuracy. Finally, the team is looking forward to do first on-site experiments with the system.

6.2 Trajectory Planning and Optimization for Automated Masonry Construction Using CDPRs

If the data for the building to be constructed is available, as described in Section 6.1.2, the question arises, as to which trajectory each building element takes from its start to its destination using a known robot. Within this, the workspace limitations, stiffness issues caused by elasticity and disturbances as well as cable collisions [Jung, 2020, Williams et al., 2008a] need to be considered. Besides that, a path might be demanded for a minimal transportation time or low energy consumption. In order to take care of these partially contradictory goals, an optimization of the trajectory is necessary. To reflect these challenges, a model based software framework is developed by the author of this thesis in [Boumann et al., 2020a, Boumann et al., 2020b, Bruckmann and Boumann, 2021] to simulate and optimize CDPR based automated masonry construction processes, while considering and optimally exploiting the constraints of the robot system. The following explanations in this section are based on [Bruckmann and Boumann, 2021] and [Herrmann et al., 2022]. The simulation is based on the approaches to robot modeling as described in Chapter 2, relies on a full digital description of the masonry as generated by the approaches described in Section 6.1.2 and can be parameterized using the robot CARLO for example, see Section 6.1.4. The framework is set up modular and highly versatile: Different optimization goals can be aimed and the robot models are interchangeable. In

[Herrmann, 2023, Herrmann et al., 2022], it is successfully demonstrated to integrate models of load sharing drones into the trajectory planning.

It is important to note that the simulation framework introduced in this section differs from the simulation environment introduced in Section 4.2. It does not include dynamic motor and cable simulation or control loop closure. This results in higher computational efficiency, required for effective optimization of the trajectories.

Since the setup of a full scale automated construction system is expensive, preliminary predictions and estimations on the construction process, the building, suitable robot variants and their performance can be done using the framework. Crucial parameters and factors can be identified in a very early stage and thus, the monetary risk can be reduced while potentially saving costs without the need for expensive experiments. In future, the framework will serve as a process model using feedback from real world data on construction sites [Bruckmann and Boumann, 2021]. Thereby, it can be enabled as a Digital Twin of the automated construction process as well as a part of a system-of-systems according to [Sacks et al., 2020].

6.2.1 Parametrization of Trajectories

As outlined in Section 2.5.2, a well-known description of a trajectory can be done using splines, set up by interconnected polynomials. The number of segments used per spline is n_s. The basic idea now is to change the knots of the polynomials and their derivatives within an optimization until the best possible trajectory is obtained.

To represent the platforms pose, velocity, acceleration and jerk at the connection points with a continuous profile, polynomials of the 7^{th} order are required. For each DOF of the platform, one spline is assigned. For simplicity and to reduce computational costs, a constant platform orientation is assumed. Note that the framework allows for polynomials of higher orders as well as any number of interconnected polynomials. However, a polynomial with high order tends to strong oscillation [Bruckmann and Boumann, 2021]. Choosing three connected polynomials of 7^{th} order has proved effective [Bruckmann and Boumann, 2021, Herrmann et al., 2022] and is considered further on, as a compromise between trajectory flexibility and required calculation time. Of course, a higher number n_s leads to increased computational effort, as the number of knots and thus optimization variables rises.

The start of the trajectory in case of the robot CARLO is defined by the hand over position of the masonry units, while the goal is defined by the masonry plan, see Section 6.1.2. At both poses, the platform shall be at rest. At the knots, the platform may have a certain speed or acceleration, while the jerk at the knots is set to zero to reduce the number of optimization variables. Besides the platform's pose, the motion of each of the lower four sliding pulleys $s_j, j \in \{5, 6, 7, 8\}$ is described with one spline, assuming

	Start (1st knot)	2nd knot	3rd knot	Goal (4th knot)
Spline segment	1	2	3	
Platform position; one spline per DOF; i.e. three splines in total				
Spline order	7	7	7	
Constraints	$\boldsymbol{r}_P$ is given; $\dot{\boldsymbol{r}}_P, \ddot{\boldsymbol{r}}_P$, $\dddot{\boldsymbol{r}}_P$ are set to zero	$\boldsymbol{r}_P, \dot{\boldsymbol{r}}_P, \ddot{\boldsymbol{r}}_P$ are parameters, $\dddot{\boldsymbol{r}}_P$ is set to zero	$\boldsymbol{r}_P, \dot{\boldsymbol{r}}_P, \ddot{\boldsymbol{r}}_P$ are parameters, $\dddot{\boldsymbol{r}}_P$ is set to zero	$\boldsymbol{r}_P$ is given; $\dot{\boldsymbol{r}}_P, \ddot{\boldsymbol{r}}_P$, $\dddot{\boldsymbol{r}}_P$ are set to zero
$\sum$ of constraints per DOF	4	4	4	4
$\sum$ of optimization parameters in total	0	3×3	3×3	0
Pulley position; one spline per pulley; four splines in total				
Spline order	3	5	3	
Constraints	$\boldsymbol{s}$ is a parameter; $\dot{\boldsymbol{s}}, \ddot{\boldsymbol{s}}$ are set to zero	$\boldsymbol{s}$ is a parameter; $\dot{\boldsymbol{s}}, \ddot{\boldsymbol{s}}$ are computed from first segment	$\boldsymbol{s}$ is a parameter; $\dot{\boldsymbol{s}}, \ddot{\boldsymbol{s}}$ are computed from last segment	$\boldsymbol{s}$ is a parameter; $\dot{\boldsymbol{s}}, \ddot{\boldsymbol{s}}$ are set to zero
$\sum$ of constraints per pulley	3	1 (1st segment); 3 (2nd segment)	1 (last segment); 3 (2nd segment)	3
$\sum$ of optimization parameters in total	4×1	4×1	4×1	4×1

Table 6.1: Description of spline and optimizer parameters according to [Boumann et al., 2020a].

powerful linear drives and dynamic online reconfiguration of the robot. Here, lower spline orders are chosen as the pulley movement requires less adjustment options and jerk is not considered. The first and the last polynomial are of 3rd order, while the second polynomial is of 5th order. This can be summarized as shown in table 6.1. The translational platform movement in 3 DOF can be adjusted by 18 optimization parameters while 16 parameters are added for the movement of four pulleys. The remaining polynomial parameter result from the respective boundary conditions. In addition, one time duration t_s is used per spline, which adds 3 parameters, as the trajectory time can also be adjusted. Here, platform and pulley splines are synchronized for simplicity. This leads to a total of 37 optimization parameters. If pulley movement is neglected during a trajectory and the pulleys are fixed, 21 parameters remain. It is also conceivable to adjust all pulleys to a constant (optimized) height before each trajectory, which would lead to 25 optimization parameters [Bruckmann and Boumann, 2021]. For other systems, such as load sharing drones, the number of optimization parameters may differ [Herrmann, 2023, Herrmann et al., 2022]. Now,

each spline needs to be discretized to evaluate the chosen robot model along the trajectory. The number of discretization steps along each spline is n_d, with $k \in \{1, \ldots, n_d\}$ describing the according step. In first work of the author [Boumann et al., 2020a], a constant number of steps per spline segment is used. Here, the number of steps per spline segment is scaled with each time duration, to simplify the expression of the employed cost functions, see Section 6.2.3 [Bruckmann and Boumann, 2021, Herrmann et al., 2022].

6.2.2 Optimization Approach

In this section, it is elaborated how the problem of contrary objectives for trajectory optimization is transformed into a numerical optimization process. The multiobjective problem is addressed by assigning a cost function per each criterion χ to be optimized (e.g. collision avoidance). All cost functions follow the same scheme, producing a single value at evaluation. For each criterion χ, a cost value $\mathcal{V}_\chi$ results out of a chosen individual function, which is further detailed in the upcoming sections. The cost value is then multiplied with an individual weight $\mathcal{W}_\chi$. To satisfy the constraints given by the chosen robot system, a penalty term $\mathcal{P}_\chi$ is added, which is assigned as soon as a constraint violation occurs (e.g. a collision between a cable and masonry). This leads to the total cost value

$$\mathcal{V}_{\text{total}} = \sum_{\chi} (\mathcal{W}_\chi \cdot \mathcal{V}_\chi + \mathcal{P}_\chi). \tag{6.1}$$

Minimizing this value with respect to the chosen weights and functions by adjusting the trajectory's optimization parameters, as described in the previous section, will lead to an optimal trajectory. While some cost functions can be evaluated easily for a whole trajectory (e.g. a low transportation time), other cost functions need a discretization of the spline, as described previously.

Note that, depending on the problem and parameters, usually a global optimization problem results that introduces numerous local minima and thus requires according optimization algorithms. The Optimization Toolbox as well as the Global Optimization Toolbox of `MATLAB` [The MathWorks, Inc., 2023c] introduce a variety of suitable optimization algorithms. A Particle Swarm Optimizer has proven effective for this framework [Bruckmann and Boumann, 2021]. For particular problems, e.g. time optimization of a spatially fixed trajectory, a gradient based method is also a sound choice [Herrmann et al., 2022]. The whole optimization process for a trajectory is illustrated in fig. 6.4. Note that only a solution without penalties is considered feasible. If no penalty free solution can be found, either the robot parameters or the building plan need adjustment.

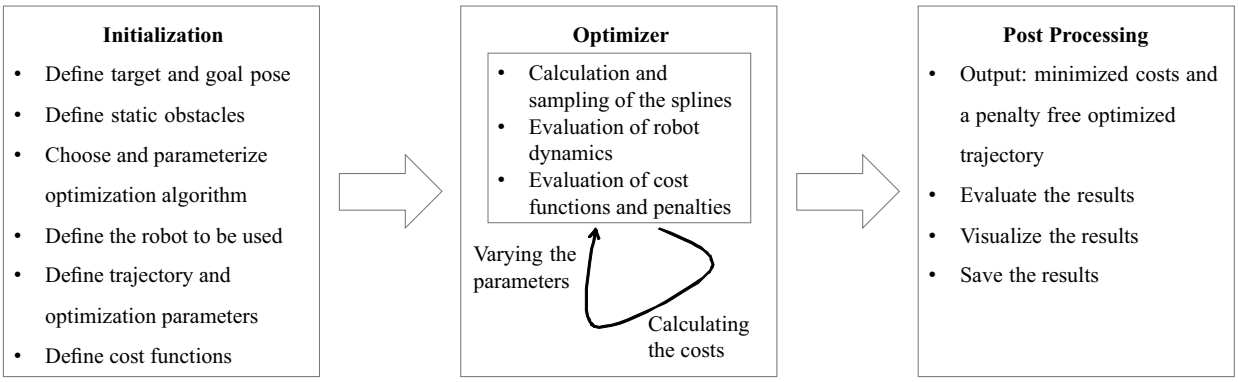

Figure 6.4: Trajectory optimization process using the proposed framework adapted from [Herrmann et al., 2022].

6.2.3 Optimization Criteria and Cost Functions

Typical optimization criteria that result from cable robot specific challenges, such as collision avoidance or workspace limitations due to cable force, are well-known from literature, see e.g. [Bosscher et al., 2007, Pott, 2018]. Further optimization criteria result from practical demands or limitations. A low transportation time and a minimal energy consumption contribute to economical feasibility, while the employed drives and gears, for example, limit the maximum speed and acceleration. An overview of useful criteria is provided by the author in [Bruckmann and Boumann, 2021, Herrmann et al., 2022]. Chapter 2 presents the underlying models to set up cost functions based upon the chosen criteria for trajectory optimization. More fundamentals can be found in contributions of [Bosscher, 2004, Pott, 2018], as well as in work of the author [Boumann et al., 2020a, Bruckmann and Boumann, 2021, Herrmann et al., 2022]. In detail, the cost functions for the individual criteria χ are elaborated in the upcoming paragraphs. Using different robotic systems in the simulation framework, different cost functions may apply. For cooperating and load sharing drones, this may include costs for rotor speed or penalties for collisions between drones [Herrmann et al., 2022].

Transportation Time For economical aspects, the trajectory time should be as low as possible. The time duration per each spline is defined within the vector of time segments $\boldsymbol{t}_s$. To achieve descending costs with shorter time, the cost function

$$\mathcal{V}_{\text{time}} = t_{\text{total}} = \sum_{i=1}^{n_s} \boldsymbol{t}_s(i) \tag{6.2}$$

is introduced. As a negative $\boldsymbol{t}_s$ is unfeasible and too long transportation times may be undesired, the boundaries $[0, t_{\max}]$ are set, raising $\mathcal{P}_{\text{time}} = 0$ if they are violated.

Trajectory Constraints On position level, the end effector is constrained by the robot's frame and the ground. The robots maximum velocity and acceleration depend on the drives, but may also be limited due to safety reasons. A violation of the trajectory's constraints on position level would lead to collisions between the platform and the robot's frame or the ground. For this criteria, only penalties in the form of $\mathcal{P}_{\text{pos}}$, $\mathcal{P}_{\text{vel}}$ or $\mathcal{P}_{\text{acc}}$ are charged if the constraints are violated. Naturally, the drive velocities can be limited separately. However, a limitation within the task space of the robot is intuitive. The boundaries $[\boldsymbol{r}_{P_{\min}}, \boldsymbol{r}_{P_{\max}}]$ and their two time derivatives are introduced as platform rotation is neglected here.

Cable Forces / Actuator Torques As elaborated in Section 2.3, the cable forces should always be in between $f_{\min}$ and $f_{\max}$ to keep the platform within the $\mathcal{WFW}$. Furthermore, the drives producing the cable forces have limited capabilities. In principal, all cable force distributions within the force boundaries $f_{\min}$ and $f_{\max}$ are acceptable along a trajectory. Every time the force boundaries are violated and the robot exits the $\mathcal{WFW}$, the penalty $\mathcal{P}_{\text{force}}$ is added. The recurring increment of the penalty supports the optimizer when resolving trajectories with multiple force limit violations. Since low cable forces are preferably for low energy consumption, this is defined as desired and the cost function

$$\mathcal{V}_{\text{force}} = \frac{1}{n_d\, m}\Big(\sum_{k=1}^{n_d}\sum_{i=1}^{m}\frac{f_i(k) - f_{\min}}{f_{\max} - f_{\min}}\Big) \tag{6.3}$$

is set up. Note that $\boldsymbol{f}_D(k)$ is the cable force distribution at the k^{th} discretization step of the trajectory and $f_i(k)$ its i^{th} cable's force. For all cables at $f_{\min}$, $\mathcal{V}_{\text{force}}$ is zero. To prevent it from getting negative, $\mathcal{V}_{\text{force}} = 0$ is also set if a penalty $\mathcal{P}_{\text{force}}$ is experienced.

According to eq. (2.51), the drives require a certain torque to overcome their friction, accelerate or decelerate their inertia and produce the required cable forces. Thus, the limited motor torque capabilities are considered additionally. Each violation of the torque constraints $[-\tau_{\max}, \tau_{\max}]$ adds a penalty $\mathcal{P}_{\text{torque}}$. A function $\mathcal{V}_{\text{torque}}$ is not used within this work. Note that a gear ratio n_g and a torque transmission efficiency η_g are also introduced according to [Bruckmann and Boumann, 2021].

Power and Energy Naturally, an electronic power supply has limitations. Only a certain amount of power can be withdrawn from the electricity supply and the total energy consumption adds to the economical and ecological aspects. Thus, the maximum power needs to be constrained adding $\mathcal{P}_{\text{Power}}$ every time time the power limit $P_{E,\max}$ is surpassed by the overall power per discretization step $P_E(k)$. For modeling of the system's power consumption, it is referred to [Herrmann et al., 2022]. The inverter efficiency η_n and the recuperation efficiency η_r are introduced. Including a monitoring of thermal load, a function $\mathcal{V}_{\text{power}}$ might

be introduced, which is neglected here. The total energy E_{total} required to perform a trajectory movement influences economic aspects as well as ecological. As an energy consumption as low as possible is preferred,

$$\mathcal{V}_{\text{energy}} = E_{\text{total}} = \sum_{k=2}^{n_d} \frac{P_E(k) + P_E(k-1)}{2} \Delta t \tag{6.4}$$

is set, using trapezoidal integration of the power [Bruckmann et al., 2019] with the time step $\Delta t = {}^{t_{\text{total}}}/_{n_d}$. For $E_{\text{total}} < 0$, which is theoretically possible in scenarios with immense recuperation, $\mathcal{V}_{\text{energy}} = 0$ is set. $\mathcal{P}_{\text{energy}}$ is not considered here.

External Collision Depending on its trajectory, a cable robot's platform or cables may collide with objects in the workspace, such as parts of the erected building. As this can cause undesired effects and possible damage, it needs to be avoided. First, collisions in between the end effector and objects are considered. The end effector is described by cuboid geometries called Axis-Aligned Bounding Boxes (AABB) [Ericson, 2004]. The framework also supports Object Oriented Bounding Boxes (OBB) [Ericson, 2004], which align with higher computational costs due to more computation steps in collision testing. Using AABBs, collisions can be checked trivially using the Separating Axis Theorem [Ericson, 2004]. In the case at hand, this approach is feasible, since it is not intended to rotate the robot's platform. The distance to each object $d_{o,ij}$ is determined and an influence distance $d_{\min}$ is defined. If $0 \leq d_{o,ij}(k) \leq d_{\min}$ at the k^{th} discretization step, costs are charged according to

$$\mathcal{V}_{\text{EEOb}} = \frac{1}{n_d\, n_{oo}} \Big(\sum_{i=1}^{n_o-1} \sum_{j=1+i}^{n_o} \sum_{k=1}^{n_d} 1 - \frac{d_{o,ij}(k)}{d_{\min}} \Big), \tag{6.5}$$

with the number of objects n_o and the binomial coefficient $n_{oo} = \binom{n_0}{2}$. For distances greater than $d_{\min}$, the objects can be ignored and no costs are charged. Every time $d_{o,ij}(k)$ gets ≤ 0, a collision is detected and the penalty $\mathcal{P}_{\text{EEOb}}$ is charged. Besides the end effector, also the cables might collide with obstacles. With each collision detected, $\mathcal{P}_{\text{CaOb}}$ is charged for the considered cable. Regarding details on the implementation, it is again referenced to [Herrmann et al., 2022]. For each cable, the Euclidean distance $w_{o,ij}$ to each object is calculated, leading to the cost function

$$\mathcal{V}_{\text{CaOb}} = \frac{1}{m\, n_d\, n_o} \Big(\sum_{i=1}^{m} \sum_{j=1}^{n_o} \sum_{k=1}^{n_d} 1 - \frac{w_{o,ij}(k)}{w_{\min}} \Big). \tag{6.6}$$

Analogous to eq. (6.5), costs are only considered for $0 \leq w_{o,ij}(k) \leq w_{\min}$ with the influence distance $w_{\min}$.

Intrinsic Collision Besides collisions with obstacles, the robot may experience self-collisions in between the cables or a cable and the platform. This needs to be prevented as well. When assessing the trajectory for collisions between the robot's cables and its end effector, the latter can simply be treated as another object using eq. (6.6). For collision detection in between all cables, it is examined if any pair of cables intersect in between two discretization steps along the continuous path of the robot. For each collision detected, $\mathcal{P}_{\text{CaCa}}$ is added. Note that no cost function $\mathcal{V}_{\text{CaCa}}$ is introduced for simplicity and to reduce computational costs. Details on the implementation can be found in [Herrmann et al., 2022], whereas the approach is inspired by Gouttefarde [Nguyen and Gouttefarde, 2015]. For further approaches on cable collision detection it is referred to [Blanchet and Merlet, 2014, Bury et al., 2019, Fabritius et al., 2018, Merlet, 2004a, Merlet and Daney, 2006, Nguyen and Gouttefarde, 2015, Perreault et al., 2010].

Platform Stiffness A higher stiffness at the platform reduces vibration or compliant movement due to disturbances, such as wind. The stiffness at the robot's platform and its displacement resulting from an external wrench $\delta\boldsymbol{w}$ can be calculated according to eq. (2.55). From the homogenized displacement $\delta\boldsymbol{x}_{P,h}(k)$, the stiffness criterion $\kappa = \|\delta\boldsymbol{x}_{P,h}(k)\|_2$ at the k^{th} discretization step is derived. The stiffness throughout the trajectory is calculated as weighted sum

$$\mathcal{V}_{\text{stiff}} = \frac{1}{n_d} \sum_{k=1}^{n_d} \kappa(k). \tag{6.7}$$

Penalties $\mathcal{P}_{\text{stiff}}$ are neglected as no boundaries for the displacement are set. Figure 6.5 exemplifies how the workspace and the stiffness within it can vary depending on the pose and the vertical placement of the four lower pulleys.

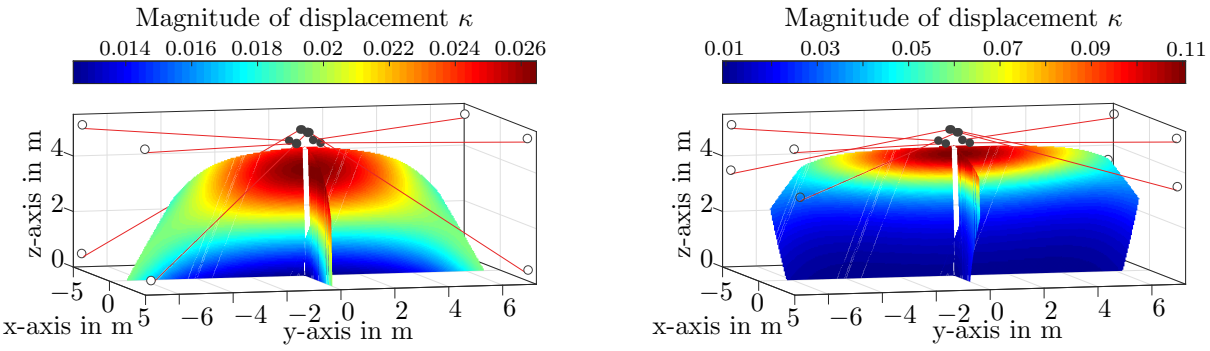

(a) Pulleys in lower position

(b) Pulleys in upper position

Figure 6.5: Workspace slices of CARLO showing stiffness with pulleys in two configurations. $\delta\boldsymbol{w} = [29.1022\text{ N}, 0\text{ N}, -1302.4\text{ N}, 0\text{ Nm}, 12.4533\text{ Nm}, 0\text{ Nm}]$ includes crosswind of $7\frac{\text{m}}{\text{s}}$ and a platform mass of 132.8 kg, carrying a masonry unit.

Dynamic Reconfiguration For the application at hand, the cable robot needs to be reconfigured with rising building. Assuming powerful linear drives, this may be done dynamically throughout a trajectory. Naturally, the drives and the pulley displacements are limited. Thus, the boundaries $[\boldsymbol{s}_{\min}, \boldsymbol{s}_{\max}]$ and its time derivative are introduced, analogous to the trajectory constraints. Violation of those constraints likewise leads to penalties $\mathcal{P}_s$ and $\mathcal{P}_{\dot{s}}$. The actuated motion of sliding pulleys alongside a trajectory with tensed cables is demonstrated in [Reichert et al., 2015a], for example. Please note that for the real prototype CARLO, such drives are not employed. A different solution is used, which is not further detailed here. Fundamentals on the dynamic modeling of the movable pulley can be found in [Bruckmann and Boumann, 2021]. Besides pulley weight m_s, Stribeck friction on the sliding mechanism and the acting cable forces depending on cable direction are considered for fully identical mechanisms. Depending on the normal force acting on the mechanism, the static and sliding friction are determined using the coefficients μ_c and μ_s. The parameters ϵ_s, $F_{v,s}$ and v_s correspond to eq. (2.49). Assuming a sprocket radius of ρ_s, gear transmission of n_ζ and and a torque transmission efficiency of η_s, additional torques $\boldsymbol{\tau}_s$ result. The additional torques are considered within the power and energy models according to [Bruckmann and Boumann, 2021].

6.2.4 Simulative Studies

For further exemplary studies, the building model depicted in fig. 6.1 and employed in fig. 6.3 is used for an automated masonry scenario based on the CDPR CARLO. Two arbitrary masonry units number 20 and 1503 out of 1556 are considered, as shown by the author in [Bruckmann and Boumann, 2021]. Out of the introduced optimization criteria, the influence of dynamic reconfiguration is contemplated in particular. The parameters are set as given

$\boldsymbol{B} = \begin{bmatrix} -4.345 & 4.345 & -4.343 & 4.345 & -4.815 & 4.815 & -4.815 & 4.815 \\ -7.1 & -7.1 & 7.1 & 7.1 & -7.0 & -7.0 & 7.0 & 7.0 \\ 5.1895 & 5.1895 & 5.1895 & 5.1895 & 0.5 & 0.5 & 0.5 & 0.5 \end{bmatrix}$ m							$f_{\min} = 150$ N $\quad f_{\max} = 4.5$ kN
$\boldsymbol{P} = \begin{bmatrix} -0.511 & 0.511 & -0.511 & 0.511 & -0.511 & 0.511 & -0.511 & 0.511 \\ -0.4555 & -0.4555 & 0.4555 & 0.4555 & -0.0315 & -0.0315 & 0.0315 & 0.0315 \\ -0.18 & -0.18 & -0.18 & -0.18 & 0.215 & 0.215 & 0.215 & 0.215 \end{bmatrix}$ m							$\boldsymbol{\Theta}_S = \begin{bmatrix} 9.7492 & 0.3318 & 0.3594 \\ 0.3318 & 12.6779 & 0.2791 \\ 0.3594 & 0.2791 & 15.4368 \end{bmatrix}$ kg m^2
$J_d = 1.4975$ kg m^2		${}_P\boldsymbol{r}_S = [-0.0069, -0.0095, -0.0006]^{\mathrm{T}}$ m			$m_P = 132.8$ kg	$\rho_d = 0.134$ m	
$[\boldsymbol{r}_{P_{\min}}, \boldsymbol{r}_{P_{\max}}] = [\min(\boldsymbol{B}), \max(\boldsymbol{B})]$ m			$[\dot{r}_{P_{\min}}, \dot{r}_{P_{\max}}] = [-6, 6]$ m/s		$[\ddot{r}_{P_{\min}}, \dot{r}_{P_{\max}}] = [-5, 5]$ m/s^2		
$[s_{\min}, s_{\max}] = [0, 3]$ m		$[\dot{s}_{\min}, \dot{s}_{\max}] = [-6, 6]$ m/s			$t_{\max} = 30$ s	$\rho = 0.063$ m	
$d_{\min} = w_{\min} = 0.1$ m	$t_d = 30$	$n_g = 10$	$\eta_g = 0.97$	$\eta_n = 0.95$	$\eta_r = 0.85$	$\eta_s = 0.97$	
$\rho_s = 0.05$ m	$n_\zeta = 20$	$m_s = 20$ kg		$P_{E,\max} = 32$ kW	$\tau_{\max} = 110$ Nm	$f_b = 50$ kN	
$\mu_c = 0.01$	$\mu_s = 0.1$	$F_{v,s} = 1$		$\epsilon_s = 1$	$v_s = 0.001$ m/s	$n_s = 3$	
$\mathcal{W}_{\text{time}} = 0.5 \cdot 1/\text{s}$	$\mathcal{W}_{\text{force}} = 1$	$\mathcal{W}_{\text{energy}} = 0.1 \cdot 1/\text{J}$		$\mathcal{W}_{\text{EEOb}} = 1$	$\mathcal{W}_{\text{CaOb}} = 1$	$\mathcal{W}_{\text{stiff}} = 5000$	

Table 6.2: Parameters of the CARLO prototype.

in table 6.2. As equal parts are used, not all parameters are explicitly stated in matrix or vector form. The platform mass includes a 6DF masonry unit and the platform itself weighs 103 kg. `MATLAB`'s `particleswarm()` algorithm is used with a swarm size of 500 and a maximum number of 10000 iterations, aiming at the identification of a global optimum of eq. (6.1). For replicability and comparability, the same initial seed is set for each trajectory optimization. The functions are employed according to the weights in table 6.2 while all $\mathcal{P}_\chi$ are set to 1000. All already placed masonry units are considered as obstacles. Whole rows or complete layers are combined to large AABBs in order to optimize the computing time. Furthermore, the mortar plant is represented by two AABBs as depicted in fig. 6.6, whereas the lifting part of the mortar plant is changed dynamically with rising building.

First, the trajectories to place the two masonry units considered are optimized with the pulleys in a fixed position throughout the trajectory. The results are displayed in fig. 6.6. For unit 20, the vertically movable pulleys (Numbers $5-8$ in $\boldsymbol{B}$) are in their lowest position. For unit 1503, they are shifted as displayed in fig. 6.6b. In both cases, feasible and penalty free trajectories are found by the optimizer. It stops before reaching the maximum number

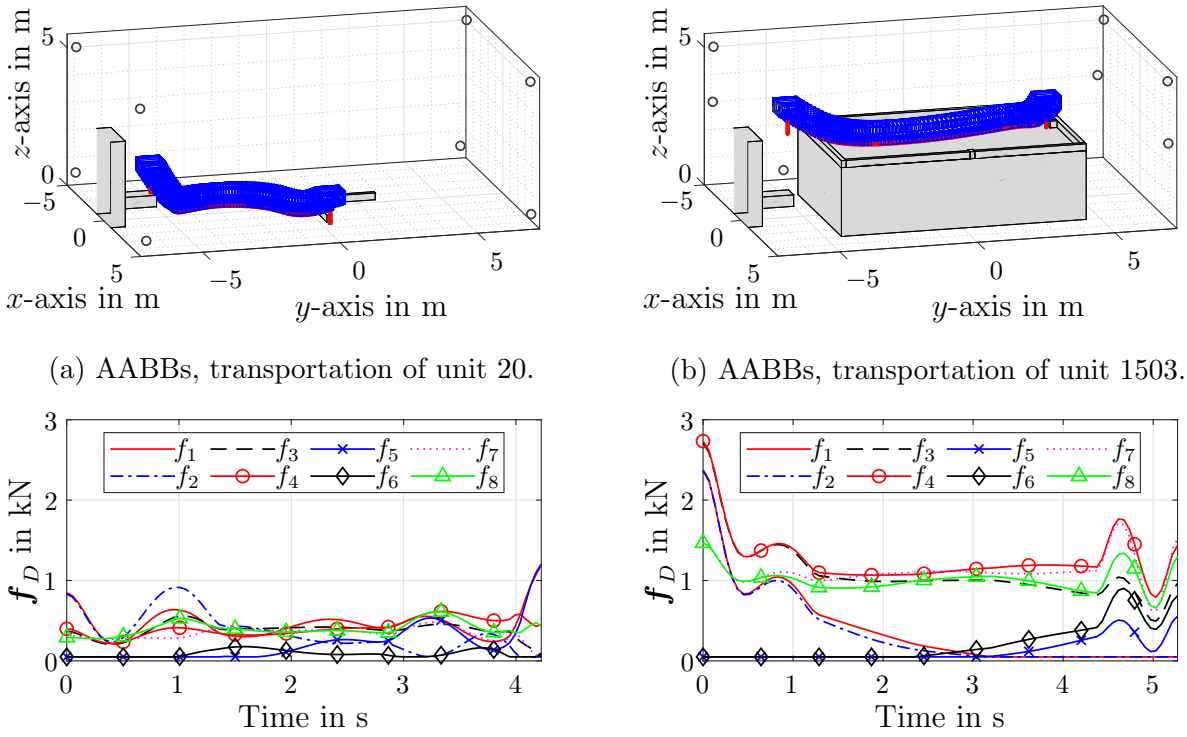

(a) AABBs, transportation of unit 20.

(b) AABBs, transportation of unit 1503.

(c) Forces, transportation of unit 20.

(d) Forces, transportation of unit 1503.

Figure 6.6: Transportation of masonry units no. 20 and no. 1503 without pulley motion. Blue boxes illustrate the bounding boxes of the robot carrying a masonry unit along the path and gray boxes illustrate the obstacle boundaries (Building parts and mortar plant).

of iterations, which indicates global optima. Collisions with the building are prevented and the cable forces progress continuously and within their boundaries. With 5.27 s, the transportation of the masonry unit 1503 takes a little longer than for unit 20 (4.23 s). This is mainly due to the position of the unit in xy-plane. Moreover, the cable forces are remarkably higher for unit 1503. As this scenario is in greater height, the angles between cables and the end effector are disadvantageous, i.e. the required cable forces to compensate for the gravitational forces must raise.

Now, the trajectory to place unit 1503 is optimized while the pulleys can move dynamically. A comparison to the scenario with fixed pulleys is depicted in fig. 6.7. Comparing both cases, it is clearly visible how the optimizer utilizes the dynamically movable pulleys in the second scenario. The trajectory duration is shortened to 4.81 s and the total energy consumption is reduced from 5.19 kJ to 4.74 kJ. The system starts with the pulleys in a higher position. Subsequently, energy is harvested temporarily by the optimizer by lowering pulleys 7 and 8 throughout the trajectory. Despite pulley movement and corresponding movement of the cables through the workspace, all collisions are prevented, which shows a successful operation of the optimizer. In all cases, the optimization is stopped before reaching the maximum number of iterations, while no penalty is raised in the final results. For further studies regarding influence of parameters and cost functions it is referred to [Boumann et al., 2020a, Boumann et al., 2020b, Bruckmann and Boumann, 2021, Herrmann, 2023, Herrmann et al., 2022].

While the optimization results for trajectory generation are promising, the prototype CARLO is already in operation using non-optimized trajectories [Heidel et al., 2022]. It is part of ongoing work to implement and test the optimized trajectories. Subsequently, the models have to be validated, which accounts in particular for the energy consumption models. Initial observations on the prototype show that the power consumption is in the same order of magnitude, but significantly higher. This is reasonable as various effects like line losses and auxiliary consumers are not yet modeled. It is to note once more, that the pulleys currently cannot be dynamically reconfigured throughout a trajectory using external drives. The reconfiguration feature however appears promising in simulation. In reality, it is a question of economical considerations and application requirements whether this feature is reasonable, since dedicated powerful drives and appropriate linear axes introduce relatively high additional costs and energy consumption.

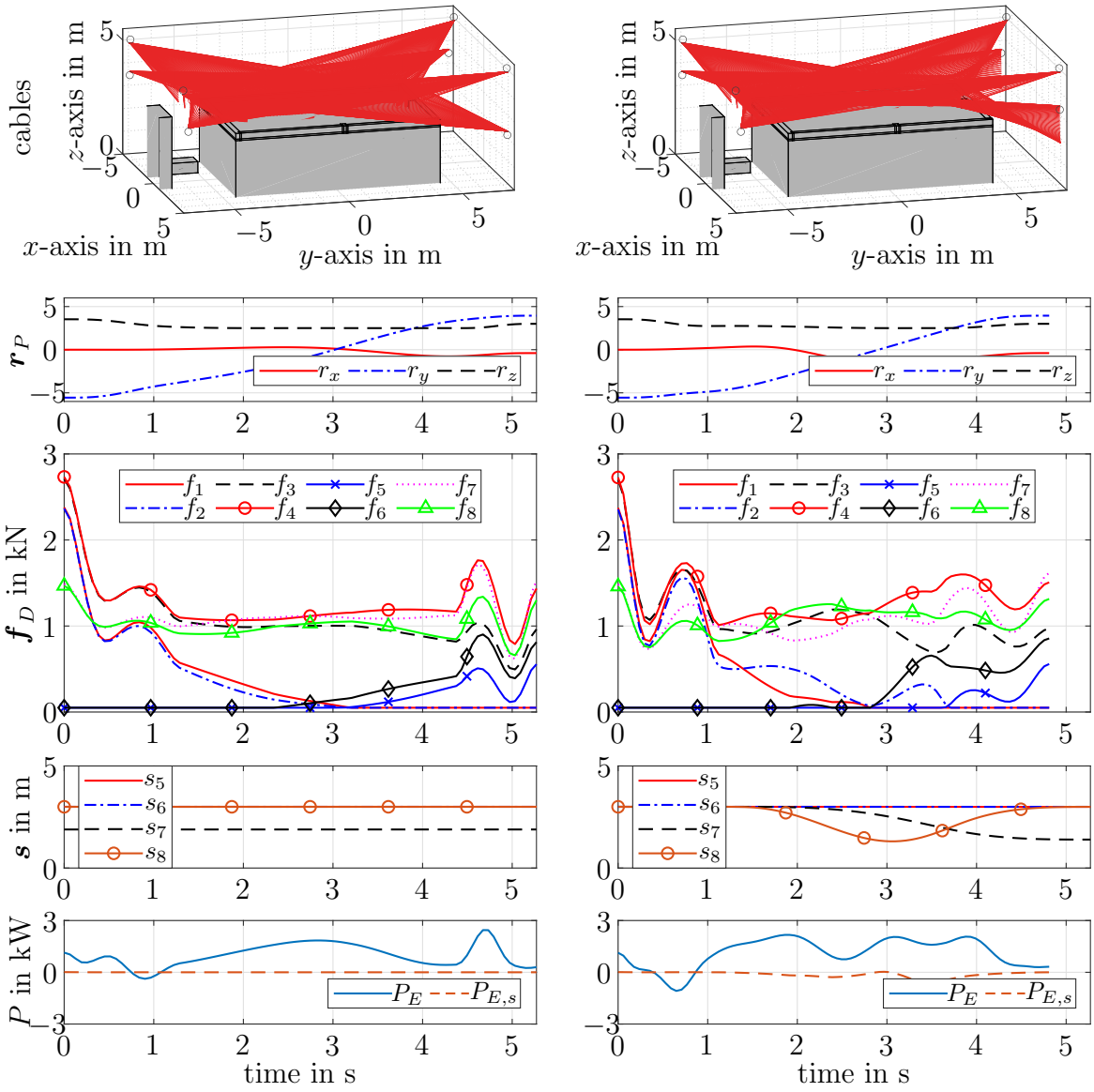

Figure 6.7: Simulation result of masonry unit no. 1503. Left side: Pulleys fastened. Right side: moving pulleys. First row: Collision checks between cables (red) and obstacles (grey boxes) along discrete poses on the path. Second row: Position of the platform. Third row: Cable forces. Fourth row: Movable pulley's positions. Last row: Power consumption of winches P_E and pulley slide drives $P_{E,s}$.

6.3 Simulation of Cable Failure in Automated Masonry Construction

Besides trajectory planning and optimization for CDPRs in automated masonry construction, the consideration of cable failure in this application is crucial, since the platform carries large weights and may cause remarkable damage to the erected building if a collision takes place. For a cooperative scenario with laborer in the robot's workspace, the outcome might be even worse. This issue is initially addressed by the author within [Boumann and Bruckmann, 2021], verifying one of the proposed emergency strategies for the prototype CARLO in a basic dynamic simulation.

In the upcoming it is now studied, if the proposed emergency strategies can be applied successfully within the multibody simulation framework displaying the prototype CARLO and if the robot and the building can be protected from damage. Subsequently, the feature of reconfiguration is examined for its benefit after cable failure.

6.3.1 Application of Damage Avoidance Strategies

For experiments, the dynamic multibody simulation environment introduced in Section 4.2 is used and the parameters of CARLO are set according to table 6.2. As discussed in Section 5.4, the simulation structure can provide a sound indication on real prototype behavior. For simplicity, the vertically movable pulleys (Numbers 5-8) are assumed to be fixed in position here. To parametrize cables and drive units, the same experiments as shown in Section 4.2 are performed with the hardware of CARLO. The friction, for example, can vary greatly within the drive units due to the manufacturing process. However, it is assumed, for simplicity, that all drives and cables are fully identical by using average values of the measurements. Using Dyneema cables with 6 mm diameter and `BECKHOFF` motors of the type AM8073, the resulting parameter values are: $f_b = 50$ kN, $e_c = 1$ % and $d_c = 390$ Ns/m for the cables, and $F_s = 1.3$ Nm, $F_c = 0.95$ Nm, $F_v = 0.025$ Nms/rad, $\epsilon = 1$ and $\theta_s = 0.5$ rad/s for the drive units. Note that the experimental friction identification was more feasible on the drive side of the gear. Thus, the resulting simulated friction of an entire drive unit is introduced on the drive side using the above parameters.

In comparison to Chapter 4 and Chapter 5, it is to note that the gap between simulation and reality is expected to be larger. This is due to the influence of unmodeled effects like cable sagging and dynamics, which have higher impact for a larger prototype with thicker cables. Nonetheless, the simulation can provide an indication on real world behavior of the robot.

Cable Failure without Emergency Strategy The scenario is chosen as follows: A part of the building up to a height of $z_b = 2.5$ m is already erected and no masonry unit is currently gripped. All elements of $\boldsymbol{K}_P$ are set to 70000 N/m and 75 Ns/m for $\boldsymbol{K}_D$. The platform of CARLO is initialized in the middle above the the building at $\boldsymbol{r}_P = [0, 0, 3.5]^{\mathrm{T}}$ m and $\boldsymbol{\Phi} = [0, 0, 0]^{\mathrm{T}}$ rad. Note that the distance from the origin of $\uparrow\!\underline{P}_{\rightarrow}$ to the bottom of the gripper tool is roughly half a meter, i.e. 0.5 m space remain between the platform and the top of the building. The assumptions from Section 4.3.4 are still taken into account. Additionally, eq. (4.6) is extended by the condition $r_z - 0.5 \leq z_b$. If this condition holds true, the gripper's bottom is likely to collide with the building, which will terminate the simulation. This is a simplification, not considering the platforms external dimensions when rotating it. Moreover, collisions between cables and the building are not explicitly checked. As described in the previous section, the robot's four lower pulleys are reconfigured in vertical dimension with rising building. Thus, for $z_b = 2.5$ m, the z-coordinates of the according pulleys in $\boldsymbol{B}$ are also set to 2.5 m. As depicted in fig. 6.8, rather high cable forces up to ~ 4.2 kN occur during initialization of the platform which settle after short time period of ~ 0.5 s. This behavior is analog to Section 4.3.2. Note that the time scale is normalized to the event of cable failure. After 2.25 s (at -5.75 s), the platform's spatial fixation is released, leading to a barely visible vibration (see $\boldsymbol{f}_{\mathrm{is}}$). To demonstrate physically meaningful performance of the simulation, an exemplary platform movement diagonal through the workspace towards $r_P = [2, -2, 3.5]^{\mathrm{T}}$ m is conducted, starting after 4.25 s (at -3.75 s). This pose is within

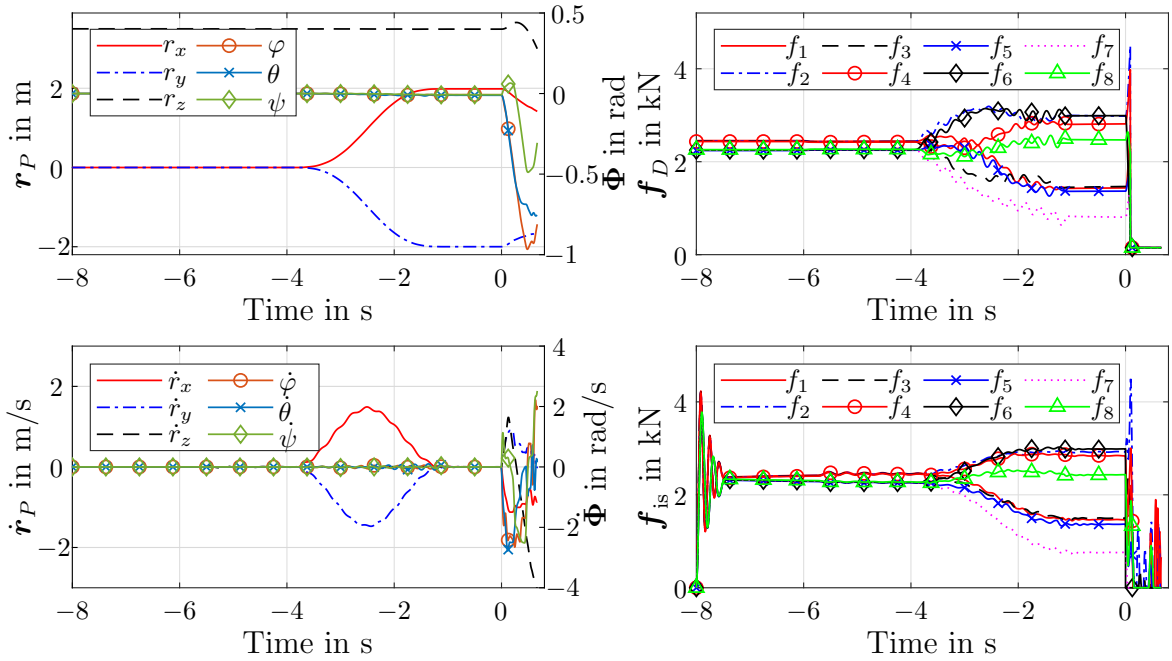

Figure 6.8: Demo movement in xy-direction and cable failure scenario of cable 6 for CARLO. No emergency strategy is used. Time scale aligned with event of cable failure.

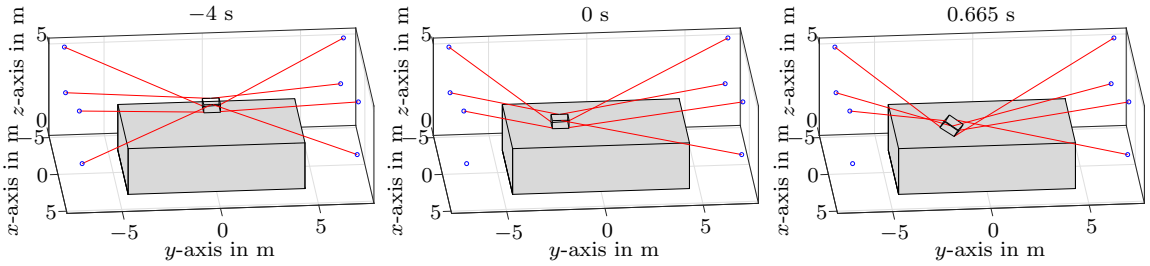

Figure 6.9: Spatial representation of demo movement for CARLO and cable failure scenario of cable 6. No emergency strategy used. Erected Building represented in gray.

the pre- but outside of the post-failure workspace. During the movement, the progression of desired and current cable forces as well as the acceleration and deceleration of the platform appear physically reasonable. The initialization of the platform and the movement to the pose where a cable failure is induced will not be displayed further on. Now the failure of cable 6, which is led from a lower pulley to the platform's top, is simulated. Due to the pre-tensioning of the remaining cables, the platform firstly moves up a few cm, as can be seen on r_z. The controller tries to take countermeasures, which can be seen on $\boldsymbol{f}_D$. However, after 0.086 s, the first desired cable force reaches $f_{\max}$, leading to a failure of the controller and crash of the platform. It collides with the building ($r_z - 0.5 \leq z_b$) after 0.665 s and the simulation is terminated. Figure 6.9 visualizes the course of the simulation spatially at three time steps.

For the failure of a cable coming from above (in that case cable 2) in the same scenario, the conventional controller fails already after 0.0685 s and the simulation is terminated due to collision after 0.279 s. For reasons of space, no detailed representation of this scenario is provided. Summing up, the failure of the controller and a crash of the platform outside of the post-failure workspace without any emergency strategy was expected, as elaborated in the prior sections. It is to note that a conventional controller with failure detection as well as the motor brake option, as described in Section 4.3.4 and Section 4.3.7, are not employed in the following, since it is expected that those approaches tend to fail if the platform gets outside of the post-failure workspace.

Kinetic Energy Minimization Method Now, the first emergency strategy based on minimization of the platform's kinetic energy is employed for the given scenario, cable 6 fails. The parameters $n_{\max} = 50$, $\boldsymbol{R} = \mathrm{diag}(10, 10, 3000, 300, 300, 200)$ and $R_1 = 6e-04$ are set. Figure 6.10 shows the simulation results. The platform is stopped after roughly 6.5 s in a stable safe position $\boldsymbol{r}_P = [-0.6826, 0.8411, 3.5419]^{\mathrm{T}}$ m, $\boldsymbol{\Phi} = [-0.1171, -0.132, 0.0909]^{\mathrm{T}}$ rad without collision with the building during the movement. Due to the chosen weights, the

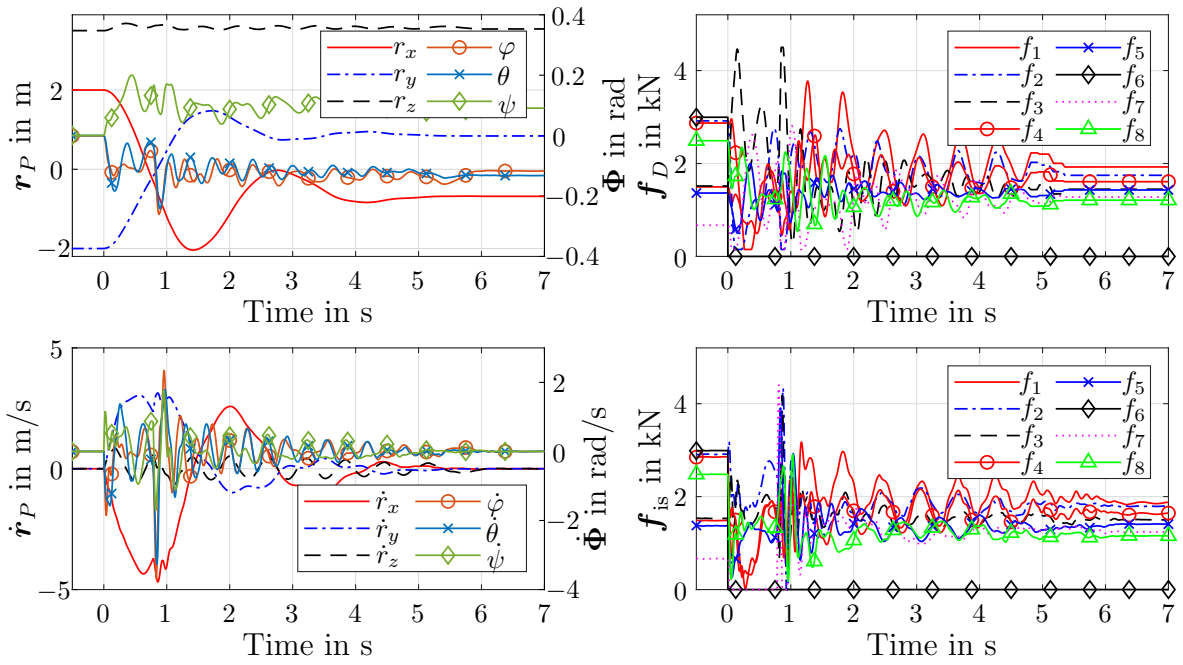

Figure 6.10: Cable failure scenario of cable 6 for CARLO using Kinetic Energy Minimization Method. Time scale aligned with event of cable failure.

algorithm demands constant $\boldsymbol{f}_D$ already after ~ 5.5 s, as the velocities are small enough. The high weight for R_3 successfully prevents the platform from building speed in z-direction and thus from collision with the building. However, the platform can't either swerve upwards, which is a disadvantage of the rescue method. According to the chosen weights, the platform should tilt as little as possible while doing compensating movement in x- and y-direction. This is well realized as fig. 6.10 displays. The maximum speed built up is ~ 4.7 m/s in x-direction. The spatial path of the platform is indicated in fig. 6.11. For failure of cable 2 (coming from above) in the same scenario, a collision free rescue of the platform can be done within roughly 5 s using identical parametrization of the algorithm.

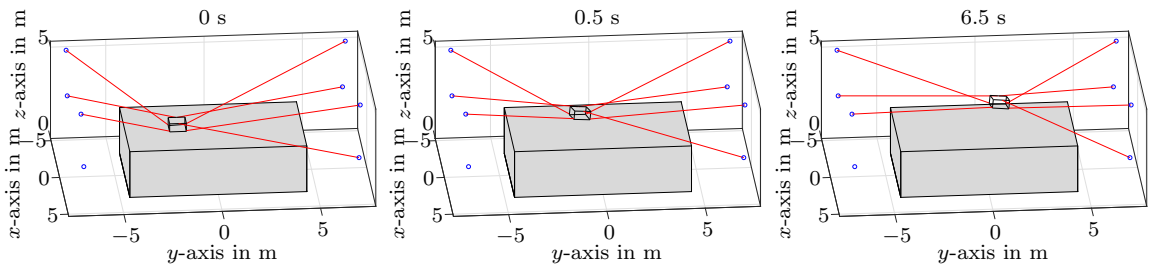

Figure 6.11: Spatial representation of cable failure scenario of cable 6 for CARLO using Kinetic Energy Minimization Method. Erected Building represented in gray.

Summing up, it can be stated that the simulation exemplifies how the first proposed strategy (Kinetic Energy Minimization Method) can prevent the platform of CARLO from collision with a building after cable failure during an automated masonry scenario. However, for the avoidance of obstacles with a more complex geometry, the approach needs to be extended with a dedicated obstacle avoidance strategy, e.g. by including a pose control loop.

Potential Field Method Subsequent to the first method, now the second emergency strategy based on the usage of potential fields in the robot's workspace is employed for the given scenario, cable 6 fails. The parameters $\boldsymbol{r}_{P,\text{final}} = [-1.5, 3, 3.75]^{\mathrm{T}}$ m, $\boldsymbol{\Phi}_{\text{final}} = [0, 0, 0]^{\mathrm{T}}$ rad, $\boldsymbol{\zeta}_r = 8000 \cdot \text{diag}(1, 1, 1)$ 1/m, $\boldsymbol{\zeta}_\Phi = 1000 \cdot \text{diag}(1, 1, 1)$ 1/rad, $d_b = 0.5$ m, $\boldsymbol{D}_1 = 40 \cdot \text{diag}(1, 1, 1)$ Ns/m, $\boldsymbol{D}_2 = 10 \cdot \text{diag}(1, 1, 1)$ Nms/rad, $p = 5$ are set. Additionally, a repulsive field is placed within the xy-plane with origin at the height of the erected building, employing the parameters $\rho_0 = 0.5$ m and $\eta = 100$, according to Section 3.4.2. The simulation results are displayed in fig. 6.12. The platform is successfully rescued and stabilized at the goal pose after ~ 5.5 s with a residual offset of $[-0.0013, 0.004, -0.0026]^{\mathrm{T}}$ m and $[0.0091, -0.0153, 0.0001]^{\mathrm{T}}$ rad. The repulsive field effectively pushes the platform away from the building, as demonstrated by the movement in z-direction after cable failure. Hence, no collision occurs. Due to the aggressive intervention of the algorithm (see $\boldsymbol{f}_D$), some force peaks exceeding $f_{\max}$ are reached in $\boldsymbol{f}_{\text{is}}$, similar to what can be observed in fig. 4.30. The highest peak ranges up to ~ 5.7 kN. In practice, $f_{\max}$ might be reduced during rescue to

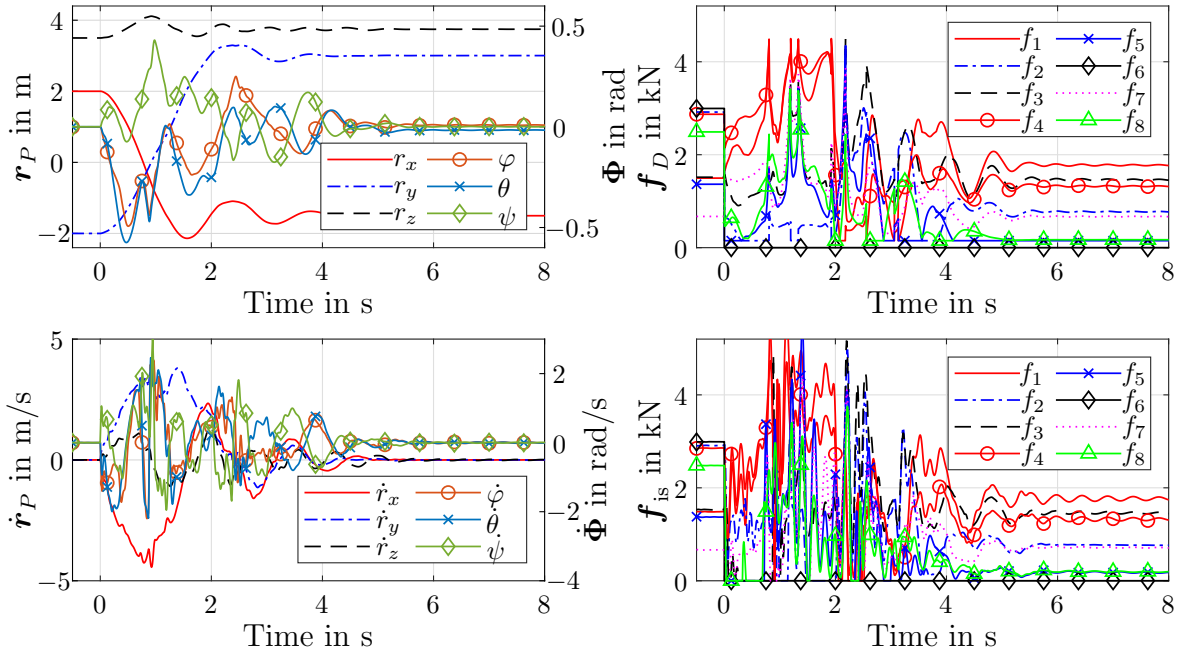

Figure 6.12: Cable failure scenario of cable 6 for CARLO using Potential Field Method. Time scale aligned with event of cable failure.

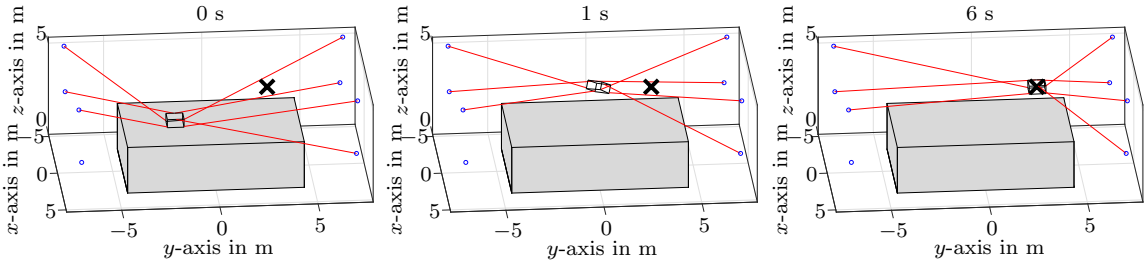

Figure 6.13: Spatial representation of cable failure scenario of cable 6 for CARLO using Potential Field Method. Erected Building represented in gray. Origin of attractive field indicated by black cross.

prevent such transgressions. The spatial path of the platform after cable failure towards the goal pose is depicted in fig. 6.13. For failure of cable 2 in the exact same scenario with unaltered parameters, the goal pose is also reached without collision and a residual offset of $[0.0009, -0.0029, -0.0028]^{\mathrm{T}}$. m and $[-0.0071, -0.0227, 0.0105]^{\mathrm{T}}$ rad after ~ 7.5 s.

Similar to the results of the first strategy, the simulation also exemplifies how the second proposed strategy (Potential Field Method) can safeguard the platform of CARLO collision free after cable failure during automated masonry construction. The repulsive field particularly supports the collision avoidance. However, parametrization of the method is more complex.

6.3.2 Employing Reconfiguration

If a cable robot can be reconfigured as explained in Section 3.3.3, it is obvious to use this feature in case of a cable failure. Within work of the author [Boumann and Bruckmann, 2021], a simple dynamic simulation is used to verify the functionality of the Kinetic Energy Minimization Method after cable failure for the prototype CARLO, employing dynamically movable pivoting pulleys. Furthermore, the movable pulleys (Numbers 5-8) are used to reconfigure the system and partly recover it from post-failure workspace loss. In this section, the approaches based on [Boumann and Bruckmann, 2021] are briefly explained and reprocessed. Note that, in contrast, it is assumed here that the CDPR is not carrying a masonry unit.

Kinetic Energy Minimization Method employing Reconfiguration In [Boumann and Bruckmann, 2021], the author presents an extension of the emergency strategy based on Kinetic Energy Minimization by employing movable pivoting pulleys (see Section 3.3.3). The usability of the method is demonstrated in a very basic dynamic simulation: The dynamics of cables, drive units and pulleys, as well as friction are omitted. Only dynamic platform movement due to gravity and cable forces is considered (see

eq. (2.38)) and the platform states are determined using numerical integration with the Euler-Cromer Method [Cromer, 1981] and a discrete time step of $\Delta t = 1$ ms.

To study the Method in the context of this thesis, the multibody simulation framework proposed in Section 4.2 and used in fig. 6.10 is extended with the feature of movable pulleys. Contrary to Section 6.2, dynamics of the slide mechanisms are neclected. Only a purely kinematic modeling of the pulley movement ($\boldsymbol{s}$) is done according to Section 3.3.3 and $\dot{\boldsymbol{s}}$ is strictly limited to $[\dot{s}_{\min}, \dot{s}_{\max}]$, see table 6.2. For comparability, the scenario displayed in fig. 6.10 is chosen for simulation using the same robot and optimizer parameters with failure of cable 6. Additionally, $r_2 = 300$ is chosen. As a part of the building is already erected up to a height of 2.5 m, the lower pulleys' movement is limited to $[s_{\min}, s_{\max}] = [0, 1]$ m. Figure 6.14 displays the simulation results. Even thou the range of pulley movement is quite limited, the optimizer uses the full capacity of $\boldsymbol{s}$ and $\dot{\boldsymbol{s}}$. In comparison to the scenario with fixed pulleys, the platform movement is qualitatively similar. However, the platform

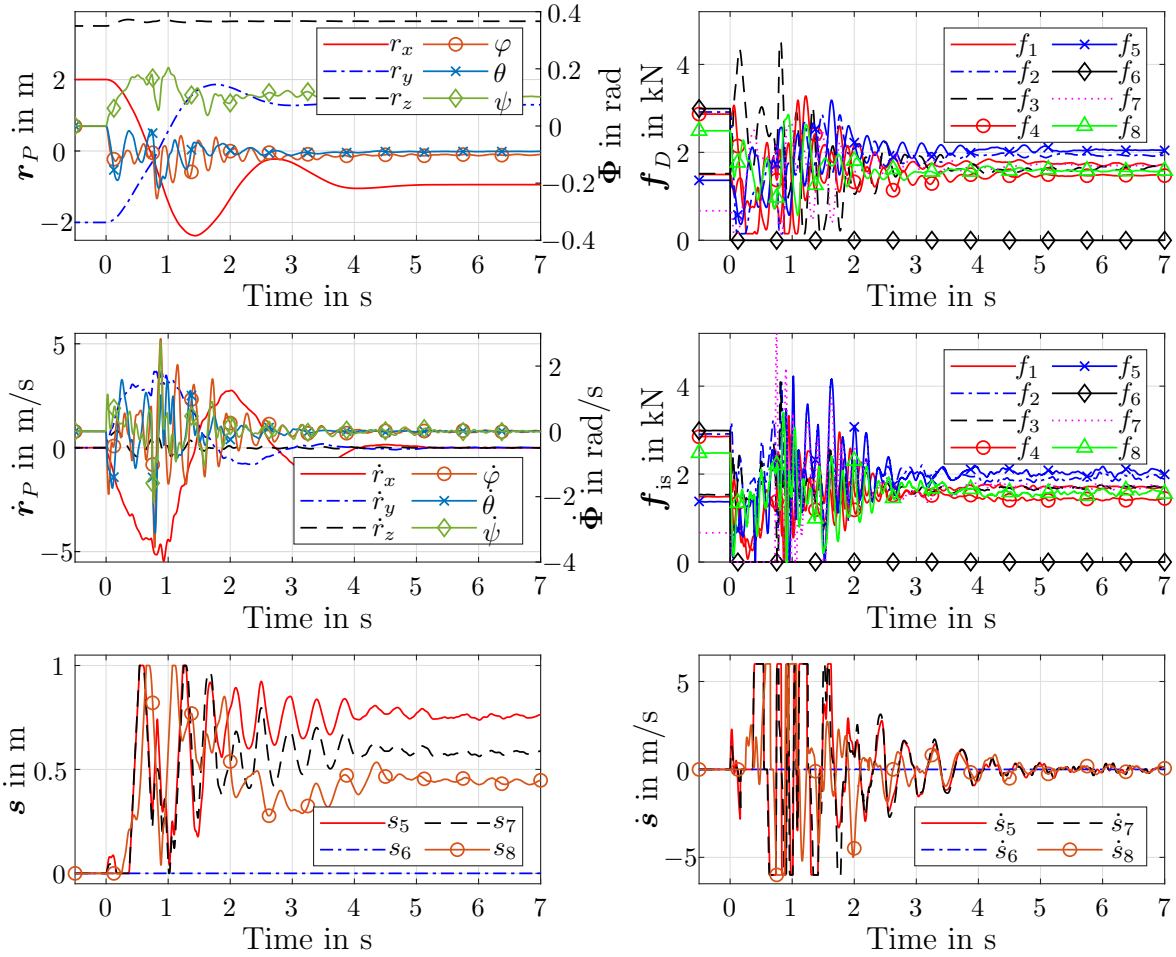

Figure 6.14: Cable failure scenario of cable 6 for CARLO using Kinetic Energy Minimization Method and dynamic pulley reconfiguration. Time scale aligned with event of cable failure.

is secured and fully stopped after roughly 5 s ($\sim$ 1.5 s quicker). The highest weighted optimization goal (no velocity in z-direction) is also achieved better. The maximum velocity in this direction is a bit lower (0.8196 m/s vs 0.8544 m/s) and after already 2 s, it is almost zero (compared to 6 s in the scenario with fixed pulleys). In return, more velocity is built up in x-direction with increased evading movement ($-5,4$ m/s vs. $-4,7$ m/s), which is desired. Also $\boldsymbol{f}_D$ and $\boldsymbol{f}_{\text{is}}$ settle quicker. In summary, as also shown in [Boumann and Bruckmann, 2021], movable pivoting pulleys can be utilized to support an emergency strategy after cable failure. It is to note that the progression of desired cable force shown here is fairly different from [Boumann and Bruckmann, 2021]. This is due to the multibody simulation environment, which includes further physical effects. Moreover, a sequential quadratic programming algorithm [Schittkowski and Zillober, 2005] is used here, while an interior-point algorithm [Waltz et al., 2006] is used in [Boumann and Bruckmann, 2021] to minimize eq. (3.17).

Workspace Recovery employing Reconfiguration As discussed in the previous chapters, the loss of workspace due to a cable failure might be dramatically. If a CDPRs owns the feature of reconfigurability, it can be employed to recover workspace after cable failure [Boumann and Bruckmann, 2021]. Assuming a successful recovery of the CDPR platform after cable failure, the robot might be used with a reduced set of pulleys and within the post-failure workspace until it is maintained and repaired, see Section 5.3.5. Figure 6.15a displays the pre-failure $\mathcal{SECOW}$ of CARLO with the movable four pulleys in lowest position. Note that only the feasible points on the grid and no convex hull are shown. Now the failure of cable 2 is considered and the post-failure $\mathcal{SECOW}$, as depicted in fig. 6.15b, is remarkably smaller. Only 22.967 % of the initial workspace remains. However, it also contains very few points that were not included before, due to the change in possible force and torque equilibria. To counteract workspace loss using pulley reconfiguration, a global optimization using `MATLAB`'s `particleswarm()` algorithm is carried out to find pulley positions that restore as much ratio of the $\mathcal{SECOW}$ as possible. In a first step, the feasible

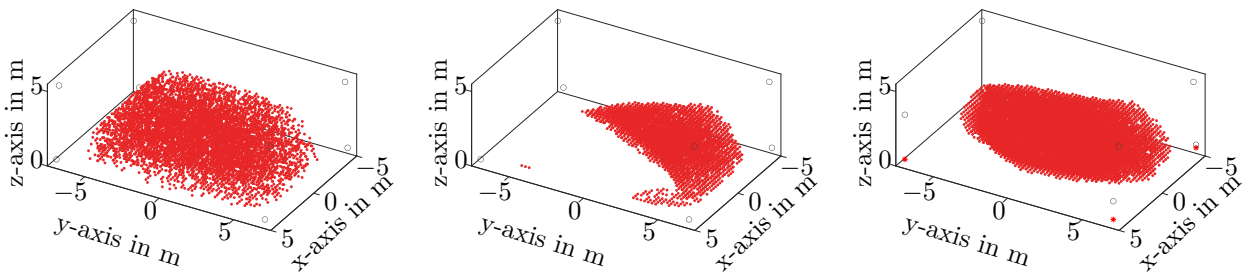

(a) Workspace without failure (b) Failure of upper cable (c) After reconfiguration

Figure 6.15: Pre- and post-failure (cable 2) $\mathcal{SECOW}$. Circles in the corners indicate the pulley positions. Red asterisks (right side) indicate the initial pulley positions.

workspace points on the grid of the pre-failure $\mathcal{SECOW}$ are stored as an optimal number n_{pre}. The total number of evaluated grid points is 27 489. After cable failure, the optimizer may change all values of $\boldsymbol{s}$ in between $[s_{\min}, s_{\max}]$ (see table 6.2), to find an optimal number of recovered workspace grid points n_{post} that match the pre-failure points. The cost function is defined as difference between n_{pre} and n_{post} assuming always $n_{\text{post}} \leq n_{\text{pre}}$. The swarm size is set to 100, and the maximum iterations are set to 200. All remaining optimizer parameter are set to default. The optimization converges after 74 iterations with the final value $\boldsymbol{s} = [0, 2.9897, 0.2045, 1.2261]^{\text{T}}$ m. After the optimization, 55.2569 % of the pre-failure $\mathcal{SECOW}$ can be restored, see fig. 6.15c. The result shows that pulley reconfiguration can be employed to counteract the immense loss of workspace after a cable failure in a CDPR to improve the usability until it can be serviced and repaired.

6.4 Conclusion

As elucidated in the introduction, robotized construction can help to counteract shortage of skilled workers and automation deficits in the construction industry. Besides well-known approaches to robotic construction, two cable robots for large scale concrete 3D-printing of wall elements and automated masonry construction have been introduced. The prototypes were developed within the team to which the author belongs during this thesis. Moreover, basics on BIM and a toolchain to generate robot inputs from BIM data were presented. Building up on this, a framework for trajectory planning and optimization for automated masonry construction using CDPRs was expound. The framework is versatile and can also include various robot models, such as cooperating drones. Exemplary results using the CDPR prototype CARLO were presented. Using the multibody robot simulation framework, see Section 4.2, cable failure in automated masonry construction was considered based on the example of CARLO. It was successfully demonstrated in a simulation scenario, that the damage avoidance strategies presented in this work can be applied. They can rescue and safeguard the platform after cable failure, while preventing collisions with a partial building in the workspace and prevent tipping over, which may lead to payload loss. Without a damage avoidance strategy, it was shown that the platform collides with the building after cable failure. Moreover, it was demonstrated that reconfiguration of movable pivoting pulleys can support an emergency strategy. Using reconfiguration after platform rescue, a significant amount of the drastically reduced workspace can be recovered. Finally, it can be concluded that, besides the applicability of the emergency strategies in reality (see Section 5.3), the usefulness within a CDPR application scenario underlines their importance.

Chapter 7

Conclusion

Within this chapter, the accomplished work of this thesis is concluded. The results are reviewed and critically discussed. Furthermore, the scientific contribution of this work is highlighted. Finally, an outlook on further ideas and future research tasks is given, introducing the upcoming research project STRADAC founded by the German Research Foundation (DFG).

7.1 Summary

This thesis deals with cable failure in redundant parallel cable robots and how to prevent subsequent damage. Cable robots are a special class of robots that use a set of cables to actuate a platform carrying a robotic tool and completing a task. As cable robots become more established in industrial applications, their safety and reliability must be critically reviewed and potential failures must be considered. If left unrecognized and untreated, the failure of a cable can cause uncontrolled platform motion that may result in payload loss or a crash, causing hardware or environmental damage and potentially harm people nearby. This is because a cable robot's static equilibrium workspace can be significantly reduced after a cable failure, increasing the likelihood of the platform getting outside of it. Still, a CDPR with many cables can be influenced in a targeted manner after failure, utilizing the remaining cables. Since norms and guidelines have been developed over centuries of experience in the usage of cables and pulleys, this failure may be rare but still its outcome can be hazardous.

Several well-known publications on cable failure exist within the literature. However, there were no strategies validated on a real prototype for bringing the end effector of a redundant CDPR with all six spatial degrees of freedom into a safe state. Additionally, most

existing strategies focused on trajectory planning along pre-defined paths, which may be time critical in the event of failure.

Building on the presented theoretical fundamentals of cable-driven parallel robots, two new emergency strategies to recover the platform after cable failure were proposed in this work. Those strategies operate without pre-defined trajectories and are intended to mimic a reflexive behavior. The first strategy aims at minimizing the platform's kinetic energy after cable failure and thus its velocity. If the strategy successfully stops the platform with the cables tensed, it is in a static force equilibrium and thus automatically in a safe state within the post-failure workspace. The approach is based upon a nonlinear model predictive control and forecasts the future platform movement depending on set cable forces using a dynamic robot model and numerical integration. To calculate continuous set-point cable forces, a cost function is defined containing the robot model and a term representing the cable forces' progression. The cable forces are further limited by a minimum force to keep the cables tensed and a maximum force for safety and due to the maximum available motor torques. The resulting constraint nonlinear optimization problem is resolved using sequential quadratic programming. A weighting scheme is also introduced to favor or avoid movement in specific degrees of freedom. For example, it can be used to avoid obstacles located below the platform.

The second strategy utilizes potential fields in the workspace that introduce virtual forces and torques to the platform. This virtual wrench is intended to lead the platform into a safe pose, which is defined in the post-failure workspace using an attractive field. Moreover, repulsive fields can be utilized to avoid collisions with obstacles in the workspace. If the required wrench can be generated using the remaining cables after failure, the platform will follow the path prescribed by the potential field. Virtual damping is furthermore introduced in all degrees of freedom, in order to increase stability of the method. However, the required platform wrench might be infeasible by the remaining cables, i.e. the platform is outside of the wrench-feasible workspace. To generate approximate cable forces in this case, a real-time capable method based on a geometric consideration of the problem was developed in this work: Introducing the lower and upper force boundaries per cable in the space of cable forces, a hypercube of feasible cable force distributions is formed. In this space, the required platform wrench can be represented by a hyperline or hyperplane, depending on the robot's degree of redundancy. If the wrench is unfeasible, no intersection between both geometrical objects exists. In this case, the developed Nearest Corner Method identifies the hypercube's corner of feasible cable forces, which is closest to the required wrench representation. This provides the cable force distribution, which optimally approximates the required wrench.

Based on the presented theoretical foundations, a multibody simulation framework was set up and parametrized according to the SEGESTA prototype, which was available for

experiments within this work. Measurements were conducted to identify frictional behavior within the drive units as well as cable elongation and damping of the used synthetic fiber cables. The pre- and post-failure workspaces of SEGESTA were determined including also minor platform rotation to assess the situation after cable failure and to find safe goal poses. An example trajectory was performed within the pre-failure workspace to demonstrate physical meaningful behavior of the simulation. By recreating a cable failure in simulation, the outcome using a conventional CDPR controller without emergency strategy was studied. This controller was further adapted assuming a fault detection and neglecting the broken cable. Following, its ability to stabilize the platform after cable failure was assessed. Hereby, the simulation allowed for the examination of numerous scenarios throughout the whole pre-failure workspace providing feasible regions for the different approaches. Subsequently, the two new emergency strategies proposed within this work were integrated into the control architecture and verified in simulation. They were able to rescue the platform after cable failure from outside of the post-failure workspace in various scenarios. Feasible regions were identified and the method's parameters, their setting options and their intended influence were substantiated to find suited parameter settings for the application on the real prototype. Finally, braking of the winch motors after cable failure was tested. In general, the use of brakes or the conventional adapted controller mainly provided successful stabilization if the platform was within the post-failure workspace after cable failure. Whereas, the two proposed new emergency strategies were able to rescue the platform in several scenarios from outside of the post-failure workspace, where a crash would otherwise occur.

Based upon the simulative studies, experiments on the SEGESTA prototype were conducted. In the preliminary studies, cable forces remarkably higher than desired occurred in various scenarios. Thus, the maximum cable forces were reduced within the prototype control and a safety enclosure was added to the robot to ensure working safety. To provoke or mimic a cable failure on the prototype, a cable decoupling device was developed and tested based on a detailed requirement analysis. The device was mounted on the end effector and is able to decouple a chosen cable from the platform. Building on that, a simple yet effective failure detection algorithm to identify the cable failure was proposed and successfully tested. It reliably detected all cable failures within the experiments. In further preparatory work, a forward kinematic algorithm used for pose and velocity estimation after cable failure was introduced to enable application of the proposed emergency strategies. Moreover, the real-time capability of the implementation was assessed. Uncontrolled movement of the platform after cable failure was demonstrated using neither a failure detection nor an emergency strategy. Within the post-failure workspace, the adjusted conventional controller with failure detection was demonstrated to successfully stabilize the platform after cable failure. Furthermore, the two proposed emergency strategies were successfully validated in exem-

plary scenarios, where the platform was rescued from outside of the post-failure workspace when the cable fails. Since it was assumed that continued operation is possible in addition to shutdown and maintenance after a safe pose is reached, this was also demonstrated. Finally, a comparison to the simulation was conducted using the experimental results. Despite inevitable differences in the test setup, the simulation provided an adequate representation of reality.

Beyond the experiments on the SEGESTA prototype, an application scenario was also considered: Two available cable robot prototypes for automated construction tasks were introduced, which can be used for large scale 3D-printing of concrete or automated masonry construction using bricks and mortar. Both prototypes were developed within the research group along the path of this thesis. Finding optimal trajectories for automated masonry construction using cable robots is a task itself, which was considered aside from the cable failure scenario. The developed algorithms can also be applied for load-sharing drone systems. Based on the prototype for automated masonry construction CARLO, the simulation framework was parametrized and the two proposed emergency strategies were applied in simulation. Both methods were proven to successfully rescue the platform carrying a masonry unit from outside of the post-failure workspace in exemplary simulations while preventing collisions with the already built masonry. Finally, the feature of pulley reconfiguration was used to recover workspace after cable failure and to support the emergency strategy based on kinetic energy minimization of the platform.

7.2 Scientific Contribution

Complementary to the state of the art, two new reflexive emergency strategies to recover the platform of a CDPR after a cable failure have been developed and experimentally validated in this thesis. Using the strategies in a real-time capable implementation on a physical prototype, it is now possible to recover kinematically redundant, spatial CDPRs with all six degrees of freedom from outside of the $\mathcal{WFW}$ back into the post-failure workspace. During rescue, uncontrolled movement and tipping over of the end effector, which might involve loss of payload or a platform crash, can be prevented. This avoids robot and environmental damage as well as harm to workers nearby. Furthermore, a cable failure can now be detected quickly and reliably using the proposed new failure detection algorithm, which also enables cable failure monitoring for CDPRs in industrial usage. In addition, damage avoidance strategies can now be tested under realistic conditions using the novel developed cable decoupling device. Finally, fig. 1.7 provides a comprehensive decision scheme for the case of cable failure. None of the above was demonstrated in this way before. Thus, the contribution of this thesis closes the research gap stated in Section 1.3.2 and enables a safer usage of

cable-driven parallel robots in upcoming industrial applications. In particular, the scientific contributions to answer all research questions are as follows:

- Using models for electronic motors, drive units, cables and the robot's platform, a computationally efficient simulation was set up in Chapter 4, which adequately represents the real CDPR as Chapter 5 shows.

- The proposed emergency strategies were integrated into a closed loop control for a redundant CDPR as shown in Chapter 4.

- Simulation studies in Chapter 4 showed that, depending on the pose and the parameter settings, it is possible to rescue the platform of a CDPR after a cable failure using the proposed strategies.

- Section 5.2.1 presented the implementation of the strategies on the physical SEGESTA prototype using a forward kinematic algorithm that adapts the cable failure. The developed Nearest Corner Method (see Section 3.5.2) ensures real-time capable cable force calculation outside of the $\mathcal{WFW}$. Successful platform recoveries after cable failure were demonstrated, which validates the strategies.

- The strategies' parameter settings obtained from simulation are suitable for prototype experiments with minor changes, as the experiments in Section 5.3 showed.

- Beyond the approach of unwinding a cable to mimic a failure [Boschetti et al., 2021], a device was developed that detaches a cable from the platform when triggered from the PLC, see Section 5.1.1. This provides testing under realistic conditions.

- Using the combination of three signals (cable length error, motor velocity and cable force), a failure detection algorithm was developed in Section 5.1.3, which successfully detected the cable failure at the SEGESTA prototype in a millisecond.

- Undetected cable failure was studied in simulation (see Section 4.3) and a prototype experiment (see Section 5.3.1). Expected miscontrolled and unpredictable platform motion due to failure of a conventional controller was evidenced.

- By adding fault detection to the adapted conventional controller, the platform can be stabilized after cable failure if it is within the post-failure workspace (see Section 4.3.4 and Section 5.3.2). The same accounts for the usage of motor brakes (see Section 4.3.7).

- It was demonstrated in Section 5.3.5 that a redundant CDPR can also continue operation after cable failure in the post-failure workspace.

- In cable failure simulations of the large redundant CDPR for automated masonry construction CARLO, the proposed emergency strategies were able bring the platform to a safe state while preventing collisions with the erected building (see Section 6.3).
- In Section 6.3.2 an algorithm to recover lost workspace after cable failure using pulley reconfiguration was demonstrated. Further, one emergency strategy was enhanced using this feature, which improved the performance in simulation (see Section 3.3.3 and fig. 6.14).

7.3 Discussion

Initially, it should be stated that the results presented in this work, particularly the experimental ones, mainly refer to the SEGESTA prototype. Considering the simulation of the CARLO prototype in addition, it can be assumed that the results are transferable to systems with a similar structure in terms of robot configuration, number of cables and number of degrees of freedom. However, no well-founded statement can be given with regards to underconstraint and underactuated systems. In this work, only redundant systems with eight cables and a redundancy of $r = 2$ were considered, i.e. seven cables and a redundancy of $r = 1$ after cable failure. The Kinetic Energy Minimization Method, based on a model predictive approach, has no limitations to incorporate more cables and thus higher redundancies in general. However, it may be limited by available calculation time as the problem's complexity increases. The same accounts for the Potential Field Method employing the Nearest Corner Method. The latter was proven to work with $r = 3$ before cable failure in [Boumann and Bruckmann, 2022]. Thus, it can be assumed that both emergency strategies are feasible for arbitrary high degrees of redundancy.

The application of both strategies in simulation, see Section 4.3, led to remarkable improvements in platform rescue compared to the conventional controller. As an example, after failure of a cable coming from above the platform (cable 4), the Kinetic Energy Minimization Method could recover the platform of SEGESTA from $\sim$ 24 % more poses than the conventional controller, even with failure detection. Those poses were primarily outside of the post-failure workspace. The same trend could be observed for the Potential Field Method with an improvement of $\sim$ 14 %. For the failure of cable 2 (coming from below the platform), the improvement was even more remarkable: Successful recovery from $\sim$ 204 % more poses using the Kinetic Energy Minimization Method and from $\sim$ 85 % more poses using the Potential Field Method was recognized. The lower improvement achieved when using potential fields may be attributed to the larger number of parameters and setting options required by this method. Using motor brakes stabilized the platform after cable 4 failed in $\sim$ 14 % more poses than using the conventional controller with failure detection and in $\sim$ 19 % less

poses if cable 2 failed. Note that, despite the same percentage in improvement between using motor brakes and the Potential Field Method for the failure of cable 4, the feasible poses differed: The Potential Field Method allowed for stabilization of more poses outside of the post-failure workspace. All in all, the conventional controller with failure detection and the usage of motor brakes were inferior to using one of the proposed new emergency strategies, especially outside of the post-failure workspace. This confirms the expectations raised in Section 1.2. Accordingly, motor brakes (if available) or the conventional controller with failure detection should be used when the platform is within or near to the post-failure workspace. Otherwise, an emergency strategy is recommended.

In addition to the improvements provided by the proposed emergency strategies, it is important to consider some potential issues: The studies showed that the platform of the SEGESTA prototype tends to tip over easily after cable failure, particularly towards the boundaries of the pre-failure workspace. This could not be prevented in several poses, even using the emergency strategies. Additionally, studies on emergency strategy parameters have revealed their sensitivity to certain settings, which may result in instability. The optimizer used for the Kinetic Energy Minimization Method may get caught in local cost function minima. However, no issue was identified in this work. Furthermore, if the weighting of the method is set to suppress or favor movement in certain degrees of freedom, both directions are affected. For example, if movement downwards is undesired, evasive motion upwards is also suppressed. The experiments in fig. 4.36 and fig. 5.10 revealed discontinuities in cable forces while using the Nearest Corner Method and the Potential Field Method. They appeared when the platform entered the wrench-feasible workspace. An ideal pose and velocity measurement was assumed in the simulations, which may lead to divergent results in comparison to a forward kinematic algorithm. Furthermore, cable force peaks significantly above $f_{\max}$ were experienced during rescue in simulation. This occurred when a cable became momentarily slack, causing the corresponding drive to accelerate, and the cable suddenly became tensed again. In reality, this might provoke further cable failure, which is why $f_{\max}$ was strictly reduced in Chapter 5. As the experiments in Section 5.3 showed, cable folding may appear earlier than stated below condition eq. (4.6), potentially restricting the number of valid simulations. Still, the experiments also revealed that the platform might even be rescued and stabilized successfully despite tipping over and cable folding. Yet, tipping over is undesired in terms of payload preservation. Thus, the criteria for successful simulation still hold true.

Clearly, the realism of simulation results is limited by the capabilities of the simulation: For instance, the cable modeling approach is rather simple and did not perfectly fit the experiment measurements in Section 4.2.2, which are also subject to further measurement inaccuracies. Additionally, the drive unit friction was simply increased by a factor to reflect

frictional effects at the pulleys. In comparison to the experiments in Section 5.3, the simulation displayed less vibration in platform and cables. Thus, these assumptions must be reconsidered. The example trajectory performed in Section 4.3.2 appears to be physically reasonable, which was assessed qualitatively by means of the prototype. However, a one-to-one comparison of this trajectory on the prototype was not conducted. It should be noted that the simulation was not intended to perfectly represent reality. Instead, it should be computationally efficient, easy to set up and physically reasonable under the given assumptions, to serve as an environment for fundamental studies on cable failure and the functionality of emergency strategies. Obtaining an accurate representation of reality requires significantly more effort, while leading to high calculation times and low computational efficiency. Thus, the proposed simulation can be understood as a trade off. Improving the simulation environment is conceivable, especially if it is intended to serve as a basis for data-driven emergency strategies using artificial intelligence.

Within the experiments in Section 5.3, the proposed new emergency strategies were successfully validated at the SEGESTA prototype. During the experiments, the decoupled cable rarely got stuck at the hook of the decoupling device. Besides the seamless and reliable function of the failure detection algorithm, it falsely detected cable failures in regular operation if strong platform vibration occurred. Beyond that, all experiments were conducted starting from a standstill platform pose. Thus, the failure detection algorithm was not tested for successful detection in dynamical states. In both the simulation and prototype experiments, it was observed that the required and measured cable forces were often unequal. This is attributed to a non existing cable force control loop. In contrast to the simulation, only a very limited number of experiments could be carried out on the prototype. Furthermore, constructive and safety limitations restricted the ability of accurate comparisons to simulation. Nonetheless, similar patterns and behaviors were observed, and the emergency strategies' parameter settings identified in simulation could be almost completely adopted at the prototype.

In Section 6.3, it was demonstrated within simulation that the emergency strategies could successfully rescue the platform of CARLO after cable failure. Without failure detection and emergency strategy the platform crashed. In case of CARLO, it can be assumed that simulation and reality are further apart in comparison to the SEGESTA prototype. As stated in Chapter 2, cable masses and sagging were neglected in simulation. For small and lightweight prototypes like SEGESTA, this assumption may hold true. However, for a large robot like CARLO, the cable mass and sagging might be non-neglectable. For the prototypes considered, the workspace after cable failure was remarkably smaller, which limits operation after rescue. In exchange, reconfigurable pulleys could be utilized to partially recover lost workspace, as shown in Section 6.3.2. In the model based approach to minimize the kinetic

energy, the drive unit inertia was not considered. While this might be feasible for a prototype with comparable small inertia, it could be worth considering it for larger robots. However, it appears that the recovery of CARLO after cable failure was not affected by this.

Finally, the flowchart introduced in fig. 1.7 should be discussed: It aimed to address all cases that may occur after cable failure. The individual modules required for this purpose were implemented and validated both in simulation and on a hardware prototype. Still, the flowchart did not cover all possible cases that may occur, including multiple cable failure or a cable getting caught. Moreover, the concepts for failure resistant design of CDPRs or fault tolerant trajectory planning for CDPRs call for future adoptions.

7.4 Outlook

This work provides an outstanding basis for further research in the field of cable failure in cable-driven parallel robots. Building upon this, the upcoming project STRADAC funded by the German Research Foundation (DFG) has been acquired, which involves several aspects and ideas shown in this work. Possible future activities involve but are not limited to the improvement of the simulation and the hardware, extension and improvement of the two new proposed emergency strategies, the exploration of AI-based algorithms for path planning and cable force calculation in case of cable failure [Gust et al., 2024] and the consideration of multiple cable failure as well as failure during platform motion. Furthermore, cable failure resistant robot design and failure resistant trajectory planning are worthwhile investigating.

The simulation can be improved including more sophisticated approaches for cable modeling [Merlet, 2015, Miermeister et al., 2015] and material modeling [Flores et al., 2012], as well as dynamic modeling of pulleys and their friction [Miyasaka et al., 2015]. Collisions in between cables or a modeling of the cable folding should be considered along with a limitation on measured cable forces to assess the simulations feasibility more proficiently. The forward kinematic algorithm should be included into the control structure in simulation, ultimately allowing for a one-to-one comparison of the emergency strategies' results to the real prototype. Also, the modeling of the drive unit brakes can be represented more realistically by including frictional effects and delay times.

At the SEGESTA prototype, the set down position can be modified, allowing to use more of the robot's workspace for experiments. The decoupling device's working principal allows for the fabrication of a device that enables tests on larger and heavier prototypes. In addition, the snagging of the cable during decoupling should be prevented more effectively.

The two new proposed emergency strategies after cable failure bear a lot of potential for improvement: Both strategies are noticeable sensitive to parameter choices. Thus, finding suitable parameter settings should be simplified, e.g. by finding an optimal parameter set

or by automated data and situation based settings. For example, a well-suited goal pose for the Potential Field Method could be suggested automatically, depending on the platform pose. Moreover, both strategies need to undergo a comprehensive stability analysis and collision avoidance in between cables might be considered within the strategies. As the quality of the forward kinematics solution is crucial for the given emergency strategies, it might be assessed using external measurements, e.g. a camera system. The model based strategy of Kinetic Energy Minimization can easily be extended by pose control, adding another term within the cost function. Furthermore, the prediction horizon can be extended, potentially until a safe pose is reached. Especially for larger CDPRs, a consideration of the drive unit inertia within the strategy seems advisable. Moreover, the weighting scheme of the degrees of freedom needs to be adjusted. For example, it should allow desired upwards movement while suppressing unwanted downwards movement of the platform. With rising computational effort of the model predictive approach, methods as described in [Graichen and Käpernick, 2012, Graichen and Kugi, 2010] may be useful. Using the Nearest Corner Method, the continuity when entering the wrench-feasible workspace and switching to a conventional cable force distribution method needs to be ensured for all cases. It is advisable to employ a conventional method that covers the entire wrench-feasible workspace, such as the Barycentric Method [Mikelsons et al., 2008], the Improved Closed Form [Pott, 2014] or the Improved Puncture Method [Müller et al., 2015]. The Nearest Corner Method could furthermore be applied within the Kinetic Energy Minimization problem, to solve for a required cable force distribution. Since commanded and measured cable forces diverge, a force control loop might be added to the control architecture in a cascade scheme. The current forward kinematic algorithm should be extended to reflect cable slackness and cable folding within the rescue process. The emergency strategies' performance should also be assessed if the failure occurs during platform motion, with varying platform angles or if multiple cables fail. In addition, more tests on prototype hardware should be conducted in general. Finally, it is to note that both emergency strategy approaches may also serve for regular CDPR control.

The fast and reliable failure detection algorithm needs to be tested in dynamical states, to assess its functionality of detecting cable failures while the platform moves. Moreover, false failure detection caused by strong platform vibration needs to be avoided. The algorithm might be improved by using redundant decisions while observing several control cycles, the consideration of different criteria or better suited threshold values. Beyond that, further possible faults must be taken into account and distinguished from a cable failure. Such could be a fault of a cable force sensor or a motor encoder defect. Additionally, it is necessary to investigate whether the locations of the sensors for cable force measurements affects the successful detection of failures. Adding external measurement devices such as a camera and

using image processing for failure detection is further conceivable. The detection of multiple cable failures is also part of future work.

As demonstrated, the workspace might be drastically reduced after a cable failure and the platform of a CDPR might tip over easily when rescued with one cable missing. Both can be addressed by developing algorithms for the synthesis of failure tolerant CDPR designs. Criteria for such algorithms may include the amount of workspace retention post-failure or the ability to rescue the platform at various poses after failure using an emergency strategy. If objects are in the workspace, such as an erected part of a building, obstacle free areas could be prioritized for workspace retention. Figure 4.27 also indicates that higher platform mass and inertia may be beneficial to avoid tipping over. Besides that, failure tolerant platform trajectories can be planned, which are routed in a way that a cable break imposes the least possible impact on trajectory tracking [Raman et al., 2023].

Beyond the emergency strategies introduced within this work, approaches based on artificial intelligence are conceivable and of high interest: Algorithms exist to solve the complex and computationally intensive problem of forward kinematics based on neural networks [Ghasemi et al., 2010] and to combine such approaches with interval arithmetic [Schmidt et al., 2014]. Moreover, neural networks can be used to control a CDPR [Ma et al., 2019, Piao et al., 2019, Wang et al., 2019, Xiong et al., 2020] or for trajectory planning [Vu and Alsmadi, 2020]. Such approaches are worth investigating for cable force calculation and trajectory planning after cable failure [Gust et al., 2024]. The basic idea is to create strategies that function like reflexes. Using physics-informed Neural Networks in particular also appears as a suitable option for robot control [Nicodemus et al., 2022].

As stated in Section 7.3, this work only considered redundant CDPRs. Thus, the proposed approaches and strategies need to be investigated for their applicability and usefulness in non-redundant CDPRs. This is relevant not only for different robots but also when considering multiple cable failures on the given ones.

Finally, the flowchart depicted in fig. 1.7 needs to be complemented with the proposed supplementary work, such as fault tolerant design and trajectory planning. Moreover, the emergency strategies need to be assessed and classified with regards to their performance level according to the applicable standards in DIN EN ISO 13849 [DIN EN ISO, 2016]. Ultimately, all of the above serves to bring cable-driven parallel robots into safe industrial application.

Bibliography

[Adamy, 2014] Adamy, J. (2014). *Nichtlineare Systeme und Regelungen*. Springer Berlin Heidelberg. https://doi.org/10.1007/978-3-642-45013-6.

[Al-Bender et al., 2005] Al-Bender, F., Lampaert, V., and Swevers, J. (2005). The generalized maxwell-slip model: a novel model for friction simulation and compensation. *IEEE Transactions on Automatic Control*, 50(11):1883–1887. https://doi.org/10.1109/TAC.2005.858676.

[Alabbasi et al., 2023] Alabbasi, M., Agkathidis, A., and Chen, H. (2023). Robotic 3d printing of concrete building components for residential buildings in saudi arabia. *Automation in Construction*, 148:104751. https://dx.doi.org/10.1016/j.autcon.2023.104751.

[Andres et al., 1994] Andres, J., Bock, T., Gebhart, F., and Steck, W. (1994). First results of the development of the masonry robot system rocco: A fault tolerant assembly tool. pages 87–93. https://dx.doi.org/10.1016/B978-0-444-82044-0.50016-3.

[Arshad, 2012] Arshad, M. I. (2012). Automated Horizontal Building Construction – A new Paradigm. In *Proceedings of the CIB IAARC W119 Workshop*, pages 6–16.

[Astour and Franz, 2014] Astour, H. and Franz, V. (2014). BIM-and simulation-based site layout planning. In *Computing in Civil and Building Engineering (2014)*, pages 291–298. https://dx.doi.org/10.1061/9780784413616.037.

[Balda, 2007] Balda, M. (2007). An algorithm for nonlinear least squares. http://dsp.vscht.cz/konference_matlab/matlab07/prispevky/balda_m/balda_m.pdf. Access on 13.12.2023.

[Barrette and Gosselin, 2005] Barrette, G. and Gosselin, C. (2005). Determination of the dynamic workspace of cable-driven planar parallel mechanisms. *Journal of Mechanical Design*, 127(2):242–248. https://doi.org/10.1115/1.1830045.

[Bauhaus-Universität Weimar, 2023] Bauhaus-Universität Weimar (2023). Robotic Printed Morphologies: 3D-Betondrucker verwandelt Forschungsstahlgerüst in eine

temporäre Skulptur. https://www.uni-weimar.de/en/university/structure/central-university-facilities/university-communications/media-service/media-information/archive/titel/robotic-printed-morphologies-3d-betondrucker-verwandelt-forschungsstahlgeruest-in-eine-temporaere-sku-1/datum///news/?no_cache=1&tx_news_pi1%5Baction%5D=detail&cHash=18597c1d82a265aa38ca7b89f9930b33. Access on 13.12.2023.

[Beckhoff Automation GmbH & Co. KG, 2023] Beckhoff Automation GmbH & Co. KG (2023). AM8031 Servomotor. https://www.beckhoff.com/de-de/produkte/motion/rotatorische-servomotoren/am8000-servomotoren/am8031.html. Access on 13.12.2023.

[Berti et al., 2018] Berti, A., Gouttefarde, M., and Carricato, M. (2018). Dynamic recovery of cable-suspended parallel robots after a cable failure. In Lenarčič, J. and Merlet, J.-P., editors, *Advances in Robot Kinematics 2016*, pages 331–339. Springer, Cham. https://doi.org/10.1007/978-3-319-56802-7_35.

[Blanchet and Merlet, 2014] Blanchet, L. and Merlet, J.-P. (2014). Interference detection for cable-driven parallel robots (cdprs). In *IEEE/ASME International Conference on Advanced Intelligent Mechatronics, AIM*. https://doi.org/10.1109/AIM.2014.6878280.

[Blanke et al., 2006] Blanke, M., Kinnaert, M., Lunze, J., Staroswiecki, M., and Schröder, J. (2006). Diagnosis and fault-tolerant control. https://dx.doi.org/10.1007/978-3-662-05344-7.

[Blom and Bar-Shalom, 1988] Blom, H. A. P. and Bar-Shalom, Y. (1988). The interacting multiple model algorithm for systems with markovian switching coefficients. *IEEE Transactions on Automatic Control*, 33(8):780–783. https://doi.org/10.1109/9.1299.

[BMWSB, 2022] BMWSB (2022). Bundesministerium für Wohnen, Stadtentwicklung und Bauwesen. Unterwegs für das Zuhause in Nordrhein-Westfalen - Bundesbauministerin Klara Geywitz zu Besuch in Aachen, Duisburg und Düsseldorf. https://www.bmwsb.bund.de/SharedDocs/topthemen/Webs/BMWSB/DE/sommertour-2022/teil3/teil3-nrw.html?cms_gcp_18499358=1. Access on 07.08.2023.

[Bock and Linner, 2016] Bock, T. and Linner, T. (2016). *Construction Robots : Elementary Technologies and Single-Task Construction Robots*. Cambridge University Press.

[Bonwetsch, 2015] Bonwetsch, T. (2015). *Robotically assembled brickwork – Manipulating assembly processes of discrete elements*. PhD thesis, ETH Zürich. https://dx.doi.org/10.3929/ethz-a-010602028.

[Borrmann et al., 2018] Borrmann, A., König, M., Koch, C., and Beetz, J. (2018). *Building Information Modeling: Technology Foundations and Industry Practice*. Springer-Verlag. https://dx.doi.org/10.1007/978-3-319-92862-3.

[Boschetti et al., 2019a] Boschetti, G., Carbone, G., and Passarini, C. (2019a). Cable failure operation strategy for a rehabilitation cable-driven robot. *Robotics*, 8(1):17. https://doi.org/10.3390/robotics8010017.

[Boschetti et al., 2019b] Boschetti, G., Carbone, G., and Passarini, C. (2019b). A fail-safe operation strategy for lawex (larm wire driven exercising device). In Gasparetto, A. and Ceccarelli, M., editors, *Mechanism Design for Robotics*, pages 424–431, Cham. Springer International Publishing. https://doi.org/10.1007/978-3-030-00365-4_50.

[Boschetti et al., 2020] Boschetti, G., Minto, R., and Trevisani, A. (2020). Improving a cable robot recovery strategy by actuator dynamics. *Applied Sciences*, 10(20):7362. https://doi.org/10.3390/app10207362.

[Boschetti et al., 2021] Boschetti, G., Minto, R., and Trevisani, A. (2021). Experimental investigation of a cable robot recovery strategy. *Robotics*, 10(1):35. https://doi.org/10.3390/robotics10010035.

[Boschetti et al., 2017] Boschetti, G., Passarini, C., and Trevisani, A. (2017). A strategy for moving cable driven robots safely in case of cable failure. In Boschetti, G. and Gasparetto, A., editors, *Advances in Italian Mechanism Science*, pages 203–211. Springer Cham. https://doi.org/10.1007/978-3-319-48375-7_22.

[Boschetti et al., 2018] Boschetti, G., Passarini, C., Trevisani, A., and Zanotto, D. (2018). A fast algorithm for wrench exertion capability computation. In Gosselin, C., Cardou, P., Bruckmann, T., and Pott, A., editors, *Cable-Driven Parallel Robots*, pages 292–303. Springer Cham. https://doi.org/10.1007/978-3-319-61431-1_25.

[Boschetti and Trevisani, 2018] Boschetti, G. and Trevisani, A. (2018). Cable robot performance evaluation by wrench exertion capability. *Robotics*, 7(2):15. https://doi.org/10.3390/robotics7020015.

[Bosscher et al., 2006] Bosscher, P., Riechel, A., and Ebert-Uphoff, I. (2006). Wrench-feasible workspace generation for cable-driven robots. *IEEE Transactions on Robotics*, 22(5):890–902. https://doi.org/10.1109/TRO.2006.878967.

[Bosscher et al., 2007] Bosscher, P., Williams, R. L., Bryson, L., and Castro-Lacouture, D. (2007). Cable-suspended robotic contour crafting system. *Automation in Construction*, 17:45–55. https://dx.doi.org/10.1016/j.autcon.2007.02.011.

[Bosscher, 2004] Bosscher, P. M. (2004). *Disturbance Robustness Measures and Wrench-Feasible Workspace Generation Techniques for Cable-Driven Robots*. PhD thesis, Georgia Institute of Technology, Atlanta, Georgia, USA.

[Boumann and Bruckmann, 2019a] Boumann, R. and Bruckmann, T. (2019a). Development of emergency strategies for cable-driven parallel robots after a cable break. In Pott, A. and Bruckmann, T., editors, *Cable-Driven Parallel Robots*, pages 269–280. Springer Cham. https://doi.org/10.1007/978-3-030-20751-9_23.

[Boumann and Bruckmann, 2019b] Boumann, R. and Bruckmann, T. (2019b). Simulation von Seilrissen und Erweiterung von Abfangstrategien für Seilroboter. In Bertram, T., Corves, B., Gräßler, I., and Janschek, K., editors, *Fachtagung Mechatronik 2019: Paderborn (March 27.-28., 2019), Proceedings*.

[Boumann and Bruckmann, 2020a] Boumann, R. and Bruckmann, T. (2020a). Computationally efficient cable force calculation outside the wrench-feasible workspace. In Kuo, C.-H., Lin, P.-C., Essomba, T., and Chen, G.-C., editors, *Robotics and Mechatronics*, pages 177–188. Springer Cham. https://doi.org/10.1007/978-3-030-30036-4_15.

[Boumann and Bruckmann, 2020b] Boumann, R. and Bruckmann, T. (2020b). Real-time cable force calculation beyond the wrench-feasible workspace. *Robotics*, 9(2):41. https://doi.org/10.3390/robotics9020041.

[Boumann and Bruckmann, 2021] Boumann, R. and Bruckmann, T. (2021). An emergency strategy for cable failure in reconfigurable cable robots. In Gouttefarde, M., Bruckmann, T., and Pott, A., editors, *Cable-Driven Parallel Robots*, pages 217–229. Springer Cham. https://doi.org/10.1007/978-3-030-75789-2_18.

[Boumann and Bruckmann, 2022] Boumann, R. and Bruckmann, T. (2022). Simulation and model-based verification of an emergency strategy for cable failure in cable robots. *Actuators*, 11(2):56. https://doi.org/10.3390/act11020056.

[Boumann et al., 2023] Boumann, R., Jeziorek, C., and Bruckmann, T. (2023). Validation of emergency strategies for cable-driven parallel robots after a cable failure. In Caro, S., Pott, A., and Bruckmann, T., editors, *Cable-Driven Parallel Robots*, pages 209–220. Springer Cham. https://doi.org/10.1007/978-3-031-32322-5_17.

[Boumann et al., 2020a] Boumann, R., Lemmen, P., Heidel, R., and Bruckmann, T. (2020a). Optimization of trajectories for cable robots on automated construction sites. In Osumi, H., Furuya, H., and Tateyama, K., editors, *Proceedings of the 37th International Symposium on Automation and Robotics in Construction (ISARC)*, pages 465–472, Kitakyushu,

Japan. International Association for Automation and Robotics in Construction (IAARC). https://doi.org/10.22260/ISARC2020/0065.

[Boumann et al., 2020b] Boumann, R., Lemmen, P., Heidel, R., Lehmann, M., Born, O., Gosedopp, J., and Bruckmann, T. (2020b). Berechnung von Trajektorien für Seilroboter auf automatisierten Baustellen. In *Sechste IFToMM D-A-CH Konferenz 2020: 27./28. Februar 2020, Campus Technik Lienz*. DuEPublico, Universität Duisburg-Essen. https://doi.org/10.17185/duepublico/71180.

[Brehm, 2019] Brehm, E. (2019). Robots for masonry construction – status quo and thoughts for the german market. *Mauerwerk*, 23(2):87–94. https://dx.doi.org/10.1002/dama.201900004.

[Brinks, 2016] Brinks, E. (2016). China opens the aperture to the cosmos. https://www.usnews.com/news/best-countries/articles/2016-07-11/china-builds-worlds-largest-radio-telescope. Access on 2023-09-21.

[Bruckmann, 2010] Bruckmann, T. (2010). *Auslegung und Betrieb redundanter paralleler Seilroboter*. PhD thesis, Universität Duisburg-Essen, Duisburg.

[Bruckmann and Boumann, 2021] Bruckmann, T. and Boumann, R. (2021). Simulation and optimization of automated masonry construction using cable robots. *Advanced Engineering Informatics*, 50:101388. https://doi.org/10.1016/j.aei.2021.101388.

[Bruckmann et al., 2012] Bruckmann, T., Lalo, W., Nguyen, K., and Salah, B. (2012). Development of a storage retrieval machine for high racks using a wire robot. In *Proceedings of the ASME 2012 International Design Engineering Technical Conferences and Computers and Information in Engineering Conference*, volume 4, pages 771–780. ASME. https://doi.org/10.1115/DETC2012-70389.

[Bruckmann et al., 2016] Bruckmann, T., Mattern, H., Spenglerc, A., Reichert, C., Malkwitz, A., and König, M. (2016). Automated construction of masonry buildings using cable-driven parallel robots. In Sattineni, A. A. U., Azhar, S. A. U., and Castro, D. G. T. U., editors, *Proceedings of the 33rd International Symposium on Automation and Robotics in Construction (ISARC)*, pages 332–340, Auburn, USA. International Association for Automation and Robotics in Construction (IAARC). https://doi.org/10.22260/ISARC2016/0041.

[Bruckmann et al., 2008a] Bruckmann, T., Mikelsons, L., Brandt, T., Hiller, M., and Schramm, D. (2008a). Wire robots part I - kinematics, analysis & design. In Ryu, J.-H., editor, *Parallel Manipulators - New Developments*, ARS Robotic Books, pages 109–132. IntechOpen Limited, London. https://doi.org/10.5772/5365.

[Bruckmann et al., 2008b] Bruckmann, T., Mikelsons, L., Brandt, T., Hiller, M., and Schramm, D. (2008b). Wire robots part II - dynamics, control & application. In Ryu, J.-H., editor, *Parallel Manipulators - New Developments*, ARS Robotic Books, pages 133–153. IntechOpen Limited, London. https://doi.org/10.5772/5366.

[Bruckmann et al., 2011] Bruckmann, T., Mikelsons, L., and Hiller, M. (2011). A design-to-task approach for wire robots. In Kecskeméthy, A., Potkonjak, V., and Müller, A., editors, *Interdisciplinary Applications of Kinematics*, pages 83–97, Dordrecht. Springer Netherlands. https://doi.org/10.1007/978-94-007-2978-0_6.

[Bruckmann and Pott, 2012] Bruckmann, T. and Pott, A. (2012). *Cable-Driven Parallel Robots*. Mechanisms and Machine Science. Springer Berlin Heidelberg. https://doi.org/10.1007/978-3-642-31988-4.

[Bruckmann et al., 2006] Bruckmann, T., Pott, A., and Hiller, M. (2006). Calculating force distributions for redundantly actuated tendon-based stewart platforms. In Lennarčič, J. and Roth, B., editors, *Advances in Robot Kinematics*, pages 403–412, Dordrecht. Springer Netherlands. https://doi.org/10.1007/978-1-4020-4941-5_44.

[Bruckmann et al., 2019] Bruckmann, T., Reichert, C., and Ji, H. (2019). Energy consumption reduction of a cable-driven storage and retrieval system. In Lenarčič, J. and Parenti-Castelli, V., editors, *Advances in Robot Kinematics 2018*, pages 383–391. Springer International Publishing. https://dx.doi.org/10.1007/978-3-319-93188-3_44.

[Bruckmann et al., 2018] Bruckmann, T., Reichert, C., Meik, M., Lemmen, P., Spengler, A., Mattern, H., and König, M. (2018). Concept studies of automated construction using cable-driven parallel robots. In Gosselin, C., Cardou, P., Bruckmann, T., and Pott, A., editors, *Cable-Driven Parallel Robots*, pages 364–375. Springer Cham. https://doi.org/10.1007/978-3-319-61431-1_31.

[Bruckmann et al., 2013] Bruckmann, T., Sturm, C., Fehlberg, L., and Reichert, C. (2013). An energy-efficient wire-based storage and retrieval system. In *2013 IEEE/ASME International Conference on Advanced Intelligent Mechatronics*, pages 631–636. IEEE. https://doi.org/10.1109/AIM.2013.6584163.

[Bury et al., 2019] Bury, D., Izard, J.-B., Gouttefarde, M., and Lamiraux, F. (2019). Continuous collision detection for a robotic arm mounted on a cable-driven parallel robot. In *2019 IEEE/RSJ International Conference on Intelligent Robots and Systems (IROS)*, pages 8097–8102. https://doi.org/10.1109/IROS40897.2019.8967836.

[Busawon and Saif, 1999] Busawon, K. and Saif, M. (1999). A state observer for nonlinear systems. *IEEE Transactions on Automatic Control*, 44(11):2098–2103. https://doi.org/10.1109/9.802924.

[Camacho, 2007] Camacho, E. F. ; Bordons, C. (2007). *Model Predictive Control*. Springer. https://doi.org/10.1007/978-0-85729-398-5.

[Cambridge University Press, 2023] Cambridge University Press (2023). Cambridge dictionary of business-english: Definition of robot. https://dictionary.cambridge.org/de/worterbuch/englisch/robot. Access on 2023-09-21.

[Caro and Merlet, 2020] Caro, S. and Merlet, J.-P. (2020). Failure analysis of a collaborative 4-1 cable-driven parallel robot. *New Trends in Mechanism and Machine Science*. https://api.semanticscholar.org/CorpusID:226372035.

[Caro et al., 2023] Caro, S., Pott, A., and Bruckmann, T. (2023). *Cable-Driven Parallel Robots: Proceedings of the 6th International Conference on Cable-Driven Parallel Robots*. Mechanisms and Machine Science. Springer Nature Switzerland. https://doi.org/10.1007/978-3-031-32322-5.

[Caseri, 2009] Caseri, W. (2009). Polycarbonate. In Böckler, F., Dill, B., Eisenbrand, G., Faupel, F., Fugmann, B., Gamse, T., Matissek, R., Pohnert, G., Rühling, A., Schmidt, S., and Sprenger, G., editors, *RÖMPP [Online]*, Stuttgart, Germany. Georg Thieme Verlag. https://roempp.thieme.de/lexicon/RD-16-03130. Access on 05.05.2023.

[Cavieres et al., 2016] Cavieres, A., Gentry, T. R., and Eastman, C. (2016). A process-driven representation schema for masonry wall assemblies. pages 914–922. The International Association for Automation and Robotics in Construction (IAARC). https://dx.doi.org/10.22260/ISARC2016/0110.

[Ceccarelli et al., 2007] Ceccarelli, M., Ottaviano, E., and Tavolieri, C. (2007). Experimental activity on cable-based parallel manipulators: issues and results at larm in cassino. In *2nd Internation Congress on Design and Modelling of Mechanical Systems*, Monastir, Tunisia.

[Cobod International A/S, 2023] Cobod International A/S (2023). PERI 3D CONSTRUCTION. https://cobod.com/projects-partners/peri/. Access on 13.12.2023.

[Coleman and Li, 1996] Coleman, T. F. and Li, Y. (1996). An interior trust region approach for nonlinear minimization subject to bounds. *SIAM Journal on Optimization*, 6(2):418–445. https://doi.org/10.1137/0806023.

[Costello and Dunleavy, 2022] Costello, B. and Dunleavy, R. (2022). SkyCam wire snap causes delay during Jets-Bills game. https://nypost.com/2022/11/06/skycam-wire-snap-causes-delay-during-jets-vs-bills-game/. Access on 13.12.2023.

[Cromer, 1981] Cromer, A. (1981). Stable solutions using the Euler Approximation. *American Journal of Physics*, pages 455–459. https://doi.org/https://doi.org/10.1119/1.12478.

[Côté et al., 2016] Côté, A. F., Cardou, P., and Gosselin, C. (2016). A tension distribution algorithm for cable-driven parallel robots operating beyond their wrench-feasible workspace. In *2016 16th International Conference on Control, Automation and Systems (ICCAS)*, pages 68–73. https://doi.org/10.1109/ICCAS.2016.7832301.

[Dassault Systèmes, 2023] Dassault Systèmes (2023). DYMOLA Systems Engineering - Multi-Engineering-Modellierung und - Simulation auf Basis von Modelica und FMI. https://www.3ds.com/de/produkte-und-services/catia/produkte/dymola/. Access on 13.12.2023.

[De Stefano et al., 2023] De Stefano, M., Vijayan, R., Stemmer, A., Elhardt, F., and Ott, C. (2023). A gravity compensation strategy for on-ground validation of orbital manipulators. In *2023 IEEE International Conference on Robotics and Automation (ICRA)*, pages 11859–11865. https://doi.org/10.1109/ICRA48891.2023.10161480.

[Dežman et al., 2022] Dežman, M., Asfour, T., Ude, A., and Gams, A. (2022). Mechanical design and friction modelling of a cable-driven upper-limb exoskeleton. *Mechanism and Machine Theory*, 171:104746. https://doi.org/10.1016/j.mechmachtheory.2022.104746.

[Detert et al., 2017] Detert, T., Eddine, S. C., Fauroux, J.-C., Haschke, T., Becchi, F., Corves, B., Guzmán, R., Herb, F. A., Linéatte, B., and Martin, D. (2017). Bots2rec: introducing mobile robotic units on construction sites for asbestos rehabilitation. *Construction Robotics*, 1:29 – 37. https://doi.org/10.1007/s41693-017-0007-1.

[DGUV, 2015] DGUV (2015). DGUV Information 209-074: Industrieroboter (bisher BGI/GUV-I 5123).

[DGUV, 2020] DGUV (2020). DGUV Information 215-313: Lasten über Personen.

[DIN, 1974] DIN (1974). DIN 15020-1:1974-02: Lifting Appliances; Principles Relating to Rope Drives; Calculation and Construction. https://dx.doi.org/10.31030/1153573.

[DIN EN, 2009] DIN EN (2009). DIN EN 12385-1:2009-01: Steel wire ropes - Safety - Part 1: General requirements; German version EN 12385-1:2002+A1:2008. https://dx.doi.org/10.31030/1476427.

[DIN EN, 2020] DIN EN (2020). DIN EN 16603-11:2020-02: Space engineering - Definition of the Technology Readiness Levels (TRLs) and their criteria of assessment (ISO 16290:2013, modified); German version EN 16603-11:2019. https://dx.doi.org/10.31030/3119848.

[DIN EN ISO, 2011] DIN EN ISO (2011). DIN EN ISO 12100:2011-03: Safety of machinery - General principles for design - Risk assessment and risk reduction (ISO 12100:2010); German version EN ISO 12100:2010. https://dx.doi.org/10.31030/1634159.

[DIN EN ISO, 2016] DIN EN ISO (2016). DIN EN ISO 13849-1:2016-06: Safety of machinery - Safety-related parts of control systems - Part 1: General principles for design (ISO 13849-1:2015); German version EN ISO 13849-1:2015. https://dx.doi.org/10.31030/2300069.

[DIN EN ISO, 2021] DIN EN ISO (2021). DIN EN ISO 16739-1:2021-11: Industry Foundation Classes (IFC) for data sharing in the construction and facility management industries - Part 1: Data schema (ISO 16739-1:2018); English version EN ISO 16739-1:2020. https://dx.doi.org/10.31030/3144077.

[Dörfler et al., 2016] Dörfler, K., Sandy, T., Giftthaler, M., Gramazio, F., Kohler, M., and Buchli, J. (2016). Mobile robotic brickwork – automation of a discrete robotic fabrication process using an autonomous mobile robot. In Reinhardt, D., editor, *Robotic Fabrication in Architecture, Art and Design 2016*, pages 204–217. Springer. https://dx.doi.org/10.1007/978-3-319-26378-6_15.

[Ebert-Uphoff and Voglewede, 2004] Ebert-Uphoff, I. and Voglewede, P. (2004). On the connections between cable-driven robots, parallel manipulators and grasping. volume 5, pages 4521 – 4526 Vol.5. https://doi.org/10.1109/ROBOT.2004.1302430.

[Elhardt et al., 2023a] Elhardt, F., Boumann, R., de Stefano, M., Heidel, R., Lemmen, P., Heumos, M., Jeziorek, C., Roa, M. A., Schedl, M., and Bruckmann, T. (2023a). System requirements elicitation and conceptualization for a novel space robot suspension system. In *17th Symposium on Advanced Space Technologies in Robotics and Automation*.

[Elhardt et al., 2023b] Elhardt, F., Boumann, R., De Stefano, M., Heidel, R., Lemmen, P., Heumos, M., Jeziorek, C., Roa, M. A., Schedl, M., and Bruckmann, T. (2023b). The Motion Suspension System – MSS: A Cable-Driven System for On-Ground Tests of Space

Robots. In Okada, M., editor, *Advances in Mechanism and Machine Science*, pages 379–388, Cham. Springer Nature Switzerland. https://doi.org/10.1007/978-3-031-45770-8_38.

[Ericson, 2004] Ericson, C. (2004). *Real-Time Collision Detection*. CRC Press.

[European Parliament, 2006] European Parliament (2006). Directive 2006/42/EC of the European Parliament and of the Council of 17 May 2006 on machinery, and amending Directive 95/16/EC (recast). http://data.europa.eu/eli/dir/2006/42/oj.

[Eurosport, 2022] Eurosport (2022). Kamera-Panne sorgt für Spielunterbrechung: Kurioser Zwischenfall bei Borussia Gladbach gegen Eintracht Frankfurt. https://www.eurosport.de/fussball/bundesliga/2022-2023/spidercam-sorgt-fur-spielunterbrechung-kurioser-zwischenfall-bei-borussia-monchengladbach-gegen-eint_sto9197882/story.shtml. Access on 13.12.2023.

[Fabritius et al., 2018] Fabritius, M., Martin, C., and Pott, A. (2018). Calculation of the collision-free printing workspace for fully-constrained cable-driven parallel robots. volume Volume 5B: 42nd Mechanisms and Robotics Conference of *International Design Engineering Technical Conferences and Computers and Information in Engineering Conference*. https://doi.org/10.1115/DETC2018-85961.

[Fang, 2005] Fang, S. (2005). *Design, Modeling and Motion Control of Tendon-based Parallel Manipulators*. PhD thesis, Gerhard-Mercator-Universität, Duisburg. Fortschritt-Berichte VDI, Reihe 8, Nr. 1076, Düsseldorf.

[Fang et al., 2004] Fang, S., Franitza, D., Torlo, M., Bekes, F., and Hiller, M. (2004). Motion control of a tendon-based parallel manipulator using optimal tension distribution. *IEEE/ASME Transactions on Mechatronics*, 9(3):561–568. https://doi.org/10.1109/TMECH.2004.835336.

[Fattah and Agrawal, 2005] Fattah, A. and Agrawal, S. K. (2005). On the Design of Cable-Suspended Planar Parallel Robots. *Journal of Mechanical Design*, 127(5):1021–1028. https://doi.org/10.1115/1.1903001.

[FBR Ltd, 2023] FBR Ltd (2023). Robotic construction is here. https://www.fbr.com.au/view/hadrian-x. Access on 13.12.2023.

[Fingrut et al., 2019] Fingrut, A., Crolla, K., and Lau, D. (2019). Automation complexity - brick by brick. In *Intelligent & Informed, Proceedings of the 24th International Conference of the Association for Computer-Aided Architectural Design Research in Asia (CAADRIA)*

2019, volume 1, pages 93–102, Hong Kong. Association for Computer-Aided Architectural Design Research in Asia (CAADRIA).

[Flores et al., 2012] Flores, P., Machado, M., Silva, M., and Martins, J. (2012). On the continuous contact force models for soft materials in multibody dynamics. *Multibody System Dynamics*, 25:357–375. https://doi.org/10.1007/s11044-010-9237-4.

[Frevel, 2016] Frevel, B. (2016). *Sicherheit: Ein (un)stillbares Grundbedürfnis*. essentials. Springer Fachmedien Wiesbaden. https://doi.org/10.1007/978-3-658-12458-8.

[Gasparetto et al., 2015] Gasparetto, A., Boscariol, P., Lanzutti, A., and Vidoni, R. (2015). *Path Planning and Trajectory Planning Algorithms: A General Overview*. Springer International Publishing, Cham. https://doi.org/10.1007/978-3-319-14705-5_1.

[Gentry, 2013] Gentry, T. R. (2013). Digital tools for masonry design and construction. In *The Visibility of Research*, pages 34–41, Charlotte, North Carolina, USA. ARCC Conference Repository.

[Ghaffar and Hassan, 2015] Ghaffar, A. and Hassan, M. (2015). Failure analysis of cable based parallel manipulators. In *Recent Trends in Materials, Mechanical Engineering, Automation and Information Engineering*, volume 736 of *Applied Mechanics and Materials*, pages 203–210. Trans Tech Publications Ltd. https://doi.org/10.4028/www.scientific.net/AMM.736.203.

[Ghasemi et al., 2010] Ghasemi, A., Eghtesad, M., and Farid, M. (2010). Neural network solution for forward kinematics problem of cable robots. *Journal of Intelligent and Robotic Systems*, 60:201–215. https://doi.org/10.1007/s10846-010-9421-z.

[Gifary, 2020] Gifary, N. (2020). Automatic decomposition of sand-lime brick walls based on the industry foundation classes (ifc). Bachelorarbeit, Universität Duisburg-Essen, Fakultät für Ingenieurwissenschaften.

[Goldsmith, 2007] Goldsmith, P. (2007). Large—scale surveys with the arecibo multibeam system. In Lobanov, A. P., Zensus, J. A., Cesarsky, C., and Diamond, P. J., editors, *Exploring the Cosmic Frontier*, pages 209–214, Berlin, Heidelberg. Springer Berlin Heidelberg. https://doi.org/10.1007/978-3-540-39756-4_58.

[Gosselin et al., 2017] Gosselin, C., Cardou, P., Bruckmann, T., and Pott, A. (2017). *Cable-Driven Parallel Robots: Proceedings of the Third International Conference on Cable-Driven Parallel Robots*. Mechanisms and Machine Science. Springer International Publishing. https://doi.org/10.1007/978-3-319-61431-1.

[Gough and Whitehall, 1962] Gough, V. E. and Whitehall, S. (1962). Universal tyre test machine. In *FISITA Ninth International Technical Congress*, pages 117–137.

[Gouttefarde et al., 2021] Gouttefarde, M., Bruckmann, T., and Pott, A. (2021). *Cable-Driven Parallel Robots: Proceedings of the 5th International Conference on Cable-Driven Parallel Robots*. Mechanisms and Machine Science. Springer International Publishing. https://doi.org/10.1007/978-3-030-75789-2.

[Gouttefarde et al., 2015] Gouttefarde, M., Lamaury, J., Reichert, C., and Bruckmann, T. (2015). A versatile tension distribution algorithm for n-dof parallel robots driven by $n+2$ cables. *IEEE Transactions on Robotics*, 31(6):1444 – 1457. https://doi.org/10.1109/TRO.2015.2495005.

[Gouttefarde et al., 2006] Gouttefarde, M., Merlet, J.-P., and Daney, D. (2006). Determination of the wrench-closure workspace of 6-dof parallel cable-driven mechanisms. pages 315–322. https://doi.org/10.1007/978-1-4020-4941-5_34.

[Gouttefarde et al., 2007] Gouttefarde, M., Merlet, J.-P., and Daney, D. (2007). Wrench-feasible workspace of parallel cable-driven mechanisms. In *Proceedings 2007 IEEE International Conference on Robotics and Automation*, pages 1492–1497. https://doi.org/10.1109/ROBOT.2007.363195.

[Graichen and Käpernick, 2012] Graichen, K. and Käpernick, B. (2012). A real-time gradient method for nonlinear model predictive control. In Zheng, T., editor, *Frontiers of Model Predictive Control*, Rijeka. IntechOpen. https://dx.doi.org/10.5772/37638.

[Graichen and Kugi, 2010] Graichen, K. and Kugi, A. (2010). Stability and incremental improvement of suboptimal mpc without terminal constraints. *IEEE Transactions on Automatic Control*, 55(11):2576–2580. https://dx.doi.org/10.1109/TAC.2010.2057912.

[Grüne, 2011] Grüne, L. ; Pannek, J. (2011). *Nonlinear Model Predictive Control: Theory and Algorithms*. Springer London. https://doi.org/10.1007/978-0-85729-501-9.

[Gust et al., 2024] Gust, P., Hürten, C., Boumann, R., and Bruckmann, T. (2024). Methoden des maschinellen Lernens als Notfallstrategie nach Seilrissen bei parallelen Seilrobotern. *Zehnte IFToMM D-A-CH Konferenz 2024*. Submitted.

[Hahlbrock et al., 2022] Hahlbrock, D., Braun, M., Heidel, R., Lemmen, P., Boumann, R., Bruckmann, T., Schramm, D., Helm, V., and Willmann, J. (2022). Cable robotic 3d-printing: additive manufacturing on the construction site. *Construction Robotics*, 2022:1 – 14. https://doi.org/10.1007/s41693-022-00082-3.

[Hahn, 2002] Hahn, H. (2002). *Rigid Body Dynamics of Mechanisms: 1 Theoretical Basis*. Springer, 1 edition. https://doi.org/10.1007/978-3-662-04831-3.

[Hairer et al., 1993] Hairer, E., Nørsett, S., and Wanner, G. (1993). *Solving Ordinary Differential Equations I: Nonstiff Problems*. Springer Series in Computational Mathematics. Springer Berlin Heidelberg. https://doi.org/10.1007/978-3-540-78862-1.

[Hairer et al., 1996] Hairer, E., Nørsett, S., and Wanner, G. (1996). *Solving Ordinary Differential Equations II: Stiff and Differential-Algebraic Problems*. Springer Series in Computational Mathematics. Springer Berlin, Heidelberg. https://doi.org/10.1007/978-3-642-05221-7.

[He and Wu, 2012] He, K.-Y. and Wu, I.-C. (2012). Dynamic simulation and visualization for site layout planning. In van Bronswijk, J. E. M. H. A., Maas, G. J., and van Gassel, F. J. M., editors, *Proceedings of the 36th International Symposium on Automation and Robotics in Construction and Mining (ISARC)*, Eindhoven, Niederlande. The International Association for Automation and Robotics in Construction (IAARC). https://dx.doi.org/10.22260/ISARC2012/0008.

[Héder, 2017] Héder, M. (2017). From NASA to EU: the evolution of the TRL scale in Public Sector Innovation. *The Innovation Journal*, 22:1. https://api.semanticscholar.org/CorpusID:108288388.

[Heidel et al., 2022] Heidel, R., Lemmen, P., Boumann, R., and Bruckmann, T. (2022). Auslegung und Inbetriebnahme eines Seilroboters zum automatisierten Mauern von Gebäudewänden. In Bertram, T., Corves, B., Janschek, K., and Rinderknecht, S., editors, *Fachtagung VDI MECHATRONIK 2022*, pages 126–132, Darmstadt. https://doi.org/10.26083/tuprints-00020963.

[Helm, 2014] Helm, V. (2014). In-situ fabrication: Mobile robotic units on construction sites. *Architectural Design*, 84(3):100–107. https://dx.doi.org/10.1002/ad.1763.

[Helm et al., 2012] Helm, V., Ercan, S., Gramazio, F., and Kohler, M. (2012). In-situ robotic construction: Extending the digital fabrication chain in architecture. In *Synthetic Digital Ecologies: Proceedings of the 32nd Annual Conference of the Association for Computer Aided Design in Architecture (ACADIA)*, pages 169–176. CUMINCAD.

[Herrmann, 2023] Herrmann, L. (2023). *Konzeptionierung und Umsetzung einer Entwicklungsumgebung für den Einsatz kooperierender Drohnen für den Lasttransport*. PhD thesis. https://doi.org/10.17185/duepublico/78533.

[Herrmann et al., 2022] Herrmann, L., Boumann, R., Lehmann, M., Müller, S., and Bruckmann, T. (2022). Simulation-based comparison of novel automated construction systems. *Robotics*, 11(6):119. https://doi.org/10.3390/robotics11060119.

[Hexagon AB, 2023] Hexagon AB (2023). Adams - Die Lösung der Mehrkörperdynamik-Simulation. https://hexagon.com/de/products/product-groups/computer-aided-engineering-software/adams. Access on 13.12.2023.

[Heyden et al., 2002] Heyden, T., Maier, T., and Woernle, C. (2002). Trajectory tracking control for a cable suspension manipulator. In Lenarčič, J. and Thomas, F., editors, *Advances in Robot Kinematics: Theory and Applications*, pages 125–134, Dordrecht. Springer Netherlands. https://doi.org/10.1007/978-94-017-0657-5_14.

[Hidayah et al., 2020] Hidayah, R., Bishop, L., Jin, X., Chamarthy, S., Stein, J., and Agrawal, S. (2020). Gait Adaptation Using a Cable-Driven Active Leg Exoskeleton (C-ALEX) With Post-Stroke Participants. *IEEE Transactions on Neural Systems and Rehabilitation Engineering*, PP:1–1. https://doi.org/10.1109/TNSRE.2020.3009317.

[Hiller et al., 2005] Hiller, M., Fang, S., Mielczarek, S., Verhoeven, R., and Franitza, D. (2005). Design, analysis and realization of tendon-based parallel manipulators. *Mechanism and Machine Theory*, 40(4):429–445. https://doi.org/10.1016/j.mechmachtheory.2004.08.002.

[Hilti Deutschland AG, 2023] Hilti Deutschland AG (2023). BIM & ROBOTIK: DAS KANN DER HILTI BOHRROBOTER. https://www.hilti.de/content/hilti/E3/DE/de/business/business/productivity/semi-autonomer-baustellenroboter-jaibot.html. Access on 13.12.2023.

[Hoevenaars, 2016] Hoevenaars, T. (2016). *Parallel manipulators with two end-effectors: Getting a grip on Jacobian-based stiffness analysis*. PhD thesis, Delft University of Technology. https://doi.org/10.4233/uuid:d684f024-ab7f-4863-a2c6-d456238c6c39.

[Hufnagel, 2014] Hufnagel, T. (2014). *Theoretische und praktische Entwicklung von Regelungskonzepten für redundant angetriebene parallelkinematische Maschinen*. PhD thesis, Universität Duisburg-Essen, Duisburg.

[Husty et al., 2001] Husty, M., Mielczarek, S., and Hiller, M. (2001). Constructing an Overconstrained Planar 4RPRManipulator with Maximal Forward Kinematics Solution Set. In *Proceedings of the 10th Workshop RAAD*.

[Husty et al., 2002] Husty, M., Mielczarek, S., and Hiller, M. (2002). A redundant spatial stewart-gough platform with a maximal forward kinematics solution set. In Lenarčič,

J. ; Thomas, F., editor, *Advances in Robot Kinematics: Theory and Applications*, pages 147–154. Springer Netherlands. https://doi.org/10.1007/978-94-017-0657-5_16.

[Idà et al., 2019] Idà, E., Bruckmann, T., and Carricato, M. (2019). Rest-to-rest trajectory planning for underactuated cable-driven parallel robots. *IEEE Transactions on Robotics*, 35(6):1338–1351. https://doi.org/10.1109/TRO.2019.2931483.

[Ikeda and Harada, 2006] Ikeda, Y. and Harada, T. (2006). Application of the automated building construction system using the conventional construction method together. In *Proceedings of the 23rd International Symposium on Automation and Robotics in Construction (ISARC)*, pages 722–727, Tokyo, Japan. The International Association for Automation and Robotics in Construction (IAARC). https://dx.doi.org/10.22260/ISARC2006/0134.

[International Federation of Robotics, 2022] International Federation of Robotics (2022). World robotics 2022. https://ifr.org/downloads/press2018/2022_WR_extended_version.pdf. Access on 13.12.2023.

[ISO, 2007] ISO (2007). ISO 10303-28:2007-10: Industrial automation systems and integration - Product data representation and exchange - Part 28: Implementation methods: XML representations of EXPRESS schemas and data, using XML schemas.

[ISO, 2013] ISO (2013). ISO 16625:2013-07: Cranes and hoists - Selection of wire ropes, drums and sheaves.

[ISO, 2016] ISO (2016). ISO 10303-21:2016-03: Industrial automation systems and integration - Product data representation and exchange - Part 21: Implementation methods: Clear text encoding of the exchange structure.

[Iturralde et al., 2020] Iturralde, K., Feucht, M., Hu, R., Pan, W., Schlandt, M., Linner, T., Bock, T., Izard, J.-B., Eskudero, I., Rodriguez, M., Gorrotxategi, J., Astudillo, J., Cavalcanti, J., Gouttefarde, M., Fabritius, M., Martin, C., Henninge, T., Normes, S., Jacobsen, Y., Pracucci, A., Cañada, J., Jimenez-Vicaria, J. D., Paulotto, C., Alonso, R., and Elia, L. (2020). A cable driven parallel robot with a modular end effector for the installation of curtain wall modules. In Osumi, H., Furuya, H., and Tateyama, K., editors, *Proceedings of the 37th International Symposium on Automation and Robotics in Construction and Mining (ISARC)*, pages 1472–1479, Kitakyshu, Japan. The International Association for Automation and Robotics in Construction (IAARC). https://dx.doi.org/10.22260/ISARC2020/0204.

[Iturralde et al., 2022] Iturralde, K., Feucht, M., Illner, D., Hu, R., Pan, W., Linner, T., Bock, T., Eskudero, I., Rodriguez, M., Gorrotxategi, J., Izard, J., Astudillo, J., Cavalcanti

Santos, J., Gouttefarde, M., Fabritius, M., Martin, C., Henninge, T., Nornes, S., Jacobsen, Y., Pracucci, A., Cañada, J., Jimenez-Vicaria, J., Alonso, R., and Elia, L. (2022). Cable-driven parallel robot for curtain wall module installation. *Automation in Construction*, 138:104235. https://dx.doi.org/10.1016/j.autcon.2022.104235.

[Izard et al., 2018] Izard, J.-B., Dubor, A., Hervé, P.-E., Cabay, E., Culla, D., Rodriguez, M., and Barrado, M. (2018). On the improvements of a cable-driven parallel robot for achieving additive manufacturing for construction. In Gosselin, C., Cardou, P., Bruckmann, T., and Pott, A., editors, *Cable-Driven Parallel Robots*, pages 353–363, Cham. Springer International Publishing. https://dx.doi.org/10.1007/978-3-319-61431-1_30.

[Jeziorek et al., 2023] Jeziorek, C., Pfeil, A., Piechullik, M., Romanowski, S., Heidel, R., Boumann, R., Lemmen, P., Malkwitz, A., and Bruckmann, T. (2023). Auswahlverfahren für geeignete Deckensysteme zur Automatisierung der Rohbauerstellung. *Neunte IFToMM D-A-CH Konferenz 2023: 16./17. März 2023, Universität Basel*, 2023.

[Jiang and Gosselin, 2016] Jiang, X. and Gosselin, C. (2016). Dynamic point-to-point trajectory planning of a three-dof cable-suspended parallel robot. *IEEE Transactions on Robotics*, 32(6):1550–1557. https://doi.org/10.1109/TRO.2016.2597315.

[Jung, 2020] Jung, J. (2020). Workspace and stiffness analysis of 3d printing cable-driven parallel robot with a retractable beam-type end-effector. *Robotics*, 9(3):65. https://dx.doi.org/10.3390/robotics9030065.

[Katliar et al., 2017] Katliar, M., Fischer, J., Frison, G., Diehl, M., Teufel, H., and Bülthoff, H. H. (2017). Nonlinear model predictive control of a cable-robot-based motion simulator. *IFAC-PapersOnLine*, 50(1):9833–9839. 20th IFAC World Congress. https://doi.org/10.1016/j.ifacol.2017.08.901.

[Kock and Schumacher, 1998] Kock, S. and Schumacher, W. (1998). A parallel x-y manipulator with actuation redundancy for high-speed and active-stiffness applications. In *Proceedings. 1998 IEEE International Conference on Robotics and Automation (Cat. No.98CH36146)*, volume 3, pages 2295–2300 vol.3. https://doi.org/10.1109/ROBOT.1998.680665.

[Krämer and Kempkes, 2013] Krämer, A. and Kempkes, J. (2013). Modellierung und Simulation von nichtlinearen Reibungseffekten bei der Lageregelung von Servomotoren. *FHWS Science Journal*, 2:47–57.

[Kraus, 2016] Kraus, W. (2016). *Force control of cable-driven parallel robots*. PhD thesis, University of Stuttgart, Stuttgart, Germany.

[Krijnen, 2023] Krijnen, T. (2023). Ifcopenshell. http://www.ifcopenshell.org. Access on 13.12.2023.

[Lalo, 2014] Lalo, W. (2014). *Ein Beitrag zur Entwicklung von Assistenzsystemen für serielle und parallele Roboter am Beispiel von Autobetonpumpen und seilbasierten Regalbediengeräten*. PhD thesis, Universität Duisburg-Essen, Duisburg.

[Lalo et al., 2013] Lalo, W., Bruckmann, T., and Schramm, D. (2013). Optimal control for a wire-based storage retrieval machine. In Viadero, F. and Ceccarelli, M., editors, *New Trends in Mechanism and Machine Science*, pages 631–639, Dordrecht. Springer Netherlands. https://doi.org/10.1007/978-94-007-4902-3_66.

[Landsberger and Sheridan, 1985] Landsberger, S. E. and Sheridan, T. B. (1985). A new design for parallel link manipulator. In *International Conference on Cybernetics and Society*, pages 812–814, Tucson, Arizona, USA.

[Lemmen et al., 2019] Lemmen, P., Heidel, R., and Bruckmann, T. (2019). A conditional stop capable trajectory planner for cable-driven parallel robots. In Pott, A. and Bruckmann, T., editors, *Cable-Driven Parallel Robots*, pages 281–292, Cham. Springer International Publishing. https://doi.org/10.1007/978-3-030-20751-9_24.

[Lemmen et al., 2022] Lemmen, P., Heidel, R., Sonntag, S., and Bruckmann, T. (2022). Augmented Reality in Anwendungen der Seilrobotik. *Achte IFToMM D-A-CH Konferenz 2022: 24./25. Februar 2022, Online-Konferenz*, 2022. https://dx.doi.org/10.17185/duepublico/75444.

[Li et al., 2018] Li, H., Sun, J., Pan, G., and Yang, Q. (2018). Preliminary running and performance test of the huge cable robot of fast telescope. In Gosselin, C., Cardou, P., Bruckmann, T., and Pott, A., editors, *Cable-Driven Parallel Robots*, pages 402–414, Cham. Springer International Publishing. https://doi.org/10.1007/978-3-319-61431-1_34.

[LIROS GmbH, 2023a] LIROS GmbH (2023a). D-Pro, 1mm. https://www.liros.com/catalog/de/d-pro-1mm-p871/. Access on 13.12.2023.

[LIROS GmbH, 2023b] LIROS GmbH (2023b). Technische Informationen. https://www.liros.com/catalog/de/support/technische-infos/. Access on 13.12.2023.

[Lou, 2021] Lou, D.-P. (2021). Weiterentwicklung einer BIM-Toolchain zur automatisierten Zerlegung und Anpassung von Gebäudeentwürfen für den Mauerwerksbau mit Seilrobotern. Masterarbeit, Universität Duisburg-Essen, Fakultät für Ingenieurwissenschaften.

[Lunze and Steffen, 2003] Lunze, J. and Steffen, T. (2003). Rekonfiguration linearer Systeme bei Aktor- und Sensorfehlern . *At-automatisierungstechnik - AT-AUTOM*, 51:60–68. https://doi.org/10.1524/auto.51.2.60.22802.

[Lytle et al., 2008] Lytle, A., Proctor, F., and Saidi, K. (2008). Control of cable robots for construction applications. In Wu, H., editor, *Parallel Manipulators*, chapter 1. IntechOpen, Rijeka. https://dx.doi.org/10.5772/5423.

[Ma et al., 2019] Ma, T., Xiong, H., Zhang, L., and Diao, X. (2019). Control of a cable-driven parallel robot via deep reinforcement learning. In *2019 IEEE International Conference on Advanced Robotics and its Social Impacts (ARSO)*, pages 275–280. https://doi.org/10.1109/ARSO46408.2019.8948792.

[Maciejewski, 1990] Maciejewski, A. A. (1990). Fault tolerant properties of kinematically redundant manipulators. *Proceedings., IEEE International Conference on Robotics and Automation*, pages 638–642 vol.1. https://doi.org/10.1109/ROBOT.1990.126054.

[Maeda, 1994] Maeda, J. (1994). Development and application of the smart system. In Chamberlain, D. A., editor, *Automation and Robotics in Construction XI*, pages 457–464. Elsevier Science B.V.

[Mao and Agrawal, 2012] Mao, Y. and Agrawal, S. (2012). Design of a Cable-Driven Arm Exoskeleton (CAREX) for Neural Rehabilitation. *Robotics, IEEE Transactions on*, 28:922–931. https://doi.org/10.1109/TRO.2012.2189496.

[Martin et al., 2023] Martin, C., Fabritius, M., Lehnertz, C., Jurašić, P., Stoll, J. T., Ernst, M. O., Kraus, W., and Pott, A. (2023). IPAnema Silent: A CDPR for Spatial Hearing Experiments. In Caro, S., Pott, A., and Bruckmann, T., editors, *Cable-Driven Parallel Robots*, pages 407–418, Cham. Springer Nature Switzerland. https://doi.org/10.1007/978-3-031-32322-5_33.

[Martin et al., 2021] Martin, C., Fabritius, M., Stoll, J. T., and Pott, A. (2021). Accuracy Improvement for CDPRs Based on Direct Cable Length Measurement Sensors. In Gouttefarde, M., Bruckmann, T., and Pott, A., editors, *Cable-Driven Parallel Robots*, pages 348–359, Cham. Springer International Publishing. https://doi.org/10.1007/978-3-030-75789-2_28.

[Marx and König, 2013] Marx, A. and König, M. (2013). Modeling and simulating spatial requirements of construction activities. In *Proceedings of the 2013 Winter Simulation Conference - Simulation: Making Decisions in a Complex World (WSC 2013)*, pages 3294–3305. https://dx.doi.org/10.1109/WSC.2013.6721694.

[Mattioni et al., 2023] Mattioni, V., Idà, E., Gouttefarde, M., and Carricato, M. (2023). A practical approach for the hybrid joint-space control of overconstrained cable-driven parallel robots. In Caro, S., Pott, A., and Bruckmann, T., editors, *Cable-Driven Parallel Robots*, pages 149–160, Cham. Springer Nature Switzerland. https://doi.org/10.1007/978-3-031-32322-5_12.

[McNeel and Associates, 2023] McNeel, R. and Associates (2023). Grasshopper - Neu in Rhino 6. https://www.rhino3d.com/6/new/grasshopper/. Access on 13.12.2023.

[Merlet, 2004a] Merlet, J.-P. (2004a). Analysis of the influence of wires interference on the workspace of wire robots. In Lenarčič, J. and Galletti, C., editors, *On Advances in Robot Kinematics*, pages 211–218, Dordrecht. Springer Netherlands. https://doi.org/10.1007/978-1-4020-2249-4_23.

[Merlet, 2004b] Merlet, J. P. (2004b). Solving the Forward Kinematics of a Gough-Type Parallel Manipulator with Interval Analysis. *The International Journal of Robotics Research*, pages 221–235. https://doi.org/10.1177/0278364904039806.

[Merlet, 2010] Merlet, J. P. (2010). *Parallel Robots*. Springer Publishing Company, Incorporated. https://doi.org/10.1007/1-4020-4133-0.

[Merlet, 2015] Merlet, J.-P. (2015). The kinematics of cable-driven parallel robots with sagging cables: preliminary results. In *2015 IEEE International Conference on Robotics and Automation (ICRA)*, pages 1593–1598. https://doi.org/10.1109/ICRA.2015.7139401.

[Merlet and Daney, 2006] Merlet, J.-P. and Daney, D. (2006). Legs interference checking of parallel robots over a given workspace or trajectory. pages 757 – 762. https://doi.org/10.1109/ROBOT.2006.1641801.

[Miermeister et al., 2015] Miermeister, P., Kraus, W., Lan, T., and Pott, A. (2015). An elastic cable model for cable-driven parallel robots including hysteresis effects. volume 32, pages 17–28. https://doi.org/10.1007/978-3-319-09489-2_2.

[Miermeister et al., 2016] Miermeister, P., Lächele, M., Boss, R., Masone, C., Schenk, C., Tesch, J., Kerger, M., Teufel, H., Pott, A., and Bülthoff, H. H. (2016). The cablerobot simulator large scale motion platform based on cable robot technology. In *2016 IEEE/RSJ International Conference on Intelligent Robots and Systems (IROS)*, pages 3024–3029. https://doi.org/10.1109/IROS.2016.7759468.

[Miermeister et al., 2012] Miermeister, P., Pott, A., and Verl, A. (2012). Auto-calibration method for overconstrained cable-driven parallel robots. In *ROBOTIK 2012; 7th German Conference on Robotics*, pages 301–306.

[Mikelsons et al., 2008] Mikelsons, L., Bruckmann, T., Hiller, M., and Schramm, D. (2008). A real-time capable force calculation algorithm for redundant tendon-based parallel manipulators. In *2008 IEEE International Conference on Robotics and Automation*, pages 3869–3874. https://doi.org/10.1109/ROBOT.2008.4543805.

[Ming and Higuchi, 1994a] Ming, A. and Higuchi, T. (1994a). Study on multiple degree-of-freedom positioning mechanism using wires. ii: Development of a planar completely restrained positioning mechanism. *International Journal of The Japan Society for Precision Engineering*, 28:235–242.

[Ming and Higuchi, 1994b] Ming, A. and Higuchi, T. (1994b). Study on multiple degree-of-freedom positioning mechanism using wires (part 1) - concept, design and control. *International Journal of the Japan Society for Precision Engineering*, 28(2):131–138.

[Miyasaka et al., 2015] Miyasaka, M., Matheson, J., Lewis, A., and Hannaford, B. (2015). Measurement of the cable-pulley coulomb and viscous friction for a cable-driven surgical robotic system. In *2015 IEEE/RSJ International Conference on Intelligent Robots and Systems (IROS)*, pages 804–810. https://doi.org/10.1109/IROS.2015.7353464.

[Moreira et al., 2015] Moreira, E., Pinto, A. M., Costa, P., Moreira, A. P., Veiga, G., Lima, J., Sousa, J. P., and Costa, P. (2015). Cable robot for non-standard architecture and construction: A dynamic positioning system. In *2015 IEEE International Conference on Industrial Technology (ICIT)*, pages 3184–3189. https://dx.doi.org/10.1109/ICIT.2015.7125568.

[Mousavian and Gentry, 2014] Mousavian, E. and Gentry, T. R. (2014). Digital tools for automated generation of vaulted brick assemblies for construction and structural analysis. In *9th International Masonry Conference*, Guimarães, Portugal.

[Müller et al., 2014] Müller, K., Reichert, C., and Bruckmann, T. (2014). Analysis of geometrical force calculation algorithms for cable-driven parallel robots with a threefold redundancy. In Lenarčič, J. and Khatib, O., editors, *Advances in Robot Kinematics*, pages 203–211, Cham. Springer International Publishing. https://doi.org/10.1007/978-3-319-06698-1_22.

[Müller et al., 2015] Müller, K., Reichert, C., and Bruckmann, T. (2015). Analysis of a real-time capable cable force computation method. In Pott, A. and Bruckmann, T., editors, *Cable-Driven Parallel Robots*, pages 227–238, Cham. Springer International Publishing. https://doi.org/10.1007/978-3-319-09489-2_16.

[Nguyen and Gouttefarde, 2014] Nguyen, D. Q. and Gouttefarde, M. (2014). Stiffness matrix of 6-dof cable-driven parallel robots and its homogenization. In Lenarčič, J. and Khatib,

O., editors, *Advances in Robot Kinematics*, pages 181–191, Cham. Springer International Publishing. https://doi.org/10.1007/978-3-319-06698-1_20.

[Nguyen and Gouttefarde, 2015] Nguyen, D. Q. and Gouttefarde, M. (2015). On the improvement of cable collision detection algorithms. *Mechanisms and Machine Science*, 32:29–40. https://doi.org/10.1007/978-3-319-09489-2_3.

[Nicodemus et al., 2022] Nicodemus, J., Kneifl, J., Fehr, J., and Unger, B. (2022). Physics-informed neural networks-based model predictive control for multi-link manipulators. *IFAC-PapersOnLine*, 55(20):331–336. 10th Vienna International Conference on Mathematical Modelling MATHMOD 2022. https://doi.org/10.1016/j.ifacol.2022.09.117.

[Nolting, W., 1997] Nolting, W. (1997). *Grundkurs Theoretische Physik. 1. Klassische Mechanik*. Springer. https://doi.org/10.1007/978-3-642-29937-7.

[Notash, 2000] Notash, L. (2000). Joint sensor fault detection for fault tolerant parallel manipulators. *Journal of Robotic Systems*, 17(3):149–157. https://doi.org/10.1002/(SICI)1097-4563(200003)17:3<149::AID-ROB2>3.0.CO;2-N.

[Notash, 2012] Notash, L. (2012). Failure recovery for wrench capability of wire-actuated parallel manipulators. *Robotica*, 30(6):941—-950. https://doi.org/10.1017/S0263574711001160.

[Notash, 2013] Notash, L. (2013). Wrench recovery for wire-actuated parallel manipulators. In Padois, V., Bidaud, P., and Khatib, O., editors, *Romansy 19 – Robot Design, Dynamics and Control*, pages 201–208, Vienna. Springer Vienna. https://doi.org/10.1007/978-3-7091-1379-0_25.

[Notash and Huang, 2003] Notash, L. and Huang, L. (2003). On the design of fault tolerant parallel manipulators. *Mechanism and Machine Theory*, 38(1):85–101. https://doi.org/10.1016/S0094-114X(02)00067-8.

[Oh and Agrawal, 2005] Oh, S.-R. and Agrawal, S. K. (2005). Cable suspended planar robots with redundant cables: controllers with positive tensions. *IEEE Transactions on Robotics*, 21(3):457–465. https://doi.org/10.1109/TRO.2004.838029.

[Otis et al., 2009] Otis, M. J.-D., Perreault, S., Nguyen-Dang, T.-L., Lambert, P., Gouttefarde, M., Laurendeau, D., and Gosselin, C. (2009). Determination and management of cable interferences between two 6-dof foot platforms in a cable-driven locomotion interface. *IEEE Transactions on Systems, Man, and Cybernetics - Part A: Systems and Humans*, 39(3):528–544. https://doi.org/10.1109/TSMCA.2009.2013188.

[PAGEL Spezial-Beton GmbH & Co. KG, 2019] PAGEL Spezial-Beton GmbH & Co. KG (2019). TUDALIT®-FEINBETON – TF10 TUDALIT®-FEINBETON (0–1 mm). Technisches Merkblatt, Essen. https://www.pagel.com/all/pdf/de/tf10_de.pdf. Access on 13.12.2023.

[Papacharalampopoulos et al., 2020] Papacharalampopoulos, A., Bikas, H., Foteinopoulos, P., and Stavropoulos, P. (2020). A path planning optimization framework for concrete based additive manufacturing processes. *Procedia Manufacturing*, 51:649 – 654. 30th International Conference on Flexible Automation and Intelligent Manufacturing (FAIM2021). https://dx.doi.org/10.1016/j.promfg.2020.10.091.

[Passarini et al., 2019] Passarini, C., Zanotto, D., and Boschetti, G. (2019). Dynamic trajectory planning for failure recovery in cable-suspended camera systems. *Journal of Mechanisms and Robotics*, 11(2). https://doi.org/10.1115/1.4041942.

[Perreault et al., 2010] Perreault, S., Cardou, P., Gosselin, C., and Otis, M. (2010). Geometric determination of the interference-free constant-orientation workspace of parallel cable-driven mechanisms. *ASME Journal of Mechanisms and Robotics*, 2. https://doi.org/10.1115/1.4001780.

[Pfeil, 2023] Pfeil, A. (2023). *Auslegung und Betrieb einer durch Seilrobotertechnik teilautomatisierten Baustelle*. PhD thesis, Universität Duisburg-Essen, Essen. Submitted.

[Pfeil and Kemand, 2023] Pfeil, A. and Kemand, A. (2023). *BIM Basics: BIM-Automation und Robotik*. bSD Verlag.

[Pham, 2015] Pham, Q.-C. (2015). Trajectory planning. In Nee, A. Y. C., editor, *Handbook of Manufacturing Engineering and Technology*, pages 1873–1887, London. Springer London. https://doi.org/10.1007/978-1-4471-4670-4_92.

[Piao et al., 2019] Piao, J., Kim, E.-S., Choi, H., Moon, C.-B., Choi, E., Park, J.-O., and Kim, C.-S. (2019). Indirect force control of a cable-driven parallel robot: Tension estimation using artificial neural network trained by force sensor measurements. *Sensors*, 19(11). https://doi.org/10.3390/s19112520.

[Picard et al., 2018] Picard, E., Caro, S., Plestan, F., and Claveau, F. (2018). Control Solution for a Cable-Driven Parallel Robot With Highly Variable Payload. volume 5B: 42nd Mechanisms and Robotics Conference of *International Design Engineering Technical Conferences and Computers and Information in Engineering Conference*. https://doi.org/10.1115/DETC2018-85304.

[Pott, 2008] Pott, A. (2008). Forward kinematics and workspace determination of a wire robot for industrial applications. In Lenarčič, J. and Wenger, P., editors, *Advances in Robot Kinematics: Analysis and Design*, pages 451–458, Dordrecht. Springer Netherlands. https://doi.org/10.1007/978-1-4020-8600-7_47.

[Pott, 2010] Pott, A. (2010). An algorithm for real-time forward kinematics of cable-driven parallel robots. In Lenarcic, J. and Stanisic, M. M., editors, *Advances in Robot Kinematics: Motion in Man and Machine*, pages 529–538, Dordrecht. Springer Netherlands. https://doi.org/10.1007/978-90-481-9262-5_57.

[Pott, 2014] Pott, A. (2014). An improved force distribution algorithm for over-constrained cable-driven parallel robots. In Thomas, F. and Perez Gracia, A., editors, *Computational Kinematics*, pages 139–146, Dordrecht. Springer Netherlands. https://doi.org/10.1007/978-94-007-7214-4_16.

[Pott, 2018] Pott, A. (2018). *Cable-Driven Parallel Robots: Theory and Application*. Springer Tracts in Advanced Robotics. Springer. https://www.doi.org/10.1007/978-3-319-76138-1.

[Pott and Bruckmann, 2014] Pott, A. and Bruckmann, T. (2014). *Cable-Driven Parallel Robots: Proceedings of the Second International Conference on Cable-Driven Parallel Robots*. Mechanisms and Machine Science. Springer International Publishing. https://doi.org/10.1007/978-3-319-09489-2.

[Pott and Bruckmann, 2019] Pott, A. and Bruckmann, T. (2019). *Cable-Driven Parallel Robots: Proceedings of the 4th International Conference on Cable-Driven Parallel Robots*. Mechanisms and Machine Science. Springer International Publishing. https://doi.org/10.1007/978-3-030-20751-9.

[Pott et al., 2009] Pott, A., Bruckmann, T., and Mikelsons, L. (2009). Closed-form force distribution for parallel wire robots. In Kecskeméthy, A. and Müller, A., editors, *Computational Kinematics*, pages 25–34, Berlin, Heidelberg. Springer. https://doi.org/10.1007/978-3-642-01947-0_4.

[Pott et al., 2013] Pott, A., Mütherich, H., Kraus, W., Schmidt, V., Miermeister, P., and Verl, A. (2013). Ipanema: A family of cable-driven parallel robots for industrial applications. In Bruckmann, T. and Pott, A., editors, *Cable-Driven Parallel Robots*, pages 119–134, Berlin, Heidelberg. Springer Berlin Heidelberg. https://doi.org/10.1007/978-3-642-31988-4_8.

[Pott et al., 2019] Pott, A., Tempel, P., Verl, A., and Wulle, F. (2019). Design, implementation and long-term running experiences of the cable-driven parallel robot caro

printer. In Pott, A. and Bruckmann, T., editors, *Cable-Driven Parallel Robots*, pages 379–390, Cham. Springer International Publishing. https://dx.doi.org/10.1007/978-3-030-20751-9_32.

[Pritschow et al., 1994] Pritschow, G., Dalacker, M., Kurz, J., and Zeiher, J. (1994). A mobile robot for on-site construction of masonry. In *Proceedings of IEEE/RSJ International Conference on Intelligent Robots and Systems (IROS'94)*, volume 3, pages 1701–1707. IEEE. https://dx.doi.org/10.1109/IROS.1994.407628.

[Pritschow et al., 1998] Pritschow, G., Kurz, J., Fessele, T., and Scheurer, F. (1998). Robotic on-site construction of masonry. In *Proceedings of the 15th International Symposium on Automation and Robotics in Construction (ISARC)*, pages 55–64, München. The International Association for Automation and Robotics in Construction (IAARC). https://dx.doi.org/10.22260/ISARC1998/0007.

[Pusey et al., 2004] Pusey, J., Fattah, A., Agrawal, S., and Messina, E. (2004). Design and workspace analysis of a 6–6 cable-suspended parallel robot. *Mechanism and Machine Theory*, 39(7):761–778. https://doi.org/10.1016/j.mechmachtheory.2004.02.010.

[Qin and Badgwell, 2003] Qin, S. and Badgwell, T. A. (2003). A survey of industrial model predictive control technology. volume 11, pages 733–764. https://doi.org/10.1016/S0967-0661(02)00186-7.

[Raman et al., 2022] Raman, A., Walker, I., Krovi, V., and Schmid, M. (2022). A failure identification and recovery framework for a planar reconfigurable cable driven parallel robot. *IFAC-PapersOnLine*, 55(37):369–375. https://doi.org/10.1016/j.ifacol.2022.11.211.

[Raman et al., 2023] Raman, A., Walker, I., Krovi, V., and Schmid, M. (2023). Cable failure tolerant control and planning in a planar reconfigurable cable driven parallel robot. *Frontiers in Robotics and AI*, 10. https://doi.org/10.3389/frobt.2023.1070627.

[RazaviAlavi and AbouRizk, 2017] RazaviAlavi, S. and AbouRizk, S. (2017). Site layout and construction plan optimization using an integrated genetic algorithm simulation framework. *Journal of Computing in Civil Engineering*, 31(4):04017011. https://dx.doi.org/10.1061/(ASCE)CP.1943-5487.0000653.

[red cable robots GmbH, 2023] red cable robots GmbH (2023). red cable robots - expanding the dimensions of automation. https://www.redcablerobots.com/. Access on 13.12.2023.

[Reichert and Bruckmann, 2015] Reichert, C. and Bruckmann, T. (2015). Unified contact force control approach for cable-driven parallel robots using an impedance/admittance

control strategy. In *Proceedings of the 14th IFToMM World Congress*, pages 645–654, Taipei. https://doi.org/10.6567/IFToMM.14TH.WC.OS13.020.

[Reichert et al., 2015a] Reichert, C., Glogowski, P., and Bruckmann, T. (2015a). Dynamische Rekonfiguration eines seilbasierten Manipulators zur Verbesserung der mechanischen Steifigkeit. In Bertram, T., Corves, B., and Janschek, K., editors, *Fachtagung Mechatronik 2015: Dortmund (March 12.-13., 2015), Proceedings*, pages 91–96, Aachen, Germany. Institute of Mechanism Theory, Machine Dynamics and Robotics.

[Reichert et al., 2014] Reichert, C., Müller, K., and Bruckmann, T. (2014). Internal force-based impedance control for cable-driven parallel robots. In Ceccarelli, M. and Glazunov, V. A., editors, *Advances on Theory and Practice of Robots and Manipulators – Proceedings of ROMANSY 2014 - XX CISM-IFToMM Symposium on Theory and Practice of Robots and Manipulators*, volume 22, pages 435–443. Springer. https://doi.org/10.1007/978-3-319-07058-2_49.

[Reichert et al., 2015b] Reichert, C., Unterberg, U., and Bruckmann, T. (2015b). Energieoptimale Trajektorien für seilbasierte Manipulatoren unter Verwendung von passiven Elementen. In *First IFToMM D-A-CH Conference 2015, 11. März 2015, TU Dortmund*. DuEPublico, Universität Duisburg-Essen. https://doi.org/10.17185/duepublico/37261.

[Rich, 2014] Rich, H. (2014). *Kalksandstein: Die Maurerfibel*. Verlag Bau+Technik GmbH, 8 edition. Bundesverband Kalksandsteinindustrie e.V.

[Riehl et al., 2009] Riehl, N., Gouttefarde, M., Krut, S., Baradat, C., and Pierrot, F. (2009). Effects of non-negligible cable mass on the static behavior of large workspace cable-driven parallel mechanisms. In *2009 IEEE International Conference on Robotics and Automation*, pages 2193–2198. https://doi.org/10.1109/ROBOT.2009.5152576.

[Roberts et al., 1998] Roberts, R. G., Graham, T., and Lippitt, T. (1998). On the inverse kinematics, statics, and fault tolerance of cable-suspended robots. *Journal of Robotic Systems*, 15(10):581–597. https://doi.org/10.1002/(SICI)1097-4563(199810)15:10<581::AID-ROB4>3.0.CO;2-P.

[Roske et al., 2021a] Roske, T., Lipowsky, J., Palzer, U., Eden, W., Schäfers, M., Lemmen, P., Heidel, R., Boumann, R., Spengler, A., and Bruckmann, T. (2021a). Automated construction of calcium silicate mansory by cable robots. *Autoclaved Aerated Concrete (AAC) Worldwide*, (1):34–40.

[Roske et al., 2021b] Roske, T., Lipowsky, J., Palzer, U., Eden, W., Schäfers, M., Lemmen, P., Heidel, R., Boumann, R., Spengler, A., and Bruckmann, T. (2021b). Automatisierter

Bau von Kalksandstein-Mauerwerk mit Seilrobotern. *Mauerwerk*, 25(2):82–89. https://doi.org/10.1002/dama.202110011.

[Ruderman, 2012] Ruderman, M. (2012). *Zur Modellierung und Kompensation dynamischer Reibung in Aktuatorsystemen*. PhD thesis, TU Dortmund, Dortmund. https://doi.org/10.17877/DE290R-4865.

[Rushton and Khajepour, 2021] Rushton, M. and Khajepour, A. (2021). Variable-structure cable-driven parallel robots. In Gouttefarde, M., Bruckmann, T., and Pott, A., editors, *Cable-Driven Parallel Robots*, pages 206–214, Cham. Springer International Publishing. https://doi.org/10.1007/978-3-030-75789-2_17.

[Sacks et al., 2020] Sacks, R., Brilakis, I., Pikas, E., Xie, H., and Girolami, M. (2020). Construction with digital twin information systems. *Data-Centric Engineering*, 1. https://dx.doi.org/10.1017/dce.2020.16.

[Sacks et al., 2018] Sacks, R., Eastman, C., Lee, G., and Teicholz, P. (2018). *BIM Handbook: A Guide to Building Information Modeling for Owners, Designers, Engineers, Contractors, and Facility Managers*. Wiley. https://dx.doi.org/10.1002/9781119287568.

[Salah et al., 2015] Salah, B., Janeh, O., Bruckmann, T., and Noche, B. (2015). Improving the performance of a new storage and retrieval machine based on a parallel manipulator using fmea analysis. *IFAC-PapersOnLine*, 48(3):1658 – 1663. 15th IFAC Symposium on Information Control Problems in Manufacturing. https://doi.org/10.1016/j.ifacol.2015.06.324.

[Sandy et al., 2016] Sandy, T., Giftthaler, M., Dörfler, K., Kohler, M., and Buchli, J. (2016). Autonomous repositioning and localization of an in situ fabricator. In *2016 IEEE International Conference on Robotics and Automation (ICRA)*, pages 2852–2858. https://dx.doi.org/10.1109/ICRA.2016.7487449.

[Sanjuan et al., 2020] Sanjuan, J., Castillo, A., Padilla, M., Quintero, M., Gutierrez, E., Sampayo, I., Hernandez, J., and Rahman, M. (2020). Cable driven exoskeleton for upper-limb rehabilitation: A design review. *Robotics and Autonomous Systems*, 126:103445. https://doi.org/10.1016/j.robot.2020.103445.

[Schittkowski and Zillober, 2005] Schittkowski, K. and Zillober, C. (2005). Nonlinear programming: Algorithms, software, and applications. In Cagnol, J. and Zolésio, J.-P., editors, *System Modeling and Optimization*, pages 73–107, Boston, MA. Springer US. https://doi.org/10.1007/0-387-23467-5_5.

[Schmidt et al., 2014] Schmidt, V., Müller, B., and Pott, A. (2014). Solving the forward kinematics of cable-driven parallel robots with neural networks and interval arithmetic. In Thomas, F. and Perez Gracia, A., editors, *Computational Kinematics*, pages 103–110, Dordrecht. Springer Netherlands. https://doi.org/10.1007/978-94-007-7214-4_12.

[Schmidt and Pott, 2013] Schmidt, V. and Pott, A. (2013). Implementing extended kinematics of a cable-driven parallel robot in real-time. *Mechanisms and Machine Science*, 12:287–298. https://doi.org/10.1007/978-3-642-31988-4_18.

[Schramm et al., 2018] Schramm, D., Hiller, M., and Bardini, R. (2018). *Modellbildung und Simulation der Dynamik von Kraftfahrzeugen*. Springer Vieweg, 3 edition. https://doi.org/10.1007/978-3-662-54481-5.

[Shahmiri and Gentry, 2016] Shahmiri, F. and Gentry, T. R. (2016). A survey of cable-suspended parallel robots and their applications in architecture and construction. In *SIGraDi 2016, XX Congress of the Iberoamerican Society of Digital Graphics*, Blucher Design Proceedings, pages 914–920, Buenos Aires, Argentina. https://dx.doi.org/10.5151/despro-sigradi2016-484.

[Siciliano and Khatib, 2008] Siciliano, B. and Khatib, O. (2008). *Springer Handbook of Robotics*. Springer Handbook of Robotics. Springer Berlin Heidelberg. https://doi.org/10.1007/978-3-540-30301-5.

[Sieberg, 2021] Sieberg, P. M. (2021). *Hybrid Methods in Vehicle Dynamics State Estimation and Control – Exploiting Potentials and Ensuring Reliability of Artificial Intelligence*. PhD thesis, Universität Duisburg-Essen, Duisburg. https://doi.org/10.17185/duepublico/74460.

[Sousa et al., 2016] Sousa, J. P., Palop, C., Moreira, E., Pinto, A. M., Lima, J., Costa, P., Costa, P., Veiga, G., and Moreira, A. P. (2016). The spiderobot: A cable-robot system for on-site construction in architecture. In Reinhardt, D., Saunders, R., and Burry, J., editors, *Robotic Fabrication in Architecture, Art and Design 2016*, pages 230–239. Springer International Publishing. https://dx.doi.org/10.1007/978-3-319-26378-6_17.

[Spath et al., 1994] Spath, D., Andres, J., Bock, T., and Steffani, H. F. (1994). Flexible Automatisierung im Mauerwerksbau. In *Autonome Mobile Systeme 1994*, pages 306–315. Springer. https://doi.org/10.1007/978-3-642-79267-0_28.

[Spong et al., 2005] Spong, M. W., Hutchinson, S., and Vidyasagar, M. (2005). *Robot Modeling and Control*. Jon Wiley & Sons.

[Spydercam, 2023] Spydercam (2023). Academy award winning suspended camera systems. http://www.spydercam.com/. Access on 13.12.2023.

[Stark, 2022] Stark, R. (2022). *Virtual Product Creation in Industry*. https://dx.doi.org/10.1007/978-3-662-64301-3.

[Stewart, 1965] Stewart, D. (1965). A platform with six degrees of freedom. *Institution of Mechanical Engineers*, 180(15):371–385. Part 1. https://doi.org/10.1243/PIME_PROC_1965_180_029_02.

[Stewart, 1966] Stewart, D. (1966). A platform with six degrees of freedom: A new form of mechanical linkage which enables a platform to move simultaneously in all six degrees of freedom developed by elliott-automation. *Aircraft Engineering and Aerospace Technology*, 38(4):30–35. https://doi.org/10.1108/eb034141.

[Stocco et al., 1998] Stocco, L., Salcudean, S., and Sassani, F. (1998). Matrix normalization for optimal robot design. In *1998 IEEE International Conference on Robotics and Automation (Cat. No.98CH36146)*, volume 2, pages 1346–1351. https://doi.org/10.1109/ROBOT.1998.677292.

[Stribeck, 1903] Stribeck, R. (1903). Die wesentlichen Eigenschaften der Gleit- und Rollenlager. Mitteilungen über Forschungsarbeiten auf dem Gebiete des Ingenieurwesens, insbesondere aus den Laboratorien der technischen Hochschulen. Springer.

[Sturm, 2020] Sturm, C. (2020). *Realisierung, Steuerung und Regelung kinematisch zweifach redundanter paralleler Seilroboter*. PhD thesis, Universität Duisburg-Essen, Duisburg. https://doi.org/10.17185/duepublico/73291.

[Sturm et al., 2011] Sturm, C., Wildan, L., and Bruckmann, T. (2011). Wire robot suspension systems for wind tunnels. In Lerner, J. C. and Boldes, U., editors, *Wind Tunnels and Experimental Fluid Dynamics Research*, chapter 2. IntechOpen, Rijeka. https://doi.org/10.5772/21578.

[Sunan et al., 2001] Sunan, H., Kiong, T. K., and Heng, L. T. (2001). *Applied Predictive Control*. Advances in Industrial Control. Springer London. https://doi.org/10.1007/978-1-4471-3725-2.

[Taghirad and Nahon, 2008] Taghirad, H. D. and Nahon, M. (2008). Kinematic analysis of a macro–micro redundantly actuated parallel manipulator. *Advanced Robotics*, 22(6-7):657–687. https://doi.org/10.1163/156855308X305263.

[Tempel, 2019] Tempel, P. (2019). *Dynamics of cable-driven parallel robots with elastic and flexible, time-varying length cables*. PhD thesis, Universität Stuttgart, Stuttgart.

[Tempel et al., 2017] Tempel, P., Herve, P.-E., Tempier, O., Gouttefarde, M., and Pott, A. (2017). Estimating inertial parameters of suspended cable-driven parallel robots — use case on cogiro. In *2017 IEEE International Conference on Robotics and Automation (ICRA)*, pages 6093–6098. https://doi.org/10.1109/ICRA.2017.7989723.

[The MathWorks, Inc., 2023a] The MathWorks, Inc. (2023a). Constrained Nonlinear Optimization Algorithms. https://de.mathworks.com/help/optim/ug/constrained-nonlinear-optimization-algorithms.html. Access on 13.12.2023.

[The MathWorks, Inc., 2023b] The MathWorks, Inc. (2023b). Documentation fmincon. https://de.mathworks.com/help/optim/ug/fmincon.html. Access on 13.12.2023.

[The MathWorks, Inc., 2023c] The MathWorks, Inc. (2023c). Global Optimization Toolbox - Lösung von nicht glatten Optimierungsproblemen und Optimierungsproblemen mit mehreren Maxima und Minima. https://de.mathworks.com/products/global-optimization.html. Access on 13.12.2023.

[The MathWorks, Inc., 2023d] The MathWorks, Inc. (2023d). Simscape - Modellieren und Simulieren von physikalischen Mehrdomänen-Systemen. https://de.mathworks.com/products/simscape.html. Access on 13.12.2023.

[The MathWorks, Inc., 2023e] The MathWorks, Inc. (2023e). Simulink - gemacht für Model-Based Design. https://de.mathworks.com/products/simulink.html. Access on 13.12.2023.

[Ting et al., 1995] Ting, Y., Tosunoglu, S., and Freeman, R. (1995). Torque redistribution and time regulation methods for actuator of fault-tolerant parallel robots. *Journal of Robotic Systems*, 12(12):807–820. https://doi.org/10.1002/rob.4620121205.

[Trautwein et al., 2021] Trautwein, F., Reichenbach, T., Pott, A., and Verl, A. (2021). Workspace planning for in-operation-reconfiguration of cable-driven parallel robots. In Gouttefarde, M., Bruckmann, T., and Pott, A., editors, *Cable-Driven Parallel Robots*, pages 182–193, Cham. Springer International Publishing. https://doi.org/10.1007/978-3-030-75789-2_15.

[Tribune News Services, 2011] Tribune News Services (2011). No one hurt after ESPN SkyCam falls during Insight Bowl. https://www.chicagotribune.com/sports/ct-xpm-2011-12-31-chi-no-one-hurt-after-espn-skycam-falls-during-insight-bowl-20111231-story.html. Access on 13.12.2023.

[Umbreit, 2022] Umbreit, M. (2022). Industrieroboter – Grundlagen für sicheres Arbeiten. https://www.bghm.de/fileadmin/user_upload/BGHM/Presseportal/

Fachartikel2022/Idustrieroboter-Grundlagen-sicheres-Arbeiten-Factory-Innovation_-2022.pdf. Access on 13.12.2023.

[VDI/VDE, 2021] VDI/VDE (2021). VDI/VDE 2206:2021-11: Development of mechatronic and cyber-physical systems.

[Verhoeven, 2006] Verhoeven, R. (2006). *Analysis of the Workspace of Tendon-based Stewart Platforms*. PhD thesis, Universität Duisburg-Essen.

[Verhoeven and Hiller, 2002] Verhoeven, R. and Hiller, M. (2002). Tension distribution in tendon-based stewart platforms. In Lenarčič, J. and Thomas, F., editors, *Advances in Robot Kinematics: Theory and Applications*, pages 117–124, Dordrecht. Springer Netherlands. https://doi.org/10.1007/978-94-017-0657-5_13.

[Verhoeven et al., 1998] Verhoeven, R., Hiller, M., and Tadokoro, S. (1998). Workspace of tendon-driven stewart platforms: Basics, classification, details on the planar 2-dof class. In *Proceedings of the 4th International Conference on Motion and Vibration Control*, pages 871–876.

[Vertico, 2023] Vertico (2023). Robot Printing Setup. https://www.vertico.xyz/robot-printers. Access on 13.12.2023.

[Visinsky et al., 1994] Visinsky, M., Cavallaro, J., and Walker, I. (1994). Robotic fault detection and fault tolerance: A survey. *Reliability Engineering & System Safety*, 46(2):139–158. https://doi.org/10.1016/0951-8320(94)90132-5.

[Vogel and Wehking, 2004] Vogel, W. and Wehking, K.-H. (2004). Neuartige Maschinenelemente in der Fördertechnik und Logistik : Hochfeste, laufende Faserseile. *Logistics Journal*. https://doi.org/10.2195/lj_not_ref_d_vogel_1020042.

[Vu and Alsmadi, 2020] Vu, D.-S. and Alsmadi, A. (2020). Trajectory planning of a cable-based parallel robot using reinforcement learning and soft actor-critic. *WSEAS TRANSACTIONS ON APPLIED AND THEORETICAL MECHANICS*, 15:165–172. https://doi.org/10.37394/232011.2020.15.19.

[Vukorep, 2017] Vukorep, I. (2017). Autonomous big-scale additive manufacturing using cable-driven robots. In *Proceedings of the 34th International Symposium on Automation and Robotics in Construction*, volume 34, pages 254–259. The International Association for Automation and Robotics in Construction (IAARC). https://doi.org/10.22260/ISARC2017/0034.

[Wakisaka et al., 2000] Wakisaka, T., Furuya, N., Inoue, Y., and Shiokawa, T. (2000). Automated construction system for high-rise reinforced concrete buildings. *Automation in Construction*, 9(3):229–250. https://doi.org/10.1016/S0926-5805(99)00039-4.

[Waltz et al., 2006] Waltz, R., Morales, J., Nocedal, J., and Orban, D. (2006). An interior algorithm for nonlinear optimization that combines line search and trust region steps. *Math. Program.*, 107:391–408. https://doi.org/10.1007/s10107-004-0560-5.

[Wang et al., 2015] Wang, J., Zhang, X., Shou, W., Wang, X., Xu, B., Kim, M., and Wu, P. (2015). A BIM-based approach for automated tower crane layout planning. *Automation in Construction*, 59:168–178. https://doi.org/10.1016/j.autcon.2015.05.006.

[Wang et al., 2019] Wang, Y., Wang, Y., Lin, Q., Xiaoguang, W., and Zhou, F. (2019). Adaptive PD Control Based on RBF Neural Network for a Wire-Driven Parallel Robot and Prototype Experiments. *Mathematical Problems in Engineering*.

[Weger et al., 2021] Weger, D., Gehlen, C., Korte, W., Meyer-Brötz, F., Scheydt, J., and Stengel, T. (2021). Building rethought – 3D concrete printing in building practice. *Construction Robotics*, 5. https://doi.org/10.1007/s41693-022-00064-5.

[Wenz, 2008] Wenz, M. (2008). *Automatische Konfiguration der Bewegungssteuerung von Industrierobotern*. PhD thesis, Universität Karlsruhe (TH), Karlsruhe. https://doi.org/10.5445/IR/1000010508.

[Werdich, 2012] Werdich, M. (2012). *FMEA - Einführung und Moderation: Durch systematische Entwicklung zur übersichtlichen Risikominimierung (inkl. Methoden im Umfeld)*. https://doi.org/10.1007/978-3-8348-2217-8.

[Williams et al., 2008a] Williams, R., Xin, M., and Bosscher, P. (2008a). Contour-crafting-cartesian-cable robot system concepts: Workspace and stiffness comparisons. In *Proceedings of the ASME 2008 International Design Engineering Technical Conferences and Computers and Information in Engineering Conference. Volume 2: 32nd Mechanisms and Robotics Conference, Parts A and B*, pages 31–38. https://doi.org/10.1115/DETC2008-49478.

[Williams et al., 2008b] Williams, R., Xin, M., and Bosscher, P. (2008b). Contour-crafting-cartesian-cable robot system: Dynamics and controller design. In *Proceedings of the ASME 2008 International Design Engineering Technical Conferences and Computers and Information in Engineering Conference. Volume 2: 32nd Mechanisms and Robotics Conference, Parts A and B*, pages 36–45. https://doi.org/10.1115/DETC2008-49480.

[Williams II et al., 2004] Williams II, R. L., Albus, J. S., and Bostelman, R. V. (2004). 3d cable-based cartesian metrology system. *Journal of Robotic Systems*, 21(5):237–257. https://doi.org/10.1002/rob.20012.

[Winter and Ament, 2021] Winter, D. L. and Ament, C. (2021). Development of safety concepts for cable-driven parallel robots. In Gouttefarde, M., Bruckmann, T., and Pott, A., editors, *Cable-Driven Parallel Robots*, pages 360–371, Cham. Springer International Publishing. https://doi.org/10.1007/978-3-030-75789-2_29.

[Wittek, 2021] Wittek, T. (2021). Neuartiger Seilroboter vorgestellt: Mauern, schleppen, mörteln. https://idw-online.de/de/news778263. Access on 13.12.2023.

[Wittenburg, 2016] Wittenburg, J. (2016). *Kinematics: Theory and Applications*. Springer Berlin Heidelberg. https://doi.org/10.1007/978-3-662-48487-6.

[Witze, 2020] Witze, A. (2020). Gut-wrenching footage documents arecibo telescope's collapse. https://www.nature.com/articles/d41586-020-03421-y. Access on 13.12.2023.

[Wu et al., 2018] Wu, Y., Cheng, H., Fingrut, A., Crolla, K., Yam, Y., and Lau, D. (2018). Cu-brick cable-driven robot for automated construction of complex brick structures: From simulation to hardware realisation. In *IEEE International Conference on Simulation, Modeling, and Programming for Autonomous Robots (SIMPAR)*, pages 166–173. IEEE. https://doi.org/10.1109/SIMPAR.2018.8376287.

[XD motion SAS, 2023] XD motion SAS (2023). Experts in multi-axis dimensions. https://xd-motion.com/. Access on 13.12.2023.

[Xiong et al., 2020] Xiong, H., Ma, T., Zhang, L., and Diao, X. (2020). Comparison of end-to-end and hybrid deep reinforcement learning strategies for controlling cable-driven parallel robots. *Neurocomputing*, 377:73–84. https://doi.org/10.1016/j.neucom.2019.10.020.

[Zapolsky and Drumwright, 2015] Zapolsky, S. and Drumwright, E. M. (2015). Adaptive integration for controlling speed vs. accuracy in multi-rigid body simulation. In *2015 IEEE/RSJ International Conference on Intelligent Robots and Systems (IROS)*, pages 5388–5394. https://doi.org/10.1109/IROS.2015.7354139.

[Zhang et al., 2020a] Zhang, Z., Shao, Z., Peng, F., Li, H., and Wang, L. (2020a). Workspace Analysis and Optimal Design of a Translational Cable-Driven Parallel Robot With Passive Springs. *Journal of Mechanisms and Robotics*, 12(5):051005. https://doi.org/10.1115/1.4046030.

[Zhang et al., 2020b] Zhang, Z., Shao, Z., and Wang, L. (2020b). Optimization and implementation of a high-speed 3-dofs translational cable-driven parallel robot. *Mechanism and Machine Theory*, 145:103693. https://doi.org/10.1016/j.mechmachtheory.2019.103693.

[Zi et al., 2015] Zi, B., Lin, J., and Qian, S. (2015). Localization, obstacle avoidance planning and control of a cooperative cable parallel robot for multiple mobile cranes. *Robotics and Computer-Integrated Manufacturing*, 34:105–123. https://doi.org/10.1016/j.rcim.2014.11.005.

[Zickler R, 2021] Zickler R, Richter C, W. F. (2021). Wallbot: Robotersystem zur automatisierten Mauerwerkserrichtung. In Bertram, T., Corves, B., Janschek, K., and Rinderknecht, S., editors, *Digital Fachtagung VDI MECHATRONIK 2021*, Darmstadt. https://doi.org/10.26083/tuprints-00017626.

[Zitzewitz et al., 2013] Zitzewitz, J., Fehlberg, L., Bruckmann, T., and Vallery, H. (2013). Use of passively guided deflection units and energy-storing elements to increase the application range of wire robots. pages 167–184. https://doi.org/10.1007/978-3-642-31988-4_11.

List of Own Publications Related to this Work

1. Boumann, R. and Bruckmann, T. (2019a). Development of emergency strategies for cable-driven parallel robots after a cable break. In Pott, A. and Bruckmann, T., editors, Cable-Driven Parallel Robots, pages 269– 280. Springer Cham. https://doi.org/10.1007/978-3-030-20751-9_23.

2. Boumann, R. and Bruckmann, T. (2019b). Simulation von Seilrissen und Erweiterung von Abfangstrategien für Seilroboter. In Bertram, T., Corves, B., Gräßler, I., and Janschek, K., editors, Fachtagung Mechatronik 2019: Paderborn (March 27.-28., 2019), Proceedings.

3. Boumann, R. and Bruckmann, T. (2020a). Computationally efficient cable force calculation outside the wrench-feasible workspace. In Kuo, C.-H., Lin, P.-C., Essomba, T., and Chen, G.-C., editors, Robotics and Mechatronics, pages 177–188. Springer Cham. https://doi.org/10.1007/978-3-030-30036-4_15.

4. Boumann, R., Lemmen, P., Heidel, R., Lehmann, M., Born, O., Gosedopp, J., and Bruckmann, T. (2020b). Berechnung von Trajektorien für Seilroboter auf automatisierten Baustellen. In Sechste IFToMM D-A-CH Konferenz 2020: 27./28. Februar 2020, Campus Technik Lienz. DuEPublico, Universität Duisburg-Essen. https://doi.org/10.17185/duepublico/71180.

5. Boumann, R. and Bruckmann, T. (2020b). Real-time cable force calculation beyond the wrench-feasible workspace. Robotics, 9(2):41. https://doi.org/10.3390/robotics9020041

6. Boumann, R., Lemmen, P., Heidel, R., and Bruckmann, T. (2020a). Optimization of trajectories for cable robots on automated construction sites. In Osumi,H., Furuya, H., and Tateyama, K., editors, Proceedings of the 37th International Symposium on Automation and Robotics in Construction (ISARC), pages 465–472, Kitakyushu, Japan.

International Association for Automation and Robotics in Construction (IAARC). https://doi.org/10.22260/ISARC2020/0065.

7. Roske, T., Lipowsky, J., Palzer, U., Eden, W., Schäfers, M., Lemmen, P., Heidel, R., Boumann, R., Spengler, A., and Bruckmann, T. (2021a). Automated construction of calcium silicate mansory by cable robots. Autoclaved Aerated Concrete (AAC) Worldwide, (1):34–40.

8. Roske, T., Lipowsky, J., Palzer, U., Eden, W., Schäfers, M., Lemmen, P., Heidel, R., Boumann, R., Spengler, A., and Bruckmann, T. (2021b). Automatisierter Bau von Kalksandstein-Mauerwerk mit Seilrobotern. Mauerwerk, 25(2):82–89. https://doi.org/10.1002/dama.202110011.

9. Bruckmann, T. and Boumann, R. (2021). Simulation and optimization of automated masonry construction using cable robots. Advanced Engineering Informatics, 50:101388. https://doi.org/10.1016/j.aei.2021.101388.

10. Boumann, R. and Bruckmann, T. (2021). An emergency strategy for cable failure in reconfigurable cable robots. In Gouttefarde, M., Bruckmann, T., and Pott, A., editors, Cable-Driven Parallel Robots, pages 217–229. Springer Cham. https://doi.org/10.1007/978-3-030-75789-2_18

11. Boumann, R. and Bruckmann, T. (2022). Simulation and model-based verification of an emergency strategy for cable failure in cable robots. Actuators, 11(2):56. https://doi.org/10.3390/act11020056

12. Heidel, R., Lemmen, P., Boumann, R., and Bruckmann, T. (2022). Auslegung und Inbetriebnahme eines Seilroboters zum automatisierten Mauern von Gebäudewänden. In Bertram, T., Corves, B., Janschek, K., and Rinderknecht, S., editors, Fachtagung VDI MECHATRONIK 2022, pages 126–132, Darmstadt. https://doi.org/10.26083/tuprints-00020963.

13. Hahlbrock, D., Braun, M., Heidel, R., Lemmen, P., Boumann, R., Bruckmann, T., Schramm, D., Helm, V., and Willmann, J. (2022). Cable robotic 3d–printing: additive manufacturing on the construction site. Construction Robotics, 2022:1–14. https://doi.org/10.1007/s41693-022-00082-3

14. Herrmann, L., Boumann, R., Lehmann, M., Müller, S., and Bruckmann, T. (2022). Simulation-based comparison of novel automated construction systems. Robotics, 11(6):119. https://doi.org/10.3390/robotics11060119.

15. Jeziorek, C., Pfeil, A., Piechullik, M., Romanowski, S., Heidel, R., Boumann, R., Lemmen, P., Malkwitz, A., and Bruckmann, T. (2023). Auswahlverfahren für geeignete Deckensysteme zur Automatisierung der Rohbauerstellung. Neunte IFToMM D-A-CH Konferenz 2023: 16./17. März 2023, Universität Basel, 2023.

16. Boumann, R., Jeziorek, C., and Bruckmann, T. (2023). Validation of emergency strategies for cable-driven parallel robots after a cable failure. In Caro, S., Pott, A., and Bruckmann, T., editors, Cable-Driven Parallel Robots, pages 209–220. Springer Cham. https://doi.org/10.1007/978-3-031-32322-5_17.

17. Elhardt, F., Boumann, R., de Stefano, M., Heidel, R., Lemmen, P., Heumos, M., Jeziorek, C., Roa, M. A., Schedl, M., and Bruckmann, T. (2023a). System requirements elicitation and conceptualization for a novel space robot suspension system. In 17th Symposium on Advanced Space Technologies in Robotics and Automation.

18. Elhardt, F., Boumann, R., De Stefano, M., Heidel, R., Lemmen, P., Heumos, M., Jeziorek, C., Roa, M. A., Schedl, M., and Bruckmann, T. (2023b). The Motion Suspension System – MSS: A Cable-Driven System for On-Ground Tests of Space Robots. In Okada, M., editor, Advances in Mechanism and Machine Science, pages 379–388, Cham. Springer Nature Switzerland. https://doi.org/10.1007/978-3-031-45770-8_38.

19. Gust, P., Hürten, C., Boumann, R., and Bruckmann, T. (2024). Methoden des maschinellen Lernens als Notfallstrategie nach Seilrissen bei parallelen Seilrobotern. Zehnte IFToMM D-A-CH Konferenz 2024. Submitted.

DOI: 10.17185/duepublico/81869
URN: urn:nbn:de:hbz:465-20240419-135530-7